BEILSTEIN JOURNAL OF NANOTECHNOLOGY

Silicene, germanene and other group IV 2D materials

Edited by Patrick Vogt

Imprint

Beilstein Journal of Nanotechnology
www.bjnano.org
ISSN 2190-4286
Email: journals-support@beilstein-institut.de

The *Beilstein Journal of Nanotechnology* is published by the Beilstein-Institut zur Förderung der Chemischen Wissenschaften.

Beilstein-Institut zur Förderung der Chemischen Wissenschaften
Trakehner Straße 7–9
60487 Frankfurt am Main
Germany
www.beilstein-institut.de

BEILSTEIN JOURNAL OF NANOTECHNOLOGY

Silicene, germanene and other group IV 2D materials

Patrick Vogt

Editorial

Open Access

Address:
Institut für Physik, Technische Universität Chemnitz, Reichenhainer Str. 70, Chemnitz, Germany

Email:
Patrick Vogt - patrick.vogt@hrz.tu-chemnitz.de

Keywords:
2D materials; germanene, silicene

Beilstein J. Nanotechnol. **2018,** *9,* 2665–2667.
doi:10.3762/bjnano.9.248

Received: 11 September 2018
Accepted: 26 September 2018
Published: 10 October 2018

This article is part of the Thematic Series "Silicene, germanene and other group IV 2D materials".

Editor-in-Chief: T. Schimmel

The discovery of graphene and its tremendous impact on scientific research has initiated the search for other elemental two-dimensional (2D) honeycomb materials with potentially similar exotic properties, as predicted by theoretical investigations. These properties may allow the application of these layered structures in novel electronic devices, including ultrafast electronics, spintronics, sensors, and novel device concepts exploiting their topological properties. In recent years this search has lead to the discovery of other members of this family of 2D materials based on other group IV elements.

In 2012 silicene was first synthesized under ultrahigh vacuum conditions on a silver(111) single crystal by Si molecular beam epitaxy (MBE) [1,2] and at around the same time on zirconium diboride thin films grown on Si(111) substrates by Si segregation through the film [3]. The synthesis of silicene further launched an intensive search for other 2D elemental materials synthesized under ultrahigh vacuum by MBE-like methods. The synthesis of germanene (2D germanium) was reported in 2014 [4] and the synthesis of stanene (2D tin) in 2016 [5].

Except for their 2D character, these materials are substantially different from prototypical graphene. First of all, these materials do not exist in nature, nor do their 3D layered parent crystals from which single layers can be exfoliated. From this it follows that these materials have to be synthesized either chemically or by epitaxial growth on a supporting substrate. Thus, it should be considered that the substrate could influence the structural and electronic properties of the 2D layer.

Secondly, of these materials, only graphene is fully flat, which results from the pure sp^2 hybridization of its constituting carbon atoms. On the contrary, other group IV elements energetically prefer hybridization with an additional sp^3 character when forming a 2D honeycomb layer, which increases with increasing atomic size. As a consequence of this mixed hybridization, the bonds between adjacent atoms of the lattice are buckled, resulting in a layer that is not completely flat. Such buckling within the layer is illustrated in Figure 1 for different elemental 2D materials. For the case of silicene, it can also be seen here that the substrate material further influences the buckling within the 2D layer, resulting from the interaction between the two systems. Free-standing silicene has a buckling around 0.44 Å [6], while epitaxial silicene on Ag(111) has a value of 0.75 Å [1].

The buckling and the significant influence of the substrate have been considered as disadvantages since they influence the prop-

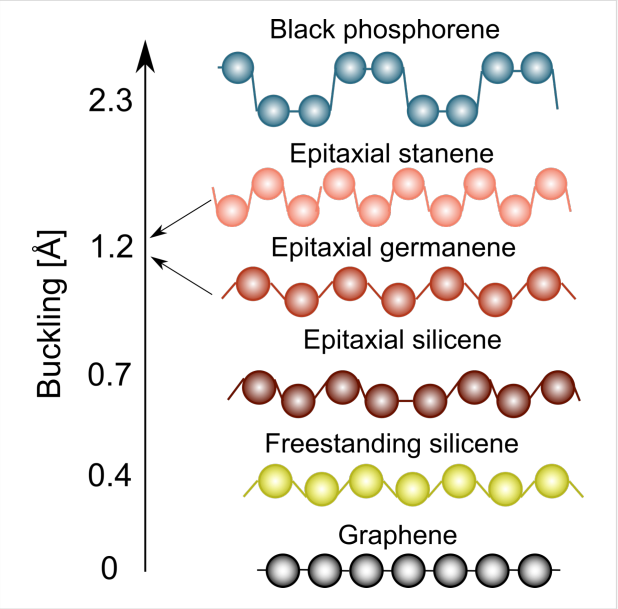

Figure 1: Illustration of the increasing buckling of different elemental 2D materials.

erties of the 2D layer. On the other hand, both characteristics also offer possibilities for tuning the properties of the 2D layer. External stimuli or the choice of the substrate can effect the buckling, which in turn, alters the properties of the 2D layer. The related modification might include, for example, the tunability of the electronic band gap, modification of the electronic band structure, or tuning the 2D topological properties. Some of these external influences might include:

- the substrate material
- external electric or magnetic fields
- tensile or compressive strain
- functionalization by atomic or molecular species

This means that the apparent disadvantage of these materials to develop a (low) buckling is in fact an advantage since it facilitates control of the 2D layer properties, for example, via chemical functionalization or external fields. This could be efficiently utilized in a transistor, where the electronic band gap can then be tuned by the electric field applied perpendicular to the lattice plane. As an example, ab initio calculations have shown that the two sub-lattices in silicene, resulting from the buckling, are moved further apart by an orthogonal electric field, which leads to a band gap opening [7,8].

Another important advantage of these new materials is the significant spin–orbit interaction, which also increases with increasing atomic size of the involved elements. This opens the way to observe a quantum spin Hall effect, for example, in germanene or stanene in an accessible temperature range, possibly even at room temperature. The occurrence of topologically nontrivial properties will be more robust for the heavier constituting elements because of the related stronger spin–orbit interaction. Topological properties are expected to enable entirely new concepts in electronic devices.

These characteristics make the young class of buckled 2D elemental materials a new progressing research field with anticipated outstanding properties of their members or as a result of their modification. In all these cases, the buckled atomic structure and the significant spin–orbit interaction may play a key role in the development of these properties.

However, before such applications are realized and final products find their way to the market, numerous technical and fundamental issues must first be solved. This concerns the synthesis of these materials, a deeper understanding of their physical properties, as well as the modification of these materials according to the factors mentioned above. Such knowledge will also help to understand the properties of 2D layers composed of elements that do not belong to group IV of the periodic table, for example, borophene [9], blue phosphorous (phosphorene) [10], or antimonene [11], most of which also show buckling.

The aim of this Thematic Series was to address the theoretical background, the growth and synthesis, the properties and application and the related difficulties still to overcome related to this new class of elemental group IV 2D materials. Of course, the included contributions can only present a snapshot of all the activities in this growing research field. I hope that the choice of articles is inspiring to the readers and reflects the important aspects of this research. I thank all authors and colleagues that have contributed their intriguing results to this Thematic Series.

Patrick Vogt

Chemnitz, September 2018

References

1. Vogt, P.; De Padova, P.; Quaresima, C.; Avila, J.; Frantzeskakis, E.; Asensio, M. C.; Resta, A.; Ealet, B.; Le Lay, G. *Phys. Rev. Lett.* **2012,** *108,* 155501. doi:10.1103/PhysRevLett.108.155501
2. Feng, B.; Ding, Z.; Meng, S.; Yao, Y.; He, X.; Cheng, P.; Chen, L.; Wu, K. *Nano Lett.* **2012,** *12,* 3507–3511. doi:10.1021/nl301047g
3. Fleurence, A.; Friedlein, R.; Ozaki, T.; Kawai, H.; Wang, Y.; Yamada-Takamura, Y. *Phys. Rev. Lett.* **2012,** *108,* 245501. doi:10.1103/PhysRevLett.108.245501
4. Dávila, M. E.; Xian, L.; Cahangirov, S.; Rubio, A.; Le Lay, G. *New J. Phys.* **2014,** *16,* 095002. doi:10.1088/1367-2630/16/9/095002
5. Zhu, F.-f.; Chen, W.-j.; Xu, Y.; Gao, C.-l.; Guan, D.-d.; Liu, C.-h.; Qian, D.; Zhang, S.-C.; Jia, J.-f. *Nat. Mater.* **2015,** *14,* 1020–1025. doi:10.1038/nmat4384

6. Cahangirov, S.; Topsakal, M.; Aktürk, E.; Şahin, H.; Ciraci, S. *Phys. Rev. Lett.* **2009,** *102,* 236804. doi:10.1103/PhysRevLett.102.236804
7. Gürel, H. H.; Özçelik, V. O.; Ciraci, S. *J. Phys.: Condens. Matter* **2013,** *25,* 305007. doi:10.1088/0953-8984/25/30/305007
8. Yan, J.-A.; Gao, S.-P.; Stein, R.; Coard, G. *Phys. Rev. B* **2015,** *91,* 245403. doi:10.1103/PhysRevB.91.245403
9. Mannix, A. J.; Zhou, X.-F.; Kiraly, B.; Wood, J. D.; Alducin, B. D.; Myers, D.; Liu, X.; Fisher, B. L.; Santiago, U.; Guest, J. R.; Yacaman, M. J.; Ponce, A.; Oganov, A. R.; Hersam, M. C.; Guisinger, N. P. *Science* **2015,** *350,* 1513–1516. doi:10.1126/science.aad1080
10. Zhang, J. L.; Zhao, S.; Han, C.; Wang, Z.; Zhong, S.; Sun, S.; Guo, R.; Zhou, X.; Gu, C. D.; Yuan, K. D.; Li, Z.; Chen, W. *Nano Lett.* **2016,** *16,* 4903–4908. doi:10.1021/acs.nanolett.6b01459
11. Ji, J.; Song, X.; Liu, J.; Yan, Z.; Huo, C.; Zhang, S.; Su, M.; Liao, L.; Wang, W.; Ni, Z.; Hao, Y.; Zeng, H. *Nat. Commun.* **2016,** *7,* 13352. doi:10.1038/ncomms13352

License and Terms

BEILSTEIN JOURNAL OF NANOTECHNOLOGY

Two-dimensional silicon and carbon monochalcogenides with the structure of phosphorene

Dario Rocca*[1,2], Ali Abboud[1], Ganapathy Vaitheeswaran[3] and Sébastien Lebègue[1,2]

Full Research Paper

Open Access

Address:
[1]Université de Lorraine, CRM2, UMR 7036, Vandoeuvre-lès-Nancy, F-54506, France, [2]CNRS, CRM2, UMR 7036, Vandoeuvre-lès-Nancy, F-54506, France and [3]Advanced Centre of Research in High Energy Materials (ACRHEM), University of Hyderabad, Prof. C. R. Rao Road, Gachibowli, Hyderabad - 500 046, India

Email:
Dario Rocca* - dario.rocca@univ-lorraine.fr

* Corresponding author

Keywords:
electronic structure; phosphorene; two-dimensional materials

Beilstein J. Nanotechnol. **2017,** *8,* 1338–1344.
doi:10.3762/bjnano.8.135

Received: 16 February 2017
Accepted: 09 June 2017
Published: 29 June 2017

This article is part of the Thematic Series "Silicene, germanene and other group IV 2D materials".

Guest Editor: P. Vogt

Abstract

Phosphorene has recently attracted significant interest for applications in electronics and optoelectronics. Inspired by this material an ab initio study was carried out on new two-dimensional binary materials with a structure analogous to phosphorene. Specifically, carbon and silicon monochalcogenides have been considered. After structural optimization, a series of binary compounds were found to be dynamically stable in a phosphorene-like geometry: CS, CSe, CTe, SiO, SiS, SiSe, and SiTe. The electronic properties of these monolayers were determined using density functional theory. By using accurate hybrid functionals it was found that these materials are semiconductors and span a broad range of bandgap values and types. Similarly to phosphorene, the computed effective masses point to a strong in-plane anisotropy of carrier mobilities. The variety of electronic properties carried by these compounds have the potential to broaden the technological applicability of two-dimensional materials.

Introduction

Over the last ten years, the interest in two-dimensional materials has increased exponentially [1]. Following the initial report of the existence of graphene [2], it was shown that isolated sheets of other layered compounds, such as h-BN or MoS_2 among others, could be obtained as well [3,4]. These compounds demonstrate properties of the electronic structure that are markedly different from those of graphene, with, for instance, the existence of a finite bandgap in the band structure [5].

One of the latest newcomers in the family of two-dimensional materials is phosphorene [6-9], which corresponds to a single layer of black phosphorus [10,11], one of the many phases of crystalline phosphorus. Among other properties [12-15], the

values of the carrier mobility and of the on–off ratio of transistors made from phosphorene are intermediate between the values of graphene and those of transition metal dichalcogenides, making phosphorene very promising for certain applications. Additionaly, phosphorene is characterized by a strong anisotropy in the carrier mobility [14] and ferroelasticity [16]. Recently, some parent compounds to phosphorene have been considered. For example, P–As compounds were studied theoretically and experimentally [17,18]. Also, arsenene and antimonene [19], SiS [20], and SnS, SnSe, GeS, and GeSe [21,22] compounds with a crystal structure similar to the one of phosphorene were investigated by ab initio calculations. The reliability of ab initio calculations to predict and characterize new two dimensional compounds is now well established. For instance borophene and graphane were predicted theoretically [23,24] before being obtained experimentally [25,26]. In the same way, planar tetracoordinate carbon was predicted computationally and then realized experimentally [27].

In this paper, by employing ab initio methods, we discuss the properties of a number of compounds that can be obtained by chemical replacement in the crystal structure of phosphorene: CS, CSe, CTe, SiO, SiS, SiSe, and SiTe. Differently from phosphorene, no layered bulk structure is known for these compounds. In a recent study Kamal et al. showed that carbon and silicon monochalcogenides are energetically stable and have their lowest energy in a phosphorene-like structure (for SiS and SiSe the puckered phosphorene-like and buckled structures are very close in energy and nearly equally probable at room temperature) [28]. By computing phonon dispersion curves, in this work we show that carbon and silicon monochalcogenides are dynamically stable in a puckered structure. Additionally, we compute band structures using the quantitatively accurate HSE06 hybrid functional [29] and we evaluate effective masses, whose anisotropy represents one of the most exotic properties of phosphorene and phosphorene-like materials. The broad range of properties showed by carbon and silicon monochalcogenides might help to extend the technological applications of two-dimensional materials.

Theoretical Methods

The calculations presented in this paper have been performed using the Quantum Espresso package [30], which is based on a plane-wave basis set and pseudopotentials. The Perdew–Burke–Ernzerhof (PBE) [31] functional has been used to optimize the structure and to compute phonon dispersion spectra. After optimizing the structure with a force threshold of at least 10^{-4} Ry/Bohr the phonon curves have been computed by using density functional perturbation theory [32]. The kinetic-energy cut-off convergence has been carefully tested for each system and a 12 × 12 × 1 *k*-point grid was used (supposing that the *z* direction is perpendicular to the two-dimensional plane). A vacuum of at least 12 Å has been used to separate periodically repeated images.

Since the PBE functional systematically underestimates the electronic gap with respect to experiments, the band structure was obtained using the HSE06 functional [29]. Because of the numerical cost involved in HSE06 calculations electronic eigenvalues have been computed on a 16 × 16 × 1 *k*-point grid; the band structure was then extracted along the high symmetry directions and interpolated with cubic splines (see below in Figure 3).

Spin–orbit coupling often plays an important role in two-dimensional materials. For example, it was shown that SnSe and GeSe phosphorene-like monochalcogenides are characterized by an anisotropic spin splitting of energy bands, leading to potential applications involving directionally dependent spin transport [22]. In [21] it was suggested that in phosphorene-like SnS, SnSe, GeS, and GeSe the spin–orbit coupling does not significantly change the shape of bands but gives rise to a splitting of the order of a few tens of millielectronvolts. Due to the high computational cost involved in spin-orbit coupling calculations with the HSE06 functional, this effect has not been included in our results. While the inclusion of spin–orbit coupling might slightly affect the values of the gaps and introduce a splitting in some bands, we do not expect a change in the overall conclusions of this work.

In the next section we also show results concerning effective masses, of which the traditional definition requires an approximately quadratic dispersion close to band edges. Differently from graphene, this condition is always satisfied for the materials considered in this work. Effective masses calculations require the accurate evaluation of the partial second derivatives of the band structure in two directions. The 16 × 16 × 1 *k*-point grid used in HSE06 calculations is too coarse and effective masses have been evaluated only from the PBE functional. Since effective masses depend on the band structure dispersion rather then on the gap, this approximation is expected to lead to a reasonable accuracy.

Results and Discussion

Structural properties

In this section we discuss the structural properties and dynamical stability of carbon and silicon-based two-dimensional binary compounds. As a starting point we consider a phosphorene monolayer derived from the experimental structure of black phosphorous [33]. Within this system each phosphorus atom is covalently bonded with three adjacent phosphorus atoms to form a puckered honeycomb structure [33,34]

(Figure 1a). For the sake of simplicity this phosphorene monolayer will be denoted as "experimental structure". Upon optimization at the PBE level of theory the lattice parameters of the experimental structure moderately change from a = 3.31330 Å and b = 4.374 Å to a = 3.298 Å and b =4.624 Å, in good agreement with previous calculations [8,35].

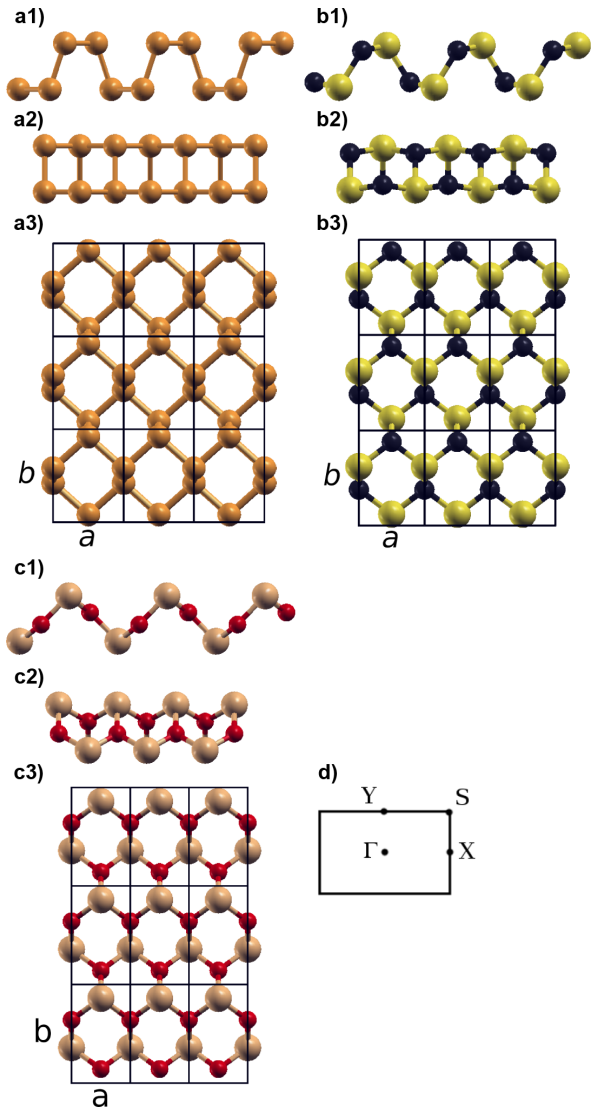

Figure 1: Optimized crystal structures of the following two-dimensional systems: a) phosphorene b) CS, CSe, CTe, SiS, SiSe, and SiTe. c) SiO d) Brillouin zone and high-symmetry points.

In order to obtain the structure of the carbon and silicon monochalcogenides we replaced phosphorus atoms in the experimental structure of phosphorene with carbon (or silicon) and chalcogen atoms (up to tellurium) by preserving the number of valence electrons involved in each bond. This starting geometry was then optimized at the PBE level of theory [36]. We found the CO monolayer to be unstable and to dissociate in independent one-dimensional chains; therefore this system was disregarded in the rest of our study. The geometry obtained for CS is shown in Figure 1b. The main features of the phosphorene structure are kept in this system: Each C atom is bound to three S atoms and vice versa. However, while in phosphorene atoms are distributed on two parallel planes (Figure 1a2), a distortion appears in CS, where C atoms tend to slightly move within the two planes formed by S atoms (Figure 1b2). In the case of CSe, CTe, SiS, SiSe, and SiTe the obtained structures are similar to the monolayer of CS [36]. The case of SiO should be considered separately: As shown in Figure 1c, in this case the distortion is particularly accentuated with respect to the initial geometry. As discussed below, this structure leads to electronic properties rather different from that of phosphorene, in particular concerning effective masses.

To better understand the ionic character of the bonds involved in the new materials we have carried out an analysis of the PBE charge density based on the theory of Bader [37] as implemented by Henkelman et al. [38]. Since silicon has a low electronegativity we found that this atom transfers about 2.4 electrons to O, S, and Se and 0.4 electrons to Te. In carbon monochalcogenides we found that 0.5 electrons were transferred from S to C, 0.8 from Se to C, and 1 from Te to C.

In order to establish the dynamical stability of these new compounds, we computed phonon dispersion curves by using density functional perturbation theory [32]. Our results in Figure 2 show that no imaginary phonon modes are present and all the compounds considered in this work are dynamically stable (the first Brillouin zone is mapped according to the convention in Figure 1d).

Electronic properties

After determining the structural properties we discuss the electronic properties of these phosphorene-like two-dimensional materials, which are fundamental for applications in nanoelectronics and nanophotonics. The band structures computed within the HSE06 approximation [29] are shown in Figure 3 where the gap type is indicated by a red line. The Fermi level has been shifted to zero and the first Brillouin zone is mapped according to the convention in Figure 1d. In Table 1 the values of bandgaps are presented.

Before discussing the characteristics of the two-dimensional carbon and silicon monochalcogenides, some preliminary remarks on phosphorene are necessary. The band gap of phosphorene has been evaluated by different ab initio methods to be about 0.8 or 0.91 eV at the PBE level of theory [35,39], 1.61 eV at the HSE level of theory [35], and 2.0 eV at the GW level of

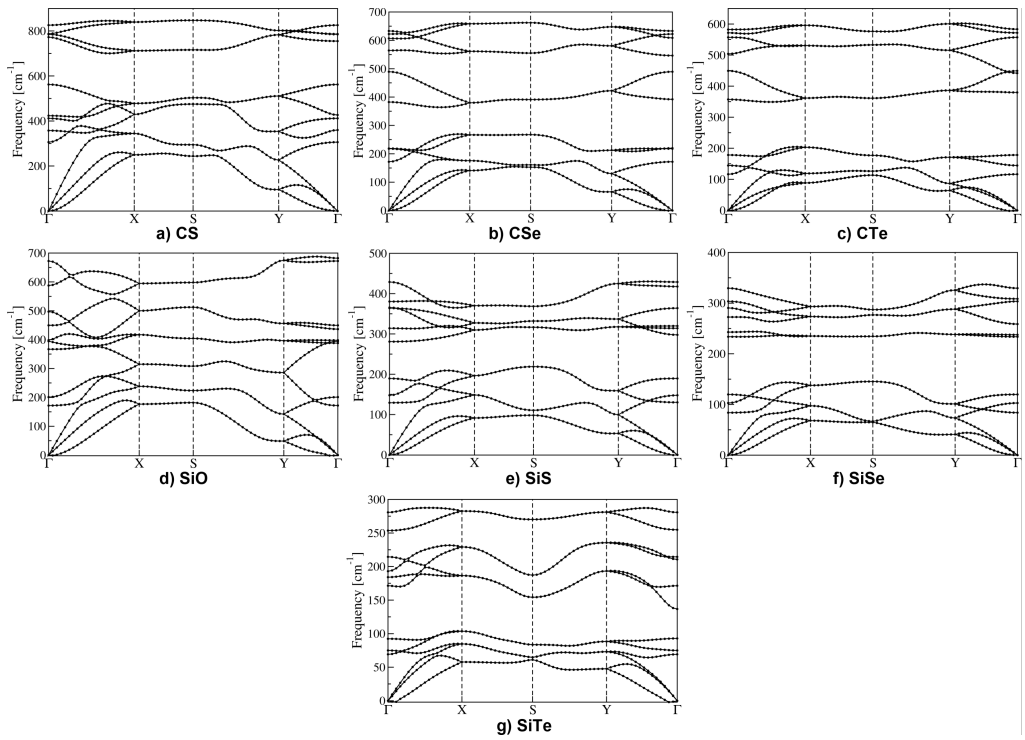

Figure 2: Phonon dispersion curves for the two-dimensional carbon and silicon monochalcogenides introduced in this work: CS, CSe, CTe, SiO, SiS, SiSe, and SiTe.

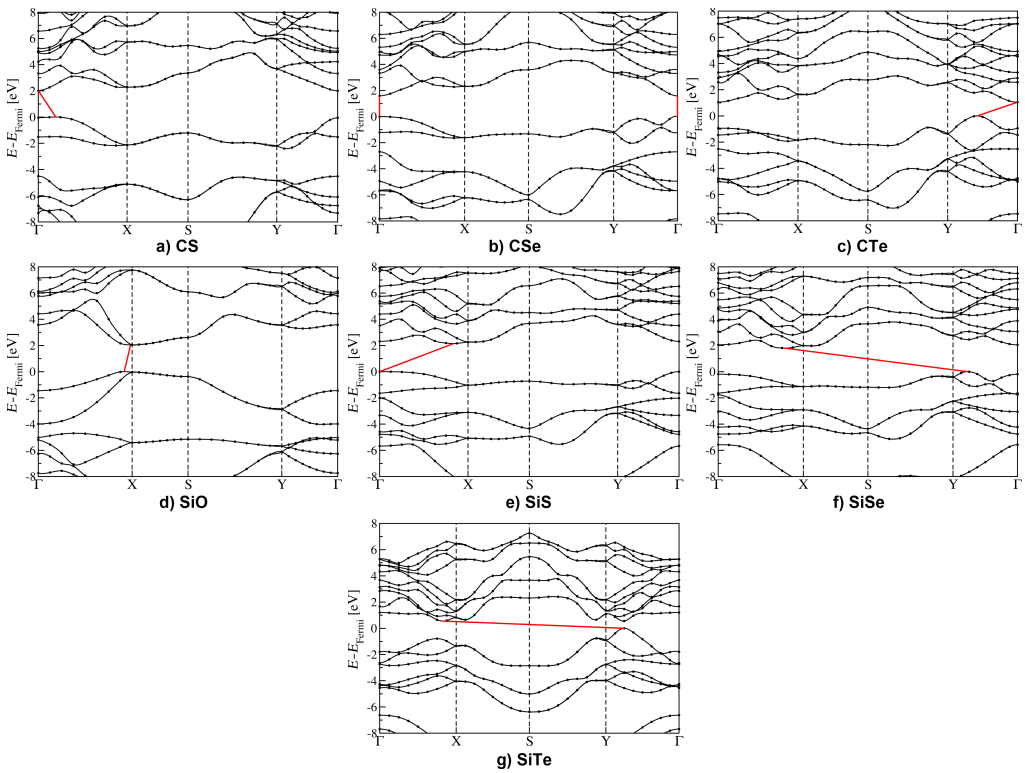

Figure 3: Band structures computed at the HSE level of theory for the two-dimensional carbon and silicon monochalcogenides introduced in this work: CS, CSe, CTe, SiO, SiS, SiSe, and SiTe.

Table 1: Electronic bandgaps computed at the PBE and HSE level of theory and effective masses for two-dimensional carbon and silicon monochalcogenides introduced in this work. In the table m_h^* denotes the hole effective mass, m_e^* the electron effective mass, and m_e the electron mass.

material	PBE gap (type)	HSE gap (type)	m_h^*/m_e zigzag direction	m_h^*/m_e armchair direction	m_e^*/m_e zigzag direction	m_e^*/m_e armchair direction
CS	1.13 (indirect)	2.02 (indirect)	1.08	0.22	0.29	0.32
CSe	0.88 (direct)	1.58 (direct)	3.75	0.14	0.35	0.16
CTe	0.56 (indirect)	1.07 (indirect)	0.87	0.20	0.55	0.35
SiO	1.37 (indirect)	2.06 (indirect)	0.36	1.66	0.20	1.60
SiS	1.42 (indirect)	2.16 (indirect)	27.1	0.28	1.10	0.53
SiSe	1.19 (indirect)	1.81 (indirect)	0.87	0.17	0.58	0.21
SiTe	0.39 (indirect)	0.55 (indirect)	0.16	0.06	0.22	0.08
phosphorene	0.91 (indirect)	1.58 (direct)	8.13	0.13	1.24	0.14

theory [39]. In [8] a value of 1.0 eV was found for the HSE gap, which does not significantly differ from the PBE estimate. As shown in Table 1 the DFT values we found are in good agreement with the results in the literature [35,39]. As previously noted [39], the top of the valence band is slightly shifted from Γ and, accordingly, phosphorene has an indirect gap at the PBE level of theory. However, the gap and the direct gap in Γ differs by less than 10 meV and for this reason phosphorene is commonly considered a direct bandgap semiconductor [8,35]. In Table 1 the HSE gap is denoted as direct. Very likely the difference with respect PBE is due to the coarser *k*-point grid used to sample the Brillouin zone.

The electronic gaps of the phosphorene-like binary compounds have been summarized in Table 1. For the sake of completeness, both PBE and HSE results have been provided but the HSE values have to be considered as more quantitative estimates in comparison to experiments. All the monolayers considered here are semiconducting and the gaps obtained span a wide energy range going from 0.55 eV for SiTe to 2.16 eV for SiS (HSE data). Accordingly, these compounds might contribute to extend the applicability of two dimensional materials to solar cells [40] and photodetection devices [14]. For several technological applications in optoelectronics the discovery of new two-dimensional materials characterized by a direct bandgap is also important. While strictly speaking, only the CSe monolayer has a direct gap, most of the other compounds have a direct bandgap only slightly larger than the minimum energy bandgap: 0.04 eV for CS, 0.02 eV for SiO, and below 0.01 eV for SiTe. Similarly to phosphorene, we can approximately consider these compounds as direct bandgap materials.

An important property of phosphorene is the high mobility of charge carriers and its in-plane anisotropy [14]. Indeed, significantly higher carrier mobilities are found in the armchair direction (along the direction of the lattice constant *b*). This behavior can be qualitatively understood from the band structure by computing effective masses. In agreement with previous calculations [35,41], the computed effective masses of phosphorene in the armchair direction are significantly smaller than in the zigzag direction. Most of the materials studied in this work present a similar behavior (the exceptions being SiO, which has a structure that significantly deviates from phosphorene, and CS, which has similar electron effective masses in the zigzag and armchair directions). Silicon and carbon monochalcogenides present a broad range of values for the effective masses. In this respect, SiTe and SiS have particularly interesting properties. While the anisotropy is less evident than in phosphorene, SiTe presents significantly small effective masses hinting to a high mobility in both the armchair and zigzag directions. This property might be useful to realize transistors [8,12]. In a different way, the SiS monolayer presents hole effective masses strongly dependent on the direction, with a value in the zigzag direction almost 100 times larger than the value in the armchair direction. Accordingly, this material is expected to exhibit a huge anisotropy in the hole mobility that might be of interest for less conventional plasmonic and thermoelectric devices, as discussed, for example, in [12].

Conclusion

In this work we applied ab initio techniques to study the properties of recently proposed two-dimensional compounds with the structure of phosphorene. Specifically, we considered carbon and silicon monochalcogenides and found the CS, CSe, CTe, SiO, SiS, SiSe, and SiTe monolayers to be dynamically stable. Then, the electronic properties of these new materials were determined, and the results indicate that these compounds span a broad range of electronic bandgaps and charge carrier mobilities, showing potential for future technological applications.

Acknowledgements

We thank the access to HPC resources from GENCI-CCRT/ CINES (Grant x2017-085106). Parts of the calculations were performed in the Computing Centre of the Slovak Academy of Sciences using the supercomputing infrastructure acquired in project ITMS 26230120002 and 26210120002 (Slovak infrastructure for high-performance computing) supported by the Research & Development Operational Programme funded by the ERDF.

References

1. Geim, A. K.; Novoselov, K. S. *Nat. Mater.* **2007,** *6,* 183–191. doi:10.1038/nmat1849
2. Novoselov, K. S.; Geim, A. K.; Morozov, S. V.; Jiang, D.; Zhang, Y.; Dubonos, S. V.; Grigorieva, I. V.; Firsov, A. A. *Science* **2004,** *306,* 666–669. doi:10.1126/science.1102896
3. Novoselov, K. S.; Jiang, D.; Schedin, F.; Booth, T. J.; Khotkevich, V. V.; Morozov, S. V.; Geim, A. K. *Proc. Natl. Acad. Sci. U. S. A.* **2005,** *102,* 10451–10453. doi:10.1073/pnas.0502848102
4. Splendiani, A.; Sun, L.; Zhang, Y.; Li, T.; Kim, J.; Chim, C.-Y.; Galli, G.; Wang, F. *Nano Lett.* **2010,** *10,* 1271–1275. doi:10.1021/nl903868w
5. Lebègue, S.; Eriksson, O. *Phys. Rev. B* **2009,** *79,* 115409. doi:10.1103/PhysRevB.79.115409
6. Xia, F.; Wang, H.; Jia, Y. *Nat. Commun.* **2014,** *5,* 4458. doi:10.1038/ncomms5458
7. Li, L.; Yu, Y.; Ye, G. J.; Ge, Q.; Ou, X.; Wu, H.; Feng, D.; Chen, X. H.; Zhang, Y. *Nat. Nanotechnol.* **2014,** *9,* 372–377. doi:10.1038/nnano.2014.35
8. Liu, H.; Neal, A. T.; Zhu, Z.; Luo, Z.; Xu, X.; Tománek, D.; Ye, P. D. *ACS Nano* **2014,** *8,* 4033–4041. doi:10.1021/nn501226z
9. Koenig, S. P.; Doganov, R. A.; Schmidt, H.; Neto, A. H. C.; Özyilmaz, B. *Appl. Phys. Lett.* **2014,** *104,* 103106. doi:10.1063/1.4868132
10. Morita, A. *Appl. Phys. A* **1986,** *39,* 227–242. doi:10.1007/BF00617267
11. Appalakondaiah, S.; Vaitheeswaran, G.; Lebègue, S.; Christensen, N. E.; Svane, A. *Phys. Rev. B* **2012,** *86,* 035105. doi:10.1103/PhysRevB.86.035105
12. Ling, X.; Wang, H.; Huang, S.; Xia, F.; Dresselhaus, M. S. *Proc. Natl. Acad. Sci. U. S. A.* **2015,** *112,* 4523–4530. doi:10.1073/pnas.1416581112
13. Churchill, H. O. H.; Jarillo-Herrero, P. *Nat. Nanotechnol.* **2014,** *9,* 330–331. doi:10.1038/nnano.2014.85
14. Xia, F.; Wang, H.; Xiao, D.; Dubey, M.; Ramasubramaniam, A. *Nat. Photonics* **2014,** *8,* 899–907. doi:10.1038/nphoton.2014.271
15. Kou, L.; Chen, C.; Smith, S. C. *J. Phys. Chem. Lett.* **2015,** *6,* 2794–2805. doi:10.1021/acs.jpclett.5b01094
16. Wu, M.; Zeng, X. C. *Nano Lett.* **2016,** *16,* 3236–3241. doi:10.1021/acs.nanolett.6b00726
17. Osters, O.; Nilges, T.; Bachhuber, F.; Pielnhofer, F.; Weihrich, R.; Schöneich, M.; Schmidt, P. *Angew. Chem., Int. Ed.* **2012,** *51,* 2994–2997. doi:10.1002/anie.201106479
18. Liu, B.; Köpf, M.; Abbas, A. N.; Wang, X.; Guo, Q.; Jia, Y.; Xia, F.; Weihrich, R.; Bachhuber, F.; Pielnhofer, F.; Wang, H.; Dhall, R.; Cronin, S. B.; Ge, M.; Fang, X.; Nilges, T.; Zhou, C. *Adv. Mater.* **2015,** *27,* 4423–4429. doi:10.1002/adma.201501758
19. Zhang, S.; Yan, Z.; Li, Y.; Chen, Z.; Zeng, H. *Angew. Chem., Int. Ed.* **2015,** *54,* 3112–3115. doi:10.1002/anie.201411246
20. Zhu, Z.; Guan, J.; Liu, D.; Tománek, D. *ACS Nano* **2015,** *9,* 8284–8290. doi:10.1021/acsnano.5b02742
21. Gomes, L. C.; Carvalho, A. *Phys. Rev. B* **2015,** *92,* 085406. doi:10.1103/PhysRevB.92.085406
22. Shi, G.; Kioupakis, E. *J. Appl. Phys.* **2015,** *117,* 065103. doi:10.1063/1.4907805
23. Piazza, Z. A.; Hu, H.-S.; Li, W.-L.; Zhao, Y.-F.; Li, J.; Wang, L.-S. *Nat. Commun.* **2014,** *5,* 3113. doi:10.1038/ncomms4113
24. Sofo, J. O.; Chaudhari, A. S.; Barber, G. D. *Phys. Rev. B* **2007,** *75,* 153401. doi:10.1103/PhysRevB.75.153401
25. Mannix, A. J.; Zhou, X.-F.; Kiraly, B.; Wood, J. D.; Alducin, D.; Myers, B. D.; Liu, X.; Fisher, B. L.; Santiago, U.; Guest, J. R.; Yacaman, M. J.; Ponce, A.; Oganov, A. R.; Hersam, M. C.; Guisinger, N. P. *Science* **2015,** *350,* 1513–1516. doi:10.1126/science.aad1080
26. Elias, D. C.; Nair, R. R.; Mohiuddin, T. M. G.; Morozov, S. V.; Blake, P.; Halsall, M. P.; Ferrari, A. C.; Boukhvalov, D. W.; Katsnelson, M. I.; Geim, A. K.; Novoselov, K. S. *Science* **2009,** *323,* 610–613. doi:10.1126/science.1167130
27. Yang, L.-M.; Ganz, E.; Chen, Z.; Wang, Z.-X.; von Ragué Schleyer, P. *Angew. Chem., Int. Ed.* **2015,** *54,* 9468–9501. doi:10.1002/anie.201410407
28. Kamal, C.; Chakrabarti, A.; Ezawa, M. *Phys. Rev. B* **2016,** *93,* 125428. doi:10.1103/PhysRevB.93.125428
29. Heyd, J.; Scuseria, G. E.; Ernzerhof, M. *J. Chem. Phys.* **2003,** *118,* 8207–8215. doi:10.1063/1.1564060
30. Giannozzi, P.; Baroni, S.; Bonini, N.; Calandra, M.; Car, R.; Cavazzoni, C.; Ceresoli, D.; Chiarotti, G. L.; Cococcioni, M.; Dabo, I.; Dal Corso, A.; de Gironcoli, S.; Fabris, S.; Fratesi, G.; Gebauer, R.; Gerstmann, U.; Gougoussis, C.; Kokalj, A.; Lazzeri, M.; Martin-Samos, L.; Marzari, N.; Mauri, F.; Mazzarello, R.; Paolini, S.; Pasquarello, A.; Paulatto, L.; Sbraccia, C.; Scandolo, S.; Sclauzero, G.; Seitsonen, A. P.; Smogunov, A.; Umari, P.; Wentzcovitch, R. M. *J. Phys.: Condens. Matter* **2009,** *21,* 395502. doi:10.1088/0953-8984/21/39/395502
31. Perdew, J. P.; Burke, K.; Ernzerhof, M. *Phys. Rev. Lett.* **1996,** *77,* 3865–3868. doi:10.1103/PhysRevLett.77.3865
32. Baroni, S.; de Gironcoli, S.; Dal Corso, A.; Giannozzi, P. *Rev. Mod. Phys.* **2001,** *73,* 515–562. doi:10.1103/RevModPhys.73.515
33. Cartz, L.; Srinivasa, S.; Riedner, R.; Jorgensen, J. D.; Worlton, T. G. *J. Chem. Phys.* **1979,** *71,* 1718–1721. doi:10.1063/1.438523
34. Brown, A.; Rundqvist, S. *Acta Crystallogr.* **1965,** *19,* 684–685. doi:10.1107/S0365110X65004140
35. Peng, X.; Wei, Q.; Copple, A. *Phys. Rev. B* **2014,** *90,* 085402. doi:10.1103/PhysRevB.90.085402
36. PBE optimized lattice constants: a = 3.30 Å and b = 4.62 Å for phosphorene; a = 2.77 Å and b = 4.04 Å for CS; a = 3.04 Å and b = 4.05 Å for CSe; a = 3.40 Å and b = 3.89 Å for CTe; a = 2.69 Å and b = 4.50 Å for SiO; a = 3.34 Å and b = 4.81 Å for SiS; a = 3.61 Å and b = 4.76 Å for SiSe; a = 4.11 Å and b = 4.30 Å for SiTe.
37. Bader, R. F. W. *Atoms in molecules;* Wiley, 1990.
38. Henkelman, G.; Arnaldsson, A.; Jónsson, H. *Comput. Mater. Sci.* **2006,** *36,* 354–360. doi:10.1016/j.commatsci.2005.04.010
39. Tran, V.; Soklaski, R.; Liang, Y.; Yang, L. *Phys. Rev. B* **2014,** *89,* 235319. doi:10.1103/PhysRevB.89.235319
40. Bernardi, M.; Palummo, M.; Grossman, J. C. *Nano Lett.* **2013,** *13,* 3664–3670. doi:10.1021/nl401544y
41. Qiao, J.; Kong, X.; Hu, Z.-X.; Yang, F.; Ji, W. *Nat. Commun.* **2014,** *5,* 4475. doi:10.1038/ncomms5475

BEILSTEIN JOURNAL OF NANOTECHNOLOGY

3D continuum phonon model for group-IV 2D materials

Morten Willatzen*[1], Lok C. Lew Yan Voon[2], Appala Naidu Gandi[3] and Udo Schwingenschlögl[3]

Full Research Paper

Open Access

Address:
[1]Department of Photonics Engineering, Technical University of Denmark, Kgs. Lyngby, 2800, Denmark, [2]College of Science and Mathematics, The University of West Georgia, 1601 Maple St, Carrollton, GA 30117. USA and [3]PSE Division, King Abdullah University of Science and Technology, Thuwal 23955-6900, Kingdom of Saudi Arabia

Email:
Morten Willatzen* - morwi@fotonik.dtu.dk

* Corresponding author

Keywords:
graphene; molybdenum disulfide; phonon; silicene; two-dimensional materials

Beilstein J. Nanotechnol. **2017,** *8,* 1345–1356.
doi:10.3762/bjnano.8.136

Received: 16 February 2017
Accepted: 14 June 2017
Published: 30 June 2017

This article is part of the Thematic Series "Silicene, germanene and other group IV 2D materials".

Guest Editor: P. Vogt

Abstract

A general three-dimensional continuum model of phonons in two-dimensional materials is developed. Our first-principles derivation includes full consideration of the lattice anisotropy and flexural modes perpendicular to the layers and can thus be applied to any two-dimensional material. In this paper, we use the model to not only compare the phonon spectra among the group-IV materials but also to study whether these phonons differ from those of a compound material such as molybdenum disulfide. The origin of quadratic modes is clarified. Mode coupling for both graphene and silicene is obtained, contrary to previous works. Our model allows us to predict the existence of confined optical phonon modes for the group-IV materials but not for molybdenum disulfide. A comparison of the long-wavelength modes to density-functional results is included.

Introduction

Phonon spectra in two-dimensional (2D) nanomaterials have almost exclusively been computed using density-functional theory (DFT) based codes. One of the earliest applications to group-IV elemental 2D materials was for the important prediction of the stability of silicene and germanene [1]. These are complex calculations and prone to qualitative errors due to the various approximations such as convergence criteria and use of approximate functionals [2]. Even the stability or not of a given structure could be incorrectly inferred. For example, borophene and indiene have been predicted to be unstable in one paper [3], though other calculations (and in the case of borophene, even experiments [4]) have obtained opposite results [5,6]. In addition to obtaining a spectrum, it is often also useful to be able to predict and/or interpret properties of the spectrum based upon either microscopic or symmetric arguments. An excellent example is the prediction of a Dirac cone for silicene on the basis of symmetry [7] when DFT calculations either failed to recognize it [8] or were unable to explain it [1].

An alternative model of lattice vibrations is a classical continuum model, which is expected to reproduce most accurately phonons with wavelengths longer than lattice separations, i.e., near $k = 0$. One of the earliest such models applied to an ionic crystal slab is that of Fuchs and Kliewer [9], from which they deduced that transverse optical (TO) and longitudinal optical (LO) modes have different frequencies at $k \approx 0$ as well as the existence of surface optical (SO) modes with an exponential dependence away from the slab. Slightly different models have been introduced by a number of authors for graphene [10-13]. One commonality is to treat the sheet as strictly two-dimensional. Additionally, instead of deriving the phonon dispersion relations from first principles, they all assumed the known results that there are in-plane acoustic modes with linear dispersions and out-of-plane transverse acoustic modes with quadratic dispersions (the latter being consistent with the elastic theory of thin plates) to construct either a Lagrangian [10] or equations of motion [11]. Goupalov also considered optical phonons but simply parameterized the dispersion relations to match the experimental data. In all of the above, the out-of-plane vibrations were assumed decoupled from the in-plane ones.

In this paper, a continuum theory of acoustic and optical phonons in 2D nanomaterials is derived from first principles, contrary to earlier approaches, by starting with the elastic and electric equations, and taking into account the full crystalline symmetry and piezoelectric couplings when allowed by symmetry. We apply the theory to obtain the phonons in group-IV elemental 2D materials. Given that there are two fundamental structures for the free-standing sheets (the flat hexagonal structure of graphene and the buckled hexagonal structure of the other elements – we will refer to silicene as the prototypical example of the latter), we will consider both of them. It should be recognized that, to date, silicene has been grown on substrates in different reconstruction state. The reconstruction is an atomic-scale distinction that is not describable by the current continuum model. Substrate effects on the phonons can be considered in an extended model that would need to be solved numerically. This can be studied in a future publication as it is beyond the analytical solutions sought for in the current manuscript. Furthermore, we have included a study of a well-known compound 2D material (molybdenum disulfide MoS_2) in order to further understand the properties derived for the elemental materials.

Results and Discussion

Continuum model

The 2D materials will be treated as 3D thin-plate materials in the following, well aware that the out-of-plane dimension contains one or a few atomic layers. In general, this would allow one to study multilayers though we will only focus on monolayers in this paper. Nonetheless, it is important to keep the third coordinate in the analysis to reveal the true phonon dispersions as observed experimentally and in DFT calculations.

The general 3D elastic equations are given by the equation of motion [14]

$$\frac{\partial T_{ik}}{\partial x_k} = \rho \ddot{u}_i, \tag{1}$$

where T_{ik} is the stress tensor, ρ is the mass density, and u_i is the displacement. Equation 1 contains all the physics of the problem. In order to simplify and then solve it, it is necessary to specify the crystal symmetry of the vibrating system.

The three problems considered in this article are graphene, silicene and MoS_2. The Bravais lattice symmetries of the single-layer graphene ($D_{6h} \equiv 6/mmm$) and MoS_2 ($D_{3h} \equiv \bar{6}m2$) structures belong to the hexagonal system, while silicene belongs to the trigonal system (point group D_{3d}). Graphene and silicene are non-piezoelectric materials because of the inversion symmetry of the unit cell, while MoS_2 is piezoelectric because its unit cell exhibits inversion asymmetry.

Application: graphene

For both graphene and MoS_2, the general form of the stiffness tensor for hexagonal structures is

$$c_{IJ} = \begin{bmatrix} c_{11} & c_{12} & c_{13} & 0 & 0 & 0 \\ c_{12} & c_{11} & c_{13} & 0 & 0 & 0 \\ c_{13} & c_{13} & c_{33} & 0 & 0 & 0 \\ 0 & 0 & 0 & c_{44} & 0 & 0 \\ 0 & 0 & 0 & 0 & c_{44} & 0 \\ 0 & 0 & 0 & 0 & 0 & \frac{1}{2}(c_{11}-c_{12}) \end{bmatrix}, \tag{2}$$

and the stress–strain relations $T_I = c_{IJ}S_J$ for graphene become

$$\begin{aligned} T_1 &= c_{11}S_1 + c_{12}S_2 + c_{13}S_3, \\ T_2 &= c_{12}S_1 + c_{11}S_2 + c_{13}S_3, \\ T_3 &= c_{13}S_1 + c_{13}S_2 + c_{33}S_3, \\ T_4 &= c_{44}S_4, T_5 = c_{44}S_5, \\ T_6 &= \frac{1}{2}(c_{11}-c_{12})S_6, \end{aligned} \tag{3}$$

where T_I and S_J denote stress and strain, respectively. Here we have used Voigt notation for tensors. The latter equations are different for MoS_2 due to the presence of piezoelecticity.

Elastic equations

Combining Equation 1 and Equation 3, we obtain for graphene

$$c_{11}\frac{\partial S_1}{\partial x}+c_{12}\frac{\partial S_2}{\partial x}+c_{13}\frac{\partial S_3}{\partial x}+\frac{1}{2}\left(c_{11}-c_{12}\right)\frac{\partial S_6}{\partial y}+c_{44}\frac{\partial S_5}{\partial z}=-\rho\omega^2 u_x, \tag{4}$$

$$\frac{1}{2}\left(c_{11}-c_{12}\right)\frac{\partial S_6}{\partial x}+c_{12}\frac{\partial S_1}{\partial y}+c_{11}\frac{\partial S_2}{\partial y}+c_{13}\frac{\partial S_3}{\partial y}+c_{44}\frac{\partial S_4}{\partial z}=-\rho\omega^2 u_y, \tag{5}$$

$$c_{44}\frac{\partial S_5}{\partial x}+c_{44}\frac{\partial S_4}{\partial y}+c_{13}\frac{\partial S_1}{\partial z}+c_{13}\frac{\partial S_2}{\partial z}+c_{33}\frac{\partial S_3}{\partial z}=-\rho\omega^2 u_z, \tag{6}$$

where ω is the vibrational (angular) frequency. The displacements u_x and u_y are in-plane displacements, and u_z is the out-of-plane displacement.

Expressing the latter set of equations in the displacements, we get

$$c_{11}\frac{\partial^2 u_x}{\partial x^2}+c_{12}\frac{\partial^2 u_y}{\partial x\partial y}+c_{13}\frac{\partial^2 u_z}{\partial x\partial z}+\frac{1}{2}\left(c_{11}-c_{12}\right)\left(\frac{\partial^2 u_x}{\partial y^2}+\frac{\partial^2 u_y}{\partial x\partial y}\right)+c_{44}\left(\frac{\partial^2 u_x}{\partial z^2}+\frac{\partial^2 u_z}{\partial x\partial z}\right)=-\rho\omega^2 u_x, \tag{7}$$

$$\frac{1}{2}\left(c_{11}-c_{12}\right)\left(\frac{\partial^2 u_x}{\partial x\partial y}+\frac{\partial^2 u_y}{\partial x^2}\right)+c_{12}\frac{\partial^2 u_x}{\partial x\partial y}+c_{11}\frac{\partial^2 u_y}{\partial y^2}+c_{13}\frac{\partial^2 u_z}{\partial y\partial z}+c_{44}\left(\frac{\partial^2 u_y}{\partial z^2}+\frac{\partial^2 u_z}{\partial y\partial z}\right)=-\rho\omega^2 u_y, \tag{8}$$

$$c_{44}\left(\frac{\partial^2 u_x}{\partial x\partial z}+\frac{\partial^2 u_z}{\partial x^2}+\frac{\partial^2 u_y}{\partial y\partial z}+\frac{\partial^2 u_z}{\partial y^2}\right)+c_{13}\left(\frac{\partial^2 u_x}{\partial x\partial z}+\frac{\partial^2 u_y}{\partial y\partial z}\right)+c_{33}\frac{\partial^2 u_z}{\partial z^2}=-\rho\omega^2 u_z. \tag{9}$$

A solution of the combined system (Equation 7–Equation 9) with appropriate boundary conditions allows for the determination of the displacements u_x, u_y, u_z. Note that the displacements in the three directions are coupled. This is different from the 2D model assumed before, which led to a decoupling of the out-of-plane vibrations. The coupling is a consequence of the finite thickness of the sheet with no mirror symmetry imposed. Thus, our model is sufficiently general to apply to multilayers. Earlier DFT calculations [15] had argued that there is no coupling between the in-plane and out-of-plane modes due to the mirror symmetry of graphene, leading to fewer scattering channels and, therefore, a higher thermal conductivity compared to, e.g., silicene. Our model reveals that such mode coupling, even when present, would occur for large k_z values (due to the small thicknesses) and, hence, would be unlikely to have a significant impact.

Acoustic phonons

The phonons are normal mode solutions to the equations of motion. To proceed from the graphene elastic equations, we make the following plane wave ansatz

$$u_x = f_x(z)\exp\left(ik_x x+ik_y y-i\omega t\right), \tag{10}$$

$$u_y = f_y(z)\exp\left(ik_x x+ik_y y-i\omega t\right), \tag{11}$$

$$u_z = f_z(z)\exp\left(ik_x x+ik_y y-i\omega t\right), \tag{12}$$

where k_x and k_y are wave numbers. Inserting Equation 10–Equation 12 into Equation 7–Equation 9 yields the following matrix expression in the unknown functions f_x, f_y, and f_z:

$$\begin{bmatrix} A_1+B_1\mathcal{D}^2 & C & D_1\mathcal{D} \\ C & A_2+B_2\mathcal{D}^2 & D_2\mathcal{D} \\ D_1\mathcal{D} & D_2\mathcal{D} & A_3+B_3\mathcal{D}^2 \end{bmatrix}\begin{bmatrix} f_x \\ f_y \\ f_z \end{bmatrix}=\begin{bmatrix} 0 \\ 0 \\ 0 \end{bmatrix}, \tag{13}$$

where $\mathcal{D}\equiv\left(\partial/\partial z\right)$, and

$$
\begin{aligned}
A_1 &= -c_{11}k_x^2 - \frac{1}{2}\left(c_{11}-c_{12}\right)k_y^2 + \rho\omega^2,\\
A_2 &= -c_{11}k_y^2 - \frac{1}{2}\left(c_{11}-c_{12}\right)k_x^2 + \rho\omega^2,\\
A_3 &= -c_{44}\left(k_x^2 + k_y^2\right) + \rho\omega^2,\\
B_1 &= B_2 = c_{44},\\
B_3 &= c_{33},\\
C &= \left[-c_{12} - \frac{1}{2}\left(c_{11}-c_{12}\right)\right]k_x k_y,\\
D_1 &= ik_x\left(c_{13}+c_{44}\right),\\
D_2 &= ik_y\left(c_{13}+c_{44}\right).
\end{aligned}
\tag{14}
$$

A semi-analytic solution can be easily obtained for the case when $k_y = 0$. In this case, $C = D_2 = 0$ and the u_y displacement decouples from the displacements u_x and u_z. It follows that f_y obeys the wave equation

$$
\left(A_2 + B_2\mathcal{D}^2\right)f_y = 0. \tag{15}
$$

The solution to this differential equation can be found immediately by imposing the vacuum boundary condition

$$
T_{yz} = 0 \quad \text{when} \quad z = \pm h, \tag{16}
$$

i.e.,

$$
\left.\frac{\partial u_y}{\partial z}\right|_{z=\pm h} = 0, \tag{17}
$$

where $2h$ is the graphene layer thickness and $-h,h$ define the graphene layer boundaries.

We obtain

$$
\begin{aligned}
u_y &= A\cos\left(\frac{n\pi}{h}z\right)\exp\left(ik_x x - i\omega t\right),\\
\omega &= \sqrt{\frac{c_{44}\left(\frac{n\pi}{h}\right)^2 + \frac{1}{2}\left(c_{11}-c_{12}\right)k_x^2}{\rho}},
\end{aligned}
\tag{18}
$$

where $n = 0,1,2,3,\ldots$

For the coupled system f_x–f_z, the determinantal system obtained from Equation 13 leads to the solutions

$$
\mathcal{D} = \pm\alpha_1, \pm\alpha_2, \tag{19}
$$

where

$$
\begin{aligned}
\alpha_1^2 &= \frac{1}{2B_1B_3}\left[-\left(A_1B_3 + B_1A_3 - D_1^2\right)\right.\\
&\quad \left.+\sqrt{\left(A_1B_3 + B_1A_3 - D_1^2\right)^2 - 4A_1A_3B_1B_3}\right],\\
\alpha_2^2 &= \frac{1}{2B_1B_3}\left[-\left(A_1B_3 + B_1A_3 - D_1^2\right)\right.\\
&\quad \left.-\sqrt{\left(A_1B_3 + B_1A_3 - D_1^2\right)^2 - 4A_1A_3B_1B_3}\right],
\end{aligned}
\tag{20}
$$

and

$$
f_z = -\frac{A_1 + B_1\mathcal{D}^2}{D_1\mathcal{D}}f_x \equiv \gamma f_x. \tag{21}
$$

Let us introduce the notation $\{\alpha_1,\alpha_2,\alpha_3,\alpha_4\} \equiv \{\alpha_1,-\alpha_1,\alpha_2,-\alpha_2\}$ and

$$
\gamma_i = -\frac{A_i + B_i\alpha_i^2}{D_1\alpha_i}. \tag{22}
$$

Then we have

$$
\begin{aligned}
f_x &= \beta_1\exp\left(\alpha_1 z\right) + \beta_2\exp\left(\alpha_2 z\right)\\
&\quad + \beta_3\exp\left(\alpha_3 z\right) + \beta_4\exp\left(\alpha_4 z\right),\\
f_z &= \gamma_1\beta_1\exp\left(\alpha_1 z\right) + \gamma_2\beta_2\exp\left(\alpha_2 z\right)\\
&\quad + \gamma_3\beta_3\exp\left(\alpha_3 z\right) + \gamma_4\beta_4\exp\left(\alpha_4 z\right),
\end{aligned}
\tag{23}
$$

where β_i are unknown coefficients.

A 4×4 matrix equation in β_i is finally obtained by invoking the mechanical boundary conditions (graphene in vacuum)

$$
T_{zz}(z = h) = T_{zz}(z = -h) = 0, \tag{24}
$$

$$
T_{xz}(z = h) = T_{xz}(z = -h) = 0. \tag{25}
$$

Observe that

$$
\begin{aligned}
T_{zz} &= ik_x c_{13} f_x + c_{33}\mathcal{D}f_z,\\
T_{xz} &= c_{44}\mathcal{D}f_x + ik_x c_{44} f_z.
\end{aligned}
\tag{26}
$$

Solving the determinantal equation for the latter 4 × 4 matrix equation as a function of k_x specifies a discrete set of (band) eigenfrequencies $\omega_i(k_x)$ and the corresponding eigenmodes f_x, f_z where i denotes the band index. A numerical solution reveals the out-of-plane mode to be quadratic in nature.

Surface optical phonons

Surface optical phonons can be derived by solving for the electrostatic potential via the Maxwell–Poisson equation for the displacement field D_i.

For graphene,

$$D_i = \varepsilon_{ij} E_j . \tag{27}$$

Using the fact that the dielectric function is given by

$$\varepsilon_{ij} = \begin{bmatrix} \varepsilon_{xx} & 0 & 0 \\ 0 & \varepsilon_{xx} & 0 \\ 0 & 0 & \varepsilon_{zz} \end{bmatrix}, \tag{28}$$

we find

$$D_x = \varepsilon_{xx} E_1, D_y = \varepsilon_{xx} E_2, D_z = \varepsilon_{zz} E_3 . \tag{29}$$

The Maxwell–Poisson equation in the absence of free charges reads

$$\frac{\partial D_x}{\partial x} + \frac{\partial D_y}{\partial y} + \frac{\partial D_z}{\partial z} = 0, \tag{30}$$

and finally becomes

$$-\varepsilon_{xx} \frac{\partial^2 \phi}{\partial x^2} - \varepsilon_{zz} \frac{\partial^2 \phi}{\partial z^2} = 0. \tag{31}$$

The solution in the graphene slab becomes

$$\phi^i (x, z) = \left(\phi_1 e^{\alpha_1 z} + \phi_2 e^{\alpha_2 z} \right) e^{i k_x x}, \tag{32}$$

where

$$\alpha_1 = -\alpha_2 = \sqrt{\frac{\varepsilon_{xx}}{\varepsilon_{zz}}} k_x . \tag{33}$$

This gives for the electric field components

$$\begin{aligned} E_x^i &= -\frac{\partial \phi^i}{\partial x} = -i k_x \left(\phi_1 e^{\alpha_1 z} + \phi_2 e^{\alpha_2 z} \right) e^{i k_x x}, \\ E_z^i &= -\frac{\partial \phi^i}{\partial z} = \left(-\alpha_1 \phi_1 e^{\alpha_1 z} - \alpha_2 \phi_2 e^{\alpha_2 z} \right) e^{i k_x x}. \end{aligned} \tag{34}$$

Continuity in E_x at the slab interfaces with vacuum at $z = \pm h$ requires

$$\begin{aligned} -i k_x \left(\phi_1 e^{\alpha_1 h} + \phi_2 e^{\alpha_2 h} \right) &= -i k_x \phi_+ e^{-k_x h}, \\ -i k_x \left(\phi_1 e^{-\alpha_1 h} + \phi_2 e^{-\alpha_2 h} \right) &= -i k_x \phi_- e^{-k_x h}, \end{aligned} \tag{35}$$

and, similarly, continuity in the normal electric displacement requires

$$\begin{aligned} \varepsilon_{zz} \left(-\alpha_1 \phi_1 e^{\alpha_1 h} - \alpha_2 \phi_2 e^{\alpha_2 h} \right) &= \varepsilon_0 k_x \phi_+ e^{-k_x h}, \\ \varepsilon_{zz} \left(-\alpha_1 \phi_1 e^{-\alpha_1 h} - \alpha_2 \phi_2 e^{-\alpha_2 h} \right) &= -\varepsilon_0 k_x \phi_- e^{-k_x h}. \end{aligned} \tag{36}$$

Solving the secular equation in $\{\phi_1, \phi_2, \phi_+, \phi_-\}$ leads to

$$\frac{\left(1 + \dfrac{\alpha_1 \varepsilon_{zz}}{k_x \varepsilon_0} \right)^2}{\left(1 - \dfrac{\alpha_1 \varepsilon_{zz}}{k_x \varepsilon_0} \right)^2} = e^{-4\alpha_1 h},$$

which is equivalent to

$$\frac{1 + \dfrac{\sqrt{\varepsilon_{xx} \varepsilon_{zz}}}{\varepsilon_0}}{1 - \dfrac{\sqrt{\varepsilon_{xx} \varepsilon_{zz}}}{\varepsilon_0}} = \pm e^{-2\sqrt{\frac{\varepsilon_{xx}}{\varepsilon_{zz}}} k_x h}. \tag{37}$$

We note in passing that the latter equation agrees with the result of Licari and Evrard [16] for interface optical phonon modes in cubic crystals where symmetry forces $\varepsilon_{xx} = \varepsilon_{zz} \equiv \varepsilon$. In the cubic case, however, confined optical phonon modes also exist at the LO phonon frequency since $\varepsilon(\omega_{LO}) = 0$.

Confined optical phonons

Confined optical phonons are also obtained by starting with the Maxwell–Poisson equation (Equation 31). The transverse electric field and normal electric displacement are

$$D_z = -\varepsilon_{zz}\frac{\partial\phi}{\partial z},$$
$$E_x = -\frac{\partial\phi}{\partial x}, \tag{38}$$

neglecting the DC component (static polarization) to the electric displacement. Confinement of the optical phonon modes implies $\phi_+ = \phi_- = 0$. Assuming [type I]

$$\phi = \sum_{m=1,2,3,\ldots} \sin\left(\frac{m\pi}{h}z\right)\left(A_{\phi,m} + B_{\phi,m}x\right)\exp\left(-i\omega t\right), \tag{39}$$

where $A_{\phi,m}, B_{\phi,m}$ are constants, the Maxwell–Poisson equation and the boundary conditions are fulfilled if $\varepsilon_{zz}(\omega) = 0$. Hence confined optical phonons exist in graphene.

Application: silicene

We refer to silicene as the canonical example of the other group-IV materials even though the following derivation and qualitative properties apply to all of them since they all have the same symmetry of the buckled hexagonal structure, leading to the trigonal D_{3d} point group.

The general form of the stiffness tensor for D_{3d} trigonal structures is

$$c_{IJ} = \begin{bmatrix} c_{11} & c_{12} & c_{13} & c_{14} & 0 & 0 \\ c_{12} & c_{11} & c_{13} & -c_{14} & 0 & 0 \\ c_{13} & c_{13} & c_{33} & 0 & 0 & 0 \\ c_{14} & -c_{14} & 0 & c_{44} & 0 & 0 \\ 0 & 0 & 0 & 0 & c_{44} & c_{14} \\ 0 & 0 & 0 & 0 & c_{14} & \frac{1}{2}\left(c_{11}-c_{12}\right) \end{bmatrix}, \tag{40}$$

and the stress–strain relations become

$$\begin{aligned} T_1 &= c_{11}S_1 + c_{12}S_2 + c_{13}S_3 + c_{14}S_4, \\ T_2 &= c_{12}S_1 + c_{11}S_2 + c_{13}S_3 - c_{14}S_4, \\ T_3 &= c_{13}S_1 + c_{13}S_2 + c_{33}S_3, \\ T_4 &= c_{14}S_1 - c_{14}S_2 + c_{44}S_4, \\ T_5 &= c_{44}S_5 + c_{14}S_6, \\ T_6 &= c_{14}S_5 + \frac{1}{2}\left(c_{11}-c_{12}\right)S_6. \end{aligned} \tag{41}$$

The only difference compared to the corresponding equations for graphene are the terms containing c_{14}.

Elastic equations

The elastic equations for silicene then read

$$\begin{aligned} &c_{11}\frac{\partial S_1}{\partial x} + c_{12}\frac{\partial S_2}{\partial x} + c_{13}\frac{\partial S_3}{\partial x} + \frac{1}{2}\left(c_{11}-c_{12}\right)\frac{\partial S_6}{\partial y} \\ &\quad + c_{44}\frac{\partial S_5}{\partial z} + c_{14}\left(\frac{\partial S_4}{\partial x} + \frac{\partial S_5}{\partial y} + \frac{\partial S_6}{\partial z}\right) = -\rho\omega^2 u_x, \end{aligned} \tag{42}$$

$$\begin{aligned} &\frac{1}{2}\left(c_{11}-c_{12}\right)\frac{\partial S_6}{\partial x} + c_{12}\frac{\partial S_1}{\partial y} + c_{11}\frac{\partial S_2}{\partial y} + c_{13}\frac{\partial S_3}{\partial y} \\ &\quad + c_{44}\frac{\partial S_4}{\partial z} + c_{14}\left(\frac{\partial S_1}{\partial z} - \frac{\partial S_2}{\partial z} - \frac{\partial S_4}{\partial y} + \frac{\partial S_5}{\partial x}\right) = -\rho\omega^2 u_y, \end{aligned} \tag{43}$$

$$\begin{aligned} &c_{44}\frac{\partial S_5}{\partial x} + c_{44}\frac{\partial S_4}{\partial y} + c_{13}\frac{\partial S_1}{\partial z} + c_{13}\frac{\partial S_2}{\partial z} \\ &\quad + c_{33}\frac{\partial S_3}{\partial z} + c_{14}\left(\frac{\partial S_1}{\partial y} - \frac{\partial S_2}{\partial y}\right) = -\rho\omega^2 u_z, \end{aligned} \tag{44}$$

or, in terms of the displacements,

$$\begin{aligned} &c_{11}\frac{\partial^2 u_x}{\partial x^2} + c_{12}\frac{\partial^2 u_y}{\partial x\partial y} + c_{13}\frac{\partial^2 u_z}{\partial x\partial z} \\ &\quad + 2c_{14}\left(\frac{\partial^2 u_x}{\partial y\partial z} + \frac{\partial^2 u_y}{\partial z\partial x} + \frac{\partial^2 u_z}{\partial x\partial y}\right) \\ &\quad + \frac{1}{2}\left(c_{11}-c_{12}\right)\left(\frac{\partial^2 u_x}{\partial y^2} + \frac{\partial^2 u_y}{\partial x\partial y}\right) = -\rho\omega^2 u_x, \end{aligned} \tag{45}$$

$$\begin{aligned} &c_{14}\left(\frac{\partial^2 u_z}{\partial x^2} - \frac{\partial^2 u_z}{\partial y^2} + 2\frac{\partial^2 u_x}{\partial z\partial x} - 2\frac{\partial^2 u_y}{\partial y\partial z}\right) \\ &\quad + \frac{1}{2}\left(c_{11}-c_{12}\right)\left(\frac{\partial^2 u_x}{\partial x\partial y} + \frac{\partial^2 u_y}{\partial x^2}\right) \\ &\quad + c_{13}\frac{\partial^2 u_z}{\partial y\partial z} + c_{12}\frac{\partial^2 u_x}{\partial x\partial y} + c_{11}\frac{\partial^2 u_y}{\partial y^2} = -\rho\omega^2 u_y, \end{aligned} \tag{46}$$

$$\begin{aligned} &c_{13}\left(\frac{\partial^2 u_x}{\partial x\partial z} + \frac{\partial^2 u_y}{\partial y\partial z}\right) \\ &+ c_{14}\left(\frac{\partial^2 u_y}{\partial x^2} - \frac{\partial^2 u_y}{\partial z^2} + 2\frac{\partial^2 u_x}{\partial x\partial y} + \frac{\partial^2 u_y}{\partial x^2} - \frac{\partial^2 u_y}{\partial y^2}\right) \\ &\quad + c_{44}\left(\frac{\partial^2 u_z}{\partial x^2} + \frac{\partial^2 u_z}{\partial y^2} + \frac{\partial^2 u_x}{\partial x\partial z} + \frac{\partial^2 u_y}{\partial y\partial z}\right) = -\rho\omega^2 u_z. \end{aligned} \tag{47}$$

Again, the differences compared to graphene are the c_{14} terms. The electric equation for trigonal structures is exactly the same as for hexagonal structures since the permittivity matrix is the same. Hence, the general method for finding surface optical phonon modes repeats the description of graphene. Qualitatively, there is therefore no difference among the phonons for all the group-IV elemental 2D materials.

Application: MoS_2

While the primary focus of this paper is on the properties of phonons of the group-IV elemental materials, it is important to know if there are properties of the phonons that are due to these being elemental. Hence, we will now consider the phonons for MoS_2 as a prototypical compound 2D material because of its extensively studied properties. As already mentioned, the lack of inversion symmetry leads to the new phenomenon of piezoelectricity.

Elastic and electric equations for MoS_2

The stiffness tensor for MoS_2 is the same as for graphene, Equation 2, because of the same hexagonal symmetry. However, the stress–strain relations are different because of the presence of piezoelectricity. Specifically, there are additional contributions to the stress–strain constitutive relations:

$$\begin{aligned}
T_1 &= c_{11}S_1 + c_{12}S_2 + c_{13}S_3 - e_{x1}E_1,\\
T_2 &= c_{12}S_1 + c_{11}S_2 + c_{13}S_3 + e_{x1}E_1,\\
T_3 &= c_{13}S_1 + c_{13}S_2 + c_{33}S_3,\\
T_4 &= c_{44}S_4,\\
T_5 &= c_{44}S_5,\\
T_6 &= 1/2\left(c_{11} - c_{12}\right)S_6 + e_{x1}E_2,
\end{aligned} \tag{48}$$

by use of the piezoelectric e-tensor:

$$e_{Ij} = \begin{bmatrix} e_{x1} & 0 & 0\\ -e_{x1} & 0 & 0\\ 0 & 0 & 0\\ 0 & 0 & 0\\ 0 & 0 & 0\\ 0 & -e_{x1} & 0 \end{bmatrix}, \tag{49}$$

and the equation

$$T_I = -e_{Ij}E_j + c_{IJ}S_J. \tag{50}$$

In the above, E_j is the internal electric field.

With the above result for the stress tensor including piezoelectric contributions, we find the elastic equations for MoS_2

$$\begin{aligned}
&c_{11}\frac{\partial^2 u_x}{\partial x^2} + c_{12}\frac{\partial^2 u_y}{\partial x\partial y} + c_{13}\frac{\partial^2 u_z}{\partial x\partial z}\\
&+\frac{1}{2}\left(c_{11} - c_{12}\right)\left(\frac{\partial^2 u_x}{\partial y^2} + \frac{\partial^2 u_y}{\partial x\partial y}\right)\\
&+c_{44}\left(\frac{\partial^2 u_x}{\partial z^2} + \frac{\partial^2 u_z}{\partial x\partial z}\right) - e_{x1}\frac{\partial E_1}{\partial x} + e_{x1}\frac{\partial E_2}{\partial y} = -\rho\omega^2 u_x,
\end{aligned} \tag{51}$$

$$\begin{aligned}
&\frac{1}{2}\left(c_{11} - c_{12}\right)\left(\frac{\partial^2 u_x}{\partial x\partial y} + \frac{\partial^2 u_y}{\partial x^2}\right)\\
&+c_{12}\frac{\partial^2 u_x}{\partial x\partial y} + c_{11}\frac{\partial^2 u_y}{\partial y^2} + c_{13}\frac{\partial^2 u_z}{\partial y\partial z}\\
&+c_{44}\left(\frac{\partial^2 u_y}{\partial z^2} + \frac{\partial^2 u_z}{\partial y\partial z}\right) + e_{x1}\frac{\partial E_2}{\partial x} + e_{x1}\frac{\partial E_1}{\partial y} = -\rho\omega^2 u_y,
\end{aligned} \tag{52}$$

$$\begin{aligned}
&c_{44}\left(\frac{\partial^2 u_x}{\partial x\partial z} + \frac{\partial^2 u_z}{\partial x^2}\right) + c_{44}\left(\frac{\partial^2 u_y}{\partial y\partial z} + \frac{\partial^2 u_z}{\partial y^2}\right)\\
&+c_{13}\left(\frac{\partial^2 u_x}{\partial x\partial z} + \frac{\partial^2 u_y}{\partial y\partial z}\right) + c_{33}\frac{\partial^2 u_z}{\partial z^2} = -\rho\omega^2 u_z.
\end{aligned} \tag{53}$$

This system of equations is only complete if we also solve for the Maxwell–Poisson equation. For MoS_2, the displacement field D_i is

$$D_i = \varepsilon_{ij}E_j + e_{iI}S_I + P_{sp}, \tag{54}$$

with P_{sp} being the spontaneous polarization contribution. The dielectric function is the same as for graphene (Equation 28) and we find

$$\begin{aligned}
D_x &= \varepsilon_{xx}E_1 + e_{x1}S_1 - e_{x1}S_2 + P_{sp,x},\\
D_y &= \varepsilon_{xx}E_2 - e_{x1}S_6 + P_{sp,y},\\
D_z &= \varepsilon_{zz}E_3 + P_{sp,z},
\end{aligned} \tag{55}$$

where $P_{sp,x}$, $P_{sp,y}$ and $P_{sp,z}$ denote the spontaneous polarization components along the x-, x- and z-direction, respectively. The Maxwell–Poisson equation (Equation 30) becomes

$$\begin{aligned}
&\varepsilon_{xx}\frac{\partial E_1}{\partial x} + e_{x1}\frac{\partial S_1}{\partial x} - e_{x1}\frac{\partial S_2}{\partial x}\\
&+\varepsilon_{xx}\frac{\partial E_2}{\partial y} - e_{x1}\frac{\partial S_6}{\partial y} + \varepsilon_{zz}\frac{\partial E_3}{\partial z} = 0,
\end{aligned} \tag{56}$$

because the spontaneous polarization P_{sp} is constant in space. A solution of the combined system Equation 51–Equation 53 and Equation 56 with appropriate boundary conditions allows for the determination of the electric field (or electric potential $-\nabla\phi = \mathbf{E}$) and the displacements u_x, u_y and u_z.

Phonon modes

In the case of MoS_2, the general solutions are more complicated. One can still make the plane wave ansatz,

$$u_x = f_x(z)\exp\left(ik_x x + ik_y y - i\omega t\right), \tag{57}$$

$$u_y = f_y(z)\exp\left(ik_x x + ik_y y - i\omega t\right), \tag{58}$$

$$u_z = f_z(z)\exp\left(ik_x x + ik_y y - i\omega t\right), \tag{59}$$

$$\phi = f_\phi(z)\exp\left(ik_x x + ik_y y - i\omega t\right). \tag{60}$$

Now, inserting Equation 57–Equation 60 in Equation 51–Equation 53 and Equation 56 yields the 4 × 4 matrix expression in the unknown functions f_x, f_y, f_z and f_ϕ

$$\begin{bmatrix} A_1+B_1\mathcal{D}^2 & C & D_1\mathcal{D} & E_1 \\ C & A_2+B_2\mathcal{D}^2 & D_2\mathcal{D} & E_2 \\ D_1\mathcal{D} & D_2\mathcal{D} & A_3+B_3\mathcal{D}^2 & 0 \\ E_1 & E_2 & 0 & A_4+B_4\mathcal{D}^2 \end{bmatrix}\begin{bmatrix} f_x \\ f_y \\ f_z \\ f_\phi \end{bmatrix} = \begin{bmatrix} 0 \\ 0 \\ 0 \\ 0 \end{bmatrix}, \tag{61}$$

where

$$\begin{aligned} A_1 &= -c_{11}k_x^2 - 1/2\left(c_{11}-c_{12}\right)k_y^2 + \rho\omega^2, \\ A_2 &= -c_{11}k_y^2 - 1/2\left(c_{11}-c_{12}\right)k_x^2 + \rho\omega^2, \\ A_3 &= -c_{44}\left(k_x^2+k_y^2\right) + \rho\omega^2, \\ A_4 &= \left(k_x^2+k_y^2\right)\varepsilon_{xx}, \\ B_1 &= B_2 = c_{44}, \\ B_3 &= c_{33}, \\ B_4 &= -\varepsilon_{zz}, \\ C &= \left[-c_{12} - 1/2\left(c_{11}-c_{12}\right)\right]k_x k_y, \\ D_1 &= ik_x\left(c_{13}+c_{44}\right), \\ D_2 &= ik_y\left(c_{13}+c_{44}\right), \\ E_1 &= \left(k_y^2-k_x^2\right)e_{x1}, \\ E_2 &= 2k_x k_y e_{x1}. \end{aligned} \tag{62}$$

For the case, $k_y = 0$, we have $C = D_2 = E_2 = 0$ and u_y decouples from u_x, u_z and ϕ. The wave equation for the u_y mode is the same as for graphene. To determine the general solution for the other displacement components, we once again solve the determinantal equation for the 3 × 3 sub-matrix in the components f_x, f_z and f_ϕ . The result is

$$\alpha + \beta\mathcal{D}^2 + \gamma\mathcal{D}^4 + \delta\mathcal{D}^6 = 0, \tag{63}$$

where

$$\begin{aligned} \alpha &= A_1A_3A_4 - E_1^2A_3, \\ \beta &= A_1A_3B_4 + A_1A_4B_3 + A_3A_4B_1 - D_1^2A_4 - E_1^2B_3, \\ \gamma &= B_1B_3A_4 + B_1B_4A_3 + B_3B_4A_1 - D_1^2B_4, \\ \delta &= B_1B_3B_4, \end{aligned} \tag{64}$$

and six roots (three pairs of opposite signs) exist. It also follows that

$$\begin{aligned} f_\phi &= -\frac{E_1}{A_4+B_4\mathcal{D}^2}f_x \equiv \gamma_1 f_x, \\ f_z &= -\frac{D_1\mathcal{D}}{A_3+B_3\mathcal{D}^2}f_x \equiv \gamma_2 f_x. \end{aligned} \tag{65}$$

Hence the general solution is, using a notation similar to the case of graphene,

$$f_x = \sum_{i=1}^{6}\beta_i\exp\left(\alpha_i z\right), \tag{66}$$

$$f_\phi = \sum_{i=1}^{6}\gamma_{1,i}\beta_i\exp\left(\alpha_i z\right), \tag{67}$$

$$f_x = \sum_{i=1}^{6}\gamma_{2,i}\beta_i\exp\left(\alpha_i z\right), \tag{68}$$

where β_i are unknown coefficients.

The Maxwell–Poisson equation in vacuum ($\nabla^2\phi_v = 0$) has the general solution

$$\begin{aligned} \phi_v &= \phi_+\exp\left(-k_x z\right)\exp\left(ik_x x - i\omega t\right), \quad z \geq h, \\ \phi_v &= \phi_-\exp\left(k_x z\right)\exp\left(ik_x x - i\omega t\right), \quad z \leq -h, \end{aligned} \tag{69}$$

where ϕ_+, ϕ_- are unknown constants. An 8 × 8 matrix equation in β_i, ϕ_+, ϕ_- is finally obtained by invoking the four mechanical boundary conditions at $z = h, -h$

$$T_{zz}(z=h) = T_{zz}(z=-h) = 0, \tag{70}$$

$$T_{xz}(z=h) = T_{xz}(z=-h) = 0, \tag{71}$$

and the four electric boundary conditions at $z = h, -h$,

$$\begin{aligned} &E_1 \text{ continuous,} \\ &D_z \text{ continuous.} \end{aligned} \tag{72}$$

The mechanical boundary conditions are the same as for graphene,

$$\begin{aligned} T_{zz} &= ik_x c_{13} f_x + c_{33} \mathcal{D} f_z, \\ T_{xz} &= c_{44} \mathcal{D} f_x + ik_x c_{44} f_z, \end{aligned} \tag{73}$$

but the electric boundary conditions are (written out)

$$\begin{aligned} -ik_x f_\phi(z=h) &= -ik_x \phi_+ \exp(-k_x h), \\ -ik_x f_\phi(z=-h) &= -ik_x \phi_- \exp(-k_x h), \\ -\varepsilon_{zz} \mathcal{D}\phi(z=h) &= -\varepsilon_0 \mathcal{D}\phi_v(z=h), \\ -\varepsilon_{zz} \mathcal{D}\phi(z=-h) &= -\varepsilon_0 \mathcal{D}\phi_v(z=-h), \end{aligned} \tag{74}$$

where ε_0 is the vacuum permittivity. Solving the determinantal equation for the 8 × 8 matrix equation as a function of k_x specifies a discrete set of (band) eigenfrequencies $\omega_i(k_x)$ and the corresponding eigenmodes f_x, f_z and f_ϕ, where i denotes the band index.

Confined phonon modes

An important result concerning confined optical phonons can be obtained without solving the determinantal equations. From the elastic equations (Equation 51 and Equation 53) and the electric equation (Equation 56) we have, assuming $k_y = 0$,

$$\begin{aligned} &-k_x^2 c_{11} u_x + ik_x c_{13} \frac{\partial u_z}{\partial z} \\ &+c_{44}\left(\frac{\partial^2 u_x}{\partial z^2} + ik_x \frac{\partial u_z}{\partial z} \right) - k_x^2 e_{x1} \phi = -\rho\omega^2 u_x, \end{aligned} \tag{75}$$

$$\begin{aligned} &c_{44}\left(ik_x \frac{\partial u_x}{\partial z} - k_x^2 u_z \right) \\ &+c_{12} ik_x \frac{\partial u_x}{\partial z} + c_{33} \frac{\partial^2 u_z}{\partial z^2} = -\rho\omega^2 u_z. \end{aligned} \tag{76}$$

$$k_x^2 (\varepsilon_{xx}\phi - e_{x1} u_x) - \varepsilon_{zz} \frac{\partial^2 \phi}{\partial z^2} = 0. \tag{77}$$

Inspection of the above set of equations reveals that confined phonon solutions can be sought in the form [type I]

$$\begin{aligned} \phi &= A_{\phi,1} \sin(\delta_1 z) + A_{\phi,2} \sin(\delta_2 z) + A_{\phi,3} \sinh(\delta_3 z), \\ u_x &= A_{x,1} \sin(\delta_1 z) + A_{x,2} \sin(\delta_2 z) + A_{x,3} \sinh(\delta_3 z), \\ u_z &= A_{z,1} \cos(\delta_1 z) + A_{z,2} \cos(\delta_2 z) + A_{z,3} \cosh(\delta_3 z), \end{aligned} \tag{78}$$

or in the form [type II]

$$\begin{aligned} \phi &= A_{\phi,1} \cos(\delta_1 z) + A_{\phi,2} \cos(\delta_2 z) + A_{\phi,3} \cosh(\delta_3 z), \\ u_x &= A_{x,1} \cos(\delta_1 z) + A_{x,2} \cos(\delta_2 z) + A_{x,3} \cosh(\delta_3 z), \\ u_z &= A_{z,1} \sin(\delta_1 z) + A_{z,2} \sin(\delta_2 z) + A_{z,3} \sinh(\delta_3 z), \end{aligned} \tag{79}$$

apart from a multiplying factor $\exp(ik_x x - i\omega t)$. The above choice reflects an expectation that four roots are real (two pairs of opposite-signed roots) and two imaginary (one pair of opposite-signed roots).

From Equation 75–Equation 77 follows

$$A_{\phi,i} = \frac{k_x^2 e_{x1}}{k_x^2 \varepsilon_{xx} + \delta_i^2 \varepsilon_{zz}} A_{x,i}, \tag{80}$$

$$A_{z,i} = \frac{ik_x \delta_i (c_{12} + c_{44})}{c_{44} k_x^2 + c_{33} \delta_i^2 - \rho\omega^2} A_{x,i}, \tag{81}$$

$$A_{z,i} = \frac{\rho\omega^2 - c_{11} k_x^2 - \delta_i^2 c_{44} - \dfrac{k_x^4 e_{x1}^2}{k_x^2 \varepsilon_{xx} + \delta_i^2 \varepsilon_{zz}}}{ik_x \delta_i (c_{13} + c_{44})} A_{x,i}, \tag{82}$$

where $i = 1,2,3$. Note that a maximum of two of the latter relations can be independent since the values of δ_i are found by setting the system determinant to zero.

A general confined optical phonon mode can now be written as a Fourier series expansion [type I]

$$\phi = \sum_{m=1,2,3,\ldots} A_{\phi,m} \sin\left(\frac{m\pi}{h} z\right) \exp\left(ik_x x - i\omega t\right), \quad (83)$$

$$u_x = \sum_{m=1,2,3,\ldots} A_{x,m} \sin\left(\frac{m\pi}{h} z\right) \exp\left(ik_x x - i\omega t\right), \quad (84)$$

$$u_z = \sum_{m=1,2,3,\ldots} A_{x,m} \cos\left(\frac{m\pi}{h} z\right) \exp\left(ik_x x - i\omega t\right), \quad (85)$$

since this construction implies $E_x(z = \pm h) = 0$ and $\phi_+ = \phi_- = 0$ using continuity in the transverse electric field at the interfaces. Equation 75–Equation 77 must still apply, however, in particular combining Equation 81–Equation 82 demands

$$\rho\omega^2 - c_{11}k_x^2 - \left(\frac{m\pi}{h}\right)^2 c_{44} - \frac{k_x^4 e_{x1}^2}{k_x^2 \varepsilon_{xx} + \left(\frac{m\pi}{h}\right)^2 \varepsilon_{zz}} - \frac{ik_x \frac{m\pi}{h}\left(c_{12} + c_{44}\right)}{c_{44}k_x^2 + c_{33}\left(\frac{m\pi}{h}\right)^2 - \rho\omega^2} \cdot ik_x \frac{m\pi}{h}\left(c_{13} + c_{44}\right) = 0. \quad (86)$$

For each term m, this latter condition, in general, would lead to a different ω_m. However, a normal mode is characterized by a unique frequency ω. Hence, for confined optical phonon modes, only one term in m is allowed in the general Fourier series expansions above. Further, imposing continuity in the normal electric displacement component at $z = \pm h$ by use of the third equation in Equation 55 gives

$$\varepsilon_{zz} \frac{m\pi}{h} A_{\phi,m} = 0, \quad (87)$$

and $A_{\phi,m} = 0$ unless accidentally $\varepsilon_{zz}(\omega_m) = 0$ (treated separately in the next paragraph). For $\varepsilon_{zz}(\omega_m) \neq 0$, it follows from Equation 80 that $A_{x,m} = 0$ and Equation 81 yields $A_{z,m} = 0$. The conclusion is that confined optical phonons in the general case cannot exist in MoS_2! Note that for graphene, since it is a non-piezoelectric material, confined optical phonon modes do exist. The difference between the two materials lies in Equation 77, specifically in the term containing the piezoelectric coefficient.

If $\varepsilon_{zz} = 0$, continuity of the normal electric displacement component requires, as before, $\phi_+ = \phi_- = 0$ and we return to the situation treated in the previous subsection about confined optical phonons. We need to consider two possible cases: (a) $\varepsilon_{xx}(\omega) = 0$ when $\varepsilon_{zz}(\omega) = 0$ and (b) $\varepsilon_{xx}(\omega) \neq 0$ when $\varepsilon_{zz}(\omega) = 0$. In case (a), we immediately obtain $\phi_+ = \phi_- = 0$ from continuity in the normal electric displacement. Further, Equation 77 yields $u_x = 0$ everywhere as a function of z. Equation 83–Equation 85 must hold from continuity in the transverse electric field. Finally, Equation 75 gives

$$\phi = \frac{i\left(c_{13} + c_{44}\right)}{k_x e_{x1}} \frac{\partial u_z}{\partial z}, \quad (88)$$

and Equation 76 requires [type I]

$$u_z = \alpha \cos\left(\sqrt{\frac{\rho\omega^2 - k_x^2 c_{44}}{c_{33}}} z\right), \quad (89)$$

and the condition

$$\sqrt{\frac{\rho\omega^2 - k_x^2 c_{44}}{c_{33}}} = \frac{m\pi}{h}, \quad (90)$$

which is not fulfilled, unless accidental degeneracy applies, simultaneous with $\varepsilon_{xx}(\omega) = \varepsilon_{zz}(\omega) = 0$. In case (b), Equation 86 can be used and, unless accidental degeneracy applies, the obtained ω_m values do not fulfill $\varepsilon_{zz}(\omega) = 0$. In conclusion, confined optical phonon modes do not exist in the case $\varepsilon_{zz} = 0$.

Computed dispersion relations

In order to illustrate the validity of the phonon dispersion relations obtained from our model, we compare them to DFT calculations. The continuum theory will require as input elasticity constants, piezoelectric coefficients, and dielectric functions.

DFT

We first give the standard phonon dispersion relation as obtained from DFT calculations (Figure 1). They are obtained from first principles calculations using the Vienna ab initio simulation package (VASP) [17] with a kinetic energy cut-off of 500 eV in the expansion of the electronic wave functions. Four C and six Mo and S valence electrons are considered. The generalized gradient approximation of the exchange–correlation potential in the Perdew–Burke–Ernzerhof flavor is employed [18]. Brillouin-zone integrations are performed using the tetrahedron method with Blöchl corrections [19]. We construct cells consisting of the monolayer and an approximately 15 Å thick vacuum region along the c direction. Structure optimizations are performed on Γ-centered 24 × 24 × 1 k-meshes. A direct method based on 4 × 4 × 1 supercells is used for obtain-

ing the phonon dispersions within the harmonic approximation [20]. Forces are evaluated on 3 × 3 × 1 k-meshes, including long-range dipole contributions to the dynamical matrix following the method of [21]. Born effective charges and dielectric tensors are obtained within perturbation theory [22] and elastic constants by the homogeneous deformation method [23]. The elastic stiffness tensor and frequency-dependent dielectric tensor (independent particle approximation [24]) are calculated on Γ-centered 36 × 36 × 1 k-meshes.

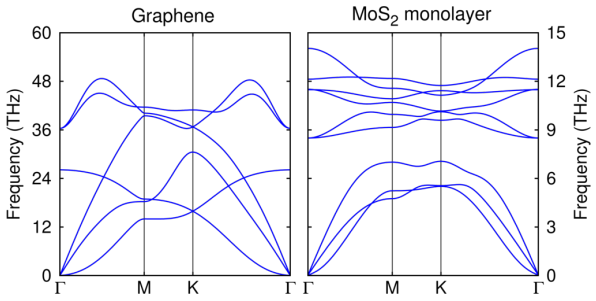

Figure 1: Dispersion relations for the phonon modes of single-layer graphene (left) and MoS_2 (right), from DFT calculations.

Continuum model: graphene

The following parameters are found using DFT calculations as explained above: $c_{11}d$ = 345 Pa·m, $c_{12}d$ = 73 Pa·m, $c_{13}d$ = 0.00387 Pa·m, $c_{33}d$ = 0.531 Pa·m, $c_{44}d$ = 0.0535 Pa·m, $c_{66}d$ = 136 Pa·m, $d = 3.4{\cdot}10^{-8}$ m, and $\rho_{2D} = 7.61{\cdot}10^{-7}$ kg/m^2. For the permittivity data we used the DC values $\varepsilon_{xx} = 4.4\varepsilon_0$ and $\varepsilon_{zz} = 1.3\varepsilon_0$.

In Figure 2, we show the frequency vs wavenumber (ω–k_x) dispersion in the vicinity of the Γ point ($k_y = 0$). Evidently, one mode shows a parabolic dispersion and one mode is linear. There are two higher-order modes originating from the boundary conditions along the z coordinate. The dispersion curves associated with the u_y vibrations decoupled from the $u_x - u_z$ vibrations are not shown in the plots. We emphasize that for graphene optical and acoustic phonon modes decouple and are computed separately as described above. In Figure 3, the dispersion curves for optical phonon modes near the Γ point are shown.

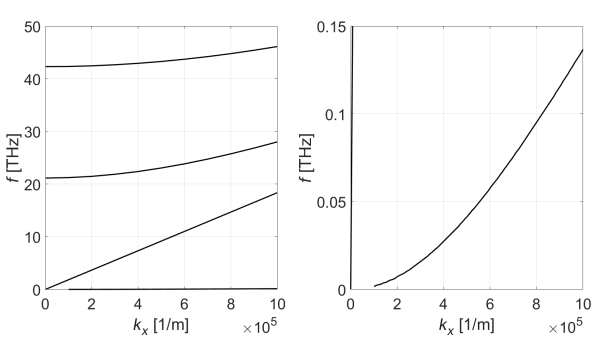

Figure 2: Dispersion relations for the coupled u_x–u_z acoustic phonon modes of single-layer graphene. The right plot is a zoomed version of the left plot. Note the nonlinear dispersion of one acoustic mode away from the Γ point. There is also one acoustic mode showing linear dispersion.

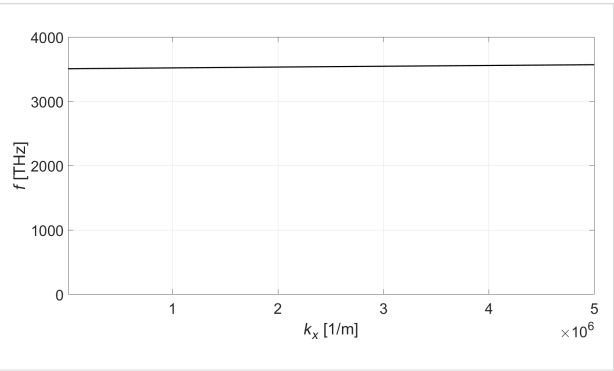

Figure 3: Dispersion relation for the optical phonon modes of single-layer graphene.

Continuum model: MoS_2

For single-layer MoS_2, we use the following parameters: $c_{11}d$ = 140 Pa·m, $c_{12}d$ = 33 Pa·m, c_{13}d=-0.013 Pa·m, $c_{33}d$ = 0.078 Pa·m, $c_{44}d$ = −1.07 Pa·m, $c_{66}d$ = 53.7 Pa·m, $d = 6.2{\cdot}10^{-10}$ m, $\rho_{2D} = 3.1 \cdot 10^{-6}$ kg/m^2, e_{x1} = 0.5 C/m^2. These elasticity parameters were again computed using VASP. The frequency-dependent permittivity values are taken from [25] and the piezoelectric constant e_{x1} is from Ref. [26]. In the case of MoS_2, all optical and acoustic phonon modes are computed by solving the combined set of elastic and electric equations and associated slab boundary conditions as described above. We note in passing that both confined and surface acousto-optical phonon modes are found using the present formalism. In Figure 4, we show the frequency vs wavenumber (ω–k_x) dispersion in the vicinity of the Γ point ($k_y = 0$).

Conclusion

A three-dimensional, first-principles, continuum elasticity theory was developed for two-dimensional materials. Piezoelectric materials required the simultaneous consideration of the electrostatics equations. Application to graphene, silicene and MoS_2 revealed a number of interesting results. The out-of-plane vibrations were coupled to the in-plane motion for graphene (and for silicene as well), contrary to previous results using infinitely thin sheets. Acoustic modes with linear and quadratic dispersions were obtained, in agreement with experimental results and other models. We predict the existence of confined optical modes in all of the elemental group-IV materials and the nonexistence of confined optical modes in MoS_2. Our model

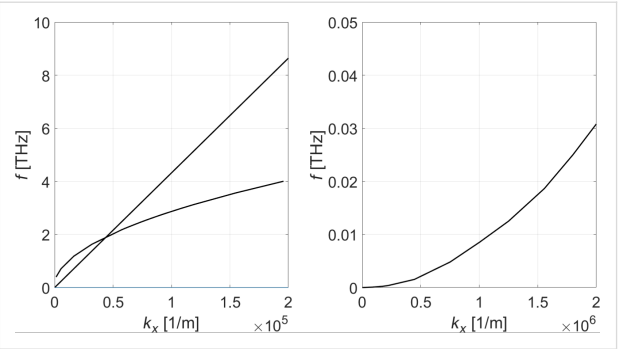

Figure 4: Dispersion relations for the coupled u_x–u_z–ϕ phonon modes of single-layer MoS_2. The right plot is a zoomed version of the left plot. Note again the parabolic dispersion of one predominantly acoustic mode away from the Γ point besides a linear dispersion predominant acoustic mode. We also obtain a second nonlinear mode starting at (k,ω) = (0,0), which stems from the rather complicated frequency-dependent permittivity of MoS_2.

will be applied to other 2D materials as well as to multilayers in future work. Additionally, the results of this model can be combined with the solution to the electron problem to compute electron–phonon scattering rates. The latter would be useful for understanding a number of physical properties as well as for applications.

Acknowledgements

MW acknowledges financial support from the Danish Council of Independent Research (Natural Sciences) grant no.: DFF - 4181-00182. The research reported in this publication was supported by funding from King Abdullah University of Science and Technology (KAUST).

References

1. Cahangirov, S.; Topsakal, M.; Aktürk, E.; Şahin, H.; Ciraci, S. *Phys. Rev. Lett.* **2009,** *102,* 236804. doi:10.1103/PhysRevLett.102.236804
2. Roome, N. J. Electronic and Phonon Properties of 2D Layered Materials. Ph.D. Thesis, University of Surrey, United Kingdom, 2015.
3. Kamal, C.; Chakrabarti, A.; Ezawa, M. *New J. Phys.* **2015,** *17,* 083014. doi:10.1088/1367-2630/17/8/083014
4. Mannix, A. J.; Zhou, X.-F.; Kiraly, B.; Wood, J. D.; Alducin, D.; Myers, B. D.; Liu, X.; Fisher, B. L.; Santiago, U.; Guest, J. R.; Yacaman, M. J.; Ponce, A.; Oganov, A. R.; Hersam, M. C.; Guisinger, N. P. *Science* **2015,** *350,* 1513–1516. doi:10.1126/science.aad1080
5. Peng, B.; Zhang, H.; Shao, H.; Xu, Y.; Zhang, R.; Zhu, H. *J. Mater. Chem. C* **2016,** *4,* 3592–3598. doi:10.1039/C6TC00115G
6. Singh, D.; Gupta, S. K.; Lukačevic, I.; Sonvane, Y. *RSC Adv.* **2016,** *6,* 8006–8014. doi:10.1039/C5RA25773E
7. Guzmán-Verri, G. G.; Lew Yan Voon, L. C. *Phys. Rev. B* **2007,** *76,* 075131. doi:10.1103/PhysRevB.76.075131
8. Takeda, K.; Shiraishi, K. *Phys. Rev. B* **1994,** *50,* 14916–14922. doi:10.1103/PhysRevB.50.14916
9. Fuchs, R.; Kliewer, K. L. *Phys. Rev.* **1965,** *140,* A2076–A2088. doi:10.1103/PhysRev.140.A2076
10. Suzuura, H.; Ando, T. *Phys. Rev. B* **2002,** *65,* 235412. doi:10.1103/PhysRevB.65.235412
11. Goupalov, S. V. *Phys. Rev. B* **2005,** *71,* 085420. doi:10.1103/PhysRevB.71.085420
12. Qian, J.; Allen, M. J.; Yang, Y.; Dutta, M.; Stroscio, M. A. *Superlattices Microstruct.* **2009,** *46,* 881–888. doi:10.1016/j.spmi.2009.09.001
13. Droth, M.; Burkard, G. *Phys. Rev. B* **2011,** *84,* 155404. doi:10.1103/PhysRevB.84.155404
14. Landau, L. D.; Lifshitz, E. M. *Theory of Elasticity,* 2nd ed.; Course of theoretical physics, Vol. 7; Pergamon Press: Oxford, United Kingdom, 1970.
15. Xie, H.; Hu, M.; Bao, H. *Appl. Phys. Lett.* **2014,** *104,* 131906. doi:10.1063/1.4870586
16. Licari, J. J.; Evrard, R. *Phys. Rev. B* **1977,** *15,* 2254–2264. doi:10.1103/PhysRevB.15.2254
17. Kresse, G.; Joubert, D. *Phys. Rev. B* **1999,** *59,* 1758–1775. doi:10.1103/PhysRevB.59.1758
18. Perdew, J. P.; Burke, K.; Ernzerhof, M. *Phys. Rev. Lett.* **1996,** *77,* 3865–3868. doi:10.1103/PhysRevLett.77.3865
19. Blöchl, P. E.; Jepsen, O.; Andersen, O. K. *Phys. Rev. B* **1994,** *49,* 16223–16233. doi:10.1103/PhysRevB.49.16223
20. Alfè, D. *Comput. Phys. Commun.* **2009,** *180,* 2622–2633. doi:10.1016/j.cpc.2009.03.010
21. Cochran, W.; Cowley, R. A. *J. Phys. Chem. Solids* **1962,** *23,* 447–450. doi:10.1016/0022-3697(62)90084-7
22. Baroni, S.; Giannozzi, P.; Testa, A. *Phys. Rev. Lett.* **1987,** *58,* 1861–1864. doi:10.1103/PhysRevLett.58.1861
23. Le Page, Y.; Saxe, P. *Phys. Rev. B* **2002,** *65,* 104104. doi:10.1103/PhysRevB.65.104104
24. Gajdoš, M.; Hummer, K.; Kresse, G.; Furthmüller, J.; Bechstedt, F. *Phys. Rev. B* **2006,** *73,* 045112. doi:10.1103/PhysRevB.73.045112
25. Mukherjee, B.; Tseng, F.; Gunlycke, D.; Amara, K. K.; Eda, G.; Simsek, E. *Opt. Mater. Express* **2015,** *5,* 447–455. doi:10.1364/OME.5.000447
26. Zhu, H.; Wang, Y.; Xiao, J.; Liu, M.; Xiong, S.; Wong, Z. J.; Ye, Z.; Ye, Y.; Yin, X.; Zhang, X. *Nat. Nanotechnol.* **2015,** *10,* 151–155. doi:10.1038/nnano.2014.309

License and Terms

BEILSTEIN JOURNAL OF NANOTECHNOLOGY

Comprehensive Raman study of epitaxial silicene-related phases on Ag(111)

Dmytro Solonenko*[1], Ovidiu D. Gordan[1], Guy Le Lay[2], Dietrich R. T. Zahn[1] and Patrick Vogt[1]

Full Research Paper

Open Access

Address:
[1]Semiconductor Physics, Chemnitz University of Technology, 09107 Chemnitz, Germany and [2]Aix-Marseille Université, CNRS, 13397 Marseille Cedex, France

Email:
Dmytro Solonenko* - dmytro.solonenko@physik.tu-chemnitz.de;
Patrick Vogt - patrick.vogt@hrz.tu-chemnitz.de

* Corresponding author

Keywords:
epitaxial silicene; in situ Raman spectroscopy; phase diagram

Beilstein J. Nanotechnol. **2017,** *8,* 1357–1365.
doi:10.3762/bjnano.8.137

Received: 02 March 2017
Accepted: 07 June 2017
Published: 03 July 2017

This article is part of the Thematic Series "Silicene, germanene and other group IV 2D materials".

Associate Editor: A. J. Meixner

Abstract

The investigation of the vibrational properties of epitaxial silicene and two-dimensional (2D) Si structures on the silver(111) surface aims for a better understanding of the structural differences and of the simplification of the seemingly complex phase diagrams reported over the last years. The spectral signatures of the main silicene phases epitaxially grown on Ag(111) were obtained using in situ Raman spectroscopy. Due to the obvious 2D nature of various epitaxial silicene structures, their fingerprints consist of similar sets of Raman modes. The reduced phase diagram also includes other Si phases, such as amorphous and crystalline silicon, which emerge on the Ag surface at low and high preparation temperatures, respectively. The Raman signatures obtained along with their interpretations provide the referential basis for further studies and for potential applications of epitaxial silicene.

Introduction

Epitaxial silicene, an elemental 2D silicon allotrope [1-3] grown on a supporting substrate such as Ag(111), has attracted considerable interest since its first discovery in 2012 [4-6]. Yet, the investigation of epitaxial silicene on Ag(111) remains challenging because of the complex phase diagram upon the formation of Si structures on Ag(111). It was shown that different substrate temperatures during Si deposition result in the formation of various 2D Si phases [7,8] with (3×3)/(4×4) and $(\sqrt{7}\times\sqrt{7})R\pm19.1°/(\sqrt{13}\times\sqrt{13})R\pm13.9°$ symmetry, where the first part refers to the translational symmetry of the structure with respect to silicene and the second part refers to the translational symmetry with respect to the Ag(111)-1×1 surface, and a so-called "$(2\sqrt{3}\times2\sqrt{3})$" superstructure. The angle given outside the parenthesis describes the rotational mismatch between the superstructure and the crystallographic directions of the silver substrate. Despite the clear assignment of these 2D

Si layers to different symmetries, their properties and assignment to silicene are controversially discussed in the literature [9-11].

The most extensively investigated structure is the prototypical (3×3)/(4×4) phase, which is so far the only one clearly shown to refer to epitaxial silicene [4,12,13]. The $(\sqrt{7}\times\sqrt{7})R\pm19.1°/(\sqrt{13}\times\sqrt{13})R\pm13.9°$ subsidiary phase can be found in four different domains [14]. These domains are explained by four different rotation angles relative to the Ag[110] direction of an initial honeycomb lattice similar to the (3×3)/(4×4) phase but slightly expanded. Because of the interaction with the Ag(111) substrate, those domains have a very different appearance in STM imaging. The $(\sqrt{7}\times\sqrt{7})R\pm19.1°/(\sqrt{13}\times\sqrt{13})R\pm13.9°$ phase always coexists with the (3×3)/(4×4) and the "$(2\sqrt{3}\times2\sqrt{3})R30°$" superstructure and forms relatively small domains. Its similarity to the honeycomb (3×3)/(4×4) phase has not been proven unambiguously yet. At growth temperatures above 250 °C, the "$(2\sqrt{3}\times2\sqrt{3})R30°$" superstructure is predominantly formed; it is the most controversially discussed Si structure on Ag(111). While Jamgotchian et al. [15] assigned this structure to a perfectly ordered silicene phase with an enhanced crystallinity if grown at 390 °C, instead, Liu et al. [16] showed that it comprises ordered and disordered areas, while Acun et al. [17] underlined the beginning of the distortion of epitaxial silicene, which leads to its destruction at 300 °C, caused by a dewetting process. Angle-resolved photoemission spectroscopy measurements of this superstructure by Wang et al. [18] showed that its electronic band structure mostly comprises bands pointing to an sp^3 hybridization of its Si atoms. Moreover, there are also claims that this superstructure is stabilized by Ag atoms, found either on the top or inside the 2D layer [19,20] and, therefore, it would not be a real silicene phase.

In order to elucidate the complex formation of the diverse 2D Si structures on Ag(111) and to probe the nature of the silicene-related ones, we have employed Raman spectroscopy, a versatile and non-destructive optical method, highly sensitive to the structural properties of the materials [21,22]. The first results on 2D Si structures, obtained using in situ Raman spectroscopy, conclusively confirmed the 2D nature of epitaxial (3×3)/(4×4) silicene and demonstrated an easy access to its chemical and physical properties [23]. Based on these results, the spectral signatures of silicene-related superstructures are established. Our results reveal a fundamental difference among these superstructures, related to the ratio of structural order and disorder. Furthermore, the in situ Raman results allow the phase diagram to be determined for the silicon deposition onto the Ag(111) surface from room temperature (RT) up to 500 °C.

Results

Scanning tunneling microscopy

Figure 1 shows the STM images for Si deposited onto Ag(111) at different substrate temperatures in agreement with previous reports [4,8]. For deposition of about 0.1 of a ML at room temperature filled-states STM images (Figure 1a) show the formation of cluster-like structures on the otherwise atomically flat Ag(111) surface. The number and sizes of the clusters increase with Si deposition time but do not show any additional corrugation, which would be indicative for any order within the clusters. This is in agreement with the LEED observation, which shows no additional diffraction spots besides the integer-order ones of Ag(111)-1×1 even for the deposition of a complete ML. The formation of these clusters takes place up to a preparation temperature of around 170 °C. At temperatures between 180 and 210 °C the Ag terraces start to show some decoration by locally ordered features developing from the Ag step edges into the terraces (not shown). Still, no long-range order is observed. For deposition temperatures of approximately 220 °C a very clear new symmetry of (4×4) with respect to the original Ag(111) one can be seen by LEED (Figure 1b, inset). It indicates the formation of the (3×3)/(4×4) epitaxial silicene structure, shown in the STM image in Figure 1b.

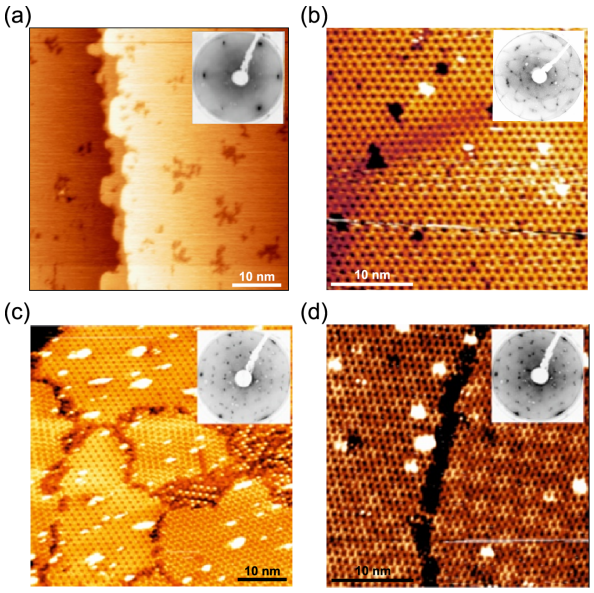

Figure 1: (a) STM topographic images (U_{bias} = −1.0 V, I = 1.08 nA) and corresponding low-energy electron diffraction (LEED) patterns (insets) of (a) 0.1 ML of Si deposited onto Ag(111) at room temperature, (b) 1 ML of Si deposited at 220 °C resulting in (3×3) silicene formation, (c) 1 ML of Si deposited at 240 °C showing the formation of several phases, and (d) 1 ML of Si deposited at 280 °C with a clear "$(2\sqrt{3}\times2\sqrt{3})R30°$" reconstruction.

At temperatures above 220 but below 250 °C the formation of multiple phases including (3×3)/(4×4),

$(\sqrt{7}\times\sqrt{7})R\pm19.1°/(\sqrt{13}\times\sqrt{13})R\pm13.9°$ ($(\sqrt{13}\times\sqrt{13})R13.9°$, in short) and domains of a third 2D Si configuration, the "$(2\sqrt{3}\times2\sqrt{3})$", are found by using STM (Figure 1c). The related LEED patterns show a superposition of these three distinct symmetries, yet a slight domination of one of the symmetries depends on the exact preparation temperatures (Figure 1c, inset). The $(\sqrt{7}\times\sqrt{7})R\pm19.1°/(\sqrt{13}\times\sqrt{13})R\pm13.9°$ structure comprises four different domains as a result of the combination of the different rotation angles. These four domains can be clearly distinguished in STM but refer to a very similar underlying silicene honeycomb structure [14]. Contrary to the (3×3)/(4×4), it is not possible to prepare dominant multiple or single $(\sqrt{13}\times\sqrt{13})R13.9°$ domains.

At higher preparation temperatures the "$(2\sqrt{3}\times2\sqrt{3})$" symmetry becomes dominant in LEED measurements and is finally observed solely for deposition temperatures above 250 °C (Figure 1d, inset). The STM topography image of this debated structure (Figure 1d) reveals a Moiré-like surface pattern [6,16]. This pattern originates from locally ordered areas that are surrounded by distorted or disordered zones. The ordered areas appear brighter in filled-states STM images, thus mimicking a Moiré pattern. Because of the inherent intrinsic disorder (ID) it is not reasonable to assign any silicene symmetry to this structure, which will be referred to as "$(2\sqrt{3}\times2\sqrt{3})$". At higher temperatures, around 300 °C, the "$(2\sqrt{3}\times2\sqrt{3})$" structure finally disappears because of a dewetting process [17].

Raman spectroscopy

Figure 2 shows the Raman spectra, obtained after Si deposition onto Ag(111) at different growth temperatures related to the different aforementioned structures. Firstly, we notice that these Raman spectra differ significantly, pointing to fundamental structural differences between the diverse growth conditions. For the growth at room temperature, the spectra exhibit a broad Raman band at 480 cm^{-1} with a shoulder around 350 cm^{-1}. Narrow phonon modes indicative of crystalline order are not observed in this case. At a temperature of 220 °C at which (3×3)/(4×4) epitaxial silicene is formed, the prototypical phase with C_{6v} symmetry is identified by the presence of narrow A^1 and A^2 modes at 175 and 216 cm^{-1}, respectively, and by an E mode at 514 cm^{-1}. The detailed description of the Raman signature and vibrational properties of epitaxial (3×3)/(4×4) silicene can be found in [23].

The Raman spectra of the "mixed phase" (grown at temperatures between 220 and 280 °C) exhibit similar features as those of (3×3)/(4×4) epitaxial silicene, but show also several deviations: The E mode at 514 cm^{-1} seemingly shifts to 518 cm^{-1},

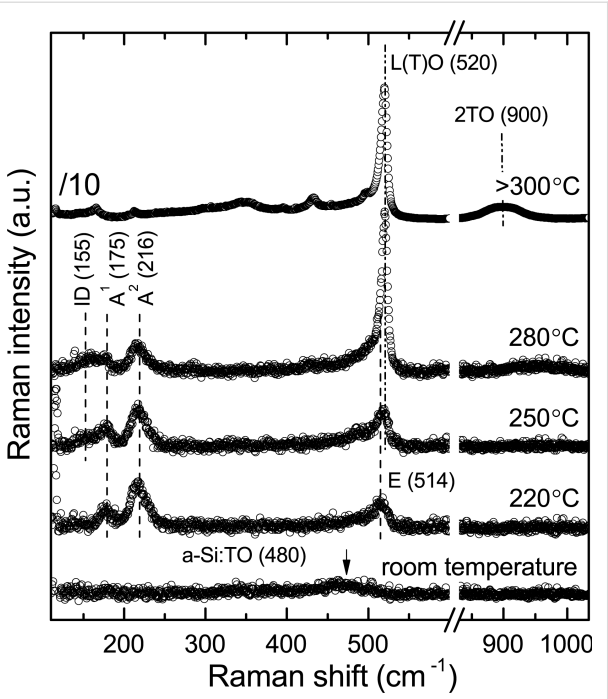

Figure 2: Raman spectra of the various structures obtained upon Si deposition at room temperature RT, 220, 250, 280, and 300 °C. In the spectral range between 550 and 830 cm^{-1}, no features were observed. The spectra are stacked for clarity. The topmost Raman spectrum was divided by 10 to fit the rest of spectra in the plot.

and a new shoulder appears at 155 cm^{-1}. For even higher deposition temperatures around 280 °C the Raman spectra are dominated by a mode at 520 cm^{-1}, accompanied by a decrease of all modes observed at lower deposition temperatures with the exception of the mode at 155 cm^{-1}, also present in this growth regime. Its energy and line shape indicate the disorder-related nature of this Raman band, particularly evident in the case of the "$(2\sqrt{3}\times2\sqrt{3})$" structure, known to be mostly disordered [16]. If the growth temperature further increases above 300 °C, the related Raman spectra become dominated by an intense mode at 520 cm^{-1} and a broad band at 900 cm^{-1}, showing a strong similarity to bulk diamond-like silicon. The low-intensity Raman bands below the band at 520 cm^{-1} will be discussed elsewhere.

Our Raman results differ significantly from recently published ex situ and in situ Raman observations. Previous ex situ Raman results showed the presence of an "E_{2g}" mode at 516 cm^{-1} for the (3×3)/(4×4) phase, whereas the Raman spectrum of the "$(2\sqrt{3}\times2\sqrt{3})R30°$" structure was reported to exhibit strong bands at 521 and 900 cm^{-1}, interpreted as a graphene-like behaviour [24]. The in situ Raman results of epitaxial (3×3)/(4×4) silicene at one monolayer coverage from Zhuang et al. [25] show bands at 230 and 530 cm^{-1}, while in the work of Diaz Alvarez et al. [26] vibrational modes of the same structure are

reported at 246 and 518.7 cm^{-1}. In the latter case, the Raman peak at 246 cm^{-1} is found at low silicene coverages. In none of the cases the spectral signature of the accompanying $(\sqrt{13}\times\sqrt{13})R13.9°$ structures could be distinguished from that of the dominant (3×3)/(4×4) phases.

In order to elucidate the formation of the different Si phases on Ag(111) and their related properties we now look at the Raman signatures of these phases (shown in Figure 2) and compare them to the signatures of (3×3)/(4×4) epitaxial silicene. We start with the lowest (<170 °C) and the highest (≥300 °C) growth temperatures, which also mark the 3D transition for the 2D structures on Ag(111).

Si deposition at room temperature

A detailed Raman spectrum recorded on a sample after the deposition of nominally 1 ML of Si at room temperature is shown in Figure 3a together with a sample prepared under identical conditions but with 5 MLs of Si deposited. It is clearly seen that the sample with 5 MLs of Si shows similar broad bands at 350 and 480 cm^{-1} when compared to the sample with 1 ML of Si but the shoulder at 350 cm^{-1} and a less intense broad band at 150 cm^{-1} are more pronounced. The shoulder at 350 cm^{-1} is actually a combination of several Raman bands located around 310 and 380 cm^{-1}. This spectrum shows strong similarity to the one of amorphous Si, which is characterized by comparable Raman bands [27,28]. For the deposition of 1 ML the Raman intensity of all bands is very weak: Practically, only the most intense mode at 480 cm^{-1} is detected.

Ex situ AFM images of this sample recorded under ambient conditions, i.e., after oxidation in air, are displayed in Figure 3b. Raman spectra obtained before and after air exposure are identical confirming that the oxidation process in air does not cause the appearance of those new features. Numerous bright features having an average height of about 2 nm (Figure 3c) can be found now on the surface within the scanning range. The contrast in the AFM phase image in the inset of Figure 3b demonstrates the different chemical compositions of the bright features and of the Ag(111) surface. In combination with the Raman results we conclude that these small structures are related to amorphous silicon (a-Si). This demonstrates that the Si deposition at low temperatures (≤150 °C) produces neither ordered 2D nor 3D crystalline Si structures. We can assume that the Si deposition at even lower temperatures (≤20 °C) leads to a similar result. It was recently suggested that impinging Si atoms at room temperature penetrate the Ag(111) surface, exchange with Ag atoms and act as seeds for the growth of recessed islands [29]. At the same time the released Ag atoms would form new Ag(111) terraces by a process described to occur more rapidly as the size of the embedded islands increases.

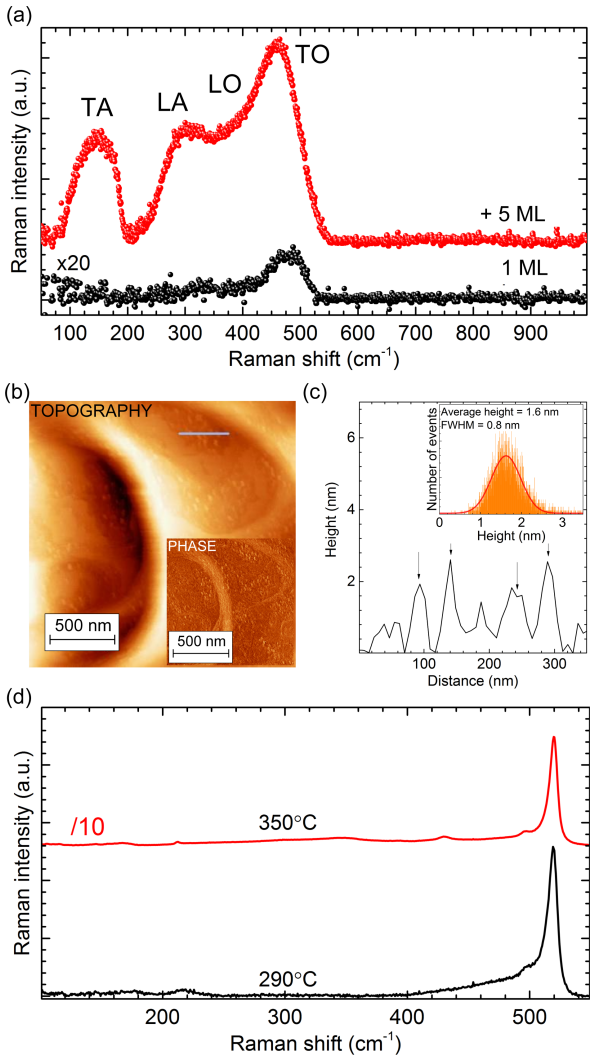

Figure 3: (a) Raman spectra recorded on samples after Si deposition at room temperature with coverages of 1 ML and 5 MLs. (b) Ex situ AFM topography measurement of the Ag(111) surface after the 1 ML deposition at room temperature. Inset: phase image. (c) Height profile, along the line in (b). Inset: height distribution of the features in the AFM topography image. (d) Raman spectra of samples with nominal 1 ML amount of Si deposited at 290 °C and 350 °C.

These assumptions are not supported by our results, which demonstrate that room-temperature deposition only leads to the formation of amorphous Si clusters.

Si deposition at temperatures above 300 °C

If Si is deposited onto Ag(111) at substrate temperatures exceeding 300 °C, only the characteristic (1×1) pattern of the initial Ag 1×1 surface is found without any distinctive additional diffraction spots.

Figure 3d shows the Raman spectra after deposition of 1 ML of Si at 290 and 350°C, both dominated by an intense band at 520 cm^{-1} with a FWHM of 8 cm^{-1}. This mode is similar to the

L(T)O phonon mode of diamond-like silicon, clearly indicating the formation of Si crystallites. Additionally, the second-order TO phonon mode around 900 cm^{-1} (Figure 2, top spectrum) supports the bulk-like nature of the structures formed. The fact that the intensity of the L(T)O phonon mode gets higher for deposition at 350 °C demonstrates that the sizes of the crystallites enlarge with increasing deposition temperatures. However, this temperature is still low compared to the growth temperature of crystalline Si, which usually exceeds 1000 °C [30]. Such a low crystallization temperature is surprising, but it can be explained by metal mediation. For a layered Si–Ag system a temperature as low as 400 °C was reported [31].

These results are in agreement with Auger electron spectroscopy measurements [16] and low-energy electron microscopy observations [17] as well as Raman results after post-annealing of the (3×3)/(4×4) epitaxial silicene phase [23], which demonstrated a dewetting process of the Si layer from the Ag(111) surface around 300 °C. Hence, a temperature of 300 °C marks the high temperature limit for 2D Si layer formation on Ag(111), where a 2D-to-3D phase transition takes place. Reports of an almost perfectly ordered 2D Si layer formed on Ag(111) at almost 400 °C may be related to problems with temperature determination [15].

Si deposition at temperatures between 220 and 290 °C

All the results presented so far show that the formation of 2D Si layers on Ag(111) is limited to a temperature range between 220 and 290 °C. We show fitted Raman spectra of 2D Si layers prepared at three different deposition temperatures within this temperature range in Figure 4.

At 220 °C the spectrum of a dominant (3×3)/(4×4) silicene layer shows all the modes of epitaxial silicene as well as a small contribution from a-Si (orange feature). The Raman spectra after Si deposition at 250 °C referred to as "mixed phase" are composed of six modes. At a deposition temperature of 280 °C a single "$(2\sqrt{3}\times 2\sqrt{3})$" structure is observed. We first focus on the "mixed phase".

The spectrum of the sample prepared at 250 °C exhibits the same Raman bands as those of epitaxial silicene (Figure 4, bottom) plus two additional Raman modes at 155 and 520 cm^{-1}. The latter is consistent with the position of the L(T)O phonon mode of Si crystallites clearly visualized in AFM at higher deposition temperature (300 °C). This indicates that the formation of diamond-type Si starts to take place below 300 °C. It is noteworthy that the shoulder at the lower-energy side of the L(T)O mode is assigned to the crystallites and not to amorphous Si because of its consistency with the defect-TO band of

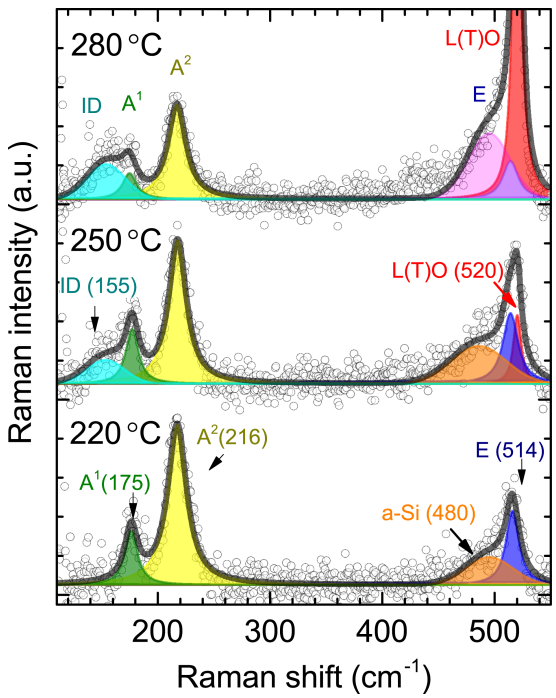

Figure 4: Fitted Raman spectra of silicene-related structures: dominant (3*times*3)/(4×4) (epitaxial silicene) (220 °C), "mixed phase" (250 °C), and "$(2\sqrt{3}\times 2\sqrt{3})$" structure (280 °C). The experimental data are shown as circles, while the smooth curves overlaid are the envelopes of all features observed and fitted. The spectral features are fitted with Voigt functions, where the Gaussian contribution of the peaks stems from the instrumental resolution (2.4 cm^{-1}) unless stated otherwise.

bulk silicon at 495 cm^{-1}. Moreover, it remains in the Raman spectrum after oxidation of the corresponding sample (Figure 5b).

The Raman band at 155 cm^{-1}, however, can be attributed to the formation of the "$(2\sqrt{3}\times 2\sqrt{3})$" structure, which is co-formed with epitaxial silicene in the "mixed phase". Indeed, this Raman mode is also observed in the Raman spectrum of the sample that shows a LEED pattern assigned only to the "$(2\sqrt{3}\times 2\sqrt{3})$" structure (Figure 5a). In this case, the respective intensity of this mode is higher than those of the modes of epitaxial silicene. Our results of the fitting suggest that the "mixed phase" can be understood as the lateral co-existence of two different 2D structures. At the same time, it contains patches of the $(\sqrt{13}\times\sqrt{13})R13.9°$ structure, which, however, cannot be distinguished from (3×3)/(4×4) silicene spectroscopically. Such spectral blending clearly suggests their structural similarity, which was also argued based on the STM results [10].

Raman spectroscopy of the "(2√3×2√3)" structure

To elucidate the origin of the spectral signatures of the "$(2\sqrt{3}\times 2\sqrt{3})$" structure, the sample was oxidized. After ox-

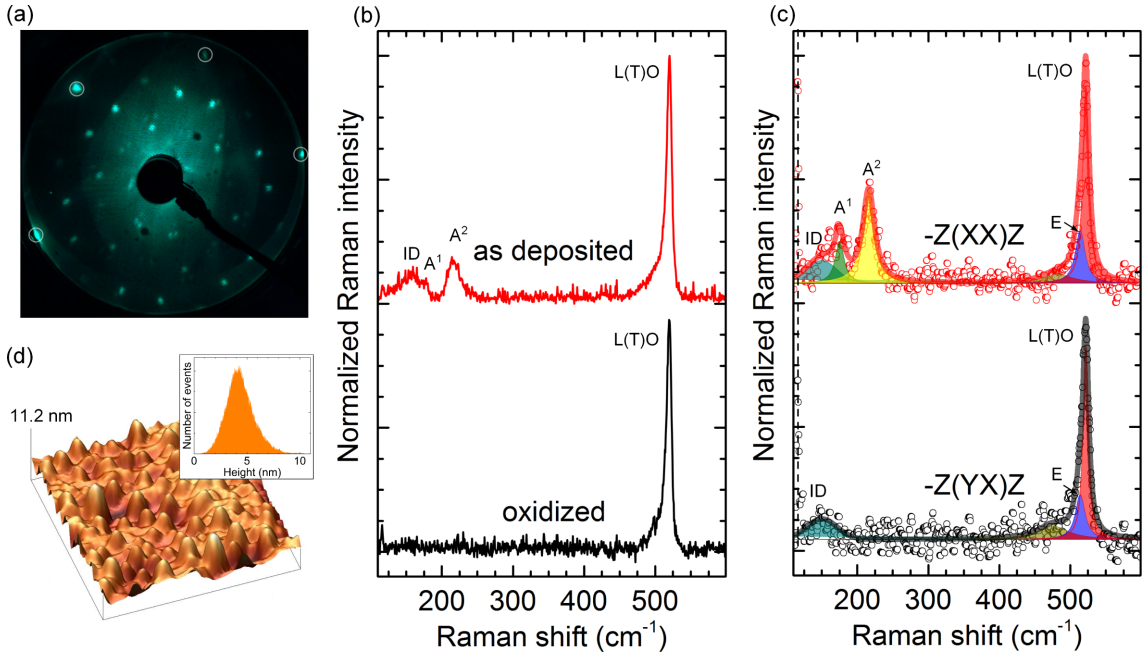

Figure 5: (a) LEED pattern of the sample prepared at 280 °C. The integer-order diffraction spots of Ag(111) are marked with circles. (b) Raman spectra of the sample with the "$(2\sqrt{3}\times2\sqrt{3})$" structure after deposition (corresponding to panel a) and after ex situ oxidation. (c) Polarization-dependent Raman spectra of the 280 °C sample, recorded in parallel ($-z(xx)z$) and crossed ($-z(yx)z$) geometries. (d) Ex situ AFM image (1 µm × 1 µm) of the Ag(111) surface, measured after the oxidation. Inset: height distribution of the small features observed in the AFM topograph.

idation no LEED diffraction spots, except for the integer Ag(111) spots can be seen (Figure 5a) and the Raman modes related to the epitaxial silicene vanish (Figure 5b). In Figure 5b the Raman spectra of the "$(2\sqrt{3}\times2\sqrt{3})$" structure before and after oxidation are shown. In the latter case the remaining Raman bands are the one at 520 cm^{-1} as well as its low-energy shoulder around 495 cm^{-1}. This clearly resolves the assignment of this shoulder to Si crystallites. Ex situ AFM measurements of the same sample show protrusions with an average height of 4.4 ± 0.1 nm and a lateral size of up to 100 ± 10 nm (Figure 5d).

In combination with the Raman results after the oxidation of the "$(2\sqrt{3}\times2\sqrt{3})$" structure, it can be stated that these protrusions are diamond-like Si crystallites. Their broad size distribution explains the linewidth of the Raman band at 520 cm^{-1}: The biggest crystallites (>7 nm) exhibit the intense L(T)O phonon mode, while the small ones (<7 nm) are responsible for the large linewidth and the low-energy shoulder. The formation of such crystallites is clearly temperature-dependent. Solely 3D growth is observed when the temperature reaches 300 °C, i.e., the limit of the 2D Si-layer growth mode on Ag(111). The Raman and AFM results confirm the co-existence of Si crystallites and of the "$(2\sqrt{3}\times2\sqrt{3})$" structure at temperatures between 250 and 300 °C.

To substantiate the understanding of the "$(2\sqrt{3}\times2\sqrt{3})$" structure polarization dependent Raman measurements were performed. Figure 5c shows Raman spectra of a sample with the "$(2\sqrt{3}\times2\sqrt{3})$" structure in both parallel (Porto notation: $-z(xx)z$ and crossed $-z(yx)z$ geometries. According to the selection rules of the six-fold symmetry, the depolarized (degenerate) modes are measured in both parallel and crossed geometries, while the polarized vibrational modes can solely be detected in the parallel configuration. One notices that only A modes at 175 and 216 cm^{-1} are missing in the crossed geometry, while the Raman modes at 155, 514 (E mode), and 520 cm^{-1} remain. The polarization dependence of A and E modes fully reproduces our previous results [23]. The behaviour of the triple-degenerate Raman band at 520 cm^{-1} is also identical. The presence of symmetric modes in the Raman spectrum of the "$(2\sqrt{3}\times2\sqrt{3})$" structure at the same positions as the ones of epitaxial (3×3) silicene suggests structural similarities for these two cases. Indeed, the bright hexagons (Figure 1d) are nicely ordered and, therefore, can provide the same spectral response. We can surmise the appearance of the E mode in the asymmetric shoulder of the L(T)O phonon mode of Si nanocrystallites, yet the analysis is complicated.

The Raman band at 155 cm^{-1} is present in both geometries, which hints at its disorder-related origin, since only the vibra-

tions of ordered crystalline structures follow Raman selection rules. Its broad linewidth of 30 cm^{-1} further corroborates this assignment. Finally, its position could be related to the softening of the A^1 mode, in connection with the intrinsic disorder (ID) of the "$(2\sqrt{3}\times 2\sqrt{3})$" structure. Since this Raman mode is the one that distinguishes this structure from epitaxial silicene, it can be used as a marker. Due to its evident relation to the intrinsic disorder of the "$(2\sqrt{3}\times 2\sqrt{3})$" superstructure, we refer to it as the "ID" mode. It is noteworthy that the intrinsically complex atomic arrangement of the "$(2\sqrt{3}\times 2\sqrt{3})$" structure shows the spectral features both of ordered and disordered nature. This has to be explicitly considered in the modeling of this structure and of its properties in DFT calculations. Proposed structural models that are entirely based on the ordered parts of this structure are genuinely bound to fail in the correct description of the "$(2\sqrt{3}\times 2\sqrt{3})$" structure.

Discussion

Based on the in situ Raman results in combination with STM and LEED described above, a generic phase diagram for the formation of Si structures on the Ag(111) surface can be obtained (Figure 6). At low temperatures, i.e., from room temperature to ca. 150 °C only amorphous Si is formed. In the temperature range between 200 and 300 °C 2D and 3D Si phases are formed, while at high temperatures above 300 °C only 3D Si crystallites develop.

In the narrow temperature window between 220 and 280 °C the metastable 2D Si phases are observed. Starting at 220 °C a dominant (3×3)/(4×4) silicene phase is formed; it is characterized by two vibrational A modes at 175 and 216 cm^{-1} and an E mode at 514 cm^{-1}. At higher temperatures an increasing mixture of $(\sqrt{13}\times\sqrt{13})R13.9°$ domains and around 250 °C also of a "$(2\sqrt{3}\times 2\sqrt{3})$" structure are formed. All these structures show similar vibrational modes in the Raman spectra. Only the "$(2\sqrt{3}\times 2\sqrt{3})$" structure shows the additional characteristic ID mode at 155 cm^{-1}, which stems from its inherent disorder. For preparation temperatures around 250 °C the beginning of the co-development of diamond-like Si crystallites is observed. They further grow with increasing deposition temperatures. This scenario is in agreement with LEED observations, which show that these different structures are simultaneously observed in this temperature range. For higher preparation temperatures, the contribution of the "$(2\sqrt{3}\times 2\sqrt{3})R30°$" structure increases. It is mainly described by an appearance of the ID mode at 155 cm^{-1}. Accordingly, the features at 175 and 216 cm^{-1}, which are dominating in the spectrum of (3×3)/(4×4) silicene, decline gradually. This means that the evolution of the Raman spectra for any multiple-phase sample can be simply explained by the weighted superposition of the Raman spectra of (3×3)/(4×4) silicene and of "$(2\sqrt{3}\times 2\sqrt{3})R30°$" structures.

The incidence of a Raman band around 520 cm^{-1} is a direct evidence of bulk Si crystallites present on the Ag(111) surface, but not of a 2D layer, in particular not the "$(2\sqrt{3}\times 2\sqrt{3})$" structure, as reported earlier [24,32]. However, due to their possible co-existence, the occurrence of diamond-like Si crystallites does not exclude the presence of 2D Si layers on Ag(111).

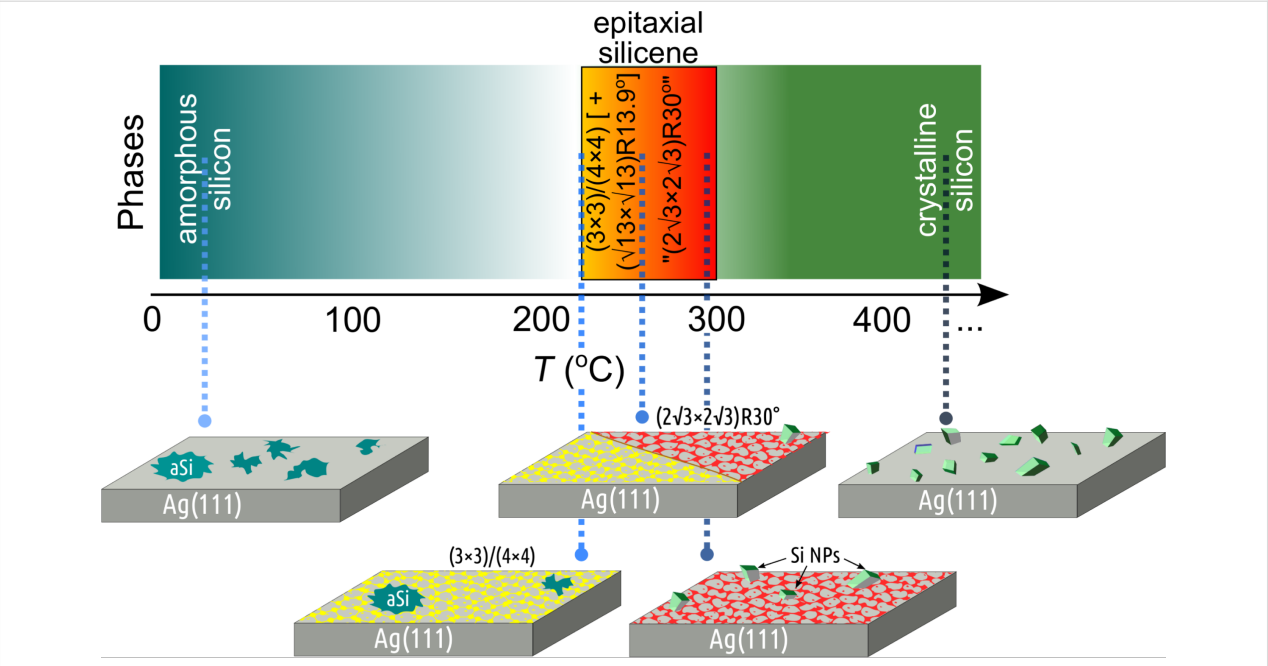

Figure 6: Reduced phase diagram of Si structures that can be grown on the Ag(111) surface at various deposition temperatures.

Conclusion

We performed a comprehensive spectroscopic study of the silicene-related superstructures epitaxially grown on the Ag(111) surface by in situ Raman spectroscopy. The structural differences between the silicene-related phases, consistent with the scanning tunnelling microscopy observations, are manifested in the sets of Raman bands, i.e., in different spectral signatures. Our results confirm a close link between epitaxial (3×3)/(4×4) silicene and the silicene-related "$(2\sqrt{3}\times 2\sqrt{3})R30°$" structure since both share similar spectral fingerprints. The ordered parts of the "$(2\sqrt{3}\times 2\sqrt{3})R30°$" structure exhibit a spectrum similar to that of the epitaxial (3×3/(4×4) silicene, while the disordered parts yield a broad Raman band (ID) at 155 cm^{-1}. We have established that Si deposition onto the Ag(111) surface in the range from 220 to 290 °C usually results in the co-formation of 2D and 3D structures, whereas only structures with sp^3-hybridized Si atoms are obtained outside this temperature range. Raman spectroscopy results were consistently confirmed by AFM and STM observations. According to these findings we could build up a generic phase diagram that reflects the complicated interplay of the formation of both 2D and 3D moieties.

Experimental

Clean Ag(111) surfaces were prepared by alternating cycles of sputtering (Ar^+, 1.5 keV, $1\cdot10^{-5}$ mbar) and annealing (520 °C) until sharp 1×1 spots of the unreconstructed surface were observed by LEED. Si was evaporated subsequently from a directly heated silicon wafer piece placed at a distance of 10 cm from the Ag substrate. The Si deposition, at which a complete Si monolayer is formed, i.e., no formation of a second layer occurs, refers to "1 ML deposition". The temperature of the Ag substrate was varied from room temperature up to 500 °C. In situ Raman measurements were performed in macro configuration, using a Dilor XY800 triple monochromator, equipped with a CCD camera as a detector. All spectra were recorded at room temperature and under ultrahigh-vacuum conditions at a base pressure of $2\cdot10^{-10}$ mbar. For the excitation the 514.5 nm line of an Ar^+ laser, with a power density below 10^3 W/cm^2, was used. LEED patterns were acquired in the energy range below 50 eV using a SPECTALEED, Omicron NanoScience optics.

Acknowledgements

This work was financially supported by the Deutsche Forschungsgemeinschaft (DFG) under Grant No. VO1261/4-1.

References

1. Takeda, K.; Shiraishi, K. *Phys. Rev. B* **1994,** *50,* 14916. doi:10.1103/PhysRevB.50.14916
2. Guzmán-Verri, G. G.; Lew Yan Voon, L. C. *Phys. Rev. B* **2007,** *76,* 075131. doi:10.1103/PhysRevB.76.075131
3. Cahangirov, S.; Topsakal, M.; Aktürk, E.; Şahin, H.; Ciraci, C. *Phys. Rev. Lett.* **2009,** *102,* 236804. doi:10.1103/PhysRevLett.102.236804
4. Vogt, P.; De Padova, P.; Quaresima, C.; Avila, J.; Frantzeskakis, E.; Asensio, M. C.; Resta, A.; Ealet, B.; Le Lay, G. *Phys. Rev. Lett.* **2012,** *108,* 155501. doi:10.1103/PhysRevLett.108.155501
5. Lin, C.-L.; Arafune, R.; Kawahara, K.; Tsukahara, N.; Minamitani, E.; Kim, Y.; Takagi, N.; Kawai, M. *Appl. Phys. Express* **2012,** *5,* 045802. doi:10.1143/APEX.5.045802
6. Feng, B.; Ding, Z.; Meng, S.; Yao, Y.; He, X.; Cheng, P.; Chen, L.; Wu, K. *Nano Lett.* **2012,** *12,* 3507–3511. doi:10.1021/nl301047g
7. Moras, P.; Mentes, T. O.; Sheverdyaeva, P. M.; Locatelli, A.; Carbone, C. *J. Phys.: Condens. Matter* **2014,** *26,* 185001. doi:10.1088/0953-8984/26/18/185001
8. Liu, Z.-L.; Wang, M.-X.; Xu, J.-P.; Ge, J.-F.; Le Lay, G.; Vogt, P.; Qian, D.; Gao, C.-L.; Liu, C.; Jia, J.-F. *New J. Phys.* **2014,** *16,* 075006. doi:10.1088/1367-2630/16/7/075006
9. Jamgotchian, H.; Colignon, Y.; Ealet, B.; Parditka, B.; Hoarau, J.-Y.; Girardeaux, C.; Aufray, B.; Bibérian, J.-P. *J. Phys.: Conf. Ser.* **2014,** *491,* 012001. doi:10.1088/1742-6596/491/1/012001
10. Liu, H.; Feng, H.; Du, Y.; Chen, J.; Wu, K.; Zhao, J. *2D Mater.* **2016,** *3,* 025034. doi:10.1088/2053-1583/3/2/025034
11. Curcella, A.; Bernard, R.; Borensztein, Y.; Resta, A.; Lazzeri, M.; Prévot, G. *Phys. Rev. B* **2016,** *94,* 165438. doi:10.1103/PhysRevB.94.165438
12. Pflugradt, P.; Matthes, L.; Bechstedt, F. *Phys. Rev. B* **2014,** *89,* 035403. doi:10.1103/PhysRevB.89.035403
13. Johnson, N. W.; Vogt, P.; Resta, A.; De Padova, P.; Perez, I.; Muir, D.; Kurmaev, E. Z.; Le Lay, G.; Moewes, A. *Adv. Funct. Mater.* **2014,** *24,* 5253–5259. doi:10.1002/adfm.201400769
14. Resta, A.; Leoni, T.; Barth, C.; Ranguis, A.; Becker, C.; Bruhn, T.; Vogt, P.; Le Lay, G. *Sci. Rep.* **2013,** *3,* 2399. doi:10.1038/srep02399
15. Jamgotchian, H.; Ealet, B.; Colignon, Y.; Maradj, H.; Hoarau, J.-Y.; Biberian, J.-P.; Aufray, B. *J. Phys.: Condens. Matter* **2015,** *27,* 395002. doi:10.1088/0953-8984/27/39/395002
16. Liu, Z.-L.; Wang, M.-X.; Liu, C.; Jia, J.-F.; Vogt, P.; Quaresima, C.; Ottaviani, C.; Olivieri, B.; De Padova, P.; Le Lay, G. *Materials* **2014,** *2,* 092513. doi:10.1063/1.4894871
17. Acun, A.; Poelsema, B.; Zandvliet, H. J. W.; van Gastel, R. *Appl. Phys. Lett.* **2013,** *103,* 263119. doi:10.1063/1.4860964
18. Wang, W.; Olovsson, W.; Uhrberg, R. I. G. *Phys. Rev. B* **2015,** *92,* 205427. doi:10.1103/PhysRevB.92.205427
19. Prévot, G.; Bernard, R.; Cruguel, H.; Borensztein, Y. *Appl. Phys. Lett.* **2014,** *105,* 213106. doi:10.1063/1.4902811
20. Bernard, R.; Borensztein, Y.; Cruguel, H.; Lazzeri, M.; Prévot, G. *Phys. Rev. B* **2015,** *92,* 045415. doi:10.1103/PhysRevB.92.045415
21. Wagner, V.; Drews, D.; Esser, N.; Zahn, D. R. T.; Geurts, J.; Richter, W. *J. Appl. Phys.* **1994,** *75,* 7330–7333. doi:10.1063/1.356644
22. Esser, N.; Geurts, J. Raman Spectroscopy. In *Optical Characterization of Epitaxial Semiconductor Layers;* Bauer, P. D. G.; Richter, P. D. W., Eds.; Springer: Berlin, Germany, 1996; pp 129–202.
23. Solonenko, D.; Gordan, O. D.; Le Lay, G.; Sahin, H.; Cahangirov, S.; Zahn, D. R. T.; Vogt, P. *2D Mater.* **2017,** *4,* 015008. doi:10.1088/2053-1583/4/1/015008
24. Cinquanta, E.; Scalise, E.; Chiappe, D.; Grazianetti, C.; van den Broek, B.; Houssa, M.; Fanciulli, M.; Molle, A. *J. Phys. Chem. C* **2013,** *117,* 16719–16724. doi:10.1021/jp405642g
25. Zhuang, J.; Xu, X.; Du, Y.; Wu, K.; Chen, L.; Hao, W.; Wang, J.; Yeoh, W. K.; Wang, X.; Dou, S. X. *Phys. Rev. B* **2015,** *91,* 161409. doi:10.1103/PhysRevB.91.161409

26. Díaz Álvarez, A.; Zhu, T.; Nys, J. P.; Berthe, M.; Empis, M.; Schreiber, J.; Grandidier, B.; Xu, T. *Surf. Sci.* **2016,** *653,* 92–96. doi:10.1016/j.susc.2016.06.005
27. Wu, X. L.; Siu, G. G.; Tong, S.; Liu, X. N.; Yan, F.; Jiang, S. S.; Zhang, X. K.; Feng, D. *Appl. Phys. Lett.* **1996,** *69,* 523–525. doi:10.1063/1.117774
28. Iqbal, Z.; Veprek, S. *J. Phys. C: Solid State Phys.* **1982,** *15,* 377. doi:10.1088/0022-3719/15/2/019
29. Satta, M.; Colonna, S.; Flammini, R.; Cricenti, A.; Ronci, F. *Phys. Rev. Lett.* **2015,** *115,* 026102. doi:10.1103/PhysRevLett.115.026102
30. Allison, J. F.; Dumin, D. J.; Heiman, F. P.; Mueller, C. W.; Robinson, P. H. *Proc. IEEE* **1969,** *57,* 1490–1498. doi:10.1109/PROC.1969.7324
31. Konno, T. J.; Sinclair, R. *Philos. Mag. B* **1995,** *71,* 163–178. doi:10.1080/01418639508240304
32. Tao, L.; Cinquanta, E.; Chiappe, D.; Grazianetti, C.; Fanciulli, M.; Dubey, M.; Molle, A.; Akinwande, D. *Nat. Nanotechnol.* **2015,** *10,* 227–231. doi:10.1038/nnano.2014.325

License and Terms

BEILSTEIN JOURNAL OF NANOTECHNOLOGY

Group-13 and group-15 doping of germanane

Nicholas D. Cultrara, Maxx Q. Arguilla, Shishi Jiang, Chuanchuan Sun, Michael R. Scudder, R. Dominic Ross and Joshua E. Goldberger*

Full Research Paper

Open Access

Address:
Department of Chemistry and Biochemistry, Ohio State University, Columbus, Ohio, 43210-1340, United States of America

Email:
Joshua E. Goldberger* - goldberger@chemistry.ohio-state.edu

* Corresponding author

Keywords:
doping; electronic behavior; germanane; two-dimensional materials

Beilstein J. Nanotechnol. **2017,** *8,* 1642–1648.
doi:10.3762/bjnano.8.164

Received: 31 March 2017
Accepted: 19 July 2017
Published: 09 August 2017

This article is part of the Thematic Series "Silicene, germanene and other group IV 2D materials".

Guest Editor: P. Vogt

Abstract

Germanane, a hydrogen-terminated graphane analogue of germanium has generated interest as a potential 2D electronic material. However, the incorporation and retention of extrinsic dopant atoms in the lattice, to tune the electronic properties, remains a significant challenge. Here, we show that the group-13 element Ga and the group-15 element As, can be successfully doped into a precursor $CaGe_2$ phase, and remain intact in the lattice after the topotactic deintercalation, using HCl, to form GeH. After deintercalation, a maximum of 1.1% As and 2.3% Ga can be substituted into the germanium lattice. Electronic transport properties of single flakes show that incorporation of dopants leads to a reduction of resistance of more than three orders of magnitude in H_2O-containing atmosphere after As doping. After doping with Ga, the reduction is more than six orders of magnitude, but with significant hysteretic behavior, indicative of water-activation of dopants on the surface. Only Ga-doped germanane remains activated under vacuum, and also exhibits minimal hysteretic behavior while the sheet resistance is reduced by more than four orders of magnitude. These Ga- and As-doped germanane materials start to oxidize after one to four days in ambient atmosphere. Overall, this work demonstrates that extrinsic doping with Ga is a viable pathway towards accessing stable electronic behavior in graphane analogues of germanium.

Introduction

Since the discovery of graphene [1], the quest to discover and measure novel two dimensional and layered materials has led to the investigation of group-14 and group-15 allotropes of graphene and graphane [1-14], transition-metal dichalcogenides [15-19], and layered van der Waals materials [20-22]. Germanane, a hydrogen-terminated graphane analogue of germanium, has garnered considerable attention in the field of 2D materials on account of its direct band gap [5,23,24], large predicted electron mobility, and the ability to controllably tune the optoelectronic properties via covalent modification with surface ligands [3,24-28]. While the electron mobility of germanane at room temperature has been predicted to be greater

than 18,000 $cm^2 \cdot V^{-1} \cdot s^{-1}$, transport measurements on non-extrinsically doped crystals were highly resistive, indicating the need of extrinsic dopants to access devices with lower resistivity. In previous studies, the resistivity of germanane was reduced through the incorporation of phosphorus only when activated in the presence of atmospheric water [29]. Recently [30], undoped germanane field-effect transistors were reported with device hole mobilites ranging from 70 to 150 $cm^2 \cdot V^{-1} \cdot s^{-1}$ from room temperature to low temperature, indicating that germanane has the potential to be a viable electronic building block for 2D transistors. Together, this emphasizes the need for further control of doping behavior in these materials.

The preparation of GeH requires the synthesis of a $CaGe_2$ precursor phase followed by its topotactic deintercalation in HCl. GeH is a metastable phase, and begins to amorphize when annealed above 75 °C. Consequently, traditional doping processes such as the direct ion-implantation of GeH cannot be used as they require a high-temperature for post annealing to heal the lattice. Due to the existence of a large number of closely related layered Zintl phases with group-13 and group-15 elements that are structurally similar to $CaGe_2$ dopant elements can be partially substituted into the germanium lattice of the $CaGe_2$ precursor [29,31]. Providing that these elements are retained in the germanium framework after the topotactic deintercalation process, the effect on the electronic transport behavior of GeH should be appreciable. Having previously grown phosphorus-doped GeH (P:GeH) [29] using this method, here, we explored whether other group-13 and group-15 elements (Al, Ga, As and Sb) can be included as dopants onto the germanane framework, and how these dopants affect the stability and electronic properties of GeH.

Herein, we show that Ga and As can be doped into the $CaGe_2$ precursor phase and are retained on the germanane lattice after topotactic deintercalation. Using X-ray fluorescence (XRF) and X-ray photoelectron spectroscopy (XPS) we show that up to 1.1% and 2.3% of As and Ga, respectively, can be substituted onto the germanane lattice. In contrast to pristine GeH, these materials begin to oxidize after 24 to 96 hours in ambient atmosphere. In both cases, the incorporation of more dopant produced lower sheet resistances in H_2O-containing ambient atmosphere, while only the gallium-doped samples continue to show dopant activation under vacuum and H_2O-free conditions.

Results and Discussion

First, we explored whether crystals of $CaGe_2$ doped with Al, Ga, As, and Sb at 0.1% could be synthesized (Figure 1a). Of these dopants only Al, Ga, and As were successfully incorporated into the $CaGe_2$ framework. After topotactic deintercalation in HCl, GeH platelets doped with Ga and As were successfully obtained (Figure 1b), while the Al-doped $CaGe_2$ crystals disintegrated into small micrometer-sized particles not suitable for bulk transport measurements. Subsequently, we tried to synthesize Ga- and As-doped $CaGe_2$ with 0.1–9% atomic substitutions. However, $CaGe_2$ crystals only formed with less than 3% of added dopant. Figure 1c shows the powder X-ray diffraction (XRD) pattern of undoped GeH reported by Bianco et al. [25], and those of the highest doped Ga:GeH and As:GeH samples. All the deintercalated phases can be indexed [32] to a 6-layer rhombohedral unit cell with lattice parameters a = 3.97 Å and c = 33.22 Å. Neither a significant difference between the phases nor other peaks indicative of impurity phases are observed. The peaks labeled with asterisks show residual germanium in the sample. The Raman spectra (Figure 1d) of these doped crystals all exhibit A_1 (out-of-plane) and E_2 (in-plane) modes at 228 cm^{-1} and 302 cm^{-1}, respectively, with no change in peak location, shape or A_1/E_2 intensity ratio compared to undoped

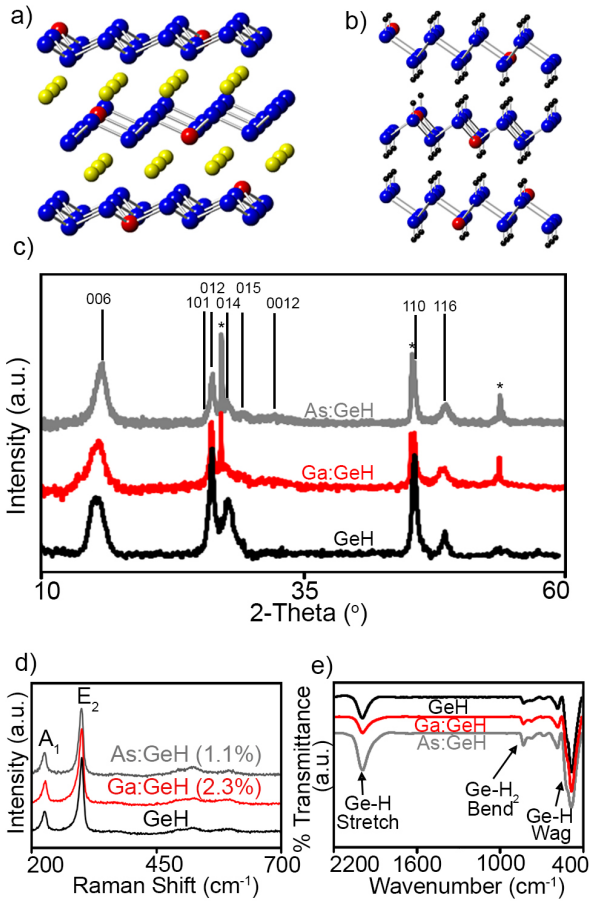

Figure 1: Schematic diagram of doped a) $CaGe_2$ and b) GeH after detintercalation. Red represents the dopant atom, blue is germanium, yellow is calcium and black is hydrogen. The number of dopants depicted here is purposefully inflated for visual effect. c) Powder XRD, d) Raman spectra, and e) FTIR spectra of GeH (black), 2.3% Ga:GeH (red), and 1.1% As:GeH (gray). The starred peaks in the XRD show residual germanium.

GeH. Fourier transform infrared spectra of these samples (FTIR) also further show clear spectroscopic signatures for the formation of GeH. An extremely strong Ge–H stretching mode is observed at about 2000 cm^{-1} as well as characteristic wagging modes at 570, 507 and 475 cm^{-1}, and the edge/defect Ge–H_2 defect modes at 770 and 820 cm^{-1}. No additional features indicative of As–H or Ga–H were observed, because the small concentration of Ga and As makes it impossible to completely determine the actual chemical environment of these dopants using a bulk technique such as IR spectroscopy.

The retention and concentration of Ga and As dopants in the lattice was determined for each system using XRF (Figure 2). A calibration curve using the ratio of Ga/As Kα to Ge Kα was prepared with standards of elemental Ge and As or of Ga_2O_3. The XRF measurements showed that the highest concentration of Ga in Ga:GeH to be 2.3%, and the highest concentration of As in As:GeH was 1.1%. XRF analysis of GeH synthesized with greater than 1% As substitution, always yielded a ratio As/Ge of ca. 1.1% in GeH indicating that this is the maximum amount of As that can be substituted in $CaGe_2$. The lack of any other distinguishing phase in the XRD suggests that Ga and As are part of the germanane lattice.

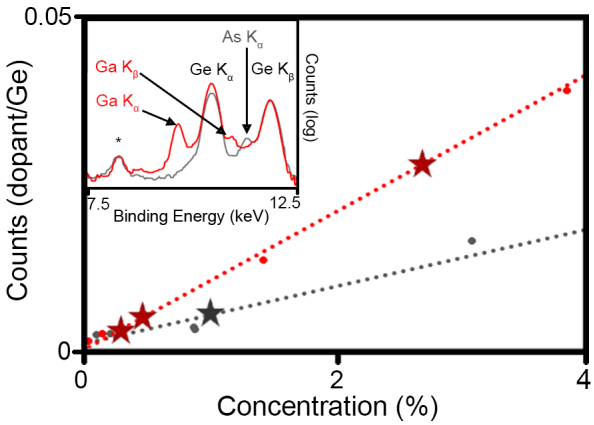

Figure 2: XRF calibration curve of Ga:GeH (red) and As:GeH (gray). The stars represent measured concentrations in the samples. Inset shows XRF spectra of the Ga:GeH (red) and As:GeH (gray) samples with the highest doping content. The asterisk denotes a silicon escape peak from the major Ge K_α peak.

Scanning electron microscopy (SEM) with energy-dispersive X-ray spectroscopy (EDX) provided further verification of the incorporation of dopant atoms into GeH. As a representative example, the EDX spectrum of a single 2.3% Ga:GeH platelet shows the presence of both Ge K and Ga K peaks (Figure 3a). Figure 3b–d shows an SEM image, and the maps of Ga K_α signal and Ge K_α signal, of a corner of a Ga:GeH platelet. These EDX maps show that there is a uniform distribution of gallium and germanium throughout the germanane crystal. This confirms the retention of the Ga dopant into the germanane lattice.

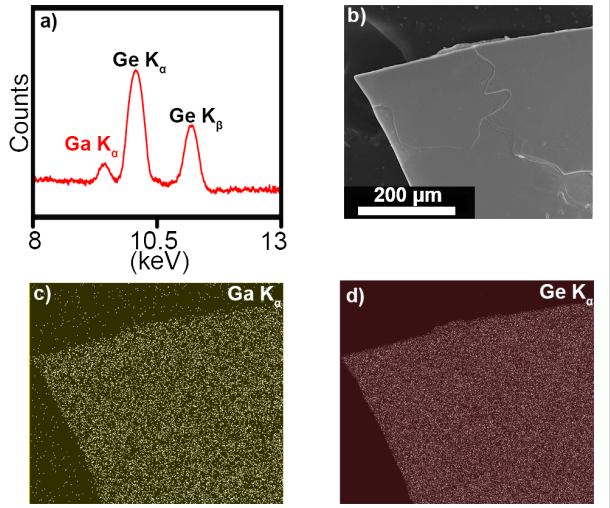

Figure 3: a) EDX spectrum of the 2.3% Ga:GeH platelet shown in the SEM image in panel b). EDX maps of c) gallium (yellow) and d) germanium (red) show retention of the dopants in the germanane crystal as well as their uniform distribution.

X-ray photoelecton spectroscopy (XPS) measurements confirmed dopant retention in the lattice and elucidated the local chemical environment of the dopant (Figure 4). The Ge $2p_{3/2}$ peak for the 2.3% Ga:GeH and 1.1% As:GeH occur at 1217.7 and 1217.6 eV (Figure 4a), respectively, which is relatively close to the value of undoped GeH at 1217.8 eV [25]. These Ge $2p_{3/2}$ energies are indicative of a Ge^{1+} oxidation state. For comparison, a Ge(111) wafer having surface oxide contains Ge $2p_{3/2}$ peaks at 1216.3 for Ge^0, and peaks of oxidized Ge^{2+} to Ge^{4+}, which range from 1218.2 to 1220.6 eV. Figure 4b shows the Ga $3d_{5/2}$ and Ge $3d_{5/2}$ XPS spectra for the 2.3% Ga:GeH crystals after exposure to ambient conditions for 0–8 days. Immediately after synthesis (zero days of air exposure) the Ga and Ge $3d_{5/2}$ peaks can be fit to single peaks at 19.9 eV and 30.3 eV, respectively. These binding energies occur in the range expected for Ga^{3+} [33] and Ge^{1+} [25] oxidation states. Minimal changes are observed after one day of exposure to air. However, after four days of ambient air exposure, the XPS spectra shows the emergence of Ge $3d_{5/2}$ peaks at higher energies, which are indicative of surface oxidation. Fitting the higher-energy spectra shows that 83% of Ge^{1+} at the surface is not oxidized. The binding energies of the Ga $3d_{5/2}$ peak and of the Ga $2p_{3/2}$ peak that occurs at 1117.5 eV [34] do not change after exposure to ambient atmosphere. As a dopant in GeH, Ga is bonded to three more electronegative Ge atoms, and locally exists in an electron-deficient state. Consequently, minimal changes in the Ga

XPS spectra would be expected if Ga:GeH were to become oxidized to form Ga_2O_3.

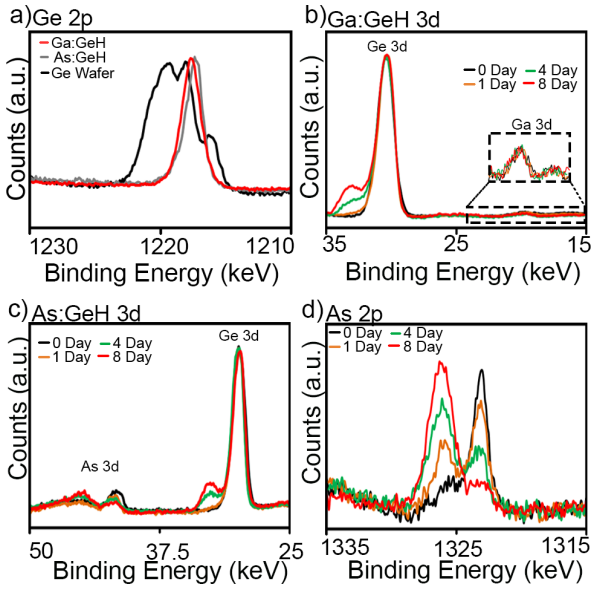

Figure 4: a) Ge $2p_{3/2}$ Ge wafer (black) with surface oxide and 2.3% Ga:GeH (red) and 1.1% As:GeH (gray) exposed for 0 days. b) Time-dependent XPS of 2.3% Ga:GeH and c,d) 1.1% As:GeH at 0 day (black), 1 day (yellow), 4 days (green), and 8 day (red).

Figure 4c shows the XPS spectra for As:GeH after exposure to air for 1–8 days. Again, immediately after synthesis (0 days of air exposure) the As and Ge $3d_{5/2}$ peaks can be fit to single peaks at 41.8 eV and 30.0 eV, respectively. Also, in As:GeH there are only minimal changes of the observed Ge $2p_{3/2}$ peak after one day of exposure to air. However, surface oxidation is prevalent after four days, evident from the emergence of a peak with higher binding energy, indicative of an oxidized Ge $3d_{5/2}$ environment. Fitting the intensity of the peaks shows 84% of Ge remains as Ge^{1+}. The similarity of the change in Ge binding energy for both As:GeH and Ga:GeH implies that the rates of oxidation of Ge in both samples are similar. In contrast to Ga:GeH, the changes in the As $2p_{3/2}$ binding energy (Figure 4d) indicates that significant oxidation of As occurs. The As $2p_{3/2}$ peak centered at 1323 eV in as-grown As:GeH starts disappearing in favor of a 1326.1 eV [35] oxidized state.

The effect of dopants on the electronic transport of single-crystal flakes of Ga:GeH and As:GeH were measured with contacts fabricated by using a shadow mask technique (Figure 5b). Two-probe *I–V* measurements were carried out on single crystals with device geometries that typically featured a channel length of 25 µm, a width of 2–4 mm and a thickness of 5–20 µm (Figure 5b). After exploring numerous metals, nearly ohmic contacts (under vacuum) to Ga:GeH were observed using 100 nm Au as a contact metal. Furthermore, the highest ambient and vacuum conductivities in As:GeH were achieved when contacting with Ag (80 nm)/Au (20 nm). The fact that Au with its higher work function is needed to make ohmic contacts for Ga:GeH, compared to Ag for As:GeH, suggests that Ga and As are likely to act as p-type and n-type dopants, respectively. *I–V* measurements were carried out with a direct probe contact to each metal pad, and measured in a range of −5 to 5 V. 20–30 devices were fabricated for each doping concentration. Each measurement was normalized to a sheet resistance. Undoped GeH exhibited sheet resistances approaching the noise limit of the instrumentation of the order of ca. 10^{15} Ω/sq in both vacuum and under ambient conditions, similar to previous studies [29].

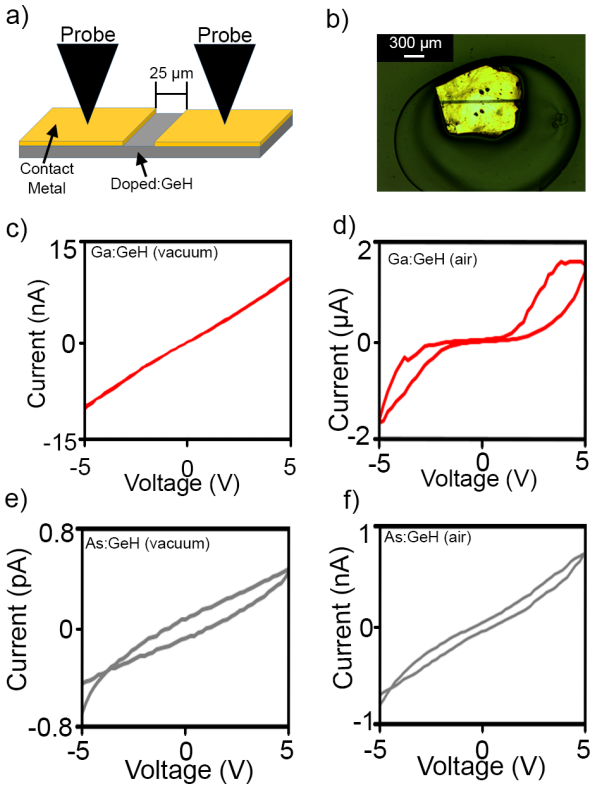

Figure 5: a) Diagram and b) photo of typical device for two-probe *I–V* measurements. Representative curves of 2.3% Ga:GeH (red) in c) vacuum and d) air and 1.1% As:GeH (gray) in e) vacuum and f) air.

Figure 5c,d shows a representative *I–V* plot for 2.3% Ga:GeH in vacuum and air, respectively. The *I–V* plot for the device measured under vacuum in Figure 5c shows ohmic contact behavior, with a typical sheet resistance of 9.5×10^{10} Ω/sq. The *I–V* behavior when measured in H_2O-containing atmosphere such as air, is highly hysteretic, non-ohmic, and with much higher current. Previously, we had shown that for P:GeH [29], H_2O-containing atmospheres are necessary to activate the phos-

phorus (group 15) dopants. For Ga:GeH, the presence of atmospheric water, while significantly increasing conductivity, also introduces a significantly non-linear behavior in the *I–V* plots, suggesting that H_2O plays an additional role in these gallium samples in addition to dopant activation. This also makes it difficult to extract an accurate value for sheet resistance, leading to the omission of its use as a metric for these samples. Regardless of the chemical state of the dopant atom in H_2O atmosphere, under vacuum there is a systematic decrease of sheet resistance for Ga:GeH with increasing amounts of Ga doping. With 0.08%, 0.14%, and 2.3% of gallium doping, the sheet resistance drops to 8.4×10^{12}, 1.3×10^{12}, and 9.5×10^{10} Ω/sq, respectively (Figure 6). This means a marked improvement of more than four orders of magnitude over undoped GeH of our samples with the highest doping.

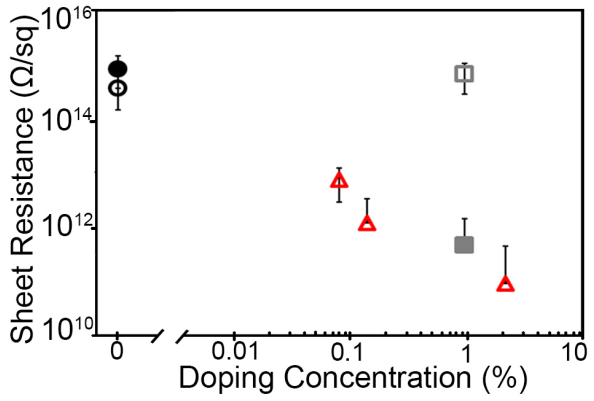

Figure 6: Sheet resistance of GeH (black), 1.1% As:GeH (gray), and 2.3% Ga:GeH (red) in vacuum (empty) and air (filled). Each doped data point represents 20–30 device measurements.

On the contrary, As:GeH does not exhibit any dopant activation under vacuum. Figure 5e shows a representative *I–V* plot of a 1.1% As:GeH device under vacuum. With the application of ±5 V, a current of less than 1 pA is observed, which is again at the actual noise limit of our instrumentation. However, in air, there is an increase in conductivity of at least three orders of magnitude. Figure 5f shows a representative *I–V* plot of As:GeH in ambient conditions. In contrast to Ga:GeH, the *I–V* plot is linear, with minimal hysteresis. The *I–V* behavior both in air and vacuum is similar to what was previously reported to occur in P:GeH, another group-15 dopant. In air, the average sheet resistance for 30 As:GeH devices was 5.0×10^{11} Ω/sq (Figure 6).

Conclusion

Here we have demonstrated that gallium and arsenic can be incorporated into a precursor $CaGe_2$ Zintl phase and are retained in the 2D germanium framework after the topotactic deintercalation process. These dopants do not significantly change the structure of germanane. The doped materials are stable in ambient atmosphere conditions for at least 24 h but start to oxidize after one to four days. The introduction of Ga and As to the lattice decreases the resistance under ambient conditions with large amounts of hysteresis, suggesting that the presence of water can activate these dopants. As was previously observed with P:GeH [29], As:GeH is highly resistive under vacuum, indicating the presence of water is required to activate group-15 dopants. In contrast, Ga:GeH exhibited sheet resistances in vacuum decreased by over four orders of magnitude, proportional to the amount of gallium and with minimal hysteretic behavior. This indicates that the activated state of the dopant in Ga:GeH is stable under vacuum, enabling robust electronic properties through encapsulation. Overall, this work provides a pathway to dope germanane and enable future explorations of electronic devices.

Experimental

Single crystalline platelets of doped and undoped GeH were synthesized using methods adapted from those reported previously [25]. For undoped GeH, stoichiometric amounts of calcium (Acros, 99%) and germanium (Acros, 99.999%) were sealed in quartz tubes under vacuum of less than 60 mTorr. The sample was annealed at 950 °C for 18 h, and slowly cooled to room temperature over the course of 2–10 days. $CaGe_2$ crystals were collected and placed in concentrated HCl at −40 °C for more than 8 days resulting in flakes having lateral dimensions of 5 × 5 mm. To prepare extrinsically doped $CaGe_2$, elemental aluminium (Johnson Matthey Electronics 99.9%), gallium (Acros 99.9%), arsenic (Sigma 99.999%), or antimony (Strem 99%) was used to replace germanium in the initial calcium and germanium mixture. Again, these materials were sealed in quartz tubes under vacuum and annealed following the same procedures as undoped germanane. The experiments with Sb resulted in the formation of a mixture of different phases, none of which were structurally similar to any known layered $CaGe_2$ polymorph. Subsequently, the single crystals of the *x*:$CaGe_2$ (*x* = Al, Ga, As) were placed in −40 °C HCl for at least 8 days, until deintercalation was complete and a lack of crystalline $CaGe_2$ peaks appeared in the XRD. The products were first rinsed with deionized water followed by rinsing with methanol, three times each. The crystals were collected via slow centrifugation and subsequently dried in vacuum.

The structure of doped GeH was confirmed using capilary X-ray diffraction using Cu $K\alpha_1$ radiation (λ = 1.54 nm) on a Bruker D8 powder X-ray diffractometer. XRD was performed using with finely ground powders packed in capillaries. Raman spectroscopy was used to confirm vibrational modes using a Renishaw InVia Raman equipped with a CCD detector exciting

with a 633 nm He–Ne laser. The relative elemental composition was measured using X-ray fluorescence on an Olympus X-5000 Mobile XRF System. SEM and EDX were performed using a FEI Helios Nanolab 600 dual beam focussed ion beam/scanning electron microscope. X-ray photoelectron spectroscopy was performed using a Kratos Axis ultra X-ray photoelectron spetrometer with a monochromatic aluminium X-ray gun. Samples were mounted in a glovebox and then stored in ambient atmosphere for 1, 4 and 8 days to determine the stability in air. Fourier transform infrared spectra were collected with a Perkin-Elmer frontier dual-range FIR/Mid-IR spectrometer that was loaded in an Ar-filled glovebox and using an attenuated total internal reflection (ATR) sample geometry.

Electrical properties were measured in top-contact device geometry, where metal contacts were first deposited via e-beam deposition using a shadow mask resulting in a 25 μm channel length. The contact metals used for undoped GeH and As:GeH were 80 nm/20 nm (Ag/Au). Ga:GeH device contacts were prepared using 100 nm Au. Contact materials were selected after testing with multiple metals and selecting the metal that gave the highest current and most linear *I*–*V* characteristics. Additionally, four-probe measurements indicate that the contact resistance for the 2.3% Ga:GeH is at least two orders of magnitude lower than the resistance of the material, indicating that contact resistance is negligible for these samples. All devices were stored in an Ar-filled glovebox until atmospheric measurements were carried out. Electronic measurements were conducted using a Keithley 4200-SCS attached to a Lake Shore Cryonics Inc. probe station. Two-probe current–voltage measurements were performed in both vacuum (ca. 10^{-4} mbar) and under ambient conditions in the dark.

Acknowledgements

We acknowledge the Analytical Spectroscopy Laboratory and the Surface Analysis Laboratory (NSF DMR-0114098) of The Ohio State University Department of Chemistry and Biochemistry and The Ohio State University Nanosystems Laboratory (NSL). Funding for this research was primarily provided by the NSF EFRI-1433467. We acknowledge partial support from the Center for Emergent Materials: an NSF MRSEC under award number DMR-1420451, to support M.Q.A. and S.J. Partial funding for shared facilities used in this research was provided by the Center for Emergent Materials: an NSF MRSEC under award number DMR-1420451. J.E.G. acknowledges the Camille and Henry Dreyfus Foundation for partial support.

References

1. Novoselov, K. S.; Geim, A. K.; Morozov, S. V.; Jiang, D.; Katsnelson, M. I.; Grigorieva, I. V.; Dubonos, S. V.; Firsov, A. A. *Nature* **2005,** *438,* 197–200. doi:10.1038/nature04233
2. Garcia, J. C.; de Lima, D. B.; Assali, L. V. C.; Justo, J. F. *J. Phys. Chem. C* **2011,** *115,* 13242–13246. doi:10.1021/jp203657w
3. Jiang, S.; Arguilla, M. Q.; Cultrara, N. D.; Goldberger, J. E. *Acc. Chem. Res.* **2015,** *48,* 144–151. doi:10.1021/ar500296e
4. Pulci, O.; Gori, P.; Marsili, M.; Garbuio, V.; Del Sole, R.; Bechstedt, F. *Europhys. Lett.* **2012,** *98,* 37004. doi:10.1209/0295-5075/98/37004
5. Vogg, G.; Brandt, M. S.; Stutzmann, M. *Adv. Mater.* **2000,** *12,* 1278–1281. doi:10.1002/1521-4095(200009)12:17<1278::AID-ADMA1278>3.0.CO;2-Y
6. Vogt, P.; De Padova, P.; Quaresima, C.; Avila, J.; Frantzeskakis, E.; Asensio, M. C.; Resta, A.; Ealet, B.; Le Lay, G. *Phys. Rev. Lett.* **2012,** *108,* 155501. doi:10.1103/PhysRevLett.108.155501
7. Wei, W.; Dai, Y.; Huang, B.; Jacob, T. *Phys. Chem. Chem. Phys.* **2013,** *15,* 8789–8794. doi:10.1039/c3cp51078f
8. Bonaccorso, F.; Colombo, L.; Yu, G.; Stoller, M.; Tozzini, V.; Ferrari, A. C.; Ruoff, R. S.; Pellegrini, V. *Science* **2015,** *347,* 1246501. doi:10.1126/science.1246501
9. De Padova, P.; Vogt, P.; Resta, A.; Avila, J.; Razado-Colambo, I.; Quaresima, C.; Ottaviani, C.; Olivieri, B.; Bruhn, T.; Hirahara, T.; Shirai, T.; Hasegawa, S.; Asensio, M. C.; Le Lay, G. *Appl. Phys. Lett.* **2013,** *102,* 163106. doi:10.1063/1.4802782
10. Zhang, R.-W.; Zhang, C.-W.; Ji, W.-X.; Li, S.-S.; Hu, S.-J.; Yan, S.-S.; Li, P.; Wang, P.-J.; Li, F. *New J. Phys.* **2015,** *17,* 083036. doi:10.1088/1367-2630/17/8/083036
11. Zhang, R.-w.; Zhang, C.-w.; Ji, W.-x.; Li, S.-s.; Yan, S.-s.; Hu, S.-j.; Li, P.; Wang, P.-j.; Li, F. *Sci. Rep.* **2016,** *6,* 18879. doi:10.1038/srep18879
12. Zhao, H.; Ji, W.-x.; Zhang, C.-w.; Li, P.; Zhang, S.-f.; Li, F.; Wang, P.-j.; Li, S.-s.; Yan, S.-s. *J. Mater. Chem. C* **2017,** *5,* 2656–2661. doi:10.1039/C7TC00153C
13. Zhang, R.-w.; Ji, W.-x.; Zhang, C.-w.; Li, S.-s.; Li, P.; Wang, P.-j. *J. Mater. Chem. C* **2016,** *4,* 2088–2094. doi:10.1039/C6TC00160B
14. Wang, Y.-p.; Ji, W.-x.; Zhang, C.-w.; Li, P.; Li, F.; Ren, M.-j.; Chen, X.-L.; Yuan, M.; Wang, P.-j. *Sci. Rep.* **2016,** *6,* 20342. doi:10.1038/srep20342
15. Radisavljevic, B.; Kis, A. *Nat. Mater.* **2013,** *12,* 815–820. doi:10.1038/nmat3687
16. Radisavljevic, B.; Radenovic, A.; Brivio, J.; Giacometti, V.; Kis, A. *Nat. Nanotechnol.* **2011,** *6,* 147–150. doi:10.1038/nnano.2010.279
17. Wang, Q. H.; Kalantar-Zadeh, K.; Kis, A.; Coleman, J. N.; Strano, M. S. *Nat. Nanotechnol.* **2012,** *7,* 699–712. doi:10.1038/nnano.2012.193
18. Mak, K. F.; Lee, C.; Hone, J.; Shan, J.; Heinz, T. F. *Phys. Rev. Lett.* **2010,** *105,* 136805. doi:10.1103/PhysRevLett.105.136805
19. Zhang, R. W.; Ji, W. X.; Zhang, C. W.; Li, P.; Wang, P. J. *arXiv* **2016,** No. 1607.
20. Arguilla, M. Q.; Cultrara, N. D.; Baum, Z. J.; Jiang, S.; Ross, R. D.; Goldberger, J. E. *Inorg. Chem. Front.* **2017,** *4,* 378–386. doi:10.1039/C6QI00476H
21. Arguilla, M. Q.; Katoch, J.; Krymowski, K.; Cultrara, N. D.; Xu, J.; Xi, X.; Hanks, A.; Jiang, S.; Ross, R. D.; Koch, R. J.; Ulstrup, S.; Bostwick, A.; Jozwiak, C.; McComb, D. W.; Rotenberg, E.; Shan, J.; Windl, W.; Kawakami, R. K.; Goldberger, J. E. *ACS Nano* **2016,** *10,* 9500–9508. doi:10.1021/acsnano.6b04609
22. Geim, A. K.; Grigorieva, I. V. *Nature* **2013,** *499,* 419–425. doi:10.1038/nature12385
23. Dávila, M.; Xian, L.; Cahangirov, S.; Rubio, A.; Le Lay, G. *New J. Phys.* **2014,** *16,* 095002. doi:10.1088/1367-2630/16/9/095002

24. Butler, S. Z.; Hollen, S. M.; Cao, L.; Cui, Y.; Gupta, J. A.; Gutiérrez, H. R.; Heinz, T. F.; Hong, S. S.; Huang, J.; Ismach, A. F.; Johnston-Halperin, E.; Kuno, M.; Plashnitsa, V. V.; Robinson, R. D.; Ruoff, R. S.; Salahuddin, S.; Shan, J.; Shi, L.; Spencer, M. G.; Terrones, M.; Windl, W.; Goldberger, J. E. *ACS Nano* **2013,** *7,* 2898–2926. doi:10.1021/nn400280c
25. Bianco, E.; Butler, S.; Jiang, S.; Restrepo, O. D.; Windl, W.; Goldberger, J. E. *ACS Nano* **2013,** *7,* 4414–4421. doi:10.1021/nn4009406
26. Jiang, S.; Bianco, E.; Goldberger, J. E. *J. Mater. Chem. C* **2014,** *2,* 3185–3188. doi:10.1039/c3tc32489c
27. Jiang, S.; Butler, S.; Bianco, E.; Restrepo, O. D.; Windl, W.; Goldberger, J. E. *Nat. Commun.* **2014,** *5,* 3389. doi:10.1038/ncomms4389
28. Jiang, S.; Krymowski, K.; Asel, T.; Arguilla, M. Q.; Cultrara, N. D.; Yanchenko, E.; Yang, X.; Brillson, L. J.; Windl, W.; Goldberger, J. E. *Chem. Mater.* **2016,** *28,* 8071–8077. doi:10.1021/acs.chemmater.6b04309
29. Young, J. R.; Chitara, B.; Cultrara, N. D.; Arguilla, M. Q.; Jiang, S.; Fan, F.; Johnston-Halperin, E.; Goldberger, J. E. *J. Phys.: Condens. Matter* **2015,** *28,* 034001. doi:10.1088/0953-8984/28/3/034001
30. Madhushankar, B. N.; Kaverzin, A.; Giousis, T.; Potsi, G.; Gournis, D.; Rudolf, P.; Blake, G. R.; van der Wal, C. H.; van Wees, B. J. *2D Mater.* **2017,** *4,* 021009. doi:10.1088/2053-1583/aa57fd
31. Arguilla, M. Q.; Jiang, S.; Chitara, B.; Goldberger, J. E. *Chem. Mater.* **2014,** *26,* 6941–6946. doi:10.1021/cm502755q
32. Luo, X.; Zurek, E. *J. Phys. Chem. C* **2015,** *120,* 793–800. doi:10.1021/acs.jpcc.5b11770
33. Leonhardt, G.; Berndtsson, A.; Hedman, J.; Klasson, M.; Nilsson, R.; Nordling, C. *Phys. Status Solidi B* **1973,** *60,* 241–248. doi:10.1002/pssb.2220600126
34. Wagner, C. D. *Faraday Discuss. Chem. Soc.* **1975,** *60,* 291–300. doi:10.1039/dc9756000291
35. Taylor, J. A. *J. Vac. Sci. Technol. (N. Y., NY, U. S.)* **1982,** *20,* 751–755. doi:10.1116/1.571450

License and Terms

BEILSTEIN JOURNAL OF NANOTECHNOLOGY

Transport characteristics of a silicene nanoribbon on Ag(110)

Ryoichi Hiraoka[1], Chun-Liang Lin[1], Kotaro Nakamura[1], Ryo Nagao[1], Maki Kawai[1], Ryuichi Arafune[2] and Noriaki Takagi[*1]

Full Research Paper

Open Access

Address:
[1]Department of Advanced Materials Science, The University of Tokyo, 5-1-5 Kashiwanoha, Kashiwa, Chiba 277-8561, Japan and
[2]International Center for Materials Nanoarchitectonics (WPI-MANA), National Institute for Materials Science, 1-1 Namiki, Tsukuba, Ibaraki 304-0044, Japan

Email:
Noriaki Takagi[*] - n-takagi@k.u-tokyo.ac.jp

* Corresponding author

Keywords:
nanojunction; nanoribbon; scanning tunnelling microscopy; silicene; transport

Beilstein J. Nanotechnol. **2017,** *8,* 1699–1704.
doi:10.3762/bjnano.8.170

Received: 20 April 2017
Accepted: 21 July 2017
Published: 16 August 2017

This article is part of the Thematic Series "Silicene, germanene and other group IV 2D materials".

Guest Editor: P. Vogt

Abstract

We present the transport characteristics of individual silicene nanoribbons (SiNRs) grown on Ag(110). By lifting up a single SiNR with a low-temperature scanning tunneling microscope tip, a nanojunction consisting of tip, SiNR and Ag is fabricated. In the differential conductance spectra of the nanojunctions fabricated by this methodology, a peak appears at the Fermi level which is not observed in the spectra measured either for the SiNRs before being lifted up or the clean Ag substrate. We discuss the origin of the peak as it relates to the SiNR.

Introduction

The electronic transport characteristics of nanomaterials from a single molecule, nanowires, nanotubes, and nanoribbons to two-dimensional (2D) atomic sheets have garnered much attention from fundamental and application points of view [1-7]. Silicene, a single-atom-thick honeycomb layer consisting of Si atoms, is one of such promising materials [8-13]. Freestanding silicene hosts the Dirac electronic system and behaves as a 2D topological insulator (TI) as a result of the sizable spin–orbit coupling of Si [14-16].

Silicene grown on solid substrates has been studied intensively. Various superstructures such as (4×4), (2√3×2√3)R30° and (√13×√13) R13.9° are formed on Ag(111) [17-22]. These structures are composed of buckled honeycomb configurations. However, they do not host Dirac fermions and do not exhibit the 2D TI features because of the interfacial coupling between the silicene layer and the substrate, as demonstrated for the (4×4) structure [23]. The key factor for realizing the 2D-TI silicene is to reduce the interfacial coupling. Recently, Tao et al. [24] successfully fabricated a silicene field effect transistor by peeling off the (2√3×2√3)R30° silicene from the Ag substrate and demonstrated the current–voltage characteristics supporting the survival of Dirac fermions. This study indicates the importance of reducing the interfacial coupling.

Not only a 2D sheet but also a 1D ribbon of silicene can be formed. Le Lay and collaborators have reported the formation of silicene nanoribbons (denoted as SiNRs hereafter) on Ag(110) [25,26]. The SiNR takes on the structure of a 1D honeycomb of ≈1.5 nm width with the zigzag edges. Very recently, pentagonal chain models were proposed for SiNR on Ag(110) [27,28]. In this model, Si atoms constitute a five-membered ring to form a 1D chain. Density functional theory (DFT) calculations have demonstrated that freestanding honeycomb SiNR preserves the electronic states localized at the edges near the Fermi level similar to the graphene nanoribbon with zigzag edges [29-33]. Although the electronic structure of SiNR has been studied experimentally [34-36], the existence of edge states remains an open question. The interfacial coupling between the SiNR and the substrate might modify the intrinsic electronic properties of SiNR as described above for the (4×4) silicene on Ag(111). Thus, it is required to decouple SiNR from the substrate and evaluate the intrinsic properties.

Here we report the transport characteristics of SiNR on Ag(110). To isolate SiNR from the Ag substrate, we lift up an individual SiNR with the tip of a low-temperature scanning tunneling microscope (STM) and fabricate a nanojunction in which the lifted SiNR bridges the gap between the STM tip and the substrate. This method enables us to isolate the SiNR from the substrate electronic system and elucidate the intrinsic properties. We measure the differential conductance (dI/dV) spectra of the nanojunctions and find a sharp peak structure at the Fermi level.

Results and Discussion

Figure 1a shows a topographic STM image of the Ag(110) surface after the deposition of Si atoms. The lines extend along the [$\bar{1}$10] direction. Two types of lines are observed as shown in Figure 1b; one has a 1.6 nm width and the other a 0.8 nm width. The former and latter are composed of four and two bright spots across the longitudinal direction, respectively. The cross-sectional height profile in Figure 1c shows that the distance between the spots is 0.39 nm, which is nearly identical to the size of the honeycomb unit of Si. These features indicate that these lines are SiNRs with a zigzag edge structure, as demonstrated by the structural models in Figure 1d. The present results are nicely matched with those reported in the previous STM works [25,26].

We measured dI/dV spectra as a function of the STM tip location. Figure 2a,b shows the spectra measured in the narrow and wide voltage ranges. One sees that these spectra are very similar to each other and do not depend on the tip location. The spectra taken for the SiNRs are almost the same as those for the

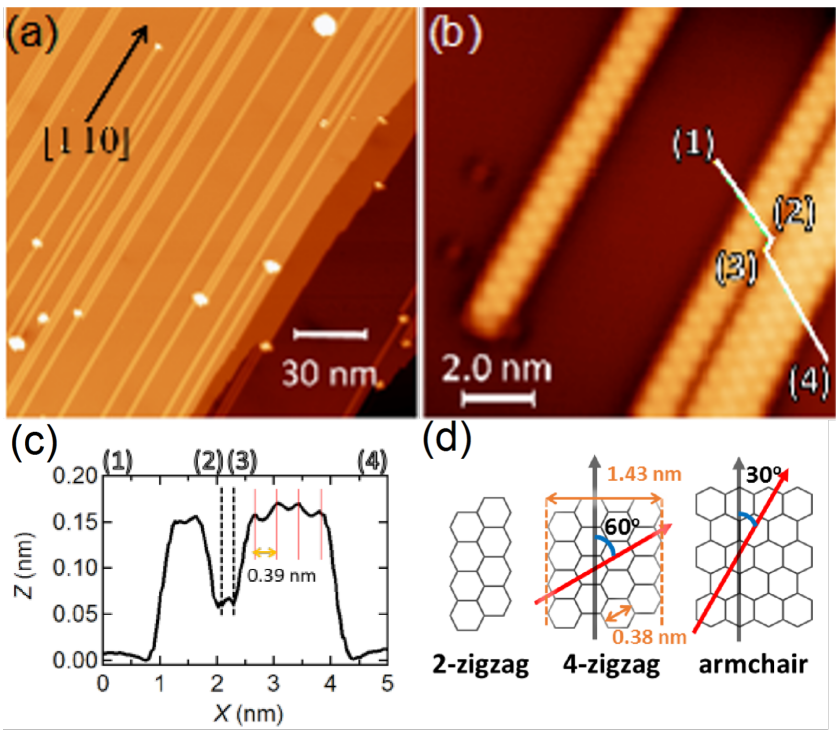

Figure 1: STM images of SiNRs on Ag(110) with (a) V_S = −500 mV, I_t = 10 pA and (b) V_S = −100 mV, I_t = 30 pA. (c) Cross-sectional height profile along the (1)–(4) line shown in (b). (d) Schematic structural models of SiNR structures. The black arrows dictate the longitudinal direction and the red arrows represent the row of the honeycomb units across the ribbons.

Ag substrate. The spectra taken at the edges are essentially identical to those spectra taken inside the SiNR and do not show a spectral signature relevant to the edge. Similar to silicene on Ag(111), the interaction of SiNRs with the substrate may hamper the emergence of intrinsic electronic features of free-standing SiNR.

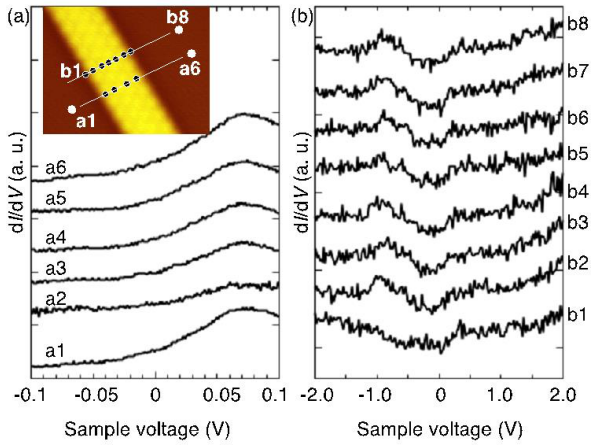

Figure 2: d*I*/d*V* spectra acquired in (a) narrow (from −0.1 to 0.1 V) and (b) wide (from −2 to 2 V) voltage ranges. The inset of (a) is an STM image showing the tip locations where the spectra are measured. The modulation voltage of 8 mV at 366.6 Hz is added to the sample voltage. Each spectrum is shifted vertically.

To reveal the intrinsic electronic features of SiNRs, we conducted transport measurements for individual SiNRs by lifting up each SiNR with the STM tip and fabricating a nanojunction consisting of an SiNR, the STM tip and the Ag substrate. This method reduces the SiNR–Ag interaction and enables us to reveal the intrinsic features of SiNRs. The measurements were performed by a scheme summarized in Figure 3a. At first, the STM tip is fixed over one end of the SiNR while the STM feedback loop is turned off. Then we approach the tip to the target SiNR while measuring the conductance G at the sample voltage of 100 mV as a function of tip vertical position (Z). We set the position where the tip is fixed initially as $Z = 0$. Once the tip touches the target, we retract the tip to lift up the SiNR and measure the dI/dV spectrum at certain tip position.

Figure 3b is an example of the conductance traces where the value of G is plotted as a function of Z. From the initial set point A to the point B, G increases as Z increases in the approaching procedure. The variation of G in this region is well fitted with an exponential function, as shown by the red curve, which is the calculated result of least-squares fitting. This indicates that the current flows through a vacuum gap. When the tip moves 0.54 nm, G suddenly increases from B ($G = 0.2G_0$) to C ($G = 1.4G_0$) where G_0 is the conductance quantum (7.75×10^{-5} S). This discontinuous increase indicates that the tip touches the SiNR. Subsequently, we lift up the SiNR by retracting the STM to fabricate a nanojunction. When we lift up the SiNR further, the nanojunction is broken at D ($Z = -0.4$ nm) and G returns to the initial value of $\approx 10^{-4}$ G_0 at E. In the retracting procedure from C to D, the nanojunction is preserved until the tip is retracted about 1 nm from the contact position. The conductance trace in this regime is different from that in the approach procedure. The conductance value remains higher than $0.1G_0$ until the junction is broken, indicating the conductance of the SiNR is almost comparable to a metallic nanowire. The resistance of a silicene field effect transistor (FET) is estimated to be about 40 kΩ from the drain current measured as a function of the drain voltage [24]. The sheet resistance of multilayer silicene sheets is measured to be 6.5 kΩ/□ [37]. These results also indicate that the silicene sheet is conductive, and the present results reasonably agree with the previous results. Figure 3c shows a histogram of the maximum gap distance, Z_{gap_max}, which corresponds to the traveling distance of the tip from C to D. The histogram indicates how long the nanojunction can be fabricated. The nanojunctions are usually broken at small values of Z_{gap_max} and SiNRs can rarely be lifted up to 1.0 nm.

It is of interest to compare the properties of SiNRs with graphene nanoribbons (GNRs). The transport properties of armchair GNRs (AGNRs) grown on Au(111) have been investigated recently by using STM [38]. Similar to the present study, the conductance of individual AGNRs has been measured by lifting up each AGNR with an STM tip. The measured conductance values are the order of 10^{-3} G_0, reflecting the semiconducting nature with a large energy gap. Comparing these results with those obtained in the present study, one can see that the SiNR is much more conductive, indicating that SiNRs would be a suitable material for a conducting wire used in nanostructured electronic devices. In contrast, the SiNR is not mechanically strong and the SiNR junction is more easily broken. The AGNR was able to be lifted up more than 3 nm. This may come from the stronger interfacial coupling between the SiNR and Ag(110) as well as the weaker bond strength of Si–Si bonding in SiNR than that of C–C bonding in AGNR. We also tried to lift up the narrower ribbons, but were not yet successful.

The dI/dV spectra of the SiNR nanojunction shows an interesting feature. Namely, we have found that a peak appears at the Fermi level as shown in the lower panel of Figure 3e. Note that the peak does not always appear in the spectra (as shown in the upper panel of Figure 3e), even though the SiNR is lifted up from the Ag(110) substrate. We measured more than 600 spectra for 250 SiNR nanojunctions. Whereas most spectra did not exhibit the remarkable structure as shown in the upper panel of

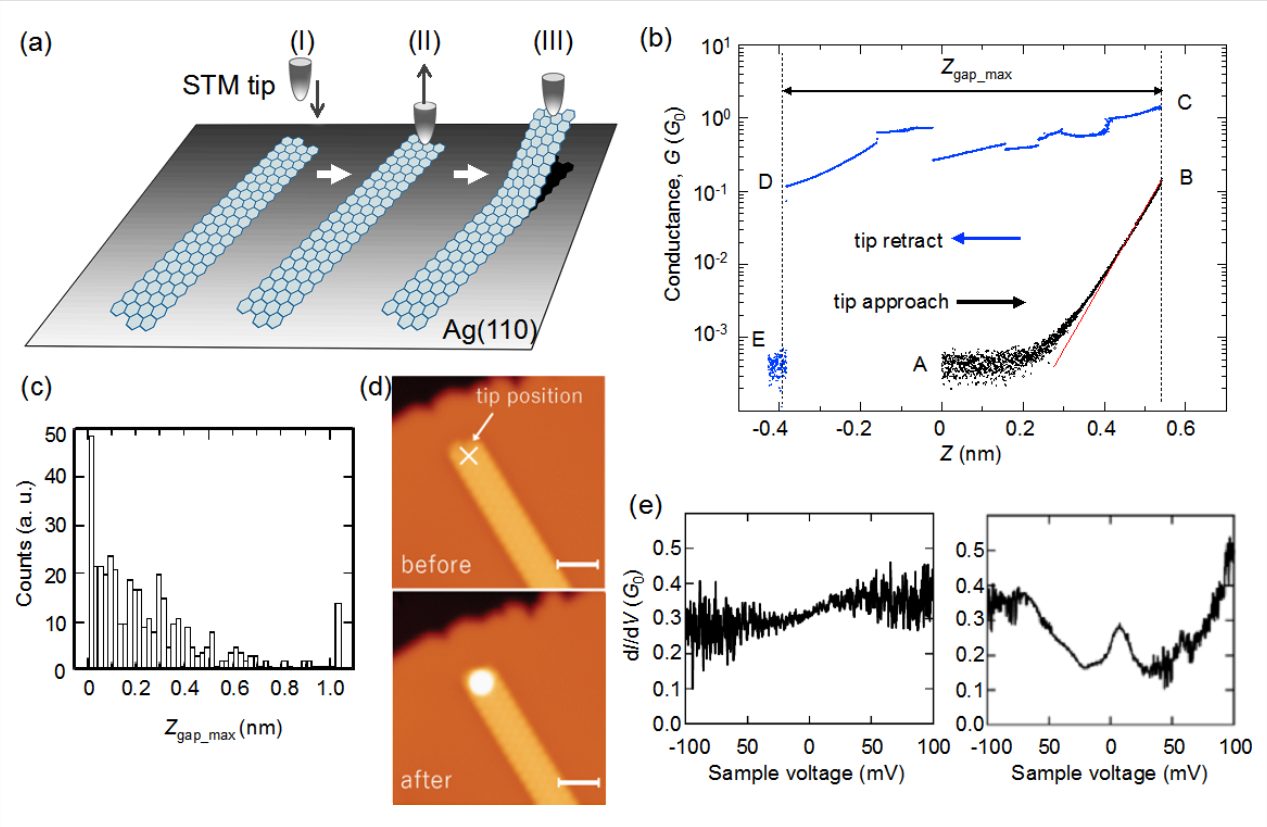

Figure 3: (a) Schematic illustration on fabrication of an SiNR nanojunction with an STM tip. (b) Conductance trace measured as a function of tip vertical position (Z). G_0 is the conductance quantum (7.75×10^{-5} S). The feedback is turned off at V_S = 100 mV and I_t = 20 pA and the conductance is measured at V_S = 100 mV. The conductance measured during the tip approach and retraction procedures is plotted with black and blue circles, respectively. The red curve shows the result of the least-squares fitting. In the conductance measurement, the gain of the current amplifier is switched from 10^9 (in the STM measurements) to 10^5 for measuring the large variation of the current in the tip approach and retraction processes. The currents in the almost flat region around label A in (b) are too small to be measured with this gain so that the conductance around A is nominally different from the value (2.6×10^{-6} G_0) taken for V_S = 100 mV and I_t = 20 pA. (c) Histogram of Z_{gap_max}. Z_{gap_max} is the maximum distance the tip travels before the SiNR nanojunction is broken after contacting the tip to the SiNR. (d) STM images before and after the conductance measurement. The scale bars correspond to 2 nm. (e) Two types of dI/dV spectra of the SiNR nanojunction. The spectra are measured with a modulation voltage of 4 mV at 312.6 Hz.

Figure 3e, 31 spectra did show a clear peak structure at the Fermi level. As a reference, we measured the spectra of the nanojunctions which are fabricated by contacting the STM tip directly to the bare Ag(110) regions and lifting up the tip. We did not observe a peak structure for this type of nanojunction. As shown in Figure 3d, the structures are not drastically changed before and after the measurement except for a bright spot which arises from a small cluster dropped from the tip apex. Thus, we have concluded that the peak structure originates from the intrinsic properties of the SiNR.

Now let us examine the origin of the peak structure observed for the SiNR nanojunctions. Since the dI/dV spectrum essentially reflects the electronic density of states (DOS), we interpret the peak by comparing the dI/dV spectrum with the DOS spectra calculated for freestanding SiNR. The DFT studies have demonstrated that the geometric and electronic structures of SiNR strongly depend on the termination of dangling bonds at the edge Si atoms [29,30,33]. The electronic states localized at the edges appear near the Fermi level for the mono-hydrogenated SiNR in which the edge Si atoms are passivated with H atoms. In the case that the edge Si atoms are not terminated with H atoms, the honeycomb structure is unstable and vulnerable to the structural reconstruction at the edges. The DOS spectrum depends on the reconstructed structure. In the DFT study of Cahangirov et al. [29], the edge undergoes a reconstruction in which two deformed 6-membered rings are alternatively arranged along the edge. As a result, the flat band dispersion arising from the edge states disappears and instead a more dispersive band crosses the Femi level. In contrast, the DFT study of Ding and Wang [33] shows that a peak appears at the Fermi level in the DOS spectrum for a reconstructed SiNR in which the combination of six- and five-membered rings constitutes the edge. Assuming that the latter type of edge reconstruction takes place for the SiNR lifted by the STM tip, the peak structure can be rationalized by the DFT results of Ding and

Wang. Finally, we briefly discuss the possibility of the pentagonal chain models proposed very recently for SiNRs on Ag(110) [27,28]. Cerdá et al. [27] calculated the energy band structures of various pentagonal chains; some of the pentagonal chains host electronic structure around the Fermi level, which may explain the peak structure observed in our conductance measurements. In the DFT calculation of Ding and Wang [33], pentagonal rings appear inside the honeycomb ribbon and the peak structure may reflect the pentagonal structure. However, further investigations are required to conclude the atomic structure and transport properties of SiNRs.

Conclusion

We investigated the geometric and electronic structure of SiNRs grown on Ag(110) using STM and STM junction measurements. We found that the dI/dV spectra of SiNRs on Ag(110) and the bare Ag(110) regions are essentially identical, indicating strong interfacial coupling between the SiNR and the Ag(110) substrate, and that SiNR is a good conductor with conductance of $0.1G_0$–$1G_0$. In addition, we have found a peak structure at the Fermi level for the SiNR nanojunctions, which is relevant to the edge of the SiNR.

Experimental

All experiments were carried out in an ultra-high vacuum (UHV) chamber equipped with a low temperature STM ($P < 10^{-10}$ Torr, $T = 6$ K). A Ag(110) single crystal surface was cleaned by repeated Ar ion sputtering and annealing at around 800 K. The STM tip was made of an electrochemically etched W wire and postannealed in the UHV chamber. The SiNRs were synthesized on Ag(110) by depositing Si atoms from the electrically heated Si wafer. The Ag(110) substrate was heated at 500 K during the Si deposition. The deposition rate was 0.03 ML/min, where 1 ML ≈ 1.5×10^{15} Si atoms/cm^2. The differential conductance spectra (dI/dV) were measured by a lock-in technique with the modulation voltage of 0.4–8.0 mV at 300–500 Hz added to the sample voltage. The conductance measurements were carried out by lifting individual SiNRs with an STM tip and fabricating a nanojunction in which the SiNR bridges the STM tip and the substrate. The conductance measurements were made at 6 K. The typical tip approach/retraction speed was set at 0.06 nm/sec.

Acknowledgements

This work was partially supported by MEXT KAKENHI Grant Number 25110008.

References

1. Nitzan, A.; Ratner, M. A. *Science* **2003,** *300,* 1384–1389. doi:10.1126/science.1081572
2. Joachim, C.; Ratner, M. A. *Proc. Natl. Acad. Sci. U. S. A.* **2005,** *102,* 8801–8808. doi:10.1073/pnas.0500075102
3. Tao, N. J. *Nat. Nanotechnol.* **2006,** *1,* 173–181. doi:10.1038/nnano.2006.130
4. Hiraoka, R.; Arafune, R.; Tsukahara, N.; Kawai, M.; Takagi, N. *Phys. Rev. B* **2014,** *90,* 241405. doi:10.1103/PhysRevB.90.241405
5. Charlier, J.-C.; Blase, X.; Roche, S. *Rev. Mod. Phys.* **2007,** *79,* 677–732. doi:10.1103/RevModPhys.79.677
6. Rurali, R. *Rev. Mod. Phys.* **2010,** *82,* 427–449. doi:10.1103/RevModPhys.82.427
7. Castro Neto, A. H.; Guinea, F.; Peres, N. M. R.; Novoselov, K. S.; Geim, A. K. *Rev. Mod. Phys.* **2009,** *81,* 109–162. doi:10.1103/RevModPhys.81.109
8. Kara, A.; Enriquez, H.; Seitsonen, A. P.; Voon, L. C. L. Y.; Vizzini, S.; Aufray, B.; Oughaddou, H. *Surf. Sci. Rep.* **2012,** *67,* 1–18. doi:10.1016/j.surfrep.2011.10.001
9. Takagi, N.; Lin, C.-L.; Kawahara, K.; Minamitani, E.; Tsukahara, N.; Kawai, M.; Arafune, R. *Prog. Surf. Sci.* **2015,** *90,* 1–20. doi:10.1016/j.progsurf.2014.10.001
10. Oughaddou, H.; Enriquez, H.; Tchalala, M. R.; Yildirim, H.; Mayne, A. J.; Bendounane, A.; Dujardin, G.; Ali, M. A.; Kara, A. *Prog. Surf. Sci.* **2015,** *90,* 46–83. doi:10.1016/j.progsurf.2014.12.003
11. Houssa, M.; Dimoulas, A.; Molle, A. *J. Phys.: Condens. Matter* **2015,** *27,* 253002. doi:10.1088/0953-8984/27/25/253002
12. Spencer, M. J. S.; Morishita, T., Eds. *Silicene–Structure, Properties and Applications;* Springer: Berlin, Germany, 2016.
13. Cahangirov, S.; Sahin, H.; Le Lay, G.; Rubio, A. *Introduction to the Physics of Silicene and Other 2D Materials;* Springer: Berlin, Germany, 2017.
14. Liu, C.-C.; Feng, W.; Yao, Y. *Phys. Rev. Lett.* **2011,** *107,* 076802. doi:10.1103/PhysRevLett.107.076802
15. Ezawa, M. *New J. Phys.* **2012,** *14,* 033003. doi:10.1088/1367-2630/14/3/033003
16. Ezawa, M. *Phys. Rev. Lett.* **2012,** *109,* 055502. doi:10.1103/PhysRevLett.109.055502
17. Lin, C.-L.; Arafune, R.; Kawahara, K.; Tsukahara, N.; Minamitani, E.; Kim, Y.; Takagi, N.; Kawai, M. *Appl. Phys. Express* **2012,** *5,* 045802. doi:10.1143/APEX.5.045802
18. Vogt, P.; De Padova, P.; Quaresima, C.; Avila, J.; Frantzeskakis, E.; Asensio, M. C.; Resta, A.; Ealet, B.; Le Lay, G. *Phys. Rev. Lett.* **2012,** *108,* 155501. doi:10.1103/PhysRevLett.108.155501
19. Jamgotchian, H.; Colignon, Y.; Hamzaoui, N.; Ealet, B.; Hoarau, J. Y.; Aufray, B.; Bibérian, J. P. *J. Phys.: Condens. Matter* **2012,** *24,* 172001. doi:10.1088/0953-8984/24/17/172001
20. Feng, B.; Ding, Z.; Meng, S.; Yao, Y.; He, X.; Cheng, P.; Chen, L.; Wu, K. *Nano Lett.* **2012,** *12,* 3507–3511. doi:10.1021/nl301047g
21. Chiappe, D.; Grazianetti, C.; Tallarida, G.; Fanciulli, M.; Molle, A. *Adv. Mater.* **2012,** *24,* 5088–5093. doi:10.1002/adma.201202100
22. Arafune, R.; Lin, C.-L.; Kawahara, K.; Kanno, M.; Tsukahara, N.; Minamitani, E.; Kim, Y.; Takagi, N.; Kawai, M. *Surf. Sci.* **2013,** *608,* 297–300. doi:10.1016/j.susc.2012.10.022
23. Lin, C.-L.; Arafune, R.; Kawahara, K.; Kanno, M.; Tsukahara, N.; Minamitani, E.; Kim, Y.; Kawai, M.; Takagi, N. *Phys. Rev. Lett.* **2013,** *110,* 076801. doi:10.1103/PhysRevLett.110.076801
24. Tao, L.; Cinquanta, E.; Chiappe, D.; Grazianetti, C.; Fanciulli, M.; Dubey, M.; Molle, A.; Akinwande, D. *Nat. Nanotechnol.* **2015,** *10,* 227–231. doi:10.1038/nnano.2014.325
25. Leandri, C.; Le Lay, G.; Aufray, B.; Girardeaux, C.; Avila, J.; Davila, M. E.; Asensio, M. C.; Ottaviani, C.; Cricenti, A. *Surf. Sci.* **2005,** *574,* L9–L15. doi:10.1016/j.susc.2004.10.052

26. Aufray, B.; Kara, A.; Vizzini, S.; Oughaddou, H.; Léandri, C.; Ealet, B.; Le Lay, G. *Appl. Phys. Lett.* **2010,** *96,* 183102. doi:10.1063/1.3419932
27. Cerdá, J. I.; Sławińska, J.; Le Lay, G.; Marele, A. C.; Goméz-Rodríguez, J. M.; Dávila, M. E. *Nat. Commun.* **2016,** *7,* 13076. doi:10.1038/ncomms13076
28. Prevot, G.; Hogan, C.; Leoni, T.; Bernard, R.; Moyen, E.; Masson, L. *Phys. Rev. Lett.* **2017,** *117,* 276102. doi:10.1103/PhysRevLett.117.276102
29. Cahangirov, S.; Topsakal, M.; Aktürk, E.; Şahin, H.; Ciraci, S. *Phys. Rev. Lett.* **2009,** *102,* 236804. doi:10.1103/PhysRevLett.102.236804
30. Ding, Y.; Ni, J. *Appl. Phys. Lett.* **2009,** *95,* 083115. doi:10.1063/1.3211968
31. Kang, J.; Wu, F.; Li, J. *Appl. Phys. Lett.* **2012,** *100,* 233122. doi:10.1063/1.4726276
32. Xu, C.; Luo, G.; Liu, Q.; Zheng, J.; Zhang, Z.; Nagase, S.; Gao, Z.; Lu, J. *Nanoscale* **2012,** *4,* 3111–3117. doi:10.1039/c2nr00037g
33. Ding, Y.; Wang, Y. *Appl. Phys. Lett.* **2014,** *104,* 083111. doi:10.1063/1.4866786
34. De Padova, P.; Quaresima, C.; Olivieri, B.; Perfetti, P.; Le Lay, G. *Appl. Phys. Lett.* **2011,** *98,* 081909. doi:10.1063/1.3557073
35. De Padova, P.; Kubo, O.; Olivieri, B.; Quaresima, C.; Nakayama, T.; Aono, M.; Le Lay, G. *Nano Lett.* **2012,** *12,* 5500–5503. doi:10.1021/nl302598x
36. Feng, B.; Li, H.; Meng, S.; Chen, L.; Wu, K. *Surf. Sci.* **2016,** *645,* 74–79. doi:10.1016/j.susc.2015.10.037
37. Vogt, P.; Capiod, P.; Berthe, M.; Resta, A.; De Padova, P.; Bruhn, T.; Le Lay, G.; Grandidier, B. *Appl. Phys. Lett.* **2014,** *104,* 021602. doi:10.1063/1.4861857
38. Koch, M.; Ample, F.; Joachim, C.; Grill, L. *Nat. Nanotechnol.* **2012,** *7,* 713–717. doi:10.1038/nnano.2012.169

License and Terms

BEILSTEIN JOURNAL OF NANOTECHNOLOGY

Adsorption and diffusion characteristics of lithium on hydrogenated α- and β-silicene

Fadil Iyikanat*[1], Ali Kandemir[2], Cihan Bacaksiz[1] and Hasan Sahin*[3,4]

Full Research Paper

Open Access

Address:
[1]Department of Physics, Izmir Institute of Technology, 35430, Izmir, Turkey, [2]Department of Materials Science and Engineering, Izmir Institute of Technology, 35430, Izmir, Turkey, [3]Department of Photonics, Izmir Institute of Technology, 35430, Izmir, Turkey and [4]ICTP-ECAR Eurasian Center for Advanced Research, Izmir Institute of Technology, 35430, Izmir, Turkey

Email:
Fadil Iyikanat* - fadiliyikanat@iyte.edu.tr; Hasan Sahin* - hasansahin@iyte.edu.tr

* Corresponding author

Keywords:
density functional theory; diffusion; Li atom; silicene; ultra-thin materials

Beilstein J. Nanotechnol. **2017,** *8,* 1742–1748.
doi:10.3762/bjnano.8.175

Received: 18 February 2017
Accepted: 04 August 2017
Published: 23 August 2017

This article is part of the Thematic Series "Silicene, germanene and other group IV 2D materials".

Guest Editor: P. Vogt

Abstract

Using first-principles density functional theory calculations, we investigate adsorption properties and the diffusion mechanism of a Li atom on hydrogenated single-layer α- and β-silicene on a Ag(111) surface. It is found that a Li atom binds strongly on the surfaces of both α- and β-silicene, and it forms an ionic bond through the transfer of charge from the adsorbed atom to the surface. The binding energies of a Li atom on these surfaces are very similar. However, the diffusion barrier of a Li atom on H-α-Si is much higher than that on H-β-Si. The energy surface calculations show that a Li atom does not prefer to bind in the vicinity of the hydrogenated upper-Si atoms. Strong interaction between Li atoms and hydrogenated silicene phases and low diffusion barriers show that α- and β-silicene are promising platforms for Li-storage applications.

Introduction

Following the first synthesis of graphene, the family of two-dimensional (2D) materials have drawn extraordinary attention [1,2]. This family consists of a large variety of materials such as hexagonal boron nitride (hBN) [3,4], silicene [5-7], germanene [8], transition-metal dichalcogenides (TMDs) [9-14], transition-metal trichalcogenides (TMTs) [15,16], phosphorene [17] and gallium chalcogenides [18]. Structural stability, chemical versatility and electronic band gaps of 2D materials that cover the range from 0 to 5 eV make them attractive for current nanoscale device applications.

In the large family of 2D materials, silicene deserves a special consideration due to its compatibility and expected integration with current nanotechnology. Silicene consists of a single layer of Si atoms arranged in a hexagonal lattice. Unlike the gapless semimetal graphene, silicene has a tiny energy gap that stems

from the intrinsic spin–orbit interaction [19]. Instead of the planar structure of graphene, silicene exhibits a low-buckled structure.

Although bulk silicon does not have a layered structure, syntheses of a 2D form of silicon via epitaxial growth on several metal substrates such as Ag(111) [5,20], Ir(111) [21], and $ZrB_2(0001)$ [22] were achieved. By performing ab initio calculations, Liu et al. predicted that the electronic properties of silicene highly depend on the substrate [23]. Johnson et al. showed that the Ag(111) surface leads to metalization of a few distinct forms of silicene [24]. Among the variety of substrates, Ag(111) surface comes to prominence for epitaxial growth of single-layer silicene. Lattice match and almost homogeneous interaction between Ag(111) and silicene support the formation of a honeycomb structure of silicene. Recently, a silicene field-effect transistor was successfully fabricated on Ag(111) with a measured room-temperature mobility of about 100 $cm^2 \cdot V^{-1} \cdot s^{-1}$ [25]. In addition to pristine forms, hydrogenated derivatives of silicene were also studied extensively. Theoretically, it was predicted that hydrogenated silicene has two different atomic configurations (chair-like and boat-like) with energy gap values ranging between 2.9 and 4.0 eV [26]. It was found that half-hydrogenated silicene exhibits ferromagnetic semiconducting behavior with a band gap of 0.95 eV [27]. Hydrogenation leads indirect-to-direct gap transitions in bilayer silicene [28]. In the experimental study of Qiu et al., the ordered and reversible hydrogenation of silicene was performed [29]. Moreover, Medina et al. demonstrated that hydrogenation leads to a structural transition from the classical α-(3×3) phase to the β-(3×3) phase [30]. It was indicated that β-(3×3) phase could coexist with α-(3×3) phase. Despite recent experimental studies on these phases, no theoretical study has ever been reported for the hydrogenated forms of α- and β-silicene on a Ag(111) surface.

The adsorption of alkali metal atoms provides various ways to modify the structural, electronic and magnetic properties of 2D materials. It was found that adsorption of alkali atoms is a proper way to dope carbon nanotubes chemically [31,32]. It was reported that the hydrogen storage capacity and conductivity of single-walled carbon nanotubes could be enhanced by doping with Li and K [33]. The adsorption of Li atoms on the graphene surface was extensively studied [34-36]. It was found that the interaction of alkali metal atoms with silicene is stronger than with graphene, and the adsorption of metal atoms leads to the metalization of silicene [37]. It was calculated that the adsorption of Li atoms results in the stabilization of the unstable distorted T-phase of MoS_2 [38]. In addition, Zr-based MXenes were found to be candidates as electrode materials for Li-ion batteries [39]. For applications in Li-ion batteries, a high coverage of Li atoms on a material is required. Due to its buckled large surface area, silicene seems to be a good candidate for Li-ion battery applications. Li adsorption on pristine silicene has been extensively studied in the last several years [40-46]. To the best of our knowledge, the adsorption characteristics of a Li atom on hydrogenated silicene are still unknown.

In the present paper, we study the diffusion and adsorption characteristics of a Li atom on recently synthesized hydrogenated forms of α- and β-silicene phases on a Ag(111) surface using ab initio calculations within density functional theory. The paper is organized as follows: Computational methodology, hydrogenated structures of the silicene phases on Ag(111) surface, and the diffusion and adsorption characteristics of Li are presented in the section "Results and Discussion". Lastly, we conclude our results in section "Conclusion".

Results and Discussion

Computational methodology

The present calculations were performed using density functional theory (DFT) and the projector-augmented wave (PAW) method, as implemented in the "Vienna ab initio Simulation Package" (VASP) [47,48]. The exchange–correlation energy was described by the generalized gradient approximation (GGA) using the Perdew–Burke–Ernzerhof (PBE) functional [49]. A plane-wave basis set with kinetic energy cutoff of 500 eV was used for all the calculations. The van der Waals (vdW) correction to the GGA functional was included by using the DFT-D2 method of Grimme [50].

To properly simulate the structures, a 3×3-reconstructed hydrogenated silicene phase was placed on top of a 4×4 supercell of a two-layer Ag(111) surface. A 3×3×1 Γ-centered *k*-point mesh was used for the Brillouin zone integration. The cohesive energy per atom was formulated as

$$E_{\text{coh}} = \left[n_{\text{Ag}} E_{\text{Ag}} + n_{\text{Si}} E_{\text{Si}} + n_{\text{H}} E_{\text{H}} - E_{\text{SL+Ag(111)}} \right] / N, \quad (1)$$

where E_{Ag}, E_{Si} and E_{H} denote the single-atom energy of atoms Ag, Si and H, respectively. n_{Ag}, n_{Si} and n_{H} are the number of Ag, Si, and H atoms contained in the unit cell, respectively. $E_{\text{SL+Ag(111)}}$ denotes the total energy of single-layer hydrogenated silicene and two-layer Ag(111). N is the number of total atoms contained in the unit cell.

Binding energies were calculated for the most favorable adsorption sites. Binding energies of the Li atom were calculated by using the formula

$$E_{\text{bind}} = E_{\text{SL+Ag(111)}} + E_{\text{Li}} - E_{\text{SL+Ag(111)+Li}}, \quad (2)$$

where E_{bind} is the binding energy of Li atom on the hydrogenated α- or β-silicene, $E_{SL+Ag(111)}$ is the energy of hydrogenated α- or β-silicene on a two-layer Ag(111) surface, E_{Li} denotes the energy of a single isolated Li atom, and $E_{SL+Ag(111)+Li}$ is the total energy of Li atom, single-layer hydrogenated silicene and two-layer Ag(111) surface.

Lattice constants and total energies were computed using the conjugate-gradient algorithm. The total energy difference between the sequential steps in the iterations was taken to be 10^{-5} eV for the convergence criterion. The total force in the unit cell was reduced to a value of less than 10^{-4} eV/Å. To hinder interactions between the adjacent cells, at least 12 Å vacuum space was used along the *z*-direction. All calculations were performed taking into account the spin-polarized case. Analysis of the charge transfers in the structures was determined by the Bader technique [51].

Hydrogenated α- and β-silicene on a Ag(111) surface

Scanning tunneling microscopy (STM) measurements revealed that hydrogenated silicene on Ag(111) surfaces exhibits two different perfectly ordered phases, which are hydrogenated α-(3×3)-silicene and hydrogenated β-(3×3)-silicene [30]. For simplicity, we name the hydrogenated α- and β-phases "H-α-Si" and "H-β-Si", respectively. Due to the existence of the Ag(111) surface, one side of silicene is accessible to hydrogenation. Previous studies showed that H atoms interact with the upper Si atoms of silicene and enhances the buckling of H-α-Si and H-β-Si [30]. Therefore, the structures of H-α-Si and H-β-Si do not exhibit significant differences to their pristine counterparts.

To determine how many layers of Ag (111) correctly simulate the supported α- and β-surfaces we examined the structural and electronic properties of these two phases on both two-layer and four-layer Ag(111) surfaces. As shown in Table 1, charge distribution and atomic distances are almost the same for both two layers and four layers. Therefore, it is reasonable to assume that characteristic properties of Ag(111)-supported silicene can be well simulated using two layers of Ag(111).

Table 1: The calculated silicene–substrate distance *d*, thickness of silicene and valence charges on upper-Si (ρ_u) and lower-Si (ρ_l) atoms of α-Si and β-Si on two-layer and four-layer Ag(111) surfaces.

	d (Å)	thickness of silicene (Å)	ρ_u/ρ_l (e^-)
α-Si/2L Ag(111)	2.40	0.80	3.9/4.0
α-Si/4L Ag(111)	2.41	0.77	3.9/4.0
β-Si/2L Ag(111)	2.40	0.67	3.9/4.0
β-Si/4L Ag(111)	2.42	0.70	3.9/4.0

Single layers of H-α-Si and H-β-Si are placed on two layers of a 4×4 supercell of Ag(111). While the bottom-layer atoms of Ag(111) are totally fixed, the upper-layer atoms are free to move. The optimized geometric structures of H-α-Si and H-β-Si on Ag(111) are shown in Figure 1a and Figure 1c, respectively. To better demonstrate the structures, the lower and upper Si atoms are shown by blue and red atoms, respectively. Grey and yellow atoms denote, respectively, Ag and H. As seen in Figure 1, H-α-Si and H-β-Si do not exhibit the conventional low-buckled structure of silicene. Our total energy calculations show that the cohesive energies of both phases are almost the same which indicates that both phases can exist at the same time. This is in good agreement with previous studies reporting the coexistence of α- and β-phases. Therefore, a detailed structural analysis of these two surfaces are important to clearly understand adsorption and diffusion characteristics of an adatom on these surfaces.

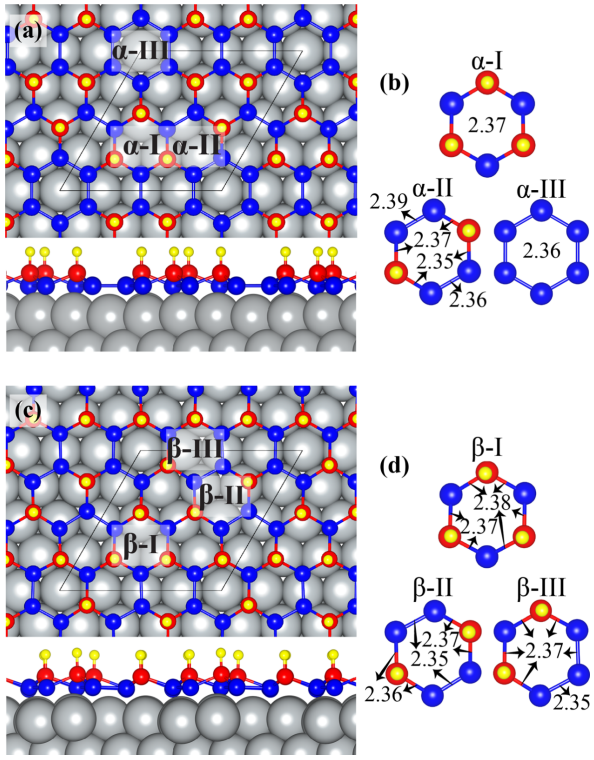

Figure 1: Top and side views of (a) H-α-Si and (b) its three different hexagonal units α-I, α-II, and α-III. Top and side views of (c) H-β-Si and (d) its three different hexagonal units β-I, β-II, and β-III. The 3×3 unitcells are represented by a black rhombus. Grey, blue, red, and yellow atoms show Ag, lower-Si, upper-Si, and H atoms, respectively.

Hexagonal units in the H-α-Si possess three different configurations, such as α-I, α-II, and α-III, which are shown in Figure 1b. α-I is similar to the low-buckled structure of pristine silicene the nearest silicene atoms of which are lower Si and upper Si

atoms. In this hexagonal unit, Si–Si bond distances are 2.37 Å. In α-II, there are two lower-Si-dimers that are placed opposite to each other. Si–Si bond lengths of two Si dimers are 2.36 Å and 2.39 Å. The bond distances between upper Si and lower Si atoms are 2.35 Å and 2.37 Å. α-III consists of six lower Si atoms. Si atoms in the α-III exhibit an almost planar structure with bond lengths of 2.36 Å. As a result, H-α-Si has six upper Si and twelve lower Si atoms. H atoms are placed at the top of the six upper Si atoms with a bond length of 1.51 Å. The cohesive energy of H-α-Si is 3.23 eV. The distance between lower Si atoms and the Ag(111) surface is about 2.07 Å.

Similar to H-α-Si, the H-β-Si structure also has three different hexagonal units, namely β-I, β-II, and β-III, which are shown in Figure 1d. β-I has a geometric structure similar to that of α-I. However, compared to α-I, the distances between lower Si and upper Si atoms are not the same and they are 2.37 Å and 2.38 Å. β-II has two lower-Si-dimers which are placed opposite to each other. Si–Si bond lengths of both lower Si dimers are 2.35 Å. The bond distances between upper Si and lower Si atoms are 2.36 Å to 2.37 Å. β-III has two neighboring lower Si dimers. Three Si atoms in these two neighboring Si dimers are almost in the same plane with bond lengths of 2.35 Å and 2.37 Å. The bond distances between upper Si and lower Si atoms are 2.37 Å. Consequently, unlike the H-α-Si, H-β-Si consists of seven upper Si and eleven lower Si atoms. H atoms are placed at the top of these seven upper Si atoms with a bond length of 1.51 Å. Because of the less symmetric atomic structure of H-β-Si the hexagonal units in H-β-Si are highly distorted. The cohesive energy of H-β-Si is 3.22 eV. The distance between lower Si atoms and the Ag(111) surface is about 2.16 Å. Therefore, one may expect quite different adsorption and diffusion characteristics of Li atoms on H-α-Si and H-β-Si.

Diffusion of a Li atom on hydrogenated α- and β-silicene

To understand how a Li atom adsorbs and migrates on H-α-Si and H-β-Si surfaces, total energy calculations are performed by placing a Li atom on 13 different points, which include the high-symmetry points. The distance between Li atom and surface is fully relaxed while the position of the Li atom parallel to the surface is kept fixed. During the adsorption, while Li and the nearest atoms to Li are fully relaxed, rest of atoms in the unit cell are fixed. Diffusion barriers are determined by setting the total energy of the most favorable site to zero. The most favorable binding sites are determined and their binding site, binding energy, height on the surface, the amount of charge transfer and energy barriers are given in Table 2.

Table 2: The calculated ground-state properties of a Li atom on H-α-Si and H-β-Si: binding site, binding energy, distance from adsorbed Li atom to the surface of H atoms Δ*h*, the amount of charge donated by the Li atom Δρ, and the energy barrier (relative to the binding site).

	binding site	binding energy (eV)	Δ*h* (Å)	Δρ (e^-)	energy barrier (meV)
Li/H-α-Si	6Si	2.79	−1.19	−1	768
Li/H-β-Si	3HSi′	2.82	0.07	−1	411

As shown in Figure 2a, four sites of 6Si, 2H, 2HT and 3H are considered as different binding sites for H-α-Si. Our calculations reveal that the most favorable site is 6Si, with the Si–Li bond length of 2.70 Å. In this binding site, Li atom binds with six lower Si atoms and the height of the Li atom is −1.19 Å lower than those of the H atoms. The binding energy of the Li atom on H-α-Si is 2.79 eV. Bader charge analysis shows that the Li atom donates $1e^-$ to H-α-Si. Since the Li atom does not prefer to bind to the vicinity of H atoms, the nearest adsorption site to 6Si is 2H. It is reasonable to assume that Li atoms diffuse through these two favorable adsorption sites. The diffusion barrier of a Li atom between these two nearest binding sites is 768 meV. However, once the Li atom overcomes the energy barrier, its diffusion through the other possible sites 2H, 2HT, and 3H (having energy barriers of 100–250 meV) is more likely. We also study diffusion of a second Li atom on H-α-Si

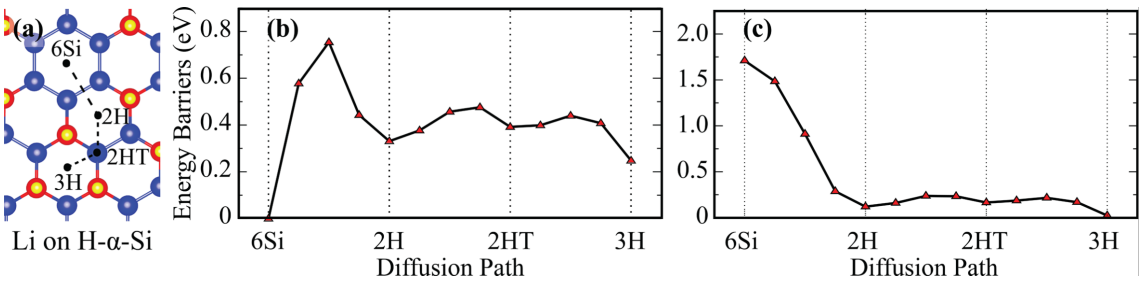

Figure 2: (a) Top view of possible adsorption sites for a Li atom on H-α-Si. Energy barrier graphs of (b) the first and (c) the second Li atom on H-α-Si. A possible diffusion path of a Li atom is illustrated by dashed black lines.

and the energy barrier graph of it is shown in Figure 2c. The most favorable site of the second Li atom is 3H and the nearest adsorption site to 3H is 2HT. The diffusion energy barrier of the second Li atom between 3H and 2HT sites is 193 meV, which is 575 meV lower than that of the first Li atom. Hence, after the 6Si sites are occupied by the first Li atoms, the diffusion of the second Li atoms occur through the other sites relatively easily. As a result, despite such a large diffusion energy barrier between two most favorable sites, diffusion of Li atoms on H-α-Si is still possible.

Five sites, namely 3HSi, 2HT′, 2H, 3H and 3HSi′ on H-β-Si are shown in Figure 3a. The most favorable site of a Li atom on this surface is 3HSi′. The Li atom is placed in the middle of three H atoms, and it is almost in the same plane with these H atoms. The bond distances from the Li atom to the three H atoms are 1.94 Å. Li atom binds to H-β-Si with a binding energy of 2.82 eV, which is ca. 30 meV higher than that on H-α-Si. Therefore, Li atoms bind to H-β-Si slightly more easier than to H-α-Si. On H-β-Si, the Li atoms forms an ionic bond and it donates 1 e^- to the surface. The nearest site to the most favorable site of 3HSi′ is 3H and this site is also energetically the second most favorable site. Thus, diffusion through these two favorable adsorption sites is most likely. The diffusion barrier of a Li atom on H-β-Si is 411 meV. Therefore, the energy barrier for the Li atom on H-β-Si is almost half of that on H-α-Si. As can be seen from Figure 3c, the 2HT′ site is the energetically most favorable site for the second Li atom on H-β-Si. The calculated diffusion energy barrier of the second Li atom between 2HT′ and 3HSi sites is 287 meV.

Contour plots of the energy barriers of a Li atom on H-α-Si and H-β-Si surfaces are shown in Figure 4a and Figure 4b, respectively. As seen from the figure, the energy differences for a Li atom on the H-β-Si surface are in a broader range than that on the H-α-Si surface. Diffusion of the Li atom around the favorable sites of H-β-Si is restricted because of high energy barriers around H atoms. In spite of the high diffusion barrier in H-α-Si, when Li atoms occupy all of the most favorable sites of 6Si, the following Li atoms on H-α-Si may diffuse more easily than on H-β-Si. The highest energy barriers seen by a Li atom are at the top of H atoms for both surfaces. These results suggest that a diffusing Li atom can follow a path of minimum energy barriers through the hydrogenated upper-Si atoms on both surfaces. In addition to the tops of the hydrogenated upper Si atoms, the tops of the lower Si atoms near to the 6Si site are also forbidden for Li atoms on H-α-Si.

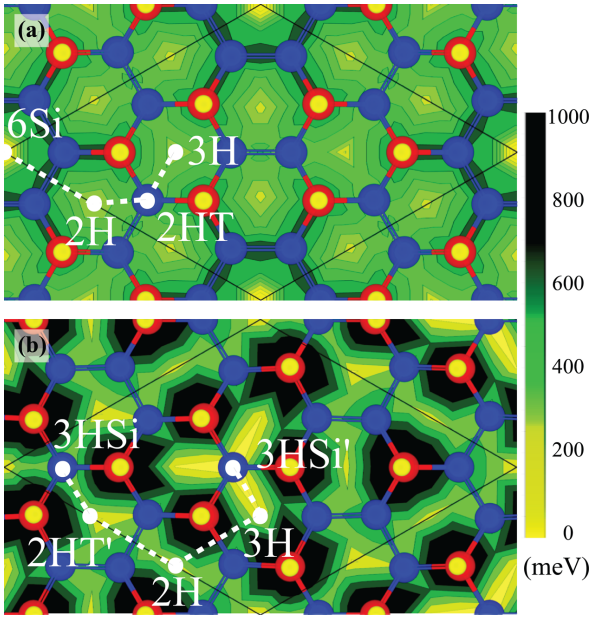

Figure 4: (Color online) Contour plots of the energy barriers (in meV) seen by Li atom adsorbed on (a) H-α-Si and (b) H-β-Si. Possible diffusion paths of Li on hydrogenated α and β silicene surfaces are illustrated by white dashed lines.

Conclusion

The adsorption properties and diffusion characteristics of a Li atom on single-layer hydrogenated silicene on a Ag(111) surface were investigated. Structural properties of recently synthe-

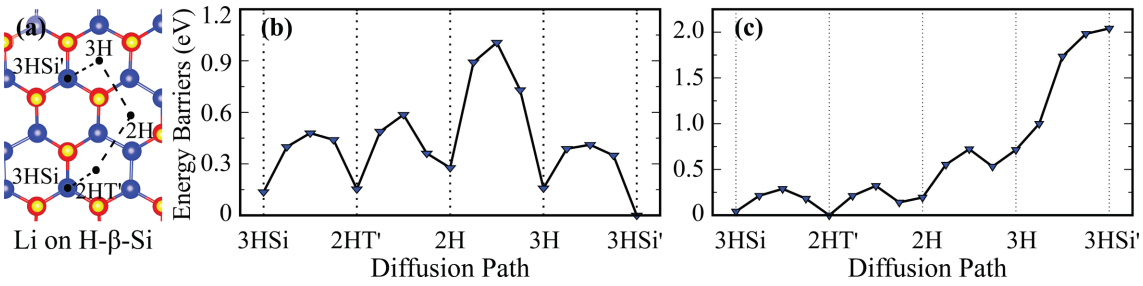

Figure 3: (a) Top view of possible adsorption sites for Li atom on H-β-Si. Energy barrier graphs of (b) the first and (c) the second Li atom on H-β-Si. A possible diffusion path of Li atom is illustrated by dashed black lines.

sized fully hydrogenated α- and β-silicene phases were investigated in detail. Our results showed that a single Li atom forms a strong ionic bond with H-α-Si and H-β-Si surfaces. The Li atom prefers to bind to the 3HSi′ site of H-β-Si with a binding energy of 2.82 eV. Due to the high diffusion energy barrier, a single Li atom is trapped at the 6Si site of H-α-Si, with a binding energy of 2.79 eV. However, when all the 6Si sites of H-α-Si are occupied, the diffusion barriers seen by Li atom decreases. Possible pathways of various diffusion processes of a Li atom were studied in detail. It was found that the Li atom does not prefer to bind in the vicinity of the hydrogenated upper-Si atoms on H-α-Si and H-β-Si. It is worth mentioning that H-α-Si surface is dominated by moderate energy regions, whereas the H-β-Si surface consists of partially convenient or forbidden regions for Li atom diffusion. High binding energies and relatively low diffusion barriers for a Li atom on H-α-Si and H-β-Si suggest that hydrogenated forms of α- and β-silicene are suitable materials for Li-ion batteries.

Acknowledgements

Computational resources were provided by TUBITAK ULAKBIM, High Performance and Grid Computing Center (TR-Grid e-Infrastructure). FI and CB acknowledge the support from TUBITAK project number 114F397. HS acknowledges financial support from the TUBITAK under the project number 116C073. HS acknowledges support from Bilim Akademisi-The Science Academy, Turkey under the BAGEP program.

References

1. Novoselov, K. S.; Geim, A. K.; Morozov, S. V.; Jiang, D.; Zhang, Y.; Dubonos, S. V.; Grigorieva, I. V.; Firsov, A. A. *Science* **2004,** *306,* 666–669. doi:10.1126/science.1102896
2. Geim, A. K.; Novoselov, K. S. *Nat. Mater.* **2007,** *6,* 183–191. doi:10.1038/nmat1849
3. Ci, L.; Song, L.; Jin, C.; Jariwala, D.; Wu, D.; Li, Y.; Srivastava, A.; Wang, Z. F.; Storr, K.; Balicas, L.; Liu, F.; Ajayan, P. M. *Nat. Mater.* **2010,** *9,* 430–435. doi:10.1038/nmat2711
4. Song, L.; Ci, L.; Lu, H.; Sorokin, P. B.; Jin, C.; Ni, J.; Kvashnin, A. G.; Kvashnin, D. G.; Lou, J.; Yakobson, B. I.; Ajayan, P. M. *Nano Lett.* **2010,** *10,* 3209–3215. doi:10.1021/nl1022139
5. Vogt, P.; De Padova, P.; Quaresima, C.; Avila, J.; Frantzeskakis, E.; Asensio, M. C.; Resta, A.; Ealet, B.; Le Lay, G. *Phys. Rev. Lett.* **2012,** *108,* 155501. doi:10.1103/PhysRevLett.108.155501
6. Cahangirov, S.; Topsakal, M.; Aktürk, E.; Şahin, H.; Ciraci, S. *Phys. Rev. Lett.* **2009,** *102,* 236804. doi:10.1103/PhysRevLett.102.236804
7. Spencer, M. J. S.; Morishita, T., Eds. *Silicene: structure, properties and applications;* Springer Series in Materials Science, Vol. 235; Springer: Berlin, Germany, 2016. doi:10.1007/978-3-319-28344-9
8. Dávila, M. E.; Xian, L.; Cahangirov, S.; Rubio, A.; Le Lay, G. *New J. Phys.* **2014,** *16,* 095002. doi:10.1088/1367-2630/16/9/095002
9. Wang, Q. H.; Kalantar-Zadeh, K.; Kis, A.; Coleman, J. N.; Strano, M. S. *Nat. Nanotechnol.* **2012,** *7,* 699–712. doi:10.1038/nnano.2012.193
10. Mak, K. F.; Lee, C.; Hone, J.; Shan, J.; Heinz, T. F. *Phys. Rev. Lett.* **2010,** *105,* 136805. doi:10.1103/PhysRevLett.105.136805
11. Ramasubramaniam, A. *Phys. Rev. B* **2012,** *86,* 115409. doi:10.1103/PhysRevB.86.115409
12. Çakır, D.; Sahin, H.; Peeters, F. M. *Phys. Chem. Chem. Phys.* **2014,** *16,* 16771–16779. doi:10.1039/C4CP02007C
13. Kang, J.; Sahin, H.; Peeters, F. M. *Phys. Chem. Chem. Phys.* **2015,** *17,* 27742–27749. doi:10.1039/C5CP04576B
14. Sahin, H.; Torun, E.; Bacaksiz, C.; Kang, J.; Senger, R. T.; Peeters, F. M. *Wiley Interdiscip. Rev.: Comput. Mol. Sci.* **2016,** *6,* 351–368. doi:10.1002/wcms.1252
15. Iyikanat, F.; Senger, R. T.; Peeters, F. M.; Sahin, H. *ChemPhysChem* **2016,** *17,* 3985–3991. doi:10.1002/cphc.201600751
16. Kang, J.; Sahin, H.; Ozaydin, H. D.; Senger, R. T.; Peeters, F. M. *Phys. Rev. B* **2015,** *92,* 075413. doi:10.1103/PhysRevB.92.075413
17. Liu, H.; Neal, A. T.; Zhu, Z.; Tomanek, D.; Ye, P. D. *arXiv* **2014,** No. 1401.4133.
18. Cai, H.; Kang, J.; Sahin, H.; Chen, B.; Suslu, A.; Wu, K.; Peeters, F.; Meng, X.; Tongay, S. *Nanotechnology* **2016,** *27,* 065203. doi:10.1088/0957-4484/27/6/065203
19. Liu, C.-C.; Feng, W.; Yao, Y. *Phys. Rev. Lett.* **2011,** *107,* 076802. doi:10.1103/PhysRevLett.107.076802
20. Lin, C.-L.; Arafune, R.; Kawahara, K.; Tsukahara, N.; Minamitani, E.; Kim, Y.; Takagi, N.; Kawai, M. *Appl. Phys. Express* **2012,** *5,* 045802. doi:10.1143/APEX.5.045802
21. Meng, L.; Wang, Y.; Zhang, L.; Du, S.; Wu, R.; Li, L.; Zhang, Y.; Li, G.; Zhou, H.; Hofer, W. A.; Gao, H.-J. *Nano Lett.* **2013,** *13,* 685–690. doi:10.1021/nl304347w
22. Fleurence, A.; Friedlein, R.; Ozaki, T.; Kawai, H.; Wang, Y.; Yamada-Takamura, Y. *Phys. Rev. Lett.* **2012,** *108,* 245501. doi:10.1103/PhysRevLett.108.245501
23. Liu, H.; Gao, J.; Zhao, J. *J. Phys. Chem. C* **2013,** *117,* 10353–10359. doi:10.1021/jp311836m
24. Johnson, N. W.; Vogt, P.; Resta, A.; De Padova, P.; Perez, I.; Muir, D.; Kurmaev, E. Z.; Le Lay, G.; Moewes, A. *Adv. Funct. Mater.* **2014,** *24,* 5253–5259. doi:10.1002/adfm.201400769
25. Tao, L.; Cinquanta, E.; Chiappe, D.; Grazianetti, C.; Fanciulli, M.; Dubey, M.; Molle, A.; Akinwande, D. *Nat. Nanotechnol.* **2015,** *10,* 227–231. doi:10.1038/nnano.2014.325
26. Houssa, M.; Scalise, E.; Sankaran, K.; Pourtois, G.; Afanas'Ev, V. V.; Stesmans, A. *Appl. Phys. Lett.* **2011,** *98,* 223107. doi:10.1063/1.3595682
27. Zhang, C.-w.; Yan, S.-s. *J. Phys. Chem. C* **2012,** *116,* 4163–4166. doi:10.1021/jp2104177
28. Huang, B.; Deng, H.-X.; Lee, H.; Yoon, M.; Sumpter, B. G.; Liu, F.; Smith, S. C.; Wei, S.-H. *Phys. Rev. X* **2014,** *4,* 021029. doi:10.1103/PhysRevX.4.021029
29. Qiu, J.; Fu, H.; Xu, Y.; Oreshkin, A. I.; Shao, T.; Li, H.; Meng, S.; Chen, L.; Wu, K. *Phys. Rev. Lett.* **2015,** *114,* 126101. doi:10.1103/PhysRevLett.114.126101
30. Beato Medina, D.; Salomon, E.; Lay, G. L.; Angot, T. *Electron Spectrosc. Relat. Phenom* **2016,** in press. doi:10.1016/j.elspec.2016.11.002
31. Lee, R. S.; Kim, H. J.; Fischer, J. E.; Thess, A.; Smalley, R. E. *Nature* **1997,** *388,* 255–257. doi:10.1038/42206
32. Rao, A. M.; Eklund, P. C.; Bandow, S.; Thess, A.; Smalley, R. E. *Nature* **1997,** *388,* 257–259. doi:10.1038/40827
33. Chen, P.; Wu, X.; Lin, J.; Tan, K. L. *Science* **1999,** *285,* 91–93. doi:10.1126/science.285.5424.91

34. Profeta, G.; Calandra, M.; Mauri, F. *Nat. Phys.* **2012,** *8,* 131–134. doi:10.1038/nphys2181
35. Zhou, J.; Sun, Q.; Wang, Q.; Jena, P. *Phys. Rev. B* **2014,** *90,* 205427. doi:10.1103/PhysRevB.90.205427
36. Liu, M.; Kutana, A.; Liu, Y.; Yakobson, B. I. *J. Phys. Chem. Lett.* **2014,** *5,* 1225–1229. doi:10.1021/jz500199d
37. Sahin, H.; Peeters, F. M. *Phys. Rev. B* **2013,** *87,* 085423. doi:10.1103/PhysRevB.87.085423
38. Nasr Esfahani, D.; Leenaerts, O.; Sahin, H.; Partoens, B.; Peeters, F. M. *J. Phys. Chem. C* **2015,** *119,* 10602–10609. doi:10.1021/jp510083w
39. Zhu, J.; Chroneos, A.; Eppinger, J.; Schwingenschlögl, U. *Appl. Mater. Today* **2016,** *5,* 19. doi:10.1016/j.apmt.2016.07.005
40. Guo, G.; Mao, Y.; Zhong, J.; Yuan, J.; Zhao, H. *Appl. Surf. Sci.* **2017,** *406,* 161. doi:10.1016/j.apsusc.2017.02.053
41. Tritsaris, G. A.; Kaxiras, E.; Meng, S.; Wang, E. *Nano Lett.* **2013,** *13,* 2258–2263. doi:10.1021/nl400830u
42. Setiadi, J.; Arnold, M. D.; Ford, M. J. *ACS Appl. Mater. Interfaces* **2013,** *5,* 10690–10695. doi:10.1021/am402828k
43. Osborn, T. H.; Farajian, A. A. *J. Phys. Chem. C* **2012,** *116,* 22916–22920. doi:10.1021/jp306889x
44. Yuan, J.; Tang, C.; Zhong, J.; Mao, Y. *Appl. Surf. Sci.* **2016,** *360, Part B,* 707. doi:10.1016/j.apsusc.2015.11.050
45. Zhu, J.; Chroneos, A.; Schwingenschlögl, U. *Nanoscale* **2016,** *8,* 7272–7277. doi:10.1039/C6NR00913A
46. Zhuang, J.; Xu, X.; Peleckis, G.; Hao, W.; Dou, S. X.; Du, Y. *Adv. Mater.* **2017,** 1606716. doi:10.1002/adma.201606716
47. Kresse, G.; Hafner, J. *Phys. Rev. B* **1993,** *47,* 558. doi:10.1103/PhysRevB.47.558
48. Kresse, G.; Furthmüller, J. *Phys. Rev. B* **1996,** *54,* 11169. doi:10.1103/PhysRevB.54.11169
49. Perdew, J. P.; Burke, K.; Ernzerhof, M. *Phys. Rev. Lett.* **1996,** *77,* 3865. doi:10.1103/PhysRevLett.77.3865
50. Grimme, S. *J. Comput. Chem.* **2006,** *27,* 1787–1799. doi:10.1002/jcc.20495
51. Henkelman, G.; Arnaldsson, A.; Jónsson, H. *Comput. Mater. Sci.* **2006,** *36,* 354–360. doi:10.1016/j.commatsci.2005.04.010

License and Terms

BEILSTEIN JOURNAL OF NANOTECHNOLOGY

α-Silicene as oxidation-resistant ultra-thin coating material

Ali Kandemir[*1], Fadil Iyikanat[2], Cihan Bacaksiz[2] and Hasan Sahin[*3,4]

Full Research Paper

Open Access

Address:
[1]Department of Materials Science and Engineering, Izmir Institute of Technology, 35430, Izmir, Turkey, [2]Department of Physics, Izmir Institute of Technology, 35430, Izmir, Turkey, [3]Department of Photonics, Izmir Institute of Technology, 35430, Izmir, Turkey and [4]ICTP-ECAR Eurasian Center for Advanced Research, Izmir Institute of Technology, 35430, Izmir, Turkey

Email:
Ali Kandemir* - alikandemir@iyte.edu.tr; Hasan Sahin* - hasansahin@iyte.edu.tr

* Corresponding author

Keywords:
coating material; density functional theory; oxidization; silicene, silver

Beilstein J. Nanotechnol. **2017,** *8,* 1808–1814.
doi:10.3762/bjnano.8.182

Received: 11 March 2017
Accepted: 16 August 2017
Published: 31 August 2017

This article is part of the Thematic Series "Silicene, germanene and other group IV 2D materials".

Guest Editor: P. Vogt

Abstract

By performing density functional theory (DFT)-based calculations, the performance of α-silicene as oxidation-resistant coating on Ag(111) surface is investigated. First of all, it is shown that the Ag(111) surface is quite reactive against O atoms and O_2 molecules. It is known that when single-layer silicene is formed on the Ag(111) surface, the 3 × 3-reconstructed phase, α-silicene, is the ground state. Our investigation reveals that as a coating layer, α-silicene (i) strongly absorbs single O atoms and (ii) absorbs O_2 molecules by breaking the strong O–O bond. (iii) Even the hollow sites, which are found to be most favorable penetration path for oxygens, serves as high-energy oxidation barrier, and (iv) α-silicene becomes more protective and less permeable in the presence of absorbed O atom. It appears that single-layer silicene is a quite promising material for ultra-thin oxidation-protective coating applications.

Introduction

Surface protection against degradation of a material due to a reaction with its environment has attracted intensive attention of researchers for decades. In order to prevent the loss of important properties (such as conductivity, reflectivity, and mechanical and thermal resistance) of a material, surface protection has been vital nearly for all application areas. As a well-known mechanism of electrochemical corrosion, the formation of rust is an un-solicited reaction between a metal and oxygen. For that reason, protection of surfaces from oxygen has become an important field. Although macroscale and microscale coatings have been used intensively in surface protection for a long time [1,2], two-dimensional (2D) materials have become new candidates for nanoscale coatings for different material groups. Therefore, coating mechanisms at the nanoscale take are of high interest in nanotechnology, and new candidates for nanostructural protection are needed to be understood in detail.

Due to its extraordinary structural and electrical properties, graphene as 2D material has garnered huge interest in nearly all science branches [3,4]. Because of the high impermeability, graphene has also been thought as a corrosion-protection barrier [5-7]. Kirkland et al. investigated the electrochemical response

of graphene-coated metal surfaces and found that graphene causes reduction in the corrosion rate [8]. In addition, Topsakal et al. showed that graphene is a suitable coating material to protect surfaces from oxidation by performing DFT-based calculations [9]. Bulk forms of transition-metal dichalcogenides (TMDs) are well-known coating materials, and the respective 2D TMDs can be used as surface protection. In addition, MoS_2 is one of the most widely used lubricant coating material [10]. Theoretical and experimental studies have demonstrated that single-layer MoS_2 and single layer $W(S/Se)_2$ can be used as a protective nanocoating material [11-14].

One of the most challenging members of the 2D material family is silicene [15-19], the silicon analogue of graphene. After theoretical prediction [18], silicene was synthesized [19] on a silver surface in the 3 × 3-reconstructed α-form. Differing from graphene, silicene exhibits low buckling in which atoms in the different sub-lattices are shifted oppositely in the out-of-plane direction. The buckled structure of silicene forms perfect sites to capture oxygen atoms. It is known that silicon atoms tend to bond oxygen atoms strongly and form various stable oxidized silicon structures. Therefore, silicene can be a potential coating material for protection at the nanoscale.

On the other hand, silver is being used in our daily life in jewelry, silverware, decorative objects and electronics. Although the oxidation of silver forms thin layer of Ag_2O, which protects from more oxygen diffusion into silver surface, it is an undesirable reaction. Previous studies have shown that oxidation of silver surfaces leads to increase in work function, color change and significant deterioration of surface quality [20,21]. For that reason, coating of silver for protection to oxidation is needed.

In this study, we examined the coating performance of α-silicene against oxidation on the most preferable substrate metal for silicene, silver. In first step, we studied the adsorption of an oxygen atom and an oxygen molecule on bare silver with ⟨111⟩ growth direction because silicene has been synthesized on Ag(111) substrates [19]. Then, the adsorption of the oxygen atom/molecule on α-silicene over Ag(111) was investigated. It was shown that α-silicene is quite reactive regarding oxidation. In addition, we focused on oxidation scenario of silver in the presence of α-silicene. A large energy barrier for oxidation was obtained by performing indentation calculations. In conclusion, it was found silicene exhibits good performance in the protection of a Ag(111) surface against oxidation.

Results and Discussion

Computational methodology

To obtain the preferable crystal structure of α-silicene on Ag(111), four-layer Ag(111) composed of two fixed bottom layers and two free upper layers, was prepared as supercell structure with dimensions of 4 × 4 × 1. Thus, the surface of silver successfully simulated with and without silicene on top of Ag(111). First principles calculations were performed using the Vienna ab initio simulation package (VASP) [22,23], which is based on density functional theory. The projector-augmented wave (PAW) [24,25] formalism was used in the calculations. For the exchange–correlation energy, the generalized gradient approximation of the Perdew–Burke–Ernzerhof (GGA-PBE) [26] functional was used in conjunction with a semi-empirical scheme for including van der Waals (vdW) interaction dispersive forces developed by Grimme [27]. The structural relaxations were performed with a plane wave cut-off energy of at 500 eV. A 3 × 3 × 1 *k*-point mesh was used for the structural relaxation. The criterion of convergence of energy was chosen as 10^{-5} eV between two ionic steps, and the maximum force allowed on each atom is 0.1 meV/Å. At least 13 Å of vacuum were applied along *z*-direction to hinder interactions between the adjacent cells.

Oxidation of the bare Ag surface

Because the buckled structure of silicene grows sleekly on a silver surface, one may expect unique and enhanced coating

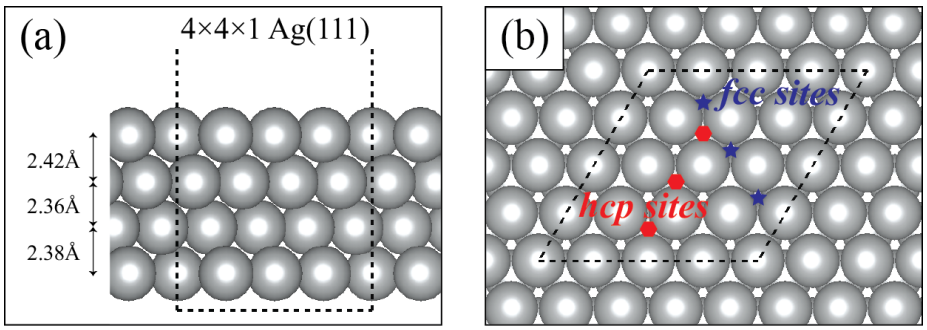

Figure 1: (a) Side view of the Ag(111) supercell structure and (b) top view of the Ag(111) supercell structure with possible oxygen captured sites. Definitions and oxygen binding energies of all sites are given in Table 1.

performance against oxidation. As shown in Figure 1, we first investigate how strongly an oxygen atom and an oxygen molecule interact with possible sites on the Ag(111) surface. Two sites were found to be preferable locations for oxygen atoms on the Ag(111) surface, the hcp and fcc hollow sites. These sites are shown in Figure 1b.

Figure 2a and Figure 2b show how an oxygen atom is adsorbed at the silver surface at the hcp and fcc hollow sites, respectively. The binding energy of single oxygen on the Ag(111) surface is about 3.9 eV. The energy difference between sites is only 110 meV. It is seen that silver surface strongly captures single oxygen atoms. Oxygen in fcc site forms a bond distance with neighbor silver atoms of about 2.14 Å. The presence of oxygen causes a distortion of about 9.8% and pushes neighbor atoms in this site. Although oxygen at a hcp site has the same bond distance with neighbor atoms as at the fcc site, the presence of oxygen causes distortion of about 8.9% at the hcp site. It appears that, absence of the lower silver atom at the fcc site results in a deeper penetration of the oxygen atom than at the hcp site.

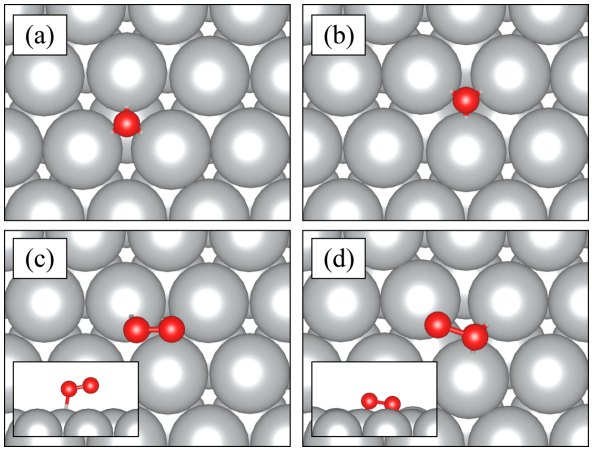

Figure 2: Top view of Ag(111) geometric structures after capturing an oxygen atom and an O_2 molecule. (a) hcp hollow site and (b) fcc hollow site for oxygen, (c) magnetic and (d) nonmagnetic O_2 molecule adsorption on Ag(111). The insets in panel (c) and panel (d) show the bonding characteristics of O_2 molecule.

Compared to a single oxygen atom, the O_2 molecule behaves differently on a bare silver surface. Figure 2c and Figure 2d) show how the O_2 molecule interacts with the silver surface. Magnetic and nonmagnetic states of O_2 molecule are observed while oxygen is captured at the silver surface. In the magnetic state, only one of the oxygens come closer to the surface. In the other case, both oxygen atoms come closer to the surface. In both cases, the binding energies are ca. 200 meV. Therefore, it is seen that O_2 molecule tends to bind to the silver surface. In the magnetic state, the oxygen–oxygen distance is around 1.26 Å, which is close to oxygen–oxygen distance in an oxygen molecule in the vacuum state. In the nonmagnetic state, the oxygen–oxygen distance is around 1.41 Å. The silver surface weakens the oxygen–oxygen bond in the nonmagnetic system. In addition, the distance between oxygen and silver is nearly the same as the distance between a single oxygen atom and silver distance, which is 2.14 Å. Similar to adsorption of a single atom, the oxygen molecule distorts silver surface at that site. Therefore, the oxygen–oxygen bond can be broken through a thermally induced process and the silver surface can exhibit oxygen atoms.

Oxidation of the silicene-coated Ag surface

In this section, the silicene-coated Ag(111) surface is investigated. We consider the experimentally realized structure of silicene on Ag(111), α-silicene [19]. Albeit with a different notation, it was also shown that α-silicene is the thermodynamically favorable phase under a wide range of conditions [17]. Differing from the theoretical predicted simply buckled silicene, α-silicene has a 3 × 3-reconstruction in which six silicon atoms form a sub-layer over the other twelve silicon atoms in the supercell as shown in Figure 3. Blue and turquoise atoms repre-

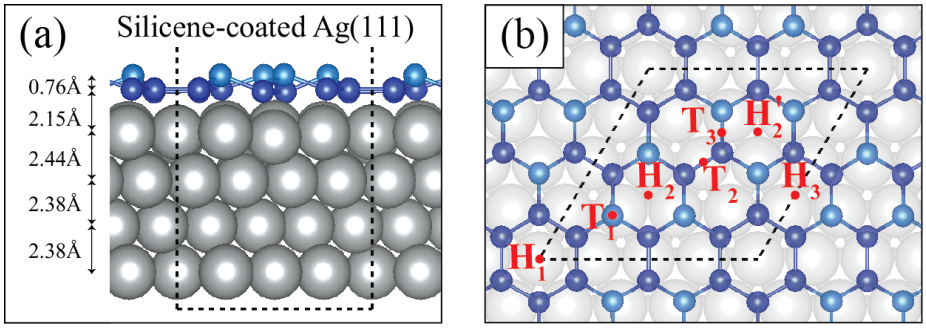

Figure 3: (a) Side view of the silicene-coated Ag(111) supercell structure and (b) top view of the silicene-coated Ag(111) supercell structure with possible oxygen-capture sites. Definitions and oxygen binding energies of all sites are given in Table 1.

sent the lower and upper Si atoms respectively. In the presence of silicene, the interlayer distance of the uppermost Ag layers are slightly changing and the distance between Ag surface and silicene is found to be ca. 2.15 Å.

In Figure 3b, possible sites for oxygen on silicene-coated Ag(111) are demonstrated. There are six possible sites due to symmetry in silicene-coated Ag(111). These sites are named according to hollow and top sites of neighboring silicon atoms in the buckled silicene structure. H_xs are for hollow sites, T_xs are for top sites. The definition of sites can be found in Table 1 in detail. These six possible sites reflect all possible final configurations in the system. Table 1 shows the oxygen binding energy of all possible sites for silicene-coated Ag(111).

Silicene captures oxygen with a binding energy range of 5.8–6.5 eV. Compared to silver, silicene has a higher tendency to bind to oxygen. Figure 4 shows the oxygen–silicene bonding characteristics when the system reaches its local lowest energy. The least preferable sites for oxygen on silicene-coated Ag(111) are the sites where the highest distortion occurs and where oxygen has a low interaction with silicon atoms, namely H_2, H_3 and T_1. On the other hand, the sites with the lowest distortion are the most preferable sites for oxygen on silicene-coated Ag(111), namely T_2, H_1 and T_3 in the order from the lowest to the highest binding energy. The final configurations of T_2 and H_1 with oxygen presence seem to be equivalent. Oxygen binds to a lower silicon atoms, but the difference lies in the fact that the upper silicon atoms in T_2 allow for more freedom and oxygen can take a position between them. Whereas, six lower silicon atoms tend to retain their hexagonal configuration and the oxygen atom finds itself in an upper-site position between two silicon atoms. The absence of a silicon–silicon bond in the T_2 configuration results in a difference of 180 meV. The highest

Table 1: Binding energies of O/O_2 on Ag(111) and silicene-coated Ag(111). Ag refers to the Ag(111) surface, Si/Ag refers to silicene-coated Ag.

system	site	name	binding energy (eV)	Δ_{BE} (meV)
O@Ag	fcc	cubic close-packed hollow site	3.90	—
	hcp	hexagonal close-packed hollow site	3.79	110
O@Si/Ag	H_1	site between six lower silicon atoms	6.45	70
	T_1	top site of upper silicon atom	5.78	740
	H_2	site between three upper and three lower silicon atoms	6.00	520
	T_2	top site between two lower silicon atoms	6.27	250
	T_3	top site between one upper and one lower silicon atom	6.52	—
	H_3	site between four lower and two upper silicon atoms	5.84	680
O_2@Ag	mag	magnetic O_2 molecule on the surface	0.21	—
	n-mag	non-magnetic O_2 molecule on the surface	0.19	20
O_2@Si/Ag	in-S	O_2 molecule inside silicene	6.70	—
	top-S	O_2 molecule on top of silicene	2.06	4640

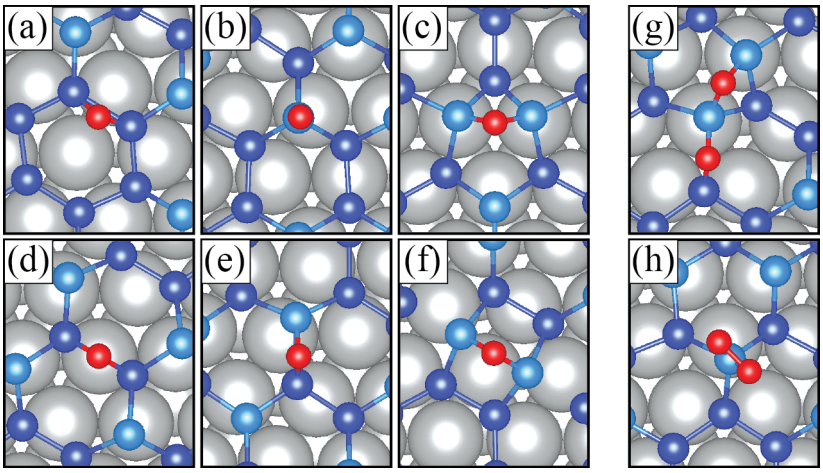

Figure 4: Final configurations of silicene-coated Ag(111) after capturing an oxygen atom at the sites (a) H_1, (b) T_1, (c) H_2, (d) T_2, (e) T_3 and (f) H_3. Final configurations (g) in-S and (h) top-S of silicene-coated Ag(111) after capturing an O_2 molecule.

binding energy is calculated for T_3 site. In this configuration, the oxygen atom enters a top-site position between upper and a lower silicon atoms. In this position, the lowest distortion occurs in the system so that oxygen binds with a high energy and leads to formation of an energetically favorable final configuration.

In the case of the O_2 molecule, there are two final configurations, "in-S" and "top-S", to be formed at the most favorable oxygen-capture sites. Figure 4g and Figure 4h show the in-S and top-S configurations, respectively. It is shown that silicon and oxygen strongly interact with each other (Table 1). SiO_2 is one of the most stable compounds in nature. Therefore, silicon tends to bind two oxygen atoms in the form of SiO_2 as depicted in Figure 4h. However, the energetically favorable configuration is the one in which oxygen atoms take separate positions between the silicon atoms (Figure 4g). In contrast to the other configuration, the silicon atoms in silicene can pluck the O_2 molecule and are allowed to diffuse in the system. This promises a good oxidation barrier for the silver surface.

Oxidation of the Ag surface in the presence of silicene coating

To investigate the application of silicene as an oxidation barrier, indentation calculations with oxygen were performed. Since O atoms and O_2 molecules strongly interact with silicene, the diffusion of O/O_2 in the lateral direction is not possible and the hollow sites of the hexagonal lattice are the only possible sites for the penetration into the structure. Therefore, the hollow sites are considered for the indentation simulation. There are four different hollow sites in the silicene structure on Ag(111), as shown in Figure 3b. The sites are denoted as H_1, H_2, H_2' and H_3. H_2 and H_2' sites coincide to the fcc and hcp sites of the Ag(111) surface, respectively.

For the indentation calculations, a single oxygen atom is placed in the middle of a hollow site. Calculations are performed as follows: First, the oxygen atom is kept at a distance of about 10 Å from the Ag surface (ca. 8 Å to the silicene surface) and is approached to the surface in 1.0 Å steps. When the oxygen atom interacts with silicene, the step size is reduced to 0.5 Å. In Figure 5, the change of the total energy as a function of the vertical distance between oxygen atom and Ag surface is given for the different hollow sites. The barrier energies (E_{br}), which are defined as the amount of energy needed for an oxygen atom to pass through a hollow site, are also shown in Figure 5. From lowest to highest, the values of E_{br} for H_1, H_2, H_2' and H_3 are found to be 1.66, 1.82, 1.85 and 1.99 eV, respectively. The H_3 hollow site has the highest energy barrier among all sites. At first, a fixed single oxygen atom attracts two upper silicon atoms to form one of the highly stable configurations. For that reason, the lowest ground-state energy occurs in this hollow site. While the single oxygen atom approaches the Ag surface, a barrier occurs up to ca. 2.5 Å where oxygen passes through hollow site exactly from upper site of silicene to the lower site of silicene. As seen in Figure 5, this also happens at the H_2, H_2' and H_3 hollow sites. H_2 and H_2' are similar hollow sites. There is a small difference, ca. 30 meV, in energy barrier at these hollow sites. The lowest energy barrier, 1.66 eV, is seen in the H_1 hollow site. Due to the planar structure of the silicon atoms at the H_1 site, it is the most suitable hollow site for an oxygen atom to pass through silicene. Since the H_1 hollow site has the lowest barrier energy, the side view of the structure for different distances is shown in the inset of Figure 5. At about 5 Å, the single oxygen atom pulls and binds one of the lower silicon atoms. Because further penetration of oxygen is not favorable at that distance from the Ag surface, a small local minimum occurs. Then, the other lower silicon atom binds the oxygen and the energy is lowered further. Due to the larger void size in the H_1 hollow site than in the other hollow sites, it is easy to pass for the oxygen atom from the upper surface of silicene to the lower surface. At a distance of around 2.0 Å, the barrier has a different value than at the other hollow sites, because of the planar formation of the lower silicon atoms and also because of the larger void of the H_1 hollow site.

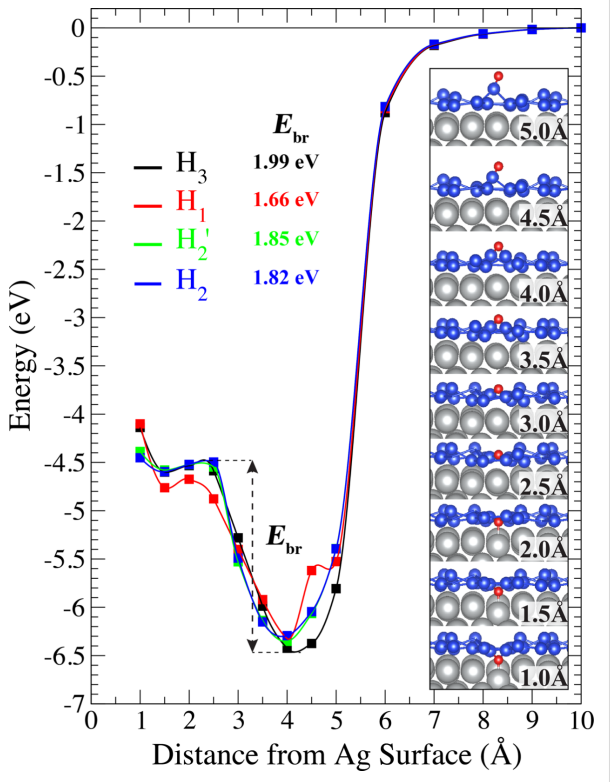

Figure 5: Indentation of an oxygen atom at different hollow sites. E_{br} is the energy barrier the oxygen atom needs to pass inside the silicene environment. Inset graph shows the oxygen progression in H_1.

H_1 is more permeable for oxygen atoms than other hollow sites. Hence, the indentation calculations for the O_2 molecule are performed at the H_1 site. One oxygen atom of the O_2 molecule is fixed, the other non-restricted oxygen follows the fixed oxygen naturally. The oxygen molecule is moved closer to the Ag surface step by step from a distance of 10 Å via the fixed oxygen atom. The indentation process is shown with a small step size after the oxygen atom is captured by a silicon atom (Figure 6). There is a local-minimum state in which oxygen is still in the molecule form (see inset graphs in Figure 6), far from the Ag surface at a distance of about 4.5 Å. While the indentation of the O_2 molecule continues, the energy increases up to some point. At distances below 3.8 Å, a sudden decrease in energy is seen. The inset graphs in Figure 6 show that the deterioration of the O_2 molecule happens due to a strong interaction between oxygen and silicon atoms and after that silicene-coated silver system reaches a global-minimum state. The figure shows that the dissociation of the oxygen molecule is favorable and requires ca. 300 meV to exceed the energy barrier of transition. Since the H_1 hollow site is the most permeable site, the maximum value of the transition energy barrier converges to ca. 300 meV. Two possible configurations, in-S and top-S (Figure 4g,h), are observed. The difference of those two minimum-energy states is similar (Table 1). In addition, oxidized silicene does not allow for a further indentation of a single oxygen atom. The locally forming silicon oxide structure attracts oxygen atoms more strongly. A local-minimum state as in FigureFigure 5 is not found between silicene and the Ag surface. Therefore, silicene becomes less permeable and more protective with increasing number of oxygen atoms. Our findings are consistent with the recent studies of oxidized silicene [28,29], which observed non-oxidized metal surfaces after the oxidation of silicene on metal substrates. One may claim that silicene retains its extreme reactivity to oxygen atoms even after forming localized silicon-oxide structures. As a result, silicene has great potential to capture unwanted atoms and to protect the metal surface.

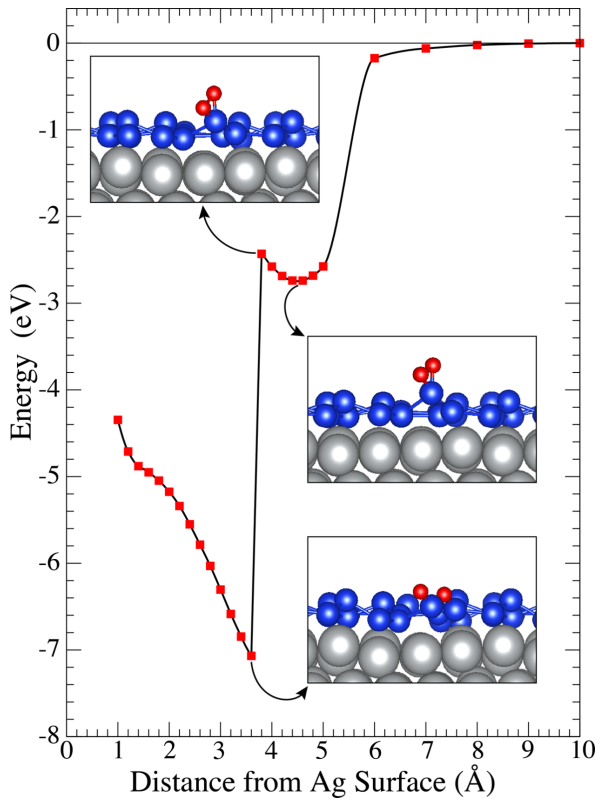

Figure 6: Indentation calculations for an O_2 molecule. Inset graphs show structures according to local-minimum states of O_2, before and after reaching the global minimum state of the system.

Conclusions

In this study, we performed first principles calculations to investigate the oxidation properties of α-silicene as a coating material on Ag(111). It was found that an O_2 molecule interact with the Ag surface with a low binding energy, while a single oxygen atom interact strongly with the surface. The silicene coating on Ag surface was demonstrated as protective material from oxidation. In particular, large binding energies between a single oxygen atom and silicene were calculated for the possible adsorption sites. This strong interaction can break the oxygen–oxygen bond as well. Moreover, the energy barriers for the oxygen atom between silicene and Ag surface are quite high and sufficient for the protection of the metal surface. Indentation calculations of the O_2 molecule showed that the molecule dissociates in the vicinity of silicene. It is also seen that an increase in oxygen atoms makes silicene more protective and silicene does not allow oxygen to pass to the metal surface. In conclusion, silicene has been proven itself as oxidation-resistant nanocoating material.

Acknowledgements

The calculations were performed at TUBITAK ULAKBIM, High Performance and Grid Computing Center (TR-Grid e-Infrastructure). H.S. acknowledges financial support from the TUBITAK under the project number 116C073. H.S. acknowledges support from Bilim Akademisi-The Science Academy, Turkey under the BAGEP program.

References

1. Sørensen, P. A.; Kiil, S.; Dam-Johansen, K.; Weinell, C. E. *J. Coat. Technol. Res.* **2009,** *6,* 135–176. doi:10.1007/s11998-008-9144-2
2. Gray, J. E.; Luan, B. *J. Alloys Compd.* **2002,** *336,* 88. doi:10.1016/S0925-8388(01)01899-0
3. Novoselov, K. S.; Geim, A. K.; Morozov, S. V.; Jiang, D.; Zhang, Y.; Dubonos, S. V.; Grigorieva, I. V.; Firsov, A. A. *Science* **2004,** *306,* 666–669. doi:10.1126/science.1102896

4. Geim, A. K.; Novoselov, K. S. *Nat. Mater.* **2007,** *6,* 183–191. doi:10.1038/nmat1849
5. Chen, S.; Brown, L.; Levendorf, M.; Cai, W.; Ju, S.-Y.; Edgeworth, J.; Li, X.; Magnuson, C. W.; Velamakanni, A.; Piner, R. D.; Kang, J.; Park, J.; Ruoff, R. S. *ACS Nano* **2011,** *5,* 1321–1327. doi:10.1021/nn103028d
6. Bunch, J. S.; Verbridge, S. S.; Alden, J. S.; van der Zande, A. M.; Parpia, J. M.; Craighead, H. G.; McEuen, P. L. *Nano Lett.* **2008,** *8,* 2458–2462. doi:10.1021/nl801457b
7. Böhm, S. *Nat. Nanotechnol.* **2014,** *9,* 741–742. doi:10.1038/nnano.2014.220
8. Kirkland, N. T.; Schiller, T.; Medhekar, N.; Birbilis, N. *Corros. Sci.* **2012,** *56,* 1. doi:10.1016/j.corsci.2011.12.003
9. Topsakal, M.; Şahin, H.; Ciraci, S. *Phys. Rev. B* **2012,** *85,* 155445. doi:10.1103/PhysRevB.85.155445
10. Winer, W. O. *Wear* **1967,** *10,* 422. doi:10.1016/0043-1648(67)90187-1
11. Sen, H. S.; Sahin, H.; Peeters, F. M.; Durgun, E. *J. Appl. Phys.* **2014,** *116,* 083508. doi:10.1063/1.4893790
12. Santosh, K. C.; Longo, R. C.; Wallace, R. M.; Cho, K. *J. Appl. Phys.* **2015,** *117,* 135301. doi:10.1063/1.4916536
13. Dixit, S.; Popat, P. P.; Rawat, S. S.; Sivarajan, S. *Indian J. Sci. Technol.* **2016,** *9*.
14. Domínguez-Meister, S.; Rojas, T. C.; Brizuela, M.; Sánchez-López, J. C. *Sci. Technol. Adv. Mater.* **2017,** *18,* 122–133. doi:10.1080/14686996.2016.1275784
15. Zhao, J.; Liu, H.; Yu, Z.; Quhe, R.; Zhou, S.; Wang, Y.; Liu, C. C.; Zhong, H.; Han, N.; Lu, J.; Yao, Y.; Wu, K. *Prog. Mater. Sci.* **2016,** *83,* 24. doi:10.1016/j.pmatsci.2016.04.001
16. Liu, H.; Feng, H.; Du, Y.; Chen, J.; Wu, K.; Zhao, J. *2D Mater.* **2016,** *3,* 025034. doi:10.1088/2053-1583/3/2/025034
17. Liu, H.; Han, N.; Zhao, J. *Appl. Surf. Sci.* **2017,** *409,* 97. doi:10.1016/j.apsusc.2017.03.007
18. Cahangirov, S.; Topsakal, M.; Aktürk, E.; Şahin, H.; Ciraci, S. *Phys. Rev. Lett.* **2009,** *102,* 236804. doi:10.1103/PhysRevLett.102.236804
19. Vogt, P.; De Padova, P.; Quaresima, C.; Avila, J.; Frantzeskakis, E.; Asensio, M. C.; Resta, A.; Ealet, B.; Le Lay, G. *Phys. Rev. Lett.* **2012,** *108,* 155501. doi:10.1103/PhysRevLett.108.155501
20. Rehren, C.; Muhler, M.; Bao, X.; Schlögl, R.; Ertl, G. *Z. Phys. Chem.* **1991,** *174,* 11. doi:10.1524/zpch.1991.174.Part_1.011
21. Chen, Z. Y.; Liang, D.; Ma, G.; Frankel, G. S.; Allen, H. C.; Kelly, R. G. *Corros. Eng., Sci. Technol.* **2010,** *45,* 169. doi:10.1179/147842209X12579401586681
22. Kresse, G.; Hafner, J. *Phys. Rev. B* **1993,** *47,* 558. doi:10.1103/PhysRevB.47.558
23. Kresse, G.; Furthmüller, J. *Phys. Rev. B* **1996,** *54,* 11169–11186. doi:10.1103/PhysRevB.54.11169
24. Kresse, G.; Joubert, D. *Phys. Rev. B* **1999,** *59,* 1758–1775. doi:10.1103/PhysRevB.59.1758
25. Blöchl, P. E. *Phys. Rev. B* **1994,** *50,* 17953–17979. doi:10.1103/PhysRevB.50.17953
26. Perdew, J. P.; Burke, K.; Ernzerhof, M. *Phys. Rev. Lett.* **1996,** *77,* 3865–3868. doi:10.1103/PhysRevLett.77.3865
27. Grimme, S. *J. Comput. Chem.* **2006,** *27,* 1787–1799. doi:10.1002/jcc.20495
28. Du, Y.; Zhuang, J.; Liu, H.; Xu, X.; Eilers, S.; Wu, K.; Cheng, P.; Zhao, J.; Pi, X.; See, K. W.; Peleckis, G.; Wang, X.; Dou, S. X. *ACS Nano* **2014,** *8,* 10019–10025. doi:10.1021/nn504451t
29. Du, Y.; Zhuang, J.; Wang, J.; Li, Z.; Liu, H.; Zhao, J.; Xu, X.; Feng, H.; Chen, L.; Wu, K.; Wang, X.; Dou, S. X. *Sci. Adv.* **2016,** *2,* e1600067. doi:10.1126/sciadv.1600067

License and Terms

BEILSTEIN JOURNAL OF NANOTECHNOLOGY

Structural model of silicene-like nanoribbons on a Pb-reconstructed Si(111) surface

Agnieszka Stępniak-Dybala and Mariusz Krawiec*

Full Research Paper

Open Access

Address:
Institute of Physics, M. Curie-Skłodowska University, Pl. M. Curie-Skłodowskiej 1, 20-031 Lublin, Poland

Email:
Mariusz Krawiec* - mariusz.krawiec@umcs.pl

* Corresponding author

Keywords:
density functional theory (DFT); scanning tunneling microscopy (STM); silicene; Si nanoribbons

Beilstein J. Nanotechnol. **2017,** *8,* 1836–1843.
doi:10.3762/bjnano.8.185

Received: 31 March 2017
Accepted: 16 August 2017
Published: 05 September 2017

This article is part of the Thematic Series "Silicene, germanene and other group IV 2D materials".

Guest Editor: P. Vogt

Abstract

A structural model of the recently observed silicene-like nanoribbons on a Pb-induced $\sqrt{3} \times \sqrt{3}$ reconstructed Si(111) surface is proposed. The model, which is based on first principles density functional theory calculations, features a deformed honeycomb structure directly bonded to the Si(111) surface underneath. Pb atoms stabilize the nanoribbons, as they passivate the uncovered substrate, thus lower the surface energy, and suppress the nanoribbon–substrate interaction. The proposed structural model reproduces well all the experimental findings.

Introduction

The discovery of the exotic nature of graphene [1,2] has stimulated a growing interest in similar materials with a two-dimensional (2D) honeycomb geometry, mainly composed of group-IV elements [3-6]. In particular silicene, a silicon counterpart of graphene, has attracted increasing attention due to its compatibility with existing semiconductor technology [7-12].

After the theoretical predictions [13-15], a great number of experimental studies has been devoted to the fabrication of silicene, but still the synthesis of this material remains a big challenge. So far a freestanding layer has not been produced. However, mainly epitaxial layers have been synthesized on Ag(111), Ir(111), ZrB_2(111) [16-24] or recently on graphite [25]. Among them epitaxial silicene on Ag(111) has been the most extensively studied. Depending on the temperature and deposition rate, various superstructures, i.e., 4×4, $2\sqrt{3} \times 2\sqrt{3}$ and $\sqrt{13} \times \sqrt{13}$ (with respect to the Ag(111) lattice) have been observed [19,26]. The 2D honeycomb structure of silicene layer with 4×4 symmetry on Ag(111) is well established and supported by many experimental and theoretical results [16-19,27-31]. Other phases of Si/Ag(111) are more controversially discussed, while the problem of the silicene formation on other substrates has been addressed only in a few reports. Nevertheless, the first silicene-based field effect transistor

device operating at room temperature has already been demonstrated [12].

To get a deeper and more detailed insight into the physics and chemistry of silicene/substrate systems density functional theory (DFT) calculations have usually been required. In all these cases silicene was reported to be formed in 2D domains with a corrugated hexagonal structure. Nevertheless, not all experiments, most notably on Ag(111), support the scenario of silicene formation, mainly due to a problem with electronic properties. Therefore there is still a significant amount of skepticism about this issue. In many cases density functional theory (DFT) calculations were required to get more detailed information on what structures have really been obtained. The same problem concerns Si nanoribbons (NRs) grown on the Ag(110) surface [32-40]. The scanning tunneling microscopy (STM) images show isolated 1.6 nm wide ribbons [32,35,41]. However, no hexagonal structure is visible in the STM topography. First DFT calculations proposed a hexagonal structure of the Si NRs. However, recent theoretical and experimental studies [42-44] have found this structure to be incorrect, and opt for the so-called "pentamer" model, in which Si atoms are arranged into chains composed of pentagonal rings running along the rows. Thus, in most cases the structure of the deposited silicon is governed by the underlying substrate.

Alternative substrates that could host silicene without destroying its remarkable electronic properties are still highly required. Recently, we have made attempts to grow silicene on a Pb substrate because the results of the DFT calculations of [45,46] were very promising in view of silicene formation. We started from the thinnest Pb substrates, which are $\sqrt{3}\times\sqrt{3}$ and $\sqrt{7}\times\sqrt{3}$ reconstructions of Pb on Si(111). Our STM studies on the Pb-reconstructed Si(111) surface revealed that deposited Si atoms form wide nanoribbons [47]. The NRs, running in three high-symmetry directions of the Si(111) surface, are several nanometers long, 1.6 nm wide and show a local $\sqrt{3}\times\sqrt{3}$ reconstruction. Although no details on the atomic structure existed, these nanostructures have been interpreted in terms of silicene-like nanoribbons grown on the bare Si(111) surface [47].

In the present work we focus on the determination of the atomic structure of the 1D Si NRs grown on the Pb-induced $\sqrt{3}\times\sqrt{3}$ reconstructed Si(111) surface, in short $\sqrt{3}$-Pb. Our combined STM and DFT studies confirm the proposed scenario of silicene-like NRs. In particular, the DFT calculations reveal the hexagonal structure of the Si nanoribbons, which are directly bonded to the bare Si(111) surface. However, Pb atoms play an important role in stabilizing the structure, as they lower the surface energy. The proposed structural model features a deformed honeycomb structure in reversed AB registry with respect to the top Si(111) substrate layer, and reproduces well the experimental data. These findings provide a deeper insight into the formation of silicene nanostructures on metal-stabilized silicon surfaces, and may serve as help for the growth of silicene on other substrates.

Experimental and Computational Details

All the measurements have been done under UHV conditions with a ^{4}He-cooled scanning tunneling microscope (Omicron) working at 4.5 K. For STM/STS measurements electrochemically etched tungsten was used. The Pb/Si(111) sample was prepared in situ by evaporation of Pb on the Si(111)-7 × 7 substrate. Next, the Si layer was deposited onto the sample held at 200 K within 20 min. Details of the preparation can be found in [47]. The presented nanoribbons were obtained by two-step annealing: first at room temperature for 1 h, and then by direct heating at around 400 K for 5 min.

Density functional theory calculations were performed within the Perdew–Burke–Ernzerhof (PBE) [48] generalized gradient approximation (GGA) using projector-augmented-wave potentials, as implemented in the VASP (Vienna ab initio simulation package) [49,50]. The plane wave energy cutoff for all calculations was set to 340 eV, and the Brillouin zone was sampled by a 5 × 2 × 1 Monkhorst–Pack *k*-points grid [51], 640 eV and 9 × 3 × 1 grid in convergence tests, which resulted in changes of the surface energies of less than 0.1 meV/Å^2. The spin–orbit interaction has not been included in calculations.

The Si(111) system has been modeled by eight Si double layers. To avoid the interaction between neighboring Si NRs, a $\sqrt{3}\times 3\sqrt{3}$ unit cell was used in calculations. Si atoms in the bottom layer were fixed at their bulk ideal positions and H atoms were used to saturate Si dangling bonds of the bottom layer, maintaining correct Si–Si bonds, to mimic bulk Si crystal. The positions of the remaining atoms were fully relaxed until the largest force in any direction was below 0.01 eV/Å. All the calculations have been performed in the same unit cell with fixed bulk Si lattice constant.

Based on the obtained electronic structure data of the Si NRs/Si(111) system described above, scanning tunneling microscopy simulations were performed by using the Tersoff–Hamann approach [52].

Results and Discussion

Typical Si nanoribbons are several nanometers long and run in one of three high-symmetry directions of the Si(111) surface. Figure 1a shows an example of such NRs as revealed by STM topography measurements. The NRs consist of Si atoms directly adsorbed on the Si(111) surface, as it was argued in [47], based

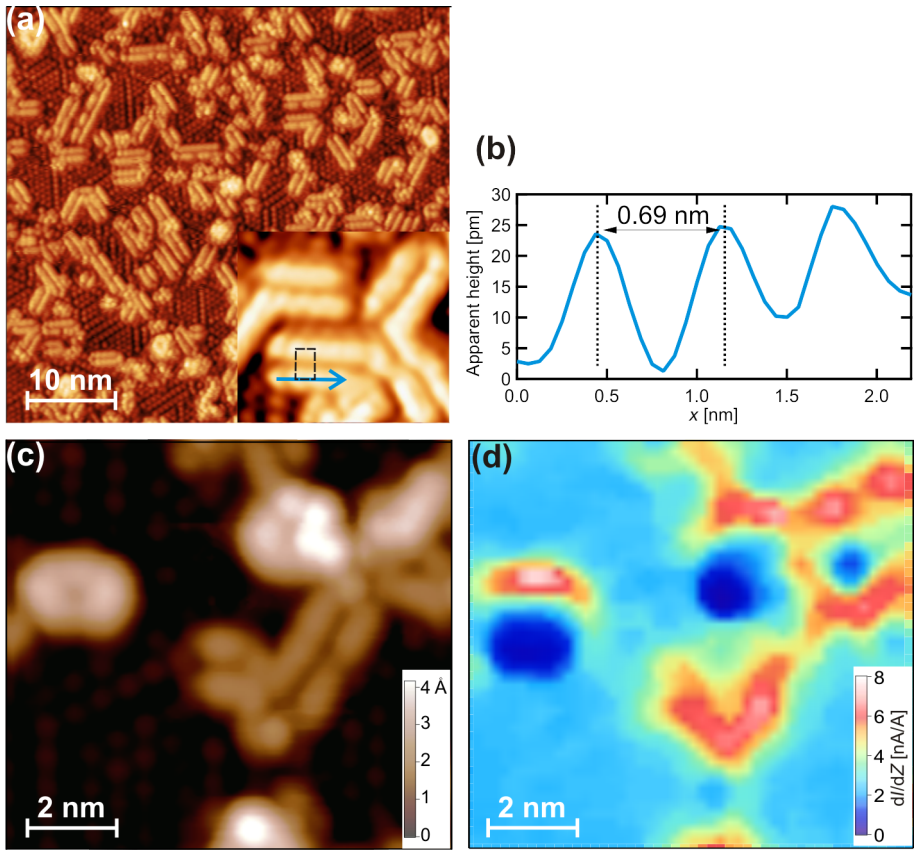

Figure 1: (a) STM topography (U = 2.0 V, I = 0.5 nA) of Si nanoribbons on a Si(111)$\sqrt{3}\times\sqrt{3}$-Pb surface. (b) Line profile along blue arrow marked in the inset of (a). The arrow points in the [1 $\bar{1}$ 0] direction. The unit cell of a nanoribbon is also marked in the inset of (a). (c, d) Results of a simultaneously measured topography and dI/dz map of the same area. Scanning parameters were U = 1 V, I = 0.5 nA.

on geometry considerations and STM measurements. It is also known, that Pb atoms strongly diffuse on Si substrates [53,54], so they can easily make room for growing Si NRs. Furthermore, different STS characteristics acquired on top of the NRs and in between them also point against Pb-composed nanoribbons. The experimental findings suggest that the observed nanostructures are wide nanoribbons rather then separated Si chains, as the inter-chain separations of 0.86 Å cannot be assigned to any Si–Si distance, and the modulations of STM topography across and along the nanostructures are very similar to each other. Moreover it is difficult to explain why the chains always grow in pairs.

An additional argument for the Si nature of nanoribbons can be provided by measurements of the local work function (Φ). In a first approximation Φ is proportional to the derivative of the tunneling current (I) with respect to the STM tip–sample distance (z) [55]. Thus, changes of Φ should be reflected in recorded dI/dz maps. Figure 1c,d shows topography and dI/dz maps simultaneously measured in the same area of the sample. A clear correlation between these quantities is observed. It is evident that the nanostructures feature a higher work function than the $\sqrt{3}$-Pb substrate, which suggests the NRs are composed of Si atoms. However, one has to remember that different values of Φ do not necessarily mean different chemical compositions. Thus the changes of the dI/dz values alone should be considered as necessary rather than sufficient condition. Nevertheless, the assumption of Si NRs is also in line with the Φ ordering of Pb and Si crystals, and with the calculated values of Φ, as it will be discussed later.

The internal structure of each NR, as revealed by STM topography measurements, consists of bright protrusions (BPs) periodically arranged within a NR. The BPs form a 6.9 Å × 8.6 Å rectangular lattice, marked in Figure 1a. Occasional zig-zag patterns have also been observed, but only in the presence of defects. The 6.9 Å periodicity matches well the length of the Si(111) $\sqrt{3}$ unit cell, which yields 6. Å, thus it can be assigned to the $\sqrt{3}$-Si reconstruction. This reconstruction of Si can be obtained while growing Si structures directly on a Si(111) surface [56,57]. The reconstruction is also known to be realized in the case of multilayer silicene [58]. Its characteristic feature is

an almost flat Si layer with sticking out Si atoms. These atoms give rise to a strong STM signal and are visible as BPs in topography images. They should not be misinterpreted as adatoms, since being shifted vertically they, in fact, still occupy honeycomb lattice sites. Such arrangement of atoms reflects a natural tendency of Si towards sp^3-bonding [45,59].

Associating distance between BPs across NRs is a more complicated issue. The $\sqrt{3}$-Si periodicity is achieved along the armchair (AC) direction, and BPs form a rectangular lattice, thus the distance of 8.6 Å must be associated with sticking out Si atoms along the zig-zag (ZZ) direction. However, the value of 8.6 Å does not fit any Si–Si distance on the Si(111) surface. In fact it is by 0.9 Å longer than the double lattice constant in the $[1\,\bar{1}0]$ direction. Thus, likely the NRs structure will consist of deformed hexagonal rings. It could also be possible that the atomic structure includes pentagons, as in the case of Si NRs on the Ag(110) surface [42-44]. However, such scenario is less favorable for symmetry reasons since NRs grow directly on the Si(111) surface and the bonding of Si atoms arranged in pentagons to those in hexagons is expected to be energetically unfavorable.

Having collected information on details of NRs from experiments, we are ready to construct a structural model. First we neglect presence of Pb atoms and focus only on Si NRs grown on the bare substrate. As we already discussed, the nanoribbons are Pb-free objects, while Pb atoms themselves appear to be important only in the process of growing Si NRs and prevent Si structures from growing in a 3D fashion. The role of Pb will be discussed later.

We have considered a number of initial atomic structures of NRs composed of hexagons, pentagons or both building blocks. In the following, the lowest-energy structural models are labeled according to the number of hexagonal and pentagonal rings per unit cell forming a NR. The relative surface energies $\gamma_{NR(Si)}$ and distances between BPs d_{BP}, if available, of some representative structural models are listed in Table 1.

The surface energy $\gamma_{NR(Si)}$ is defined as

$$\gamma_{NR(Si)} = \frac{1}{S}\left[E_{tot} - E_{bare} - N_{Si}\mu_{Si}^{bulk}\right], \qquad (1)$$

where E_{tot} and E_{bare} are total energies of the NR on the Si(111) surface and on the Si(111) surface with $\sqrt{3}\times\sqrt{3}$ reconstruction. N_{Si} stands for the number of Si atoms in a NR, while μ_{Si}^{bulk} is the chemical potential of a Si atom, taken as its bulk value. The area of the surface unit cell is denoted as S.

Table 1: Relative surface energies $\gamma_{NR(Si)}$ and BP–BP distance d_{BP} of structural models of Si NRs on the Si(111) surface. $\gamma_{NR(Si)}$, defined by Equation 1, is measured with respect to the energy of the $\sqrt{3}\times\sqrt{3}$ reconstructed bare Si(111), set as the energy zero. The models are labeled according to the number of hexagonal and pentagonal rings per unit cell constituting a NR. In some models only a single BP in the unit cell appears or there are no BPs at all. Then d_{BP} could not be determined.

model	$\gamma_{NR(Si)}$ (meV/Å^2)	d_{BP} (Å)
3hex	5.74	3.97
1hex-2pent	8.49	—
4hex	4.92	—
5hex	4.02	8.00
4hex-1pent	8.58	—

All the structures listed in Table 1 feature positive values of $\gamma_{NR(Si)}$, which means that they are less stable than the bare Si(111)-$\sqrt{3}\times\sqrt{3}$ surface. This suggests that the presence of Pb might be important in stabilizing NRs. Furthermore, it is clear, that NRs containing pentagonal rings are not preferred, as pentagons substantially increase the surface energy. This result confirms our expectation that pentagons do not fit well to the hexagonal structure of the Si(111) surface and that pentagonal objects should be less favorable. Another argument against pentamer-structure models is the lack of sticking out atoms in obtained structures. Thus, none of these models will reproduce the STM topography.

According to Table 1, the structural model with the lowest surface energy (5hex) is composed of pure hexagonal rings. The model is shown in Figure 2. The atomic structure of the NR is in reversed AB registry with respect to the substrate lattice (Figure 2b). This layer stacking has also been proposed as one of possible realizations of multilayer silicene [60]. The mean NR–substrate distance yields 2.89 Å, which suggests rather strong chemical bonding between these subsystems. The interaction with the substrate is reflected in the presence of Si atoms sticking out of the NR layer by 1.06 Å, as discussed for other systems [45,59]. The strong NR–substrate interaction also results in a substantial deformation of the outermost hexagons, which leads to a sawtooth shape of the NR edges. This arrangement of atoms increases the distance between atoms sticking out, d_{BP}, which in the present case yields 8 Å. This value is by 0.3 Å longer than the expected double lattice constant in the *ZZ* direction, but still 0.6 Å less than the observed value. In reality the difference between experimental and theoretical values is expected to be smaller due to the scanner calibration, which is expected to overestimate distances up to 3%. Nevertheless, this value of d_{BP} is the closest to the experimental BP–BP distance among the models studied. Note that most of the models either feature a single BP in the unit cell or produce no BPs at all.

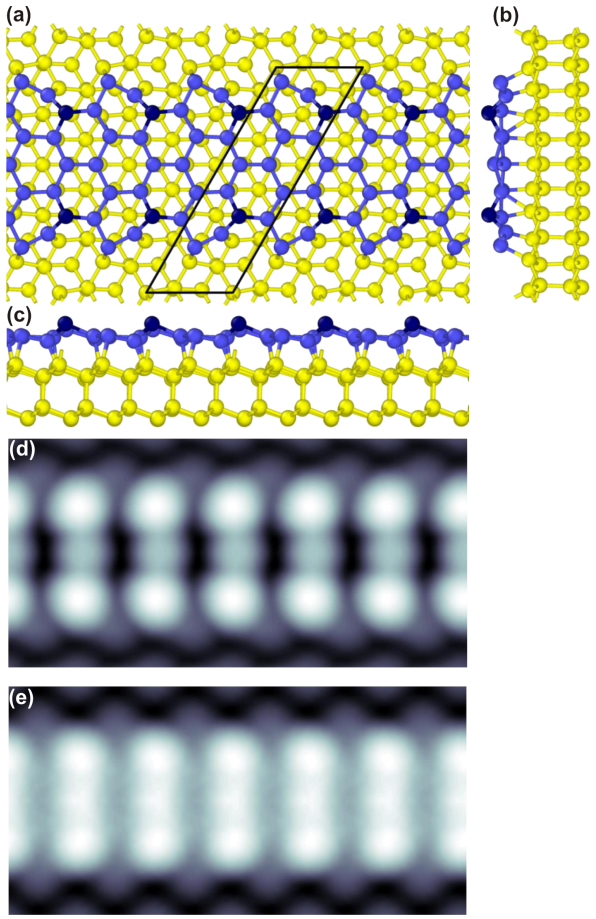

Figure 2: (a) Top and (b), (c) side views of the structural model with the lowest energy (5hex) of Si nanoribbons on a Si(111) surface. Different colors represent Si atoms of different parts of the structure: Atoms shown in blue constitute the Si NR, with sticking out atoms colored in dark blue, while yellow atoms represent the substrate. The black parallelogram in panel (a) marks the surface unit cell. (a) Filled (eU = −1 eV) and (b) empty state (eU = +1 eV) simulated STM topography (4 nm × 2 nm) of a Si NR on the Si(111) surface.

The 5hex model accounts for main experimental findings, i.e., it has $\sqrt{3}$ periodicity along the AC direction, produces two BPs per unit cell with a reasonable distance between them, and contains no Pb atoms. To further check the validity of the model we have performed STM simulations, which are presented in Figure 2d,e. Indeed, the calculations reproduce well the experimental data. In particular BPs, which reflect sticking out atoms, are well resolved. Similar as in the experiment, they form a rectangular lattice with $\sqrt{3}$ periodicity along NRs. However, in experimentally determined topography, the BPs across a NR are well separated, while calculations give additional features in between the BPs. These third protrusions come from Si atoms in the middle of NRs (compare Figure 2a,c). These atoms stick out of the NR layer by 0.6 Å, compared with 1.05 Å for BPs. Nevertheless, they contribute to the STM signal, in particular at positive sample bias, and make the topography more blurred. Another possibility for the discrepancy might be that interference processes suppress the STM current in the middle of a NR, an effect that cannot be captured by the Tersoff–Hamann approach.

So far we have discussed only pure Si structures, disregarding the role of Pb atoms in the system. We have only mentioned that Pb atoms may stabilize the NRs, because the NRs on a bare Si(111) surface increase the surface energy, and the pure Si system should be unstable. We have checked the stability of the 5hex model in the presence of Pb atoms. In this case the relative surface energy $\gamma_{\mathrm{NR(Si–Pb)}}$ reads

$$\gamma_{\mathrm{NR(Si\text{-}Pb)}} = \frac{1}{S}\left[E_{\mathrm{tot}} - E_{\mathrm{bare}} - N_{\mathrm{Si}}\mu_{\mathrm{Si}}^{\mathrm{bulk}} - N_{\mathrm{Pb}}\left(\mu_{\mathrm{Pb}}^{\mathrm{bulk}} + \Delta\mu_{\mathrm{Pb}}\right)\right], \quad (2)$$

where E_{tot} is now the total energy of a NR and Pb atoms on a Si(111) surface, N_{Pb} denotes the number of Pb atoms in a unit cell, and $\Delta\mu_{\mathrm{Pb}}$ is the chemical potential of Pb measured with respect to its bulk value $\mu_{\mathrm{Pb}}^{\mathrm{bulk}}$. In this way calculated relative surface energy $\gamma_{\mathrm{NR(Si–Pb)}}$ is shown in Figure 3.

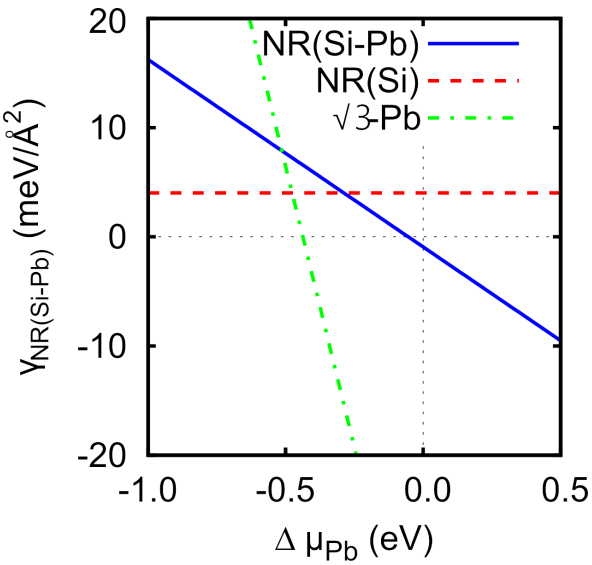

Figure 3: Relative surface energy $\gamma_{\mathrm{NR(Si–Pb)}}$ vs the chemical potential of Pb $\Delta\mu_{\mathrm{Pb}}$ measured with respect to its bulk value $\mu_{\mathrm{Pb}}^{\mathrm{bulk}}$.

Clearly, as the chemical potential of Pb, $\Delta\mu_{\mathrm{Pb}}$, increases and approaches its bulk value, the relative surface energy $\gamma_{\mathrm{NR(Si–Pb)}}$ becomes negative, indicating the stability of the system. Note that the most stable system should be the $\sqrt{3}$-Pb reconstruction, but this is in line with experimental findings suggesting that Si NRs growing on the bare surface move Pb atoms, which form the dense $\sqrt{3}$-Pb phase in between the NRs. The stability of Si NRs is achieved by passivation of the bare Si(111) surface by

Pb atoms, which in turn lowers the surface energy. The main process behind the energy lowering is the charge transfer from Pb to Si atoms. According to the Bader analysis, the largest amounts of charge, 0.26*e* and 0.09*e*, are transferred to the NR-edge Si atoms and to the third protruding atom in the middle of a NR, respectively.

The main features of the 5hex model remain unchanged in the presence of Pb atoms, as Figure 4 shows. In particular, two Si atoms forming BPs and deformed outermost hexagons are still present. Moreover, the sticking out Si atoms do not change their positions with respect to the flat NR layer. They stick out by 1.05 Å, the same value as in the Pb-free case, and maintain their original separation d_{BP}. However, looking into the details of the NR structure in the presence of Pb, it turns out that important modifications appear. The whole NR is pushed away from the surface, and the mean NR–surface separation increases by 0.1 Å with respect to its Pb-free value. This results in a weakening of the NR–substrate interaction. In fact, this should somehow be expected since Pb atoms passivate the Si(111) surface. This weaker interaction and the substantial charge doping lead to the depression of the third protrusion in the middle of a NR of the original 5hex model (compare Figure 2b and Figure 4b). Note that this protrusion had substantially spoiled the agreement between theoretical and experimental STM topography images. As a result of Pb passivation an STM topography with two protrusions is now obtained.

To further check the validity of the model, we have calculated the work function Φ for Si NRs and for Si–Pb NRs, which yielded 4.70 eV and 4.45 eV, respectively. Thus adding Pb atoms to areas between Si NRs decreases the value of Φ. We also calculated the local electrostatic potential distribution in the vacuum region (Figure 4), which can be compared to the d*I*/d*z* maps of Figure 1d. Clearly, Si NRs feature higher values of Φ then Pb areas, in full agreement with the experimental results.

To shed light on electronic properties, we provide a comparison of the measured d*I*/d*V* characteristics and calculated density of states (DOS) in Figure 5. Again, the theoretical results reproduce well the experimental data. The system is metallic with overall V-shape behavior and some fine structure imposed on it. Note that Pb atoms only slightly modify the DOS characteristics.

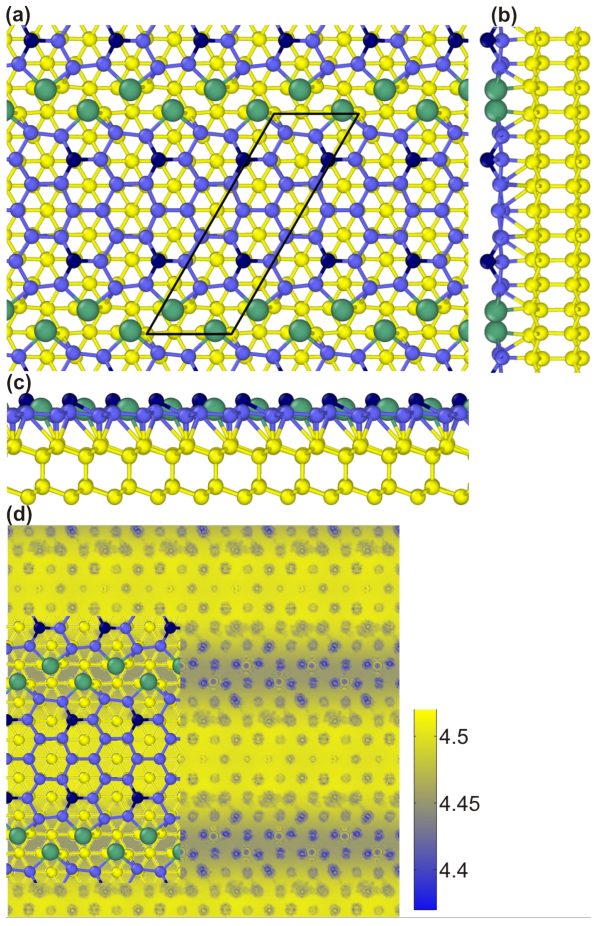

Figure 4: (a) Top and (b), (c) side views of the 5hex model in the presence of Pb atoms (shown in green). (d) Local distribution of the electrostatic potential in the vacuum region.

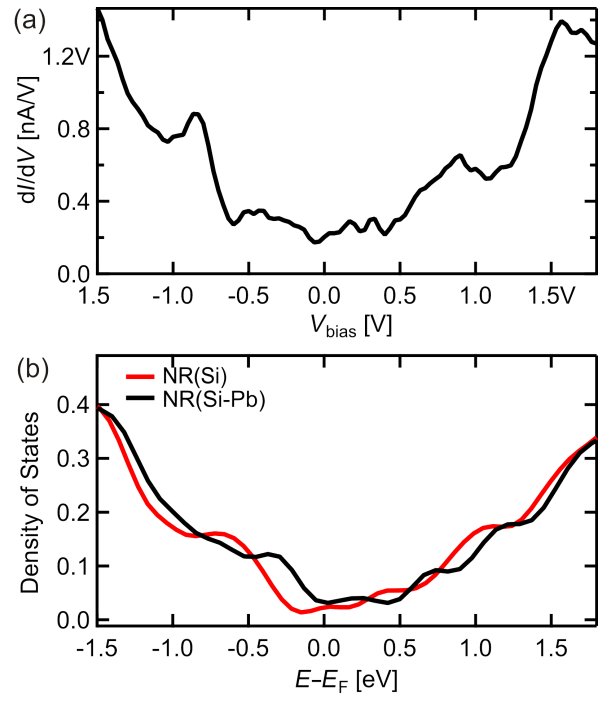

Figure 5: (a) d*I*/d*V* point spectroscopy data acquired on top of the Si NR. (b) Total density of states of Si NR system in the absence (red line) and in the presence of Pb atoms (black line). Note that the system is metallic.

The above results show that Pb atoms play an important role in the formation of Si NRs. By passivating the substrate and donating charge they lower the surface energy, suppress the NR–surface interaction, stabilize Si NRs and modify their properties. In short, they improve the agreement between theoretical and experimental results. However, it is important to stress that such scenario could only be realized owing to the fast diffusion of Pb atoms on Si substrates. Simply, Pb atoms must make room for growing NRs directly on the substrate. If the diffusion was too slow, Si would grow on top of Pb, not necessarily in a 1D or 2D fashion. Thus both, thermodynamics and kinetics, play a significant role in the formation of Si NRs. We believe that a mechanism utilizing fast diffusion of atoms on other substrates may serve as an efficient way of growing silicene nanostructures.

Conclusion

In conclusion, we have studied structural and electronic properties of silicene-like nanoribbons formed on a Si(111) surface with Pb-induced reconstrcution. Based on density functional theory calculations, we have proposed a structural model of the nanoribbons. The model features a deformed honeycomb lattice in the reversed AB registry with the top Si(111) layer, and the presence of Si atoms sticking out from the surface, which are visible as bright protrusions in the STM topography. The nanoribbons are directly bonded to the substrate, while Pb atoms stabilize the system by passivating the uncovered substrate and donating electrons to Si atoms. Thus, they lower the surface energy and suppress the nanoribbon–substrate interaction. The proposed model reproduces well all the experimental data. These findings provide a deeper insight into the formation of silicene nanostructures on metal-induced silicon surfaces and open new routes to grow silicene on other substrates utilizing the mechanism of fast atomic diffusion.

Acknowledgements

The work has been supported by the National Science Centre (Poland) under Grant No. DEC-2014/15/B/ST5/04244.

References

1. Novoselov, K. S.; Geim, A. K.; Morozov, S. V.; Jiang, D.; Katsnelson, M. I.; Grigorieva, I. V.; Dubonos, S. V.; Firsov, A. A. *Nature* **2005,** *438,* 197. doi:10.1038/nature04233
2. Geim, A. K. *Science* **2009,** *324,* 1530. doi:10.1126/science.1158877
3. Miró, P.; Audiffred, M.; Heine, T. *Chem. Soc. Rev.* **2014,** *43,* 6537. doi:10.1039/C4CS00102H
4. Bhimanapati, G. R.; Lin, Z.; Meunier, V.; Jung, Y.; Cha, J.; Das, S.; Xiao, D.; Son, Y.; Strano, M. S.; Cooper, V. R.; Liang, L.; Louie, S. G.; Ringe, E.; Zhou, W.; Kim, S. S.; Naik, R. R.; Sumpter, B. G.; Terrones, H.; Xia, F.; Wang, Y.; Zhu, J.; Akinwande, D.; Alem, N.; Schuller, J. A.; Schaak, R. E.; Terrones, M.; Robinson, J. A. *ACS Nano* **2015,** *12,* 11509. doi:10.1021/acsnano.5b05556
5. Novoselov, K. S.; Mishchenko, A.; Carvalho, A.; Castro Neto, A. H. *Science* **2016,** *353,* aac9439. doi:10.1126/science.aac9439
6. Molle, A. *ECS Trans.* **2016,** *75,* 163. doi:10.1149/07505.0163ecst
7. Houssa, M.; Dimoulas, A.; Molle, A. *J. Phys.: Condens. Matter* **2015,** *27,* 253002. doi:10.1088/0953-8984/27/25/253002
8. Le Lay, G.; Salomon, E.; Angot, T. *Europhys. News* **2016,** *47,* 17. doi:10.1051/epn/2016101
9. Grazanetti, C.; Cinquanta, E.; Molle, A. *2D Mater.* **2016,** *3,* 012001. doi:10.1088/2053-1583/3/1/012001
10. Zhao, J.; Liu, H.; Yu, Z.; Quhe, R.; Zhou, S.; Wang, Y.; Liu, C. C.; Zhong, H.; Han, N.; Lu, J.; Yao, Y.; Wu, K. *Prog. Mater. Sci.* **2016,** *83,* 24. doi:10.1016/j.pmatsci.2016.04.001
11. Molle, A.; Grazianetti, C.; Cinquanta, E. *ECS Trans.* **2016,** *75,* 703. doi:10.1149/07508.0703ecst
12. Tao, L.; Cinquanta, E.; Chiappe, D.; Grazianetti, C.; Fanciulli, M.; Dubey, M.; Molle, A.; Akinwande, D. *Nat. Nanotechnol.* **2015,** *10,* 227. doi:10.1038/nnano.2014.325
13. Takeda, K.; Shiraishi, K. *Phys. Rev. B* **1994,** *50,* 14916. doi:10.1103/PhysRevB.50.14916
14. Guzmán-Verri, G. G.; Lew Yan Voon, L. C. *Phys. Rev. B* **2007,** *76,* 075131. doi:10.1103/PhysRevB.76.075131
15. Cahangirov, S.; Topsakal, M.; Aktürk, E.; Şahin, H.; Ciraci, S. *Phys. Rev. Lett.* **2009,** *102,* 236804. doi:10.1103/PhysRevLett.102.236804
16. Vogt, P.; De Padova, P.; Quaresima, C.; Avila, J.; Frantzeskakis, E.; Asensio, M. C.; Resta, A.; Ealet, B.; Le Lay, G. *Phys. Rev. Lett.* **2012,** *108,* 155501. doi:10.1103/PhysRevLett.108.155501
17. Feng, B.; Ding, Z.; Meng, S.; Yao, Y.; He, X.; Cheng, P.; Chen, L.; Wu, K. *Nano Lett.* **2012,** *12,* 3507. doi:10.1021/nl301047g
18. Lin, C.-L.; Arafune, R.; Kawahara, K.; Tsukahara, N.; Minamitani, E.; Kim, Y.; Takagi, N.; Kawai, M. *Appl. Phys. Express* **2012,** *5,* 045802. doi:10.1143/APEX.5.045802
19. Jamgotchian, H.; Colington, Y.; Hamazaouri, N.; Ealet, B.; Hoarau, J. Y.; Aufray, B.; Bibérian, J. P. *J. Phys.: Condens. Matter* **2012,** *24,* 172001. doi:10.1088/0953-8984/24/17/172001
20. Fleurence, A.; Friedlein, R.; Ozaki, T.; Kawai, H.; Wang, Y.; Yamada-Takamura, Y. *Phys. Rev. Lett.* **2012,** *108,* 245501. doi:10.1103/PhysRevLett.108.245501
21. Meng, L.; Wang, Y.; Zhang, L.; Du, S.; Wu, R.; Li, L.; Zhang, Y.; Li, G.; Zhou, H.; Hofer, W. A.; Gao, H.-J. *Nano Lett.* **2013,** *13,* 685. doi:10.1021/nl304347w
22. Morishita, T.; Spencer, M. J. S.; Kawamoto, S.; Snook, I. K. *J. Phys. Chem. C* **2013,** *117,* 22142. doi:10.1021/jp4080898
23. Aizawa, T.; Suehara, S.; Otani, S. *J. Phys. Chem. C* **2014,** *118,* 23049. doi:10.1021/jp505602c
24. Chiappe, D.; Scalise, E.; Cinquanta, E.; Granzietti, C.; van der Broek, B.; Fanciulli, M.; Houssa, M.; Molle, A. *Adv. Mater.* **2014,** *26,* 2096. doi:10.1002/adma.201304783
25. De Crescenzi, M.; Berbezier, I.; Scarselli, M.; Castrucci, P.; Abbarchi, M.; Ronda, A.; Jardali, F.; Park, J.; Vach, H. *ACS Nano* **2016,** *10,* 11163–11171. doi:10.1021/acsnano.6b06198
26. Moras, P.; Mentes, T. O.; Sheverdyaeva, P. M.; Locatelli, A.; Carbone, C. *J. Phys.: Condens. Matter* **2014,** *26,* 185001. doi:10.1088/0953-8984/26/18/185001
27. Fukaya, Y.; Mochizuki, I.; Maekawa, M.; Wada, K.; Hyodo, T.; Matsuda, I.; Kawasuso, A. *Phys. Rev. B* **2013,** *88,* 205413. doi:10.1103/PhysRevB.88.205413
28. Takagi, N.; Lin, C.-L.; Kawahara, K.; Minamitani, E.; Tsukahara, N.; Kawai, M.; Arafune, R. *Prog. Surf. Sci.* **2015,** *90,* 1. doi:10.1016/j.progsurf.2014.10.001

29. Curcella, A.; Bernard, R.; Borensztein, Y.; Resta, A.; Lazzeri, M.; Prévot, G. *Phys. Rev. B* **2016,** *94,* 165438. doi:10.1103/PhysRevB.94.165438
30. Solonenko, D.; Gordan, O. D.; Le Lay, G.; Sahin, H.; Cahangirov, S.; Zahn, D. R. T.; Vogt, P. *2D Mater.* **2017,** *4,* 015008. doi:10.1088/2053-1583/4/1/015008
31. Zhuang, J.; Xu, X.; Du, Y.; Wu, K.; Chen, L.; Hao, W.; Wang, J.; Yeoh, W. K.; Wang, X.; Dou, S. X. *Phys. Rev. B* **2015,** *91,* 161409. doi:10.1103/PhysRevB.91.161409
32. Leandri, C.; Le Lay, G.; Aufray, B.; Girardeaux, C.; Avila, J.; Dávila, M. E.; Asensio, M. C.; Ottaviani, C.; Cricenti, A. *Surf. Sci.* **2005,** *574,* L9. doi:10.1016/j.susc.2004.10.052
33. Sahaf, H.; Masson, L.; Léandri, C.; Aufray, B.; Le Lay, G.; Ronci, F. *Appl. Phys. Lett.* **2007,** *90,* 263110. doi:10.1063/1.2752125
34. De Padova, P.; Quaresima, C.; Perfetti, P.; Olivieri, B.; Leandri, C.; Aufray, B.; Vizzini, S.; Le Lay, G. *Nano Lett.* **2008,** *8,* 271. doi:10.1021/nl072591y
35. Kara, A.; Léandri, C.; Dávila, M. E.; De Padova, P.; Ealet, B.; Oughaddou, H.; Aufray, B.; Le Lay, G. *J. Supercond. Novel Magn.* **2009,** *22,* 259. doi:10.1007/s10948-008-0427-8
36. De Padova, P.; Quaresima, C.; Ottaviani, C.; Sheverdyaeva, P. M.; Moras, P.; Carbone, C.; Topwal, D.; Olivieri, B.; Kara, A.; Oughaddou, H.; Aufray, B.; Le Lay, G. *Appl. Phys. Lett.* **2010,** *96,* 261905. doi:10.1063/1.3459143
37. Ronci, F.; Colonna, S.; Cricenti, A.; De Padova, P.; Ottaviani, C.; Quaresima, C.; Aufray, B.; Le Lay, G. *Phys. Status Solidi C* **2010,** *7,* 2716. doi:10.1002/pssc.200983839
38. De Padova, P.; Quaresima, C.; Perfetti, P.; Olivieri, B.; Leandri, C.; Aufray, B.; Vizzini, S.; Le Lay, G. *Nano Lett.* **2008,** *8,* 271. doi:10.1021/nl072591y
39. Feng, B.; Li, H.; Meng, S.; Chen, L.; Wu, K. *Surf. Sci.* **2016,** *645,* 74. doi:10.1016/j.susc.2015.10.037
40. Tchalala, M. R.; Enriquez, H.; Mayne, A. J.; Kara, A.; Roth, S.; Silly, M. G.; Bendounan, A.; Sirotti, F.; Greber, T.; Aufray, B.; Dujardin, G.; Ali, M. A.; Oughaddou, H. *Appl. Phys. Lett.* **2013,** *102,* 083107. doi:10.1063/1.4793536
41. Le Lay, G.; Aufray, B.; Léandri, C.; Oughaddou, H.; Biberian, J.-P.; Padova, P. D.; Dávila, M. E.; Ealet, B.; Kara, A. *Appl. Surf. Sci.* **2009,** *256,* 524. doi:10.1016/j.apsusc.2009.07.114
42. Hogan, C.; Colonna, S.; Flammini, R.; Cricenti, A.; Ronci, F. *Phys. Rev. B* **2015,** *92,* 115439. doi:10.1103/PhysRevB.92.115439
43. Prévot, G.; Hogan, C.; Leoni, T.; Bernard, R.; Moyen, E.; Masson, L. *Phys. Rev. Lett.* **2016,** *117,* 276102. doi:10.1103/PhysRevLett.117.276102
44. Cerdá, J. I.; Sławińska, J.; Le Lay, G.; Marele, A. C.; Gómez-Rodríguez, J. M.; Dávila, M. E. *Nat. Commun.* **2016,** *7,* 13076. doi:10.1038/ncomms13076
45. Podsiadły-Paszkowska, A.; Krawiec, M. *Phys. Rev. B* **2015,** *92,* 165411. doi:10.1103/PhysRevB.92.165411
46. Podsiadły-Paszkowska, A.; Krawiec, M. *Phys. Chem. Chem. Phys.* **2015,** *17,* 2246. doi:10.1039/C4CP05104A
47. Stępniak-Dybala, A.; Jałochowski, M.; Krawiec, M. *Condens. Matter* **2016,** *1,* 8. doi:10.3390/condmat1010008
48. Perdew, J. P.; Burke, K.; Ernzerhof, M. *Phys. Rev. Lett.* **1996,** *77,* 2865. doi:10.1103/PhysRevLett.77.3865
49. Kresse, G.; Furthmüller, J. *Phys. Rev. B* **1996,** *54,* 11169. doi:10.1103/PhysRevB.54.11169
50. Kresse, G.; Joubert, D. *Phys. Rev. B* **1999,** *59,* 1758. doi:10.1103/PhysRevB.59.1758
51. Monkhorst, H. J.; Pack, J. D. *Phys. Rev. B* **1976,** *13,* 5188. doi:10.1103/PhysRevB.13.5188
52. Tersoff, J.; Hamann, D. R. *Phys. Rev. Lett.* **1983,** *50,* 1998. doi:10.1103/PhysRevLett.50.1998
53. Nita, P.; Jałochowski, M.; Krawiec, M.; Stępniak, A. *Phys. Rev. Lett.* **2011,** *107,* 026101. doi:10.1103/PhysRevLett.107.026101
54. Nita, P.; Palotás, K.; Jałochowski, M.; Krawiec, M. *Phys. Rev. B* **2014,** *89,* 165426. doi:10.1103/PhysRevB.89.165426
55. Olesen, L.; Brandbyge, M.; Sørensen, M. R.; Jacobsen, K. W.; Lægsgaard, E.; Stensgaard, I.; Besenbacher, F. *Phys. Rev. Lett.* **1996,** *76,* 1485–1488. doi:10.1103/PhysRevLett.76.1485
56. Fan, W. C.; Ignatiev, A.; Huang, H.; Tong, S. Y. *Phys. Rev. Lett.* **1989,** *62,* 1516. doi:10.1103/PhysRevLett.62.1516
57. Wetzel, P.; Saintoney, S.; Pirri, C.; Bolmont, D.; Gewinner, G. *Phys. Rev. B* **1994,** *50,* 10886. doi:10.1103/PhysRevB.50.10886
58. De Padova, P.; Generosi, A.; Paci, B.; Ottaviani, C.; Quaresima, C.; Olivieri, B.; Salomon, E.; Angot, T.; Le Lay, G. *2D Mater.* **2016,** *3,* 031011. doi:10.1088/2053-1583/3/3/031011
59. Podsiadły-Paszkowska, A.; Krawiec, M. *Appl. Surf. Sci.* **2016,** *373,* 45. doi:10.1016/j.apsusc.2015.12.025
60. Fu, H.; Zhang, J.; Ding, Z.; Li, H.; Meng, S. *Appl. Phys. Lett.* **2014,** *104,* 131904. doi:10.1063/1.4870534

License and Terms

BEILSTEIN JOURNAL OF NANOTECHNOLOGY

Coexistence of strongly buckled germanene phases on Al(111)

Weimin Wang* and Roger I. G. Uhrberg

Full Research Paper

Open Access

Address:
Department of Physics, Chemistry, and Biology, Linköping University, S-581 83 Linköping, Sweden

Email:
Weimin Wang* - weiwa49@ifm.liu.se

* Corresponding author

Keywords:
core-level spectroscopy; DFT; germanene; STM

Beilstein J. Nanotechnol. **2017,** *8,* 1946–1951.
doi:10.3762/bjnano.8.195

Received: 31 March 2017
Accepted: 29 August 2017
Published: 18 September 2017

This article is part of the Thematic Series "Silicene, germanene and other group IV 2D materials".

Guest Editor: P. Vogt

Abstract

We report a study of structural and electronic properties of a germanium layer on Al(111) using scanning tunneling microscopy (STM), low energy electron diffraction and core-level photoelectron spectroscopy. Experimental results show that a germanium layer can be formed at a relatively high substrate temperature showing either (3×3) or (√7×√7)R±19.1° reconstructions. First-principles calculations based on density functional theory suggest an atomic model consisting of a strongly buckled (2×2) germanene layer, which is stable in two different orientations on Al(111). Simulated STM of both orientations fit nicely with experimental STM images and the Ge 3d core-level data decomposed into four components is consistent with the suggested model.

Introduction

The properties of two-dimensional (2D) materials are currently subjected to intense experimental and theoretical studies. The research is focused on many important properties predicted by theory for various conceivable 2D materials. In similarity with graphene, some other materials are also predicted to show a linear electron dispersion near the Fermi level. Other important properties/phenomena that make 2D materials particularly interesting for incorporation in various devices are, magnetism, superconductivity, Rashba type spin-splitting, quantum spin Hall effect, amongst others. Based on the wealth of physical phenomena exhibited by various 2D materials, they are considered as important future materials of high potential for applications in nano-scale electronics and spintronics.

A sub-group of 2D materials is graphene-like structures formed by the group IV atoms Si, Ge and Sn, i.e., silicene, germanene and stanene. However, Si, Ge, and Sn atoms prefer sp^3 hybridization, resulting in a buckled honeycomb structure with a mixture of sp^2-sp^3 character [1-3]. As a result, the spin-orbital coupling is enlarged and the quantum spin Hall effect is stronger than in graphene [3-6]. The formation of 2D sheets of group IV elements is a great experimental challenge. In this paper we

address the germanene case by characterizing a layer of Ge formed on Al(111).

Experimental efforts have been made to grow germanene on metallic substrates and band gap materials. Bampoulis et al. [7] proposed a germanene layer with very small buckling (0.2 Å) when they made Pt/Ge crystals by depositing and annealing of Pt on Ge(110). In an inverse case, Li et al. [8] chose Pt(111) as a substrate onto which Ge was evaporated at room temperature. This choice of substrate was motivated by a weaker interfacial interaction compared to other metals with adsorbed two-dimensional sheets such as graphene. They reported that Ge formed a (√19×√19) superstructure on the Pt(111) surface. A model based on a distorted, buckled, germanene sheet was suggested and reported to be consistent with scanning tunneling microscopy (STM) data assuming that only 3 out of 18 Ge atoms inside the (√19×√19) unit cell were observed. These three atoms were about 0.6 Å higher than the rest of the Ge atoms. Later, Švec et al. [9] studied a (√19×√19) superstructure of "silicene" on Pt(111). Based on their theoretical calculation, they believed that a Si_3Pt surface alloy was formed that resembles a twisted kagome lattice. By an extension of their interpretation, they suggested that the (√19×√19) superstructure of Ge on Pt(111) in [8] is also a surface alloy composed of Ge_3Pt tetramers. In another study, Au(111) was chosen as a possible substrate for the formation of germanene because alloy formation was believed to be avoided using this substrate. Deposition of one monolayer (ML) of Ge on Au(111) at ≈200 °C resulted in low energy electron diffraction (LEED) data showing some superstructure spots interpreted as diffraction from (√19×√19), (√7×√7) and (5×5) germanene phases [10]. Only the (√7×√7) periodicity was observed by STM, but the resolution was not sufficient to identify an atomic structure directly from the image. Qin et al. [11] presented results of bilayer germanene on Cu(111) at room temperature. Scanning tunneling spectroscopy showed a "V" shaped density of states, which was also observed by Zhang et al. [12], who synthesized germanene on MoS_2 at room temperature. Al(111) was chosen as a substrate to deposit germanene by Derivaz et al. [13] with the motivation that it is a simple unreconstructed metal with surface density of states dominated by s-electrons. A monolayer of Ge formed at a "magic" temperature (in a range of 20 °C around 87 °C) was interpreted as a germanene layer. Well-resolved STM images showed a honeycomb arrangement of blobs corresponding to a (3×3) periodicity with respect to Al(111). An optimized model of (2×2) germanene on a (3×3) Al unit cell was presented. Two Ge atoms were located on top of Al atoms 1.21–1.23 Å higher than the other Ge atoms. Ge deposition at temperatures below the "magic" range was reported to show disorder with a blurred (1×1) LEED pattern, while higher temperatures were reported to result in a sharp (1×1) LEED pattern.

The structure of Ge on Al(111) and the model suggested in [13] were subjected to an investigation using total-reflection high-energy positron diffraction (TRHEPD) by Fukaya et al. [14]. In this study, 1 ML of Ge was deposited on Al(111) held at 350 K. The evaporation rate was ≈0.018 ML/min. These parameters are close to the ones in [13] and the formation of a (3×3) superstructure was confirmed by reflection high energy diffraction (RHEED). Interestingly, Fukaya et al. arrived at a different conclusion about the model for the (3×3) superstructure. From their TRHEPD data, they concluded that only one Ge atom per unit cell is higher than the other ones. They proposed an explanation to the discrepancy between the STM results in [13] and their results by suggesting that the second Ge atom might be displaced by the interaction with the STM tip (external electric field applied during scanning).

In this paper, we present new data on the Ge/Al(111) system which significantly broadens the view on germanene formation. We show that it is possible to grow well-ordered monolayer Ge at temperatures significantly higher than 87 °C. After deposition at a substrate temperature of ≈200 °C, sharp LEED patterns were observed for two phases, i.e., a 3×3 phase and a new √7×√7 superstructure. These phases, formed at higher temperature, deviate from the low temperature phases in the sense that the STM images show hexagonal patterns in contrast to the honeycomb pattern reported in [13]. Our experimental data in combination with DFT calculations lead to a new model that can explain the experimental observations in terms of buckled germanene.

Results and Discussion

Figure 1a shows a LEED pattern, which clearly reveals the coexistence of (3×3) and (√7×√7) periodicities. We find that these two reconstructions coexist with different relative intensities depending on the Ge deposition rate. At a higher rate, e.g., ≈0.55 ML/min the (√7×√7) spots appear clearly in the LEED pattern. When Ge is deposited at a lower rate, e.g., ≈0.37 ML/min, (3×3) spots dominate, see Figure 1b.

Considering the theoretical value for the germanene lattice (3.92–4.06 Å) and the Al(111) surface lattice (2.864 Å) the (2×2) germanene on (√7×√7) Al(111) has less mismatch than on (3×3) Al(111). Furthermore, these two reconstructions have different signs of the stress, so a coexistence could probably reduce the surface energy.

Figure 2a is an atomically resolved STM image showing two rotated domains of the (√7×√7) reconstruction with a measured periodicity of ≈7.5 Å. The orientations of these two domains are indicated by two blue lines, which are labeled ±19°, respectively. The 0° orientation is indicated by the line in Figure 2b,

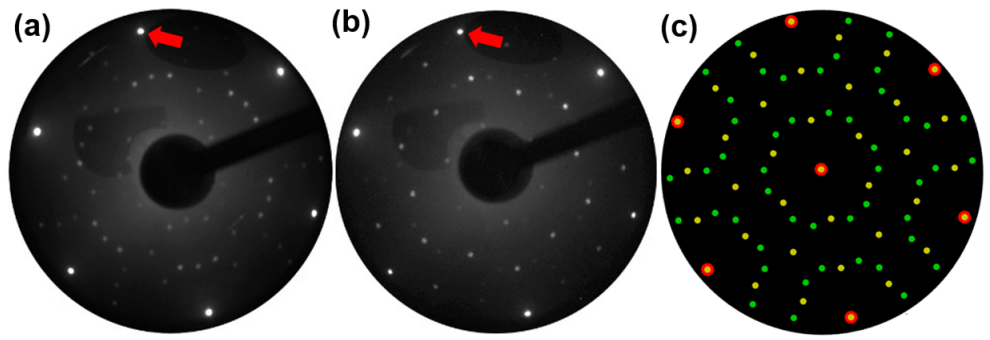

Figure 1: (a) LEED pattern obtained at an electron energy of 55 eV from Al(111) with 0.6 ML of Ge deposited at a rate of 0.55 ML/min at a sample temperature of around 200 °C. Diffraction spots corresponding to (3×3) and two domains of (√7×√7) periodicities are clearly observed. (b) LEED pattern obtained at an electron energy of 50 eV from a sample deposited at a rate of 0.37 ML/min. The (3×3) spots are dominating while the (√7×√7) spots are significantly weaker compared to (a). One (1×1) diffraction spot from Al(111) is indicated by a red arrow in (a) and (b). (c) Schematic LEED pattern showing the combination of (3×3) and two domains of (√7×√7) reconstructions. Red circles, yellow spots and blue spots represent Al (1×1), (3×3) and two domains of (√7×√7), respectively.

which is an atomically resolved STM image of the (3×3) reconstruction with a measured periodicity of ≈8.5 Å. Both reconstructions show a hexagonal structure instead of the honeycomb structure of germanene prepared at low temperature (≈87 °C) [13].

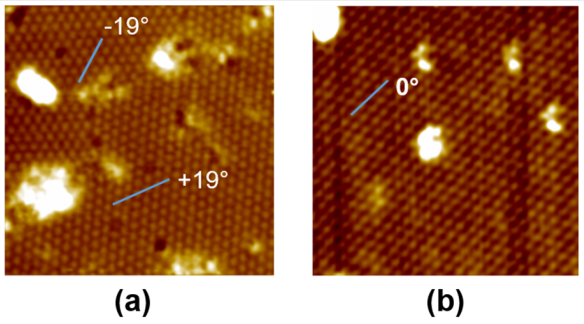

Figure 2: (a) Atomically resolved filled state STM image of a ≈19 × 19 nm^2 area showing two rotated hexagonal structures with √7×√7 periodicity. The angle difference between the two blue lines is ≈38° which corresponds to the ±19.1° orientations of the two √7×√7 domains with respect to Al(111). (b) Atomically resolved filled state STM image of a ≈19 × 19 nm^2 area showing a single hexagonal structure with (3×3) periodicity. Both images were obtained at room temperature with a sample bias of −1.20 V and a tunneling current of 200 pA.

It is interesting to consider the structural results by Fukaya et al. [14] obtained from the (3×3) reconstruction prepared in a way similar to that in [13], i.e., at low sample temperature and a low evaporation rate. The results from the TRHEPD technique favored an interpretation of the structure as a germanene layer with one Ge atom per (3×3) cell being higher than the other ones and a corresponding model was presented. However, some restrictions during the relaxation prevented their model from being fully relaxed. Starting from their hexagonal model with one Ge atom higher, we find that it relaxes to the honeycomb structure of the model in [13].

We present a natural modification of the model proposed in [14] that can explain the hexagonal appearance of the Ge layer on Al(111). By making a lateral translation of the germanene layer, one can locate two Ge atoms (Ge(4) and Ge(8) in Figure 3) above threefold hollow sites of Al(111). Figure 3a and Figure 3c show fully relaxed atomic models for (2×2) germanene on (3×3)- and (√7×√7)-Al(111). Atom 4 is high while atom 8 is close in height to the rest of the Ge atoms. The height difference (Δz) between Ge(4) and the average level of the other Ge atoms in the (3×3) and (√7×√7) models in Figure 3 is 2.13 and 1.96 Å, respectively, which is much larger than the values (1.21–1.23 Å) in [13] and 0.94 Å in [14]. Figure 3b and Figure 3d show simulated STM images for the (3×3) and (√7×√7) models, respectively, which reproduce the hexagonal structure of the STM images in Figure 2. The detailed information of these two models is available in Supporting Information File 1.

Stephan et al. [15] have presented electron spectroscopy data of the Al 2p and Ge 3d core levels for the (3×3) phase. The Ge layer was prepared at a temperature of about 87 °C and a low evaporation rate (0.005 ML/min) as in [13]. Although no structural information was obtained from the sample used for the core-level study, the authors assumed that the surface had the honeycomb type of (3×3) structure reported in [13]. A Ge 3d spectrum, obtained at a photon energy of 130 eV, was fitted by four components of which one only corresponded to 1 or 2% of the total intensity. The other three components were assigned to three groups of atoms that could be defined from the model. The assignment proposed in [15] implied that the 3d intensity from the two upper Ge atoms was significantly higher than the sum of the intensities from the six remaining Ge atoms. It was suggested that photoelectron diffraction effects could explain the obvious discrepancy between the number of atoms and the

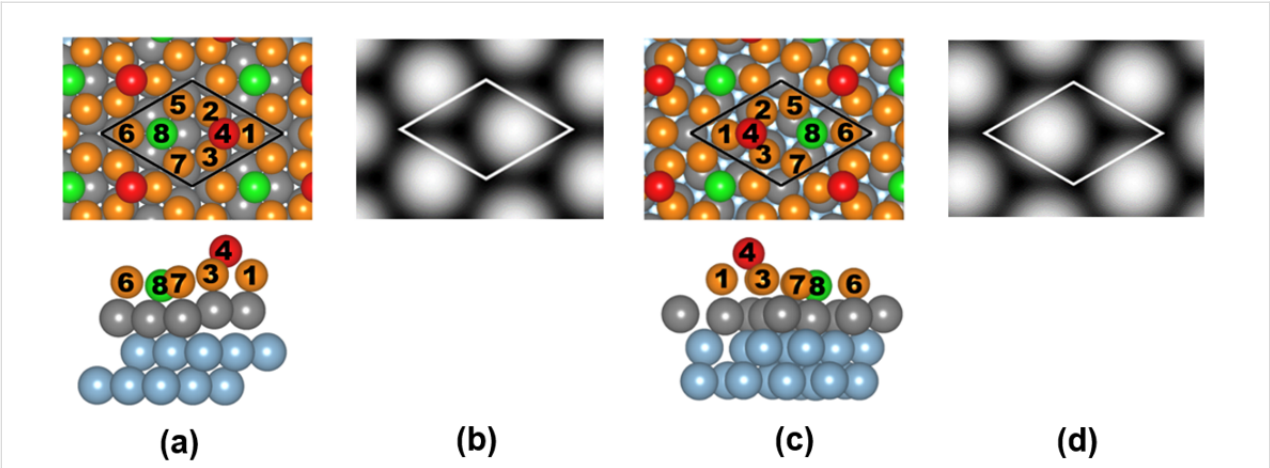

Figure 3: (a) Top and side views of the relaxed model of (2×2) germanene on (3×3) Al(111). The black cell represents a (3×3) reconstruction with respect to the Al(111) surface. (b) Calculated STM image generated from the local density of filled states and simulated in a constant current mode at a distance of ≈2 Å above Ge(4) for the model in (a). (c) Top and side views of the relaxed model of (2×2) germanene on (√7×√7) Al(111). The black cell represents a (√7×√7) reconstruction with respect to the Al(111) surface. Note that the orientation of the Al(111) substrate is different in (a) and (c). (d) Calculated STM image generated from the local density of filled states and simulated in a constant current mode at a distance of ≈2 Å above Ge(4) for the model in (c). The hexagonal structure is consistent with the experimental results in Figure 2. The highest Ge atom is colored red and labeled Ge(4), the lowest Ge atom is colored green and labeled Ge(8), the other Ge atoms are colored orange, Al atoms are colored light blue, except for the first layer Al atoms which are colored grey. The Ge(4) atom gives rise to the hexagonal pattern observed by STM.

core level intensities. An alternative assignment of the 3d components was suggested by Fukaya et al. [14]. It was proposed that the two smaller components, one on each side of the main component, should be assigned to the up and down Ge atoms and that the major component corresponds to the six remaining Ge atoms. Unfortunately, the intensities of the different components are not given in [15], so a quantitative evaluation is difficult.

In Figure 4, we present a Ge 3d core-level spectrum obtained from a surface on which the (3×3) reconstruction was dominating, as verified by LEED patterns at different electron energies. The spectrum was measured using a photon energy of 135 eV in normal emission. A first attempt to analyze the Ge 3d spectrum is based on grouping Ge atoms by their local environment. In this way one can identify four groups of atoms in the (3×3) model, i.e., Ge(1-3), Ge(4), Ge(5-7) and Ge(8). A calculation of the charges was made using the Bader scheme within VASP. The Ge(1-3) atoms gain 0.18–0.19 electron/atom, while Ge(4) loses 0.15 electron. Ge(5-7) atoms gain 0.33–0.34 electron/atom and Ge(8) gains 0.40 electron. Thus from the Bader charge, four distinct groups of Ge atoms can be verified. A fit using four spin-orbit split components is shown in Figure 4. The relative intensities of components SC1-4 deviate from the expectation that the relative intensities of the four components should be in rough agreement with 1:3:3:1. The intensity of SC2 is quite large while the intensity of SC3 is too small to match an expected intensity of the Ge(5-7) and Ge(1-3) atoms, respectively. Since the LEED pattern showed weak (√7×√7) spots, one has to

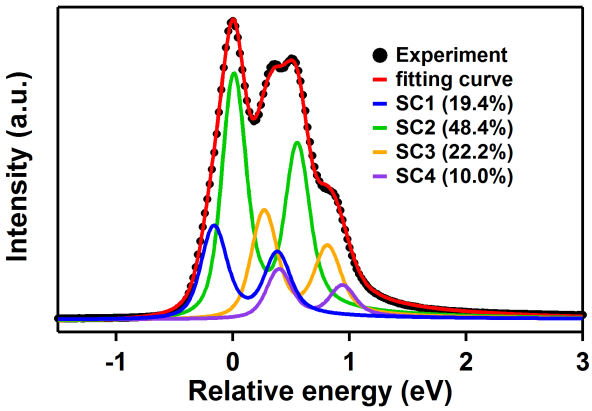

Figure 4: Ge 3d core-level spectrum obtained at a photon energy of 135 eV in normal emission. The dots are the experimental data and the fitting curve is the sum of the SC1 to SC4 components. The relative intensities of the four components are shown as a percentage of the total area in the figure. Fitting parameters: Spin-orbit split: 0.545 eV, Branching ratio: 0.67 for SC1 and SC2, 0.63 for SC3 and SC4. Gaussian widths: 177, 163, 183 and 174 meV, respectively, Lorentzian width: 110 meV. The asymmetry parameter of the Doniach–Šunjić line profile is 0.06. The energy shifts with respect to SC2 are −167, +269 and +389 meV.

consider contributions to the Ge 3d spectrum from (√7×√7) domains as well. Based on the Bader charges calculated for the (√7×√7) model, see Supporting Information File 1, one can expect contribution from (√7×√7) mainly to the intensity of SC2 while no intensity is expected at the position of SC3, which provides a plausible explanation to the difference in the SC2 and SC3 intensities. The above discussion of Ge 3d core level

spectrum is of course tentative and a rigorous analysis can only be done once truly single-phase samples can be achieved.

Conclusion

We have successfully grown monolayer Ge on Al(111) at a substrate temperature of about 200 °C, which is much higher than the "magic" temperature range mentioned in the literature. Our LEED and STM results confirm a coexistence of two well-ordered hexagonal structures with (3×3) and (√7×√7) periodicities with respect to Al (1×1). Our DFT calculations show that the Ge layer relaxes to a hexagonal structure when two Ge atoms are positioned above threefold hollow sites on Al(111). The experimental and theoretical findings are consistent with a strongly buckled (2×2) germanene layer, which is stable in two different orientations on Al(111). The structural model of the germanene is further supported by simulated STM images. The Ge 3d core-level spectrum can be fitted by four components that are suggested by the calculation of charge.

Experimental and Theoretical Details

Samples were prepared in situ in two separate ultrahigh vacuum (UHV) systems. One was equipped with LEED and STM (at Linköping University) and the other with LEED and a 2D electron analyzer for photoelectron spectroscopy (at MAX-lab in Lund). A clean Al(111) surface was prepared by repeated cycles of sputtering by Ar^+ ions (1 keV) and annealing at approximately 400 °C until a sharp (1×1) LEED pattern was obtained. About 0.6 ML of Ge was deposited at different rates between 0.37 ML/min and 0.55 ML/min while the Al(111) substrate was kept around 200 °C. The reason for depositing less than 1 ML of Ge is to avoid multi-layer formation and the confusion it may lead to. This type of preparation results in a sharp LEED pattern, which is a combination of diffraction from (3×3) and (√7×√7)R±19.1° reconstructions with respect to Al. STM images were recorded at room temperature using an Omicron variable temperature STM in the UHV system at Linköping University. All STM images were measured in constant current mode with a tunneling current of 200 pA. First-principles density functional theory (DFT) calculations were used to investigate the atomic structure of the Ge layer on the Al(111) surface. The structure was modeled by a periodic slab which was built with nine Al layers, one layer of Ge and 15 Å of vacuum spacing. (2×2) germanene was put on top of Al(111)-(3×3) and -(√7×√7)R19.1° supercells, respectively. The positions of all atoms were fully relaxed using the functional of Perdew, Burke and Ernzerhof (PBE) and the projector augmented wave (PAW) method Vienna ab initio simulation package (VASP) code [16]. The energy cutoff of the plane-wave basis set was 465 eV, and the k-point mesh was (4×4×1) for both cases. All atoms were relaxed until the average force was within 0.01 eV/Å. Simulated STM images were generated from local density of states according to the Tersoff–Hamann approach [17]. The charge transfer was calculated by the Bader scheme within VASP.

Supporting Information

Supporting Information File 1

Detailed information of the (3×3) and (√7×√7) models.
[http://www.beilstein-journals.org/bjnano/content/supplementary/2190-4286-8-195-S1.pdf]

Acknowledgements

Technical support from Dr. Johan Adell, Dr. Craig Polley and Dr. T. Balasubramanian at MAX-lab is gratefully acknowledged. Financial support was provided by the Swedish Research Council (Contract No. 621-2014-4764) and by the Linköping Linnaeus Initiative for Novel Functional Materials supported by the Swedish Research Council (Contract No. 2008-6582). The calculations were carried out at the National Supercomputer Centre (NSC), supported by the Swedish National Infrastructure for Computing (SNIC).

References

1. Takeda, K.; Shiraishi, K. *Phys. Rev. B* **1994,** *50,* 14916. doi:10.1103/PhysRevB.50.14916
2. Cahangirov, S.; Topsakal, M.; Aktürk, E.; Sahin, H.; Ciraci, S. *Phys. Rev. Lett.* **2009,** *102,* 236804. doi:10.1103/PhysRevLett.102.236804
3. Xu, Y.; Yan, B.; Zhang, H.-J.; Wang, J.; Xu, G.; Tang, P.; Duan, W.; Zhang, S.-C. *Phys. Rev. Lett.* **2013,** *111,* 136804. doi:10.1103/PhysRevLett.111.136804
4. Liu, C.-C.; Feng, W.; Yao, Y. *Phys. Rev. Lett.* **2011,** *107,* 076802. doi:10.1103/PhysRevLett.107.076802
5. Zhang, G.-F.; Li, Y.; Wu, C. *Phys. Rev. B* **2014,** *90,* 075114. doi:10.1103/PhysRevB.90.075114
6. Wu, S.-C.; Shan, G.; Yan, B. *Phys. Rev. Lett.* **2014,** *113,* 256401. doi:10.1103/PhysRevLett.113.256401
7. Bampoulis, P.; Zhang, L.; Safaei, A.; van Gastel, R.; Poelsema, B.; Zandvliet, H. J. W. *J. Phys.: Condens. Matter* **2014,** *26,* 442001. doi:10.1088/0953-8984/26/44/442001
8. Li, L.; Lu, S.-z.; Pan, J.; Qin, Z.; Wang, Y.-q.; Wang, Y.; Cao, G.-y.; Du, S.; Gao, H.-J. *Adv. Mater.* **2014,** *26,* 4820. doi:10.1002/adma.201400909
9. Švec, M.; Hapala, P.; Ondráček, M.; Merino, P.; Blanco-Rey, M.; Mutombo, P.; Vondráček, M.; Polyak, Y.; Martín, G. J. A.; Jelínek, P. *Phys. Rev. B* **2014,** *89,* 201412. doi:10.1103/PhysRevB.89.201412
10. Dávila, M. E.; Xian, L.; Cahangirov, S.; Rubio, A.; Le Lay, G. *New J. Phys.* **2014,** *16,* 095002. doi:10.1088/1367-2630/16/9/095002
11. Qin, Z.; Pan, J.; Lu, S.; Shao, Y.; Wang, Y.; Du, S.; Gao, H.-J.; Cao, G. *Adv. Mater.* **2017,** *29,* 1606046. doi:10.1002/adma.201606046
12. Zhang, L.; Bampoulis, P.; Rudenko, A. N.; Yao, Q.; van Houselt, A.; Poelsema, B.; Katsnelson, M. I.; Zandvliet, H. J. W. *Phys. Rev. Lett.* **2016,** *117,* 059902. doi:10.1103/PhysRevLett.117.059902
13. Derivaz, M.; Dentel, D.; Stephan, R.; Hanf, M.-C.; Mehdaoui, A.; Sonnet, P.; Pirri, C. *Nano Lett.* **2015,** *15,* 2510–2516. doi:10.1021/acs.nanolett.5b00085

14. Fukaya, Y.; Matsuda, I.; Feng, B.; Mochizuki, I.; Hyodo, T.; Shamoto, S.-i. *2D Mater.* **2016,** *3,* 035019. doi:10.1088/2053-1583/3/3/035019
15. Stephan, R.; Hanf, M. C.; Derivaz, M.; Dentel, D.; Asensio, M. C.; Avila, J.; Mehdaoui, A.; Sonnet, P.; Pirri, C. *J. Phys. Chem. C* **2016,** *120,* 1580–1585. doi:10.1021/acs.jpcc.5b10307
16. Kresse, G.; Joubert, D. *Phys. Rev. B* **1999,** *59,* 1758. doi:10.1103/PhysRevB.59.1758
17. Tersoff, J.; Hamann, D. R. *Phys. Rev. B* **1985,** *31,* 805. doi:10.1103/PhysRevB.31.805

License and Terms

BEILSTEIN JOURNAL OF NANOTECHNOLOGY

Intercalation of Si between MoS_2 layers

Rik van Bremen‡[1], Qirong Yao‡[1], Soumya Banerjee[2], Deniz Cakir[2], Nuri Oncel[2] and Harold J. W. Zandvliet*[1]

Full Research Paper

Open Access

Address:
[1]Physics of Interfaces and Nanomaterials, MESA+ Institute for Nanotechnology, University of Twente, P.O. Box 217, 7500AE Enschede, Netherlands and [2]Department of Physics and Astrophysics, University of North Dakota, Grand Forks, ND 58202, USA

Email:
Harold J. W. Zandvliet* - h.j.w.zandvliet@utwente.nl

* Corresponding author ‡ Equal contributors

Keywords:
intercalation; molybdenum disulfide; scanning tunneling microscopy; silicene; two-dimensional materials

Beilstein J. Nanotechnol. **2017,** *8,* 1952–1960.
doi:10.3762/bjnano.8.196

Received: 29 March 2017
Accepted: 21 August 2017
Published: 19 September 2017

This article is part of the Thematic Series "Silicene, germanene and other group IV 2D materials".

Guest Editor: P. Vogt

Abstract

We report a combined experimental and theoretical study of the growth of sub-monolayer amounts of silicon (Si) on molybdenum disulfide (MoS_2). At room temperature and low deposition rates we have found compelling evidence that the deposited Si atoms intercalate between the MoS_2 layers. Our evidence relies on several experimental observations: (1) Upon the deposition of Si on pristine MoS_2 the morphology of the surface transforms from a smooth surface to a hill-and-valley surface. The lattice constant of the hill-and-valley structure amounts to 3.16 Å, which is exactly the lattice constant of pristine MoS_2. (2) The transitions from hills to valleys are not abrupt, as one would expect for epitaxial islands growing on-top of a substrate, but very gradual. (3) $I(V)$ scanning tunneling spectroscopy spectra recorded at the hills and valleys reveal no noteworthy differences. (4) Spatial maps of dI/dz reveal that the surface exhibits a uniform work function and a lattice constant of 3.16 Å. (5) X-ray photo-electron spectroscopy measurements reveal that sputtering of the MoS_2/Si substrate does not lead to a decrease, but an increase of the relative Si signal. Based on these experimental observations we have to conclude that deposited Si atoms do not reside on the MoS_2 surface, but rather intercalate between the MoS_2 layers. Our conclusion that Si intercalates upon the deposition on MoS_2 is at variance with the interpretation by Chiappe et al. (*Adv. Mater.* **2014**, *26*, 2096–2101) that silicon forms a highly strained epitaxial layer on MoS_2. Finally, density functional theory calculations indicate that silicene clusters encapsulated by MoS_2 are stable.

Introduction

Since the discovery of graphene [1-4] interest has extended to the search for other 2D materials with properties similar to graphene. One appealing candidate is silicene, a graphene-like 2D allotrope of silicon. The first calculations of graphite-like allotropes of silicon and germanium were performed by Takeda and Shiraishi in 1994 [5]. These authors pointed out that two-dimensional silicon and germanium are not planar but buckled, i.e., the two sub-lattices of the honeycomb lattice are displaced with respect to each other in a direction normal to the two-dimensional sheet. In addition, the calculations of Takeda and

Shiraishi [5] also revealed that silicene and germanene are semi-metals, like graphene. In 2007, Guzmán-Verri and Lew Yan Voon [6] performed tight-binding calculations of two-dimensional silicon. They pointed out that the graphite-like silicon sheet has linearly dispersing energy bands near the *K* points of the Brillouin zone, very comparable to graphene. Inspired by this analogy they put forward the name silicene for the two-dimensional silicon. Interestingly, the linear dispersing energy bands at the *K* points, the so-called Dirac cones, are robust against the buckling of the silicene lattice [5,7]. In 2009, Cahangirov et al. [7] found that germanene also exhibits similar properties as graphene and silicene.

Similar to graphene, the electrons near the Fermi level in free-standing silicene are predicted to behave as massless Dirac fermions [6]. The broken sub-lattice symmetry of silicene allows for the opening of a band gap in this material [8-12]. This band gap makes silicene a very appealing candidate for field-effect-based devices. Another attractive property of silicene is its spin–orbit coupling, which is substantially larger than the spin–orbit coupling in graphene [13,14].

Silicene does not occur in nature and therefore it has to be synthesized. Several studies have reported on the growth of a 2D silicon layer on Ag(111) [15-17]. Unfortunately, due to the strong coupling between Si ad-layer and Ag substrate, the interesting Dirac properties of silicene are destroyed [18]. Although a linear dispersion relation has been observed [17], it is argued by others that this band is related to the Ag substrate rather than to silicene [19] or to combined effects of silicene and the Ag(111) substrate [20,21]. Growth of silicon was also demonstrated on graphite, a van der Waals material, with the idea to suppress the interaction with the substrate and as such to preserve the Dirac properties [22]. Unfortunately, graphite is metallic, which could also affect the electronic bands of silicene in the vicinity of the Fermi level. Van der Waals materials with a band gap do not suffer from this limitation. Molybdenum disulfide (MoS_2) is a member of the transition metal dichalcogenide (TMD) family that belongs to the class of van der Waals materials. Bulk MoS_2 has a band gap of 1.29 eV, which increases to 1.90 eV for a monolayer of MoS_2 [23]. This means that MoS_2 has no states near the Fermi level and therefore hybridization with the energy bands of silicene near the Fermi level cannot occur. Recently, germanene, a 2D allotrope of germanium [24-28], has already been successfully grown on MoS_2 [29]. Chiappe et al. [30] deposited Si on MoS_2 and found that Si forms an epitaxially strained layer on top of MoS_2 with a lattice constant identical to the MoS_2 lattice constant, i.e., 3.16 Å. A study confirming the two-dimensionality of deposited Si on MoS_2 has recently been carried out using variable-angle X-ray photoelectron spectroscopy (XPS) [31]. It should be pointed out here that this study showed that the S $2p_{3/2}$ peak in MoS_2 is at around 167.6 eV, which is considerably higher than the pure core-level line of pure S. This high value might be an indication of contamination with O [32] or Ni [33].

Here we revisit the growth of Si on MoS_2. Our scanning tunneling microscopy (STM) observations are very similar to those reported by Chiappe et al. [30]. However, we arrive at the conclusion that Si intercalates between the MoS_2 layers. In order to verify our conclusion we have performed additional spectroscopic measurements. These additional spectroscopic measurements unambiguously reveal that sub-monolayer amounts of Si deposited on MoS_2 at room temperature do not reside on top of MoS_2, but intercalate between the MoS_2 layers.

Experimental

The scanning tunneling microscopy and spectroscopy measurements were performed with an Omicron STM-1 room-temperature scanning tunneling microscope in ultra-high vacuum (UHV). The UHV system is composed of three separate chambers: a load-lock chamber for a quick entry of new samples and STM tips, a preparation chamber with facilities for sample heating, ion bombardment and evaporation of silicon and an STM chamber. The base pressures in the STM chamber and the preparation chamber are below 3×10^{-11} mbar and 5×10^{-11} mbar, respectively. The MoS_2 samples are purchased from HQ graphene. Prior to inserting the samples into the lock-load system they were cleaned by mechanical exfoliation. Silicon was deposited on the MoS_2 samples using a custom-built Si evaporator, which consists of a small piece of a Si wafer that can be heated resistively. The distance between substrate and evaporator is about 10 cm. The silicon was deposited at a rather low deposition rate of 0.8 nm·h^{-1}. The silicon evaporator was calibrated by depositing a sub-monolayer amount of Si on a Ge(001) substrate. The Ge(001) surface was cleaned by applying several cycles of Ar ion sputtering and annealing. After deposition and mild annealing at a temperature of 450–500 K, the Ge(001) substrate was inserted into the STM and subsequently the areal coverage of the epitaxial Si islands was determined. $I(V)$ curves are recorded at constant height at 450 ms per curve. Spatial maps of dI/dz are measured using a lock-in amplifier. A small high frequency (ca. 1.9 kHz) sinusoidal signal is added to the z-piezo and the tunnel current is fed into the lock-in amplifier. The output signal of the lock-in amplifier, which is proportional to dI/dz, is measured simultaneously with the topography.

MoS_2 samples used for the X-ray photoelectron spectroscopy (XPS) experiments were purchased from nanoScience Instruments. The MoS_2 samples were exfoliated before Si deposition. In a separate UHV chamber, Si was deposited on the MoS_2

sample via resistive heating of a small piece of a silicon wafer and then the MoS_2 sample was quickly transferred to the XPS chamber. During this transfer the sample was exposed to ambient conditions. The deposited amount of Si was 0.5 monolayers. The base pressure of both chambers is below 4×10^{-10} mbar. Both MoS_2 and Si/MoS_2 samples were measured with a monochromatic Al Kα (1486.6 eV) X-ray source with a pass energy of 89.5 eV and 35.75 eV for survey and high-resolution scans, respectively. During the XPS measurements, the pressure was kept at or below 1×10^{-9} mbar. The angle between the X-ray source, which is aligned along the surface normal, and spectrometer is 54.7°. All XPS core-level spectra were analyzed using Augerscan software, which is equipped with its own curve-fitting program. The core-level peaks are fitted using a Gaussian–Lorentzian (GL) function to include the instrumental response function along with the core-level line shape. The secondary-electron background was subtracted using a Shirley function [34]. The energy differences between the 3d and 2p spin–orbit couples were set to 3.13 eV and 1.18 eV, respectively. The ratios of the areas of the doublet peaks were also fixed. During sputtering the pressure is increased to 3×10^{-8} mbar by leaking in Ar gas while the pressure around the filament in the differentially pumped argon gas chamber increased to 1×10^{-4} mbar. The sample was sputtered with a beam of Ar ions with 1 kV energy. The emission current used was 25 mA, which resulted in an ion current of 0.33 μA. The shape of the beam is circular with a diameter of approximately 2 mm.

First-principles calculations are based on the projector-augmented wave (PAW) method [35,36] within DFT as implemented in the Vienna ab initio simulation package (VASP) [37]. The exchange–correlation interactions are treated using the generalized gradient approximation (GGA) within the Perdew–Burke–Ernzerhof (PBE) formulation [38]. The plane waves are expanded with an energy cut of 400 eV. Since the semi-local functionals, such as GGA, fail to describe weakly interacting systems, we also take into account the van der Waals interaction [39,40]. Brillouin-zone integrations for structure relaxations are approximated by using the special *k*-point sampling of the Monkhorst–Pack scheme with a Γ-centered $3 \times 3 \times 1$ grid [41]. In order to minimize the periodic interactions along the *z*-direction (the direction perpendicular to the plane of the hetero-trilayer) the vacuum space between the layers has a width of at least 15 Å.

Results and Discussion

In Figure 1, STM images of pristine MoS_2 and MoS_2 after the deposition of ca. 0.2 monolayers of Si at room temperature are shown. The pristine MoS_2 surface appears very smooth. Usually only the top sulfur layer is resolved, resulting in a lattice with hexagonal symmetry and a lattice constant of 3.16 Å (see

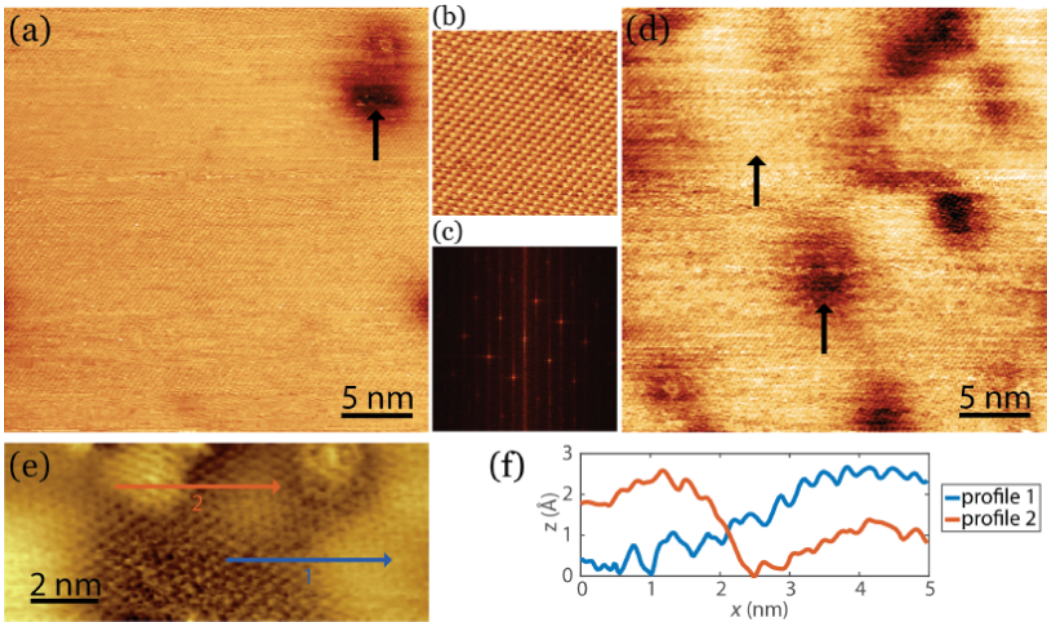

Figure 1: (a) STM image of pristine MoS_2 taken prior to the deposition of Si. The arrow indicates an intrinsic defect, which is often found on MoS_2. (b) High-resolution STM image of pristine MoS_2. (c) Fast Fourier-transform of pristine MoS_2 showing the hexagonal symmetry. (d) STM image taken after the deposition of 0.2 monolayers of Si. The arrows indicate a hill (bright) and a valley (dark). (e) High-resolution STM image taken after the deposition of 0.2 monolayers of Si. (f) Line scans taken along the lines indicated in panel (e). The sample bias is 1.2V and the tunnelling current is 0.5 nA.

Figure 1b,c). The pristine MoS_2 contains some intrinsic defects, which are visible as dark depressions as indicated by the arrow in Figure 1a. These defects are most probably caused by vacancies or interstitials and have been found to exhibit a metal-like behavior [42,43]. Upon the deposition of 0.2 monolayers of Si, the surface morphology converts to a hill-and-valley structure as shown in Figure 1d. The arrows indicate a bright hill and a dark valley. Upon further deposition of silicon, the surface becomes rougher and more difficult to scan as shown in Figure S1 in Supporting Information File 1. When even more silicon is deposited, silicon clusters on top of MoS_2 become visible. A close-up image of the transition of a hill to a valley is represented in Figure 1e. The line profiles indicated in the figure correspond to the cross sections shown in Figure 1f. The typical height variation of a transition is found to be of several angstroms. We found a similar height variation using density functional theory (DFT) calculations of the intercalation of a single silicon layer in between two MoS_2 layers. These calculations are discussed after the presentation of the experimental results. It is immediately obvious from Figure 1f that the transition from a hill to a valley is very gradual. Interestingly, the lattice constant of the hill-and-valley structure is identical to the lattice constant of pristine MoS_2, i.e. 3.16 Å. Both observations are similar to the observations reported by Chiappe et al. [30] who deposited 0.8 monolayers of silicon on MoS_2 (obtained from SPI) at 200 °C. Based on these observations Chiappe et al. [30] concluded that Si grows epitaxially on MoS_2 with a lattice constant that is identical to MoS_2. This implies that the Si layer is highly strained, indicative of a rather strong interaction between MoS_2 and Si. This seems unlikely, bearing in mind that MoS_2 is a van der Waals material. We tentatively put forward another interpretation, namely that Si intercalates between the MoS_2 layers. The gradual transition from a hill to a valley as well as the observation of the MoS_2 lattice constant after Si deposition nicely fits into this picture.

In order to verify our interpretation we have performed additional scanning tunneling spectroscopy (STS) measurements. $I(V)$ scanning tunneling spectra were recorded at the hills and valleys as indicated by the arrows in Figure 1d. Average spectroscopy curves of a hill and of a valley, which in total are comprised of 3500 spectra, are displayed in Figure 2. The $I(V)$ spectra are almost identical to each other. The small difference between both curves might be a residual effect of Si residing underneath the MoS_2 layer. If the top layer were a silicon cluster the $I(V)$ spectra would differ significantly as is shown in Figure S2 in Supporting Information File 1.

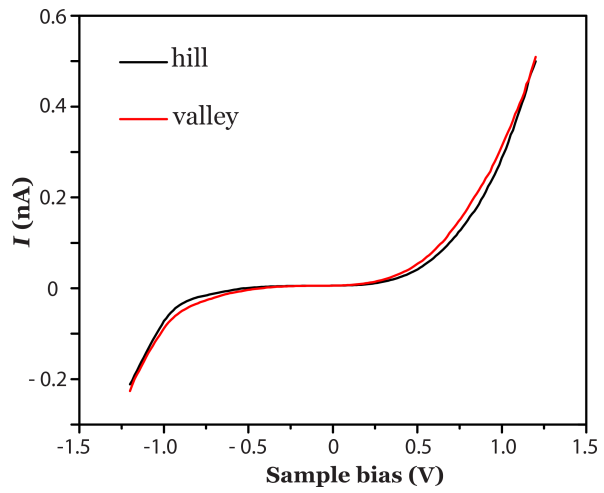

Figure 2: STS recorded at the hills (black curve) and at the valleys (red curve). Set points sample bias 1.2 V and tunnel current 0.5 nA.

In order to remove the large-scale height variation from the topography scan, we simultaneously recorded a spatial map of dI/dz (Figure 3). The dI/dz signal only depends on the effective work function, also referred to as the apparent barrier height, and not on any large-scale height variations [44,45]. It should

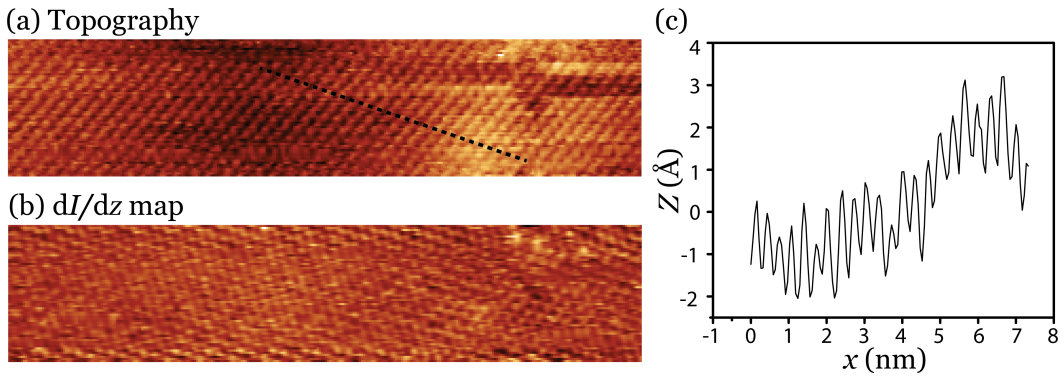

Figure 3: (a) STM image of a MoS_2 surface after the deposition of 0.2 monolayers of Si. (b) Spatial map of dI/dz. In both images the atomic structure is resolved. (c) Line- scan taken along the dotted line depicted in panel (a). Sample bias is 1.2 V and tunnel current is 0.5 nA.

be pointed out here that spatial maps of d*I*/d*z* often exhibit a resolution that is similar to normal topographic STM images without, of course, the large-scale height variations [44].

The results shown in Figure 3 make clear two points. First, since height information is not present in a d*I*/d*z* map we have to conclude that the surface is smooth and continuous. Second, d*I*/d*z* provides information on the apparent barrier height, which is a material property. No contrast is visible and therefore we have to conclude that we are dealing with the same material, i.e., MoS_2. Both these points provide compelling evidence that the deposited Si intercalates between the MoS_2 layers. For a comparable system, namely Si on WSe_2, we recently arrived at a similar conclusion [45].

XPS measurements have been performed to obtain insight of the chemical composition of the top layers. Before depositing Si, XPS measurements were carried out on pristine MoS_2 in order to find the exact positions of the Mo $3d_{5/2}$ and S $2p_{3/2}$ core-level peaks. (Figure 4a and Figure 4b, respectively). The Mo $3d_{5/2}$ and S $2p_{3/2}$ peaks were measured at 230.25 eV and 163.09 eV, respectively. The location of these peaks is in good agreement with [46,47].

The core-level spectra of Si, Mo and S after the deposition of 0.5 monolayers of Si on MoS_2 are shown in Figure 5a, Figure 5b and Figure 5c, respectively. A higher coverage than in the case of STM is used in order to yield a stronger signal in the XPS measurements. STM topography images with a higher coverage can be found in Figure S1 in Supporting Information File 1. The XPS data show two peaks associated with Si. The smaller peak, located at 98.13 eV, can be attributed to pristine Si. The other peak, measured at 103 eV, can be attributed to oxidized silicon [48]. The oxidation of Si occurs during the transfer of the sample from the growth chamber to the XPS chamber. During this transfer the sample was exposed to ambient conditions. A more detailed analysis reveals that only 5% of the Si is pristine, whereas the rest is oxidized. Upon sputtering of the MoS_2/Si sample with an Ar ion beam with 1 kV energy, we observe that the relative Si signal increases while the relative S signal decreases as can be seen in Figure S3 in Supporting Information File 1. This observation indicates that Si has intercalated between the MoS_2 layers. In addition, we also conclude that the intercalated Si can be oxidized.

It is well known that numerous elements have a strong tendency to intercalate between MoS_2 layers [49,50]. As for the intercalation mechanism of silicon in between MoS_2 layers, we can only speculate. A plethora of studies on the intercalation of different chemical species in TMDs have been reported from elements as small as lithium [51], sodium [52-54] and carbon [55] to elements as large as cesium [56,57] and gold [58]. Other studies report on the intercalation of silicon and other elements under graphene layers synthesized on metal substrates [59-61].

The driving force for intercalation is charge transfer between the intercalated atoms and the layered material [62,63] or thermodynamic stabilization [61,62]. The mechanism of intercalation was found to occur through cracks and wrinkles in the layers [60] and via edges [51]. Because the diffusion barrier of adsorbed silicon atoms on top of MoS_2 is assumed to be very low and the experiments are performed at room temperature, it is expected that silicon adatoms can easily diffuse over the surface to reach these cracks, wrinkles and step edges.

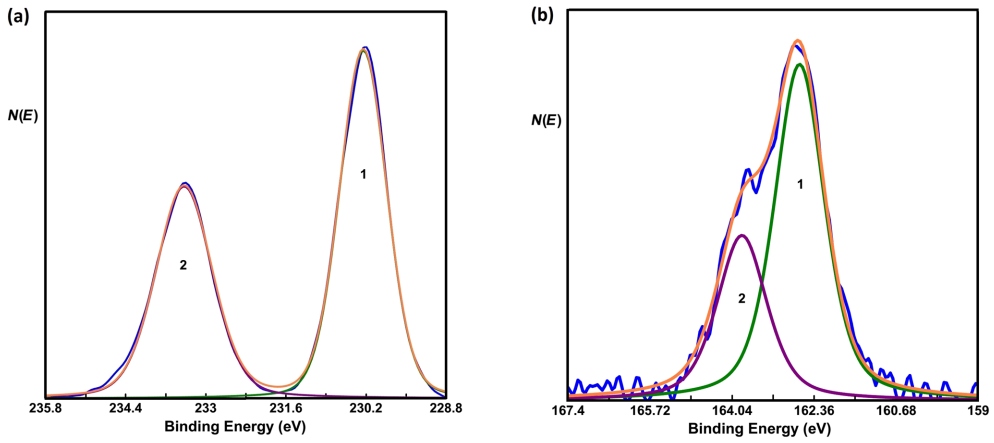

Figure 4: Core-level spectra of (a) Mo and (b) S before depositing Si. The spectra are fitted with two GL function peaks. In (a), 1 and 2 represent the Mo $3d_{5/2}$ and $3d_{3/2}$ peaks, respectively. In (b), 1 and 2 represent the S $2p_{3/2}$ and $2p_{1/2}$ peaks, respectively. In both figures, the resultant fitted spectra are represented by an orange line.

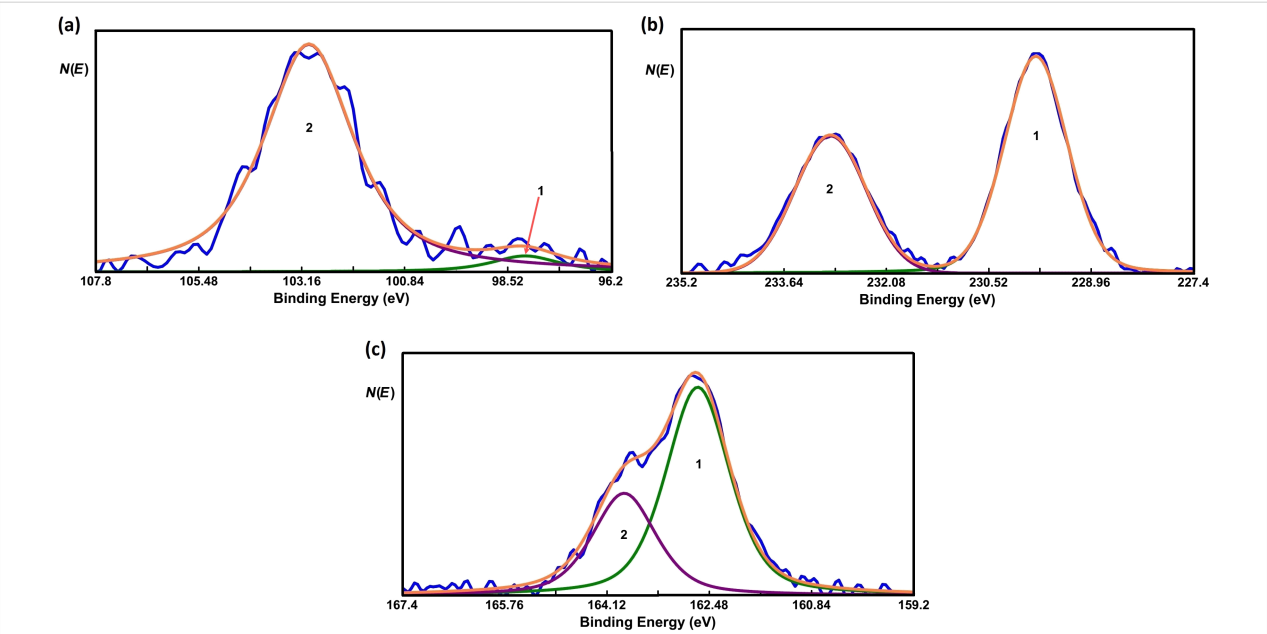

Figure 5: Core-level spectra of (a) Si, (b) Mo and (c) S after depositing Si. The peak-fitting procedure is the same as in Figure 4. In panel (a) a small peak at around 98.1 eV was needed to fit the tail of the peak at the lower-energy side. Orange lines represent the resultant fitted spectra.

In order to study the effect of the oxidation of intercalated silicon in more detail we measured the exact positions of the Mo $3d_{5/2}$ and S $2p_{3/2}$ peaks. Both peaks shift to a lower binding energy by about 0.45 eV. This shift cannot be interpreted as a simple chemical shift due to a chemical reaction of the involved elements, i.e., Mo/S/Si and O [64]. In addition, after the deposition of Si no significant changes in the FWHM of the peaks of Mo (0.97 before, 1.13 after) as well as of S (1.09 before, 1.21 after) were observed, indicating that no chemical reaction between MoS_2 and silicon oxide has occurred. It is very likely that the observed shift is attributed to a change in the position of the Fermi level.

It has been shown that the deposition of MoS_2 on a SiO_2 substrate with interface impurities leads to a charge transfer from the MoS_2 surface to the defect states and, thus, to the formation of surface dipoles [65]. These dipoles shift the Fermi level of MoS_2 closer to the valence band maximum (p-type). The shift of the Fermi level also leads to a shift in the binding energy of the Mo and S peaks to lower binding energies.

Next, we will discuss the results of our density functional theory calculations regarding the intercalated Si. To be consistent with experimental results we have fixed the lattice constant of MoS_2 to 3.16 Å. We first calculated the structural and electronic properties of hetero-trilayers composed of a silicene layer intercalated between two MoS_2 monolayers (MoS_2–silicene–MoS_2). Due to the large lattice mismatch, we have considered a commensurable supercell, in which we have placed a 5 × 5 silicene cell and a 6 × 6 MoS_2 cell on top of each other. For this configuration the lattice mismatch of the MoS_2–silicene–MoS_2 trilayer becomes less than 1%. Figure 6 shows the optimized structure of the MoS_2–silicene–MoS_2 hetero-trilayer. The calculated interlayer distance in a pristine

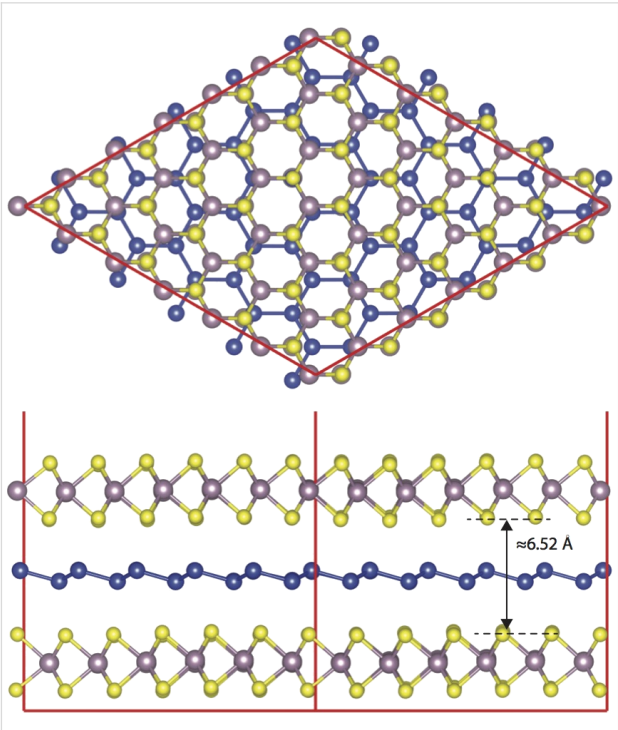

Figure 6: Top and side views of silicene intercalated in bilayer MoS_2.

MoS_2 bilayer is found to be 3.00 Å. Insertion of a silicene monolayer enlarges the interlayer separation between MoS_2 layers from 3 Å to 6.52 Å, corresponding to an increase of the interlayer separation of 3.52 Å.

In order to study the possible formation of silicene between the MoS_2 monolayers, we consider a buckled 2D silicon cluster (Si_{37}) consisting of six-membered silicon rings. We used a 7×7 super-cell structure for the MoS_2 bilayer. Initial and equilibrium geometries for both a free-standing as well as the intercalated silicon cluster inserted between the MoS_2 layers are shown in Figure 7. We found that a free-standing 2D buckled silicon cluster is, in contrast to an infinite silicene layer, not even metastable in vacuum and spontaneously transforms into a strongly buckled 3D assembly as seen in Figure 7a. The intercalated silicon cluster in Figure 7b also undergoes a remarkable structural reconstruction. The optimized structure of a silicon cluster encapsulated between two MoS_2 layers is totally different from the free-standing optimized silicon cluster in vacuum. This is noticeable in that the shape of the hexagons is not uniform as is the case for silicene. Especially at the edges, due to the presence of the Si dangling bonds, the hexagons are seriously distorted. However, intercalation between MoS_2 layers preserves the 2D buckled structure of the silicon cluster during the structure relaxation. Thus, we suggest that the intercalation of silicon atoms between MoS_2 layers may promote the formation of silicene, which interacts only weakly with the environment via van der Waals forces. We found that both top and bottom MoS_2 layers develop bumps due to the interaction with the silicon cluster. The average interlayer MoS_2 distance varies within the range of 5.5–6.2 Å, which corresponds to an increase in interlayer separation of 2.5-3.2 Å. This agrees well with the measured height variation.

Conclusion

In this work we revisited the growth of Si on MoS_2. STM topography data reveals that Si does not grow on top of the MoS_2 substrate, but rather intercalates in between the MoS_2 layers. It

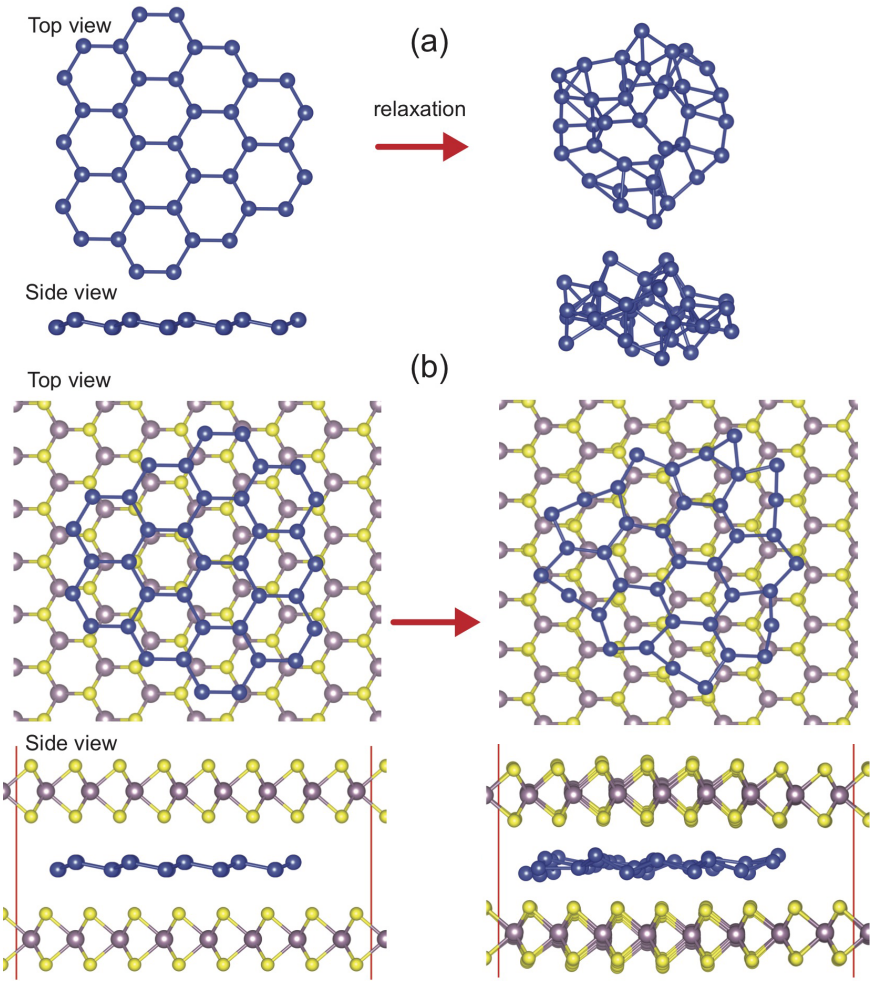

Figure 7: Initial (left) and equilibrium (right) structure of (a) a free standing and (b) an intercalated silicon cluster (Si_{37}).

is known that layered materials such as MoS_2 have a tendency to host intercalants. In this work we provide additional evidence for silicon intercalation by using STS and XPS. Since silicon intercalates it is interesting to scrutinize if there are possibilities to grow a 2D layer in between two layers of MoS_2. Our density functional theory calculations show that 2D silicon clusters intercalated between MoS_2 layers are stable.

Supporting Information

Supporting Information File 1

Additional experimental data.
[http://www.beilstein-journals.org/bjnano/content/supplementary/2190-4286-8-196-S1.pdf]

Acknowledgements

R.v.B. and H.J.W.Z. thank the Dutch organization for scientific research NWO for financial support (FV157 14TWDO07). Q.Y. thanks the China Scholarship Council for financial support. D.C. and N.O. thank ND EPSCoR (#UND0021231, #UND0014095) and UND for financial support. The computer resources used in this work are provided by the Computational Research Center (HPC-Linux cluster) at UND.

References

1. Novoselov, K. S.; Geim, A. K.; Morozov, S. V.; Jiang, D.; Zhang, Y.; Dubonos, S. V.; Grigorieva, I. V.; Firsov, A. A. *Science* **2004,** *306,* 666–669. doi:10.1126/science.1102896
2. Zhang, Y.; Tan, Y.-W.; Stormer, H. L.; Kim, P. *Nature* **2005,** *438,* 201–204. doi:10.1038/nature04235
3. Ohta, T.; Bostwick, A.; Seyller, T.; Horn, K.; Rotenberg, E. *Science* **2006,** *313,* 951–954. doi:10.1126/science.1130681
4. Castro Neto, A. H.; Guinea, F.; Peres, N. M. R.; Novoselov, K. S.; Geim, A. K. *Rev. Mod. Phys.* **2009,** *81,* 109–162. doi:10.1103/RevModPhys.81.109
5. Takeda, K.; Shiraishi, K. *Phys. Rev. B* **1994,** *50,* 14916–14922. doi:10.1103/PhysRevB.50.14916
6. Guzmán-Verri, G. G.; Lew Yan Voon, L. C. *Phys. Rev. B* **2007,** *76,* 075131. doi:10.1103/PhysRevB.76.075131
7. Cahangirov, S.; Topsakal, M.; Aktürk, E.; Şahin, H.; Ciraci, S. *Phys. Rev. Lett.* **2009,** *102,* 236804. doi:10.1103/PhysRevLett.102.236804
8. Song, Y.-L.; Zhang, S.; Lu, D.-B.; Xu, H.-r.; Wang, Z.; Zhang, Y.; Lu, Z.-W. *Eur. Phys. J. B* **2013,** *86,* 488. doi:10.1140/epjb/e2013-31078-4
9. Quhe, R.; Fei, R.; Liu, Q.; Zheng, J.; Li, H.; Xu, C.; Ni, Z.; Wang, Y.; Yu, D.; Gao, Z.; Lu, J. *Sci. Rep.* **2012,** *2,* 853. doi:10.1038/srep00853
10. Ni, Z.; Liu, Q.; Tang, K.; Zheng, J.; Zhou, J.; Qin, R.; Gao, Z.; Yu, D.; Lu, J. *Nano Lett.* **2012,** *12,* 113–118. doi:10.1021/nl203065e
11. Gao, N.; Li, J. C.; Jiang, Q. *Phys. Chem. Chem. Phys.* **2014,** *16,* 11673. doi:10.1039/C4CP00089G
12. Drummond, N. D.; Zólyomi, V.; Fal'ko, V. I. *Phys. Rev. B* **2012,** *85,* 075423. doi:10.1103/PhysRevB.85.075423
13. Kane, C. L.; Mele, E. J. *Phys. Rev. Lett.* **2005,** *95,* 226801. doi:10.1103/PhysRevLett.95.226801
14. Lew Yan Voon, L. C. *Chin. Phys. B* **2015,** *24,* 087309. doi:10.1088/1674-1056/24/8/087309
15. Lalmi, B.; Oughaddou, H.; Enriquez, H.; Kara, A.; Vizzini, S.; Ealet, B.; Aufray, B. *Appl. Phys. Lett.* **2010,** *97,* 223109. doi:10.1063/1.3524215
16. Jamgotchian, H.; Colignon, Y.; Hamzaoui, N.; Ealet, B.; Hoarau, J. Y.; Aufray, B.; Bibérian, J. P. *J. Phys.: Condens. Matter* **2012,** *24,* 172001. doi:10.1088/0953-8984/24/17/172001
17. Vogt, P.; De Padova, P.; Quaresima, C.; Avila, J.; Frantzeskakis, E.; Asensio, M. C.; Resta, A.; Ealet, B.; Le Lay, G. *Phys. Rev. Lett.* **2012,** *108,* 155501. doi:10.1103/PhysRevLett.108.155501
18. Lin, C.-L.; Arafune, R.; Kawahara, K.; Kanno, M.; Tsukahara, N.; Minamitani, E.; Kim, Y.; Kawai, M.; Takagi, N. *Phys. Rev. Lett.* **2013,** *110,* 076801. doi:10.1103/PhysRevLett.110.076801
19. Chen, M. X.; Weinert, M. *Nano Lett.* **2014,** *14,* 5189–5193. doi:10.1021/nl502107v
20. Feng, Y.; Liu, D.; Feng, B.; Liu, X.; Zhao, L.; Xie, Z.; Liu, Y.; Liang, A.; Hu, C.; Hu, Y.; He, S.; Liu, G.; Zhang, J.; Chen, C.; Xu, Z.; Chen, L.; Wu, K.; Liu, Y.-T.; Lin, H.; Huang, Z.-Q.; Hsu, C.-H.; Chuang, F.-C.; Bansil, A.; Zhou, X. J. *Proc. Natl. Acad. Sci. U. S. A.* **2016,** *113,* 14656–14661. doi:10.1073/pnas.1613434114
21. Fleurence, A.; Friedlein, R.; Ozaki, T.; Kawai, H.; Wang, Y.; Yamada-Takamura, Y. *Phys. Rev. Lett.* **2012,** *108,* 245501. doi:10.1103/PhysRevLett.108.245501
22. De Crescenzi, M.; Berbezier, I.; Scarselli, M.; Castrucci, P.; Abbarchi, M.; Ronda, A.; Jardali, F.; Park, J.; Vach, H. *ACS Nano* **2016,** *10,* 11163–11171. doi:10.1021/acsnano.6b06198
23. Mak, K. F.; Lee, C.; Hone, J.; Shan, J.; Heinz, T. F. *Phys. Rev. Lett.* **2010,** *105,* 136805. doi:10.1103/PhysRevLett.105.136805
24. Li, L.; Lu, S.; Pan, J.; Qin, Z.; Wang, Y.; Wang, Y.; Cao, G.; Du, S.; Gao, H.-J. *Adv. Mater.* **2014,** *26,* 4820–4824. doi:10.1002/adma.201400909
25. Dávila, M. E.; Xian, L.; Cahangirov, S.; Rubio, A.; Le Lay, G. *New J. Phys.* **2014,** *16,* 095002. doi:10.1088/1367-2630/16/9/095002
26. Bampoulis, P.; Zhang, L.; Safaei, A.; van Gastel, R.; Poelsema, B.; Zandvliet, H. J. W. *J. Phys.: Condens. Matter* **2014,** *26,* 442001. doi:10.1088/0953-8984/26/44/442001
27. Zhang, L.; Bampoulis, P.; van Houselt, A.; Zandvliet, H. J. W. *Appl. Phys. Lett.* **2015,** *107,* 111605. doi:10.1063/1.4931102
28. Acun, A.; Zhang, L.; Bampoulis, P.; Farmanbar, M.; van Houselt, A.; Rudenko, A. N.; Lingenfelder, M.; Brocks, G.; BPoelsema, K.; atsnelson, M. I.; Zandvliet, H. J. W. *J. Phys.: Condens. Matter* **2015,** *27,* 443002. doi:10.1088/0953-8984/27/44/443002
29. Zhang, L.; Bampoulis, P.; Rudenko, A. N.; Yao, Q.; van Houselt, A.; Poelsema, B.; Katsnelson, M. I.; Zandvliet, H. J. W. *Phys. Rev. Lett.* **2016,** *116,* 256804. doi:10.1103/PhysRevLett.116.256804
30. Chiappe, D.; Scalise, E.; Cinquanta, E.; Grazianetti, C.; van den Broek, B.; Fanciulli, M.; Houssa, M.; Molle, A. *Adv. Mater.* **2014,** *26,* 2096–2101. doi:10.1002/adma.201304783
31. Molle, A.; Lamperti, A.; Rotta, D.; Fanciulli, M.; Cinquanta, E.; Grazianetti, C. *Adv. Mater. Interfaces* **2016,** *3,* 1500619. doi:10.1002/admi.201500619
32. Wagner, C. D.; Taylor, J. A. *J. Electron Spectrosc. Relat. Phenom.* **1982,** *28,* 211–217. doi:10.1016/0368-2048(82)85044-5
33. Yu, X.-R.; Liu, F.; Wang, Z.-Y.; Chen, Y. *J. Electron Spectrosc. Relat. Phenom.* **1990,** *50,* 159–166. doi:10.1016/0368-2048(90)87059-W

34. Briggs, D.; Seah, M. P. *Practical Surface Analysis by Auger and X-Ray Photoelectron Spectroscopy;* John Wiley & Sons Ltd: New York, NY, U.S.A., 1983.
35. Kresse, G.; Furthmüller, J. *Phys. Rev. B* **1996,** *54,* 11169–11186. doi:10.1103/PhysRevB.54.11169
36. Blöchl, P. E. *Phys. Rev. B* **1994,** *50,* 17953–17979. doi:10.1103/PhysRevB.50.17953
37. Kresse, G.; Joubert, D. *Phys. Rev. B* **1999,** *59,* 1758–1775. doi:10.1103/PhysRevB.59.1758
38. Perdew, J. P.; Burke, K.; Ernzerhof, M. *Phys. Rev. Lett.* **1996,** *77,* 3865–3868. doi:10.1103/PhysRevLett.77.3865
39. Grimme, S.; Antony, J.; Ehrlich, S.; Krieg, H. *J. Chem. Phys.* **2010,** *132,* 154104. doi:10.1063/1.3382344
40. Grimme, S.; Ehrlich, S.; Goerigk, L. *J. Comput. Chem.* **2011,** *32,* 1456–1465. doi:10.1002/jcc.21759
41. Monkhorst, H. J.; Pack, J. D. *Phys. Rev. B* **1976,** *13,* 5188–5192. doi:10.1103/PhysRevB.13.5188
42. Addou, R.; Colombo, L.; Wallace, R. M. *ACS Appl. Mater. Interfaces* **2015,** *7,* 11921–11929. doi:10.1021/acsami.5b01778
43. Bampoulis, P.; van Bremen, R.; Yao, Q.; Poelsema, B.; Zandvliet, H. J. W.; Sotthewes, K. *ACS Appl. Mater. Interfaces* **2017,** *9,* 19278–19286. doi:10.1021/acsami.7b02739
44. Wiesendanger, R. *Scanning Probe Microscopy and Spectroscopy: Methods and Applications;* Cambridge University Press: Cambridge, United Kingdom, 1994. doi:10.1017/CBO9780511524356
45. Yao, Q.; van Bremen, R.; Zandvliet, H. J. W. *Appl. Phys. Lett.* **2016,** *109,* 243105. doi:10.1063/1.4972036
46. Lince, J. R.; Carré, D. J.; Fleischauer, P. D. *Effects of Argon-Ion Bombardment on the Basal Plan Surface of MoS2 – Report Sd-TR-86-95;* Space Division, Air Force Systems Command: Los Angeles, CA, U.S.A., 1987.
47. Vissers, J. P. R.; Groot, C. K.; van Oers, E. M.; Beer, D.; Prins, R. *Bull. Soc. Chim. Belg.* **1984,** *93,* 813–822. doi:10.1002/bscb.19840930822
48. Finster, J.; Klinkenberg, E.-D.; Heeg, J.; Braun, W. *Vacuum* **1990,** *41,* 1586–1589. doi:10.1016/0042-207X(90)94025-L
49. Benavente, E.; Santa Ana, M. A.; Mendizábal, F.; González, G. *Coord. Chem. Rev.* **2002,** *224,* 87–109. doi:10.1016/S0010-8545(01)00392-7
50. Vázquez, A. *Mater. Lett.* **1998,** *35,* 22–27. doi:10.1016/S0167-577X(97)00224-3
51. Xiong, F.; Wang, H.; Liu, X.; Sun, J.; Brongersma, M.; Pop, E.; Cui, Y. *Nano Lett.* **2015,** *15,* 6777–6784. doi:10.1021/acs.nanolett.5b02619
52. Brauer, H. E.; Ekvall, I.; Olin, H.; Starnberg, H. I.; Wahlström, E.; Hughes, H. P.; Strocov, V. N. *Phys. Rev. B* **1997,** *55,* 10022. doi:10.1103/PhysRevB.55.10022
53. Brauer, H. E.; Starnberg, H. I.; Holleboom, L. J.; Strocov, V. N.; Hughes, H. P. *Phys. Rev. B* **1998,** *58,* 10031–10045. doi:10.1103/PhysRevB.58.10031
54. Ekvall, I.; Brauer, H. E.; Wahlström, E.; Olin, H. *Phys. Rev. B* **1999,** *59,* 7751. doi:10.1103/PhysRevB.59.7751
55. Kwieciñski, W.; Sotthewes, K.; Poelsema, B.; Zandvliet, H. J. W.; Bampoulis, P. *J. Colloid Interface Sci.* **2017,** *505,* 776–782. doi:10.1016/j.jcis.2017.06.076
56. Pettenkofer, C.; Jaegermann, W.; Schellenberger, A.; Holub-Krappe, E.; Papageorgopoulos, C. A.; Kamaratos, M.; Papageorgopoulos, A. *Solid State Commun.* **1992,** *84,* 921–926. doi:10.1016/0038-1098(92)90459-M
57. Starnberg, H. I.; Brauer, H. E.; Holleboom, L. J.; Hughes, H. P. *Phys. Rev. Lett.* **1993,** *70,* 3111–3114. doi:10.1103/PhysRevLett.70.3111
58. Iyikanat, F.; Sahin, H.; Senger, R. T.; Peeters, F. M. *APL Mater.* **2014,** *2,* 092801. doi:10.1063/1.4893543
59. Meng, L.; Wu, R.; Zhou, H.; Li, G.; Zhang, Y.; Li, L.; Wang, Y.; Gao, H.-J. *Appl. Phys. Lett.* **2012,** *100,* 083101. doi:10.1063/1.3687688
60. Petrović, M.; Šrut Rakić, I.; Runte, S.; Busse, C.; Sadowski, J. T.; Lazić, P.; Pletikosić, I.; Pan, Z.-H.; Milun, M.; Pervan, P.; Atodiresei, N.; Brako, R.; Šokčević, D.; Valla, T.; Michely, T.; Kralj, M. *Nat. Commun.* **2013,** *4,* 2772. doi:10.1038/ncomms3772
61. Li, G.; Zhou, H.; Pan, L.; Zhang, Y.; Huang, L.; Xu, W.; Du, S.; Ouyang, M.; Ferrari, A. C.; Gao, H.-J. *J. Am. Chem. Soc.* **2015,** *137,* 7099–7103. doi:10.1021/ja5113657
62. Whittingham, M. S.; Chianelli, R. R. *J. Chem. Educ.* **1980,** *57,* 569. doi:10.1021/ed057p569
63. Odink, D. A.; Song, K.; Kauzlarich, S. M. *Chem. Mater.* **1992,** *4,* 906–911. doi:10.1021/cm00022a029
64. NIST X-ray Photoelectron Spectroscopy (XPS) Database, Version 3.5. https://srdata.nist.gov/xps/Default.aspx (accessed June 27, 2017).
65. Dolui, K.; Rungger, I.; Sanvito, S. *Phys. Rev. B* **2013,** *87,* 165402. doi:10.1103/PhysRevB.87.165402

License and Terms

BEILSTEIN JOURNAL OF NANOTECHNOLOGY

Transition from silicene monolayer to thin Si films on Ag(111): comparison between experimental data and Monte Carlo simulation

Alberto Curcella, Romain Bernard, Yves Borensztein, Silvia Pandolfi and Geoffroy Prévot*

Full Research Paper

Open Access

Address:
Sorbonne Universités, UPMC Univ Paris 06, CNRS-UMR 7588, Institut des NanoSciences de Paris, F-75005, Paris, France

Email:
Geoffroy Prévot* - prevot@insp.jussieu.fr

* Corresponding author

Keywords:
Auger electron spectroscopy; scanning tunneling microscopy; silicene; silicon; silver

Beilstein J. Nanotechnol. **2018,** *9,* 48–56.
doi:10.3762/bjnano.9.7

Received: 31 March 2017
Accepted: 08 December 2017
Published: 05 January 2018

This article is part of the Thematic Series "Silicene, germanene and other group IV 2D materials".

Guest Editor: P. Vogt

Abstract

Scanning tunneling microscopy (STM), Auger electron spectroscopy (AES) and low energy electron diffraction have been used to follow the growth of Si films on Ag(111) at various temperatures. Using a simple growth model, we have simulated the distribution of film thickness as a function of coverage during evaporation, for the different temperatures. In the temperature regime where multilayer silicene has been claimed to form (470–500 K), a good agreement is found with AES intensity variations and STM measurements within a Ag surfactant mediated growth, whereas a model with multilayer silicene growth fails to reproduce the AES measurements.

Introduction

Since their discovery in 2012 [1], silicene layers have been attracting a great interest, due to the expectation of electronic properties similar to the ones of graphene, based on theoretical studies [2]. Because of their easy synthesis, Si/Ag(111) monolayers have been intensively studied [3-6]. It has been shown that several monolayer structures can be formed, depending on the substrate temperature [7]. All of them probably correspond to a buckled honeycomb structure for Si atoms. For example, a buckling of 0.77 Å has been precisely measured for the (4 × 4) structure [8-10]. Silicene growth has also been reported on other substrates, such as Ir [11], ZrB_2 [12], or MoS_2 [13], although the precise crystallographic structure of these layers has not been elucidated yet.

In spite of its atomic structure close to the one of free standing silicene, silicene/Ag(111) displays different electronic properties [14,15]. This is due to a strong electronic coupling between the substrate and the silicene layer. Thus, the features in the angle resolved photoemission spectrometry (ARPES) [1], initially attributed to Dirac cones near the Fermi level, have

been shown to be related to a modification of the silver band structure induced by the silicene reconstruction [14,16-19]. This strong coupling also gives rise to Si–Ag atomic exchange during the deposition of Si on the Ag(111) surface [6,20-22].

In order to avoid such strong coupling, attempts have been made to grow silicene multilayers, or "silicite" thin films, with an atomic structure similar to the one of graphite, by evaporating larger amount of Si. On Ag(111), deposition on a substrate held at 470–500 K results in the formation of successive Si layers [23-26], with an interlayer spacing of ≈3Å. Such layers display an electronic band structure, measured by ARPES, that has been interpreted as a Dirac cone located 0.25 eV below the Fermi level [27]. These layers present a metallic behavior, with an electric conductivity one order of magnitude lower than the one measured for multilayer graphene [26]. Their structure slightly differs from the one of diamond, with an interlayer spacing 1% smaller than the one found between two consecutive hexagonal buckled planes in diamond-like bulk silicon, and a Raman peak also 1% shifted from the position expected for bulk Si. They have been firstly described as a new Si allotrope, made by successive stacking of silicene layers [23-26].

However, as the surface termination presents a $(\sqrt{3} \times \sqrt{3})R30°$ reconstruction relative to the silicene unit cell, which is very similar to the honeycomb-chained triangle (HCT) reconstruction observed on a Ag/Si(111) surface, it has been hypothesized that the observed films could result from the growth of diamond-like Si with Ag acting as a surfactant [28]. Such conclusions were also supported by low energy electron diffraction (LEED) [29,30], ARPES [31] and grazing incidence X-ray diffraction [32]. The diamond-like structure of the film has been confirmed by scanning tunneling microscopy (STM) [33] and optical measurements [34]. The Ag termination of the surface has been also demonstrated by Auger electron spectroscopy (AES) [34], metastable atom electron spectroscopy [35] and deuterium exposure of the film [36], whereas opposite conclusions were obtained from STM observations after applying a bias pulse at low temperature [33].

Very recently, the existence of two different growth modes on Ag(111), depending on the substrate temperature, has been proposed [37,38]. At low temperature (T = 470 K), multilayer silicene would form, without Ag at the surface, whereas diamond-like growth would occur at high temperature (T = 570 K), with Ag acting as a surfactant. Thus, open questions remain on the nature of the films formed as a function of the growth temperature and on the growth mechanisms. In this paper, we have used STM, AES and LEED to follow the growth of Si films at various temperatures. Using a simple growth model, we have simulated the distribution of film thickness as a function of coverage during evaporation, for the different temperatures. In the temperature regime where multilayer silicene has been claimed to form (470–500 K), a good agreement is found with AES intensity variations and STM measurements within a Ag surfactant mediated growth, whereas a model with multilayer silicene growth fails to reproduce the AES measurements.

Results and Discussion

Auger spectra taken before and after Si evaporation at the different temperatures are shown in Figure 1a–c. We have followed the peak-to-peak intensities of the Ag MNN and Si LVV transitions at 355 eV and 92 eV respectively, during growth at different substrate temperatures (T = 200 K, 473 K and 505 K). In the following, all intensities have been normalized to the Ag intensity measured for the clean surface prior evaporation. The evolution of the normalized Auger intensities I_{Ag} and I_{Si} is shown in Figure 1d and 1e as a function of Si coverage. For high temperature measurements, the coverage θ has been calibrated from the breaks observed in the evolution of I_{Si} that were attributed to the completion of a silicene monolayer. Here, one monolayer (ML) is referred to the honeycomb silicene plane, whose density is 15.7 atom·nm^{-2}. This also corresponds to the atomic density of a Si(111) double plane in bulk silicon. For deposition at 200 K, the coverage has been calibrated to obtain the same value of $dI_{Si}/d\theta(0)$ as the one measured at 473 K and 505 K.

For growth at 200 K, I_{Ag} decays exponentially to zero which indicates that the Si film completely covers the substrate (Figure 1d). The Si normalized intensity converges to $I_{Si}^{\infty} = 0.60 \pm 0.04$ (Figure 1e), thus corresponding to the value for a clean Si surface. Note that this value slightly differs from the one measured in [34], probably due to the different geometry used (the incidence of the electron beam with the sample normal is 30° here instead of 45° in [34]). After growth at 200 K, the LEED diagram showed only a diffuse background, which indicates that the film is amorphous. On the contrary, for growth at higher temperature, I_{Ag} does not decay to zero (Figure 1d), but to a value $I_{Ag}^{\infty} = 0.185 \pm 0.02$ for T = 473 K and $I_{Ag}^{\infty} = 0.25 \pm 0.04$ for T = 505 K. Moreover, I_{Si} saturates at a value lower than 0.6, namely $I_{Si}^{\infty} = 0.40 \pm 0.04$ for both temperatures. These two observations demonstrate that the surface is not a thick continuous pure Si layer.

Figure 1f and Figure 1g show the LEED diagrams measured at room temperature after 12 ML deposition at 473 K and 505 K. They both display the spots of the Si $(\sqrt{3} \times \sqrt{3})R30°$ reconstruction, associated with a single epitaxial relationship for T = 473 K, corresponding to $[1\,\bar{1}0]_{Si}$ // $[1\,\bar{1}0]_{Ag}$ and with a

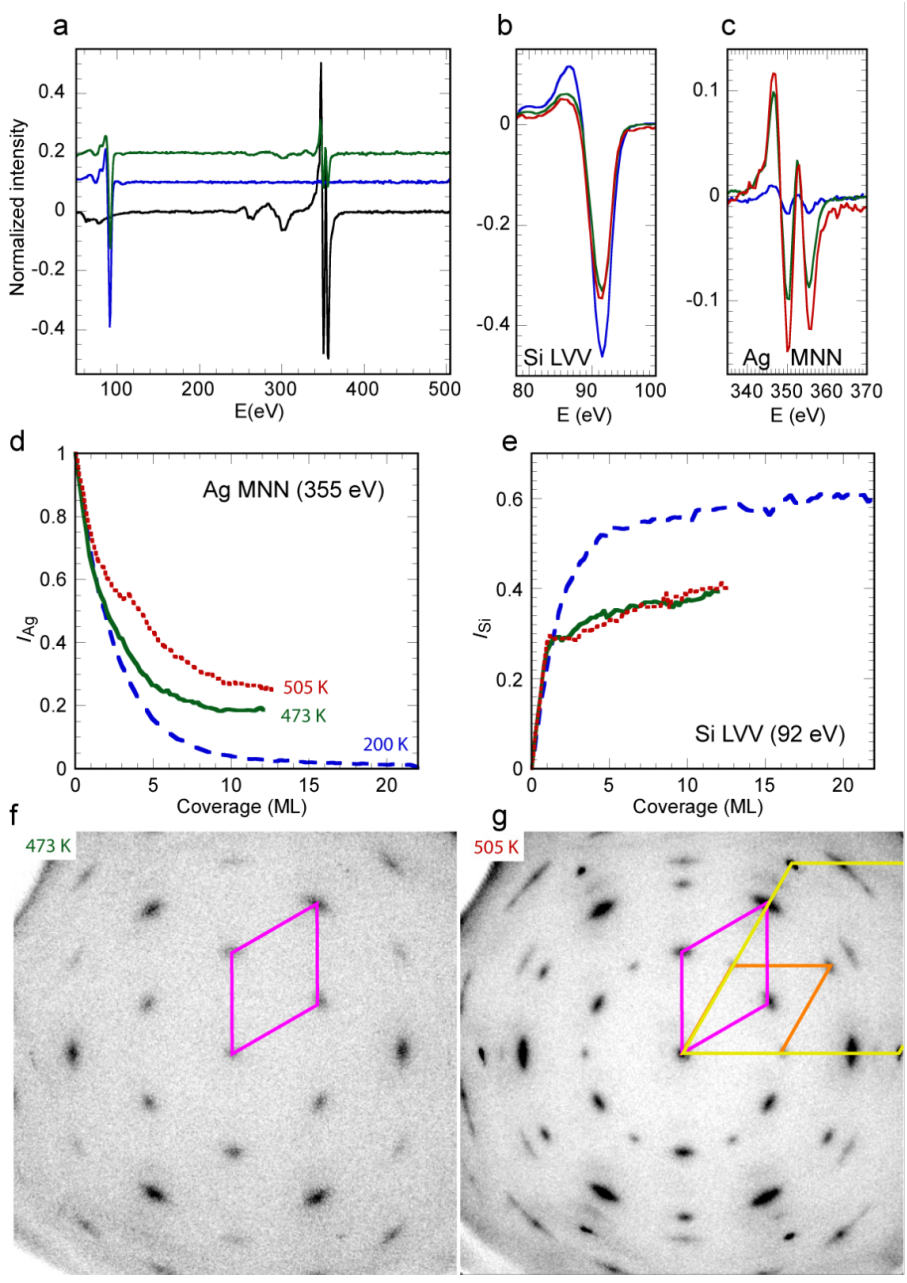

Figure 1: a) Full Auger spectra for the bare Ag surface (black line), after 22 ML Si evaporation at 200 K (blue line), and after 9 ML Si evaporation at 473 K (green line) - the spectra are shifted for clarity. b,c) Si LVV (b) and Ag MNN (c) signals after 12 ML Si evaporation at 200 K (blue line), 473 K (green line) and 505 K (red line). d,e) Evolution of the Ag (d) and Si (e) Auger intensities as a function of the Si coverage, for growth at 200 K (blue dashed line), 473 K (green continuous line) and 505 K (red dotted line). f,g) LEED diagrams obtained after 12 ML Si evaporation at 473 K (f) or 505 K (g), for E = 70 eV. The yellow lozenge is the surface unit cell of Ag(111), the purple and orange lozenges are the surface unit cells for the (√3 × √3)R30° reconstruction of Si(111).

minority epitaxial relationship for T = 505 K, corresponding to $[1\,\bar{1}0]_{Si}$ // $[1\bar{2}1]_{Ag}$.

For growth at T = 473 K, the substrate spots are practically no more visible, and the LEED intensity from these spots is around three order of magnitude less than the value measured on the bare surface. Thus, the measured Ag Auger intensity, which is equal to 20% of its initial value, cannot be due to part of the surface covered by very thin Si layers. Note that these results are completely at variance from those obtained by LEED and AES by De Padova et al. [37]: after evaporation of 10 ML Si at 473 K, they have observed that the ratio of the Si and Ag Auger intensities was very small, namely I_{Ag}/I_{Si} = 0.09, instead of I_{Ag}/I_{Si} = 1.16 for the silicene monolayer. On the contrary, the

most intense spots on their LEED diagram were the substrate spots. From that, they concluded to an imperfect wetting of the 10 ML film.

Coming back to the present results, our LEED diagram obtained after growth at $T = 505$ K shows results quite different from the 473 K ones. Substrate spots are clearly seen after deposition of 12 ML. The high intensity of the substrate spots shows that the film does not cover the whole surface homogeneously. As a consequence, the substrate must also significantly contribute to the AES signal measured at the end of growth, which is indeed larger than its value for 473 K (Figure 1d).

In Figure 2 are presented STM images of the surface after Si growth at different temperatures. Figure 2a shows the surface after evaporation of 1 ML Si at 200 K. In Figure 2b is shown the corresponding distribution of apparent height. Even if, for this low deposition temperature, the film is amorphous, the distribution shows a clear peak at 0.20 nm characteristic of the apparent height of a first Si layer, and a shoulder at 0.40 nm characteristic of a second Si level. The peak at zero corresponds to the Ag surface. For this evaporated quantity, the surface is not fully covered with Si, since nearly one quarter of the surface remains free. This indicates that the second layer starts to grow before completion of the first one, corresponding to a rough growth mode of the amorphous film.

For growth at 506 K, a similar behaviour is observed, but after completion of the monolayer: above 1 ML, thicker islands grow, with a (√3 × √3)R30° reconstruction, in a rough growth mode, as shown in Figure 2c for 2.2 ML. In Figure 2e is presented, for the same area, the apparent height of the surface modulo the Ag step height h_{Ag}. For clarity, if one applies this algorithm to the bare Ag surface, all terraces appear at the same z level. For the Si/Ag film, islands with same thickness appear at the same z value in the [0, h_{Ag}[interval. This allows to display, with a same color, Si islands of same thickness, independently of the initial Ag terrace where they have grown. In Figure 2e, brown regions correspond to Si islands. The large flat orange domains correspond to the silicene monolayer. For such coverage (2.2 ML), the monolayer covers 45% of the surface. In Figure 2g is shown the surface after evaporation of ≈3 ML at 540 K. In that case, in addition to large flat islands, very thick islands also form. For example, the apparent height of the island shown in Figure 2g is 11 nm. Note that the silicene monolayer has not dewetted for this growth temperature and that a large part of the surface is covered by this layer.

In order to discriminate between the different growth models, and to determine if the differences observed between Si growth in the 470–540 K temperature range result from two different

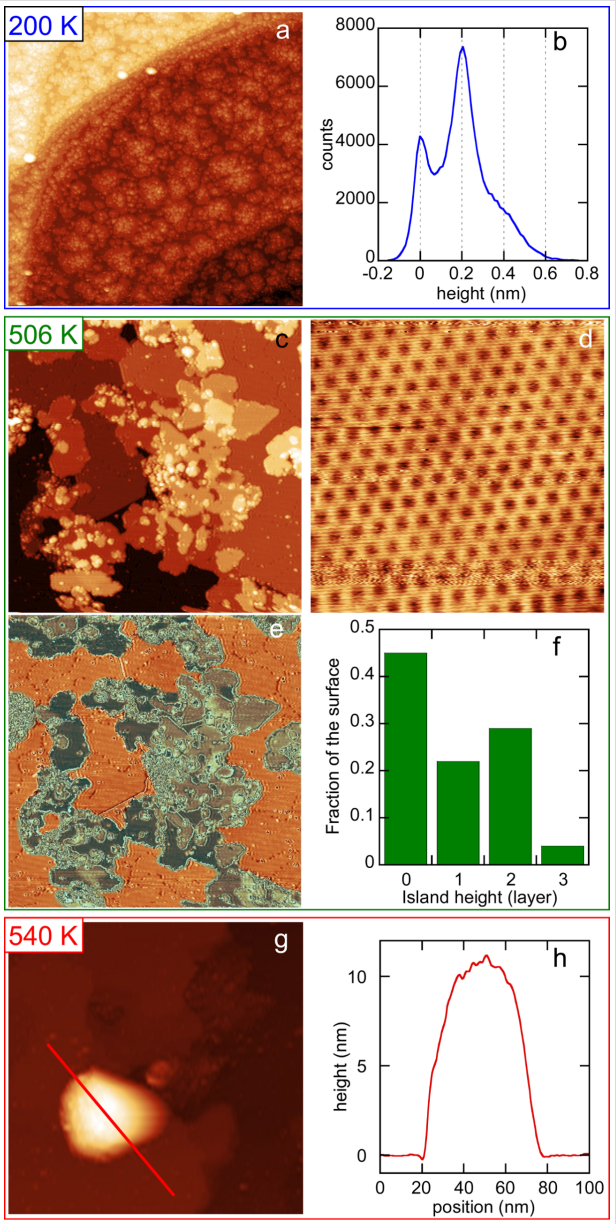

Figure 2: STM images of the Ag(111) surface after evaporation of 1 ML Si at 200 K (a), 2.2 ML Si at 506 K (c,e), ≈3 ML Si at 540 K (g). e) shows the apparent height of the surface modulo the Ag step height. Size of the images 170 × 170 nm^2. b) and f) Distribution of heights extracted from the large terrace in image (a) and from image (e) respectively. d) Detailed view (8.4 × 8.4 nm^2) of the Si film with (√3 × √3)R30° reconstruction, for growth at 506 K. h) Height profile along the line shown in (g).

growth modes, we have computed the evolution of the distribution of film thickness during evaporation, in the frame of a Monte Carlo simulation, and compared the results to the AES data. In the model chosen, the film is constituted by different terraces of various heights $h_i = i \times d_0$ where d_0 is the Si interlayer spacing. For the N_{pt} experimental points corresponding to the various coverages, the distribution of the terrace heights is used to calculate the Auger intensity. This is done by assuming

either a surface termination for the silicon film similar to the Ag-induced (√3 × √3)R30° Si(111) reconstruction, or a pure Si termination. The Auger intensities have been computed using effective attenuation lengths [39] (EAL) for electrons, that have been fitted to obtain the best agreement with the experiments, and are obviously kept fixed for all experiments. The normalized Auger intensities for Ag and Si are given by the following equations in the framework of no Ag surfactant layer:

$$I_{\mathrm{Ag}} = \sum_h f(h)\exp\left(-h/\mathrm{EAL}_{\mathrm{Si}}^{355}\right)$$

$$I_{\mathrm{Si}} = I_{\mathrm{Si}}^0\left(1-\sum_h f(h)\exp\left(-h/\mathrm{EAL}_{\mathrm{Si}}^{92}\right)\right),$$

whereas in the framework of a surfactant Ag layer, they are given by:

$$I_{\mathrm{Ag}} = f(d_0)\exp\left(-d_0/\mathrm{EAL}_{\mathrm{Si}}^{355}\right) + \sum_h f(h)\left[\begin{array}{l}\exp\left(-h/\mathrm{EAL}_{\mathrm{Si}}^{355} - e_0/\mathrm{EAL}_{\mathrm{Ag}}^{355}\right)\\ +\left(1-\exp\left(-e_0/\mathrm{EAL}_{\mathrm{Ag}}^{355}\right)\right)\end{array}\right]$$

$$I_{\mathrm{Si}} = I_{\mathrm{Si}}^0\left(1-\sum_h f(h)\exp\left(-h/\mathrm{EAL}_{\mathrm{Si}}^{92} - e_0/\mathrm{EAE}_{\mathrm{Ag}}^{92}\right)\right),$$

Where e_0 = 0.13 nm is the equivalent thickness of the surfactant Ag layer, $f(h)$ is the fraction of the surface covered by a Si layer of thickness h, and $I_{\mathrm{Si}}^0 = I_{\mathrm{Si}}^{\infty}(200\,\mathrm{K})$. The values of the EAL for 355 eV and 92 eV electrons through a Si layer, $\mathrm{EAL}_{\mathrm{Si}}^{355}$ and $\mathrm{EAL}_{\mathrm{Si}}^{92}$, have been set to obtain the best agreement with Auger data in the linear submonolayer regime. In the model of surfactant Ag, the attenuation lengths through Ag layers have been set to obtain the best agreement for the values of $I_{\mathrm{Ag}}^{\infty}(473\,\mathrm{K})$ and $I_{\mathrm{Si}}^{\infty}(473\,\mathrm{K})$. Note that they do not play any role in the case of Ag-free growth. All EAL values are given in Table 1. They are in a relative good agreement with computed values of inelastic mean free path (IMFP) [40], taking into account the fact that the attenuation length should be less than the IMFP due to a collection angle less than 90° for the escaping electrons, and the large uncertainty related to the computation of the IMFP [40].

Table 1: Effective attenuation lengths fitted from the Auger signals, and comparison with calculated IMFP [40].

	fitted values (nm)	IMFP (nm)
$\mathrm{EAL}_{\mathrm{Ag}}^{92}$	0.32	0.51
$\mathrm{EAL}_{\mathrm{Ag}}^{355}$	0.72	0.71
$\mathrm{EAL}_{\mathrm{Si}}^{92}$	0.52	0.48
$\mathrm{EAL}_{\mathrm{Si}}^{355}$	0.76	1.14

The comparison between simulated (I_{th}) and experimental (I_{exp}) intensities provides the value of

$$\chi^2 = \frac{1}{N_{\mathrm{pt}} - N_{\mathrm{par}}}\sum^{N_{\mathrm{pt}}}\left(\frac{I_{\mathrm{th}} - I_{\mathrm{exp}}}{\sigma_{\mathrm{exp}}}\right)^2,$$

associated with the model of the simulation, N_{par} being the number of free parameters. This process is used to adjust the parameters of the model until a minimum of χ^2 is reached.

At each step of the simulation, an evaporated Si atom arrives on a terrace of height h_i with a probability proportional to the fraction of the surface covered by the terraces of such height $f(i)$, giving rise to a variation δθ of the coverage. This atom has then the probabilities $p_n(i)$, $p_d(i)$, $p_u(i)$ to either nucleate on this terrace, diffuse to a lower terrace or to an upper terrace. For simplicity, we assume that these probabilities are proportional to the fraction of the surface covered with terraces of height h_i, h_{i-1} and h_{i+1} respectively, with proportion factors equal to $\alpha_n(i)$, $\alpha_d(i)$, $\alpha_u(i)$. They are thus given by:

$$p_n(i) = \alpha_n(i)f(i)/S$$
$$p_d(i) = \alpha_d(i)f(i-1)/S$$
$$p_u(i) = \alpha_u(i)f(i+1)/S$$
$$S = \alpha_n(i)f(i) + \alpha_d(i)f(i-1) + \alpha_u(i)f(i+1).$$

The atom stops diffusing when it nucleates. In the frame of multilayer silicene growth, above the monolayer, nucleation gives rise to the growth of successive terraces. In the frame of silicon growth mediated by surfactant Ag atoms, the nucleation above the Si monolayer is treated differently, as it gives rise to the formation of thick Si islands with an additional layer corresponding to the Ag–Si HCT reconstruction on top of the island. In that case, nucleation of an atom on the monolayer results in the growth of an island of height h_{min}, covering a fraction δθ of the surface, by conversion of a fraction $\delta\theta(h_{\mathrm{min}} + 0.5)$ of the monolayer into a thick island, and $p_u(0)$ becomes the probability for an atom on the substrate to jump on. Note that we have taken into account the fact that the HCT reconstruction corresponds to an additional Si amount of 0.5 ML. Note also that multilayer silicene growth would correspond to $h_{\mathrm{min}} = 2$, without HCT layer. With no loss of generality, we have set $\alpha_n(i) = 1$. The free parameters of the model are thus the values of $\alpha_d(i)$, $\alpha_u(i)$, h_{min}. For each temperature, $\alpha_d(i)$ and $\alpha_u(i)$ have been

chosen constant, except for the diffusion between the substrate and the silicene layer, and between the silicene layer and the thicker islands in the framework of Ag-surfactant growth.

All kind of growth modes can be simulated using these parameters. For example, setting $\alpha_u(i) = 0$ and $\alpha_d(i) >> 1$ leads to a classical 2D or Frank–van der Merwe growth mode. Setting $\alpha_d(i) = 0$ and $\alpha_u(i) >> 1$ leads to a classical 3D or Volmer–Weber growth. Stranski–Krastanov growth is obtained with $\alpha_u(i < i_c) = 0$, $\alpha_d(i \leq i_c) >> 1$, $\alpha_u(i \geq i_c) >> 1$ and $\alpha_d(i > i_c) = 0$, where i_c is the critical thickness above which 3D islands form.

Figure 3 presents the comparison of the experimental and simulated AES intensities for the three temperatures studied. The corresponding parameters of the simulation are given in Table 2.

For $T = 200$ K, (Figure 3a) a good agreement is found with a model of random growth, with no surfactant Ag, with a medium probability for an incoming atom to diffuse from the first Si layer to the substrate ($\alpha_d(i) = 1$), the other values of $\alpha_d(i)$ and $\alpha_u(i)$ being small. The distribution of island height after 12 ML Si evaporation at 200 K is shown in Figure 3f and is very close to the one derived from the binomial distribution, i.e., if the α_d and α_u coefficients are set to zero, with variance equal to 14.4 instead of 12. For such temperature, the notion of layer for the amorphous film is no more adequate, excepted for the very first layers. We have checked that the level of discretization used in the simulation did not change the final results.

A good agreement is also obtained between AES experimental and simulated intensity evolutions for $T = 473$ K and $T = 505$ K, if one assumes that Ag acts as a surfactant for the growth of Si/Ag(111) (Figure 3b and Figure 3d). The fits have been obtained with different probabilities for the growth parameters, which obviously depend on the temperature. Note that the $\alpha_d(1)$ coefficient is set to an arbitrary high value to ensure the continuous wetting of the substrate by the silicene layer.

For $T = 473$ K, a good fit is obtained if one now assumes a conversion of monolayer to Si islands having a height of 2 layers and covered with Si and Ag atoms forming the $(\sqrt{3} \times \sqrt{3})R30°$ reconstruction. There is a small probability to diffuse towards the lower terraces ($\alpha_d(i > 2) = 0.23$), whereas the probability to diffuse towards the upper terraces is zero. This results in a narrow distribution of film thickness, as shown in Figure 3g, where the variance of the distribution is equal to 7.7. The simulation also predicts that, at the end of the growth, the surface is fully covered by Si islands of thickness larger than 5 layers. This explains why the intensity of the LEED

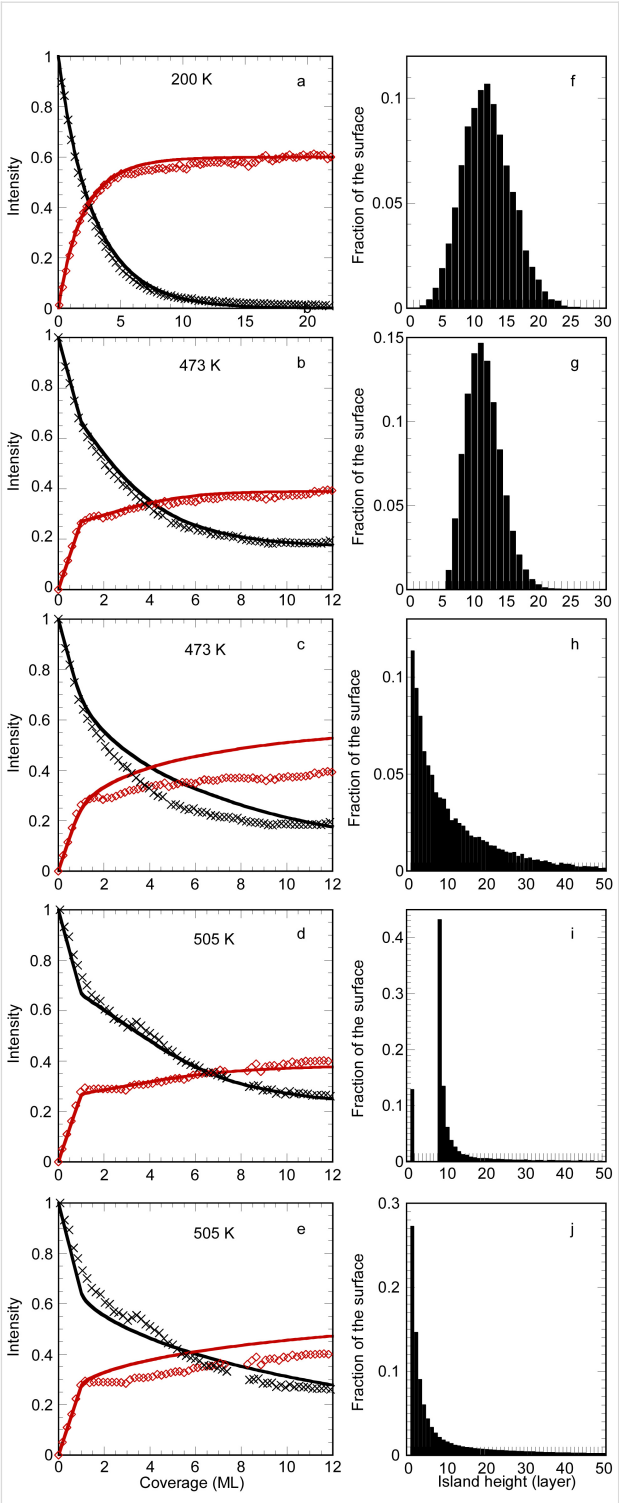

Figure 3: a–e: Evolution of the Ag (black crosses and black line) and Si (red lozenges and red lines) Auger intensities as a function of the Si coverage. Comparison between experiments (symbols) and best fits (lines) for growth at 200 K (a), 473 K (b,c) and 505 K (d,e). Fits for a), c) and e) are performed without surfactant Ag atoms, whereas fits for b) and d) are performed in the framework of a surfactant Ag layer. In f–j are drawn the corresponding histograms of the island heights at the end of the simulation.

Table 2: Parameters of the Monte Carlo simulation corresponding to the fit of the AES data shown in Figure 3a–e.

	200 K (a)	473 K (b)	473 K (c)	505 K (d)	505 K (e)
surfactant Ag	No	Yes	No	Yes	No
α_u (0)	0	0	0	0	0
α_u (1)	0.2	0.13	500	1	20
$\alpha_u(i > 1)$		0	10	12	23
$\alpha_d(1)$	1	1000	1000	1000	1000
$\alpha_d(h_{min})$	0.05	0.23	1	5	0
$\alpha_d(i > h_{min})$		0.23		0.5	
h_{min}	2	2	2	8	2

(1 × 1) spots of the substrate is very weak (Figure 1f). For this temperature, the simulation corresponds thus to an imperfect layer by layer growth mode [41] for which, after the completion of the silicene layer, the $n + 1$ layer starts to grow before completion of the n layer.

For $T = 505$ K, the best fit is obtained by conversion of the monolayer to similar islands having a height of 8 ML. At this temperature, there is a high probability, for the atoms in the islands, to diffuse towards the higher terraces ($\alpha_u(i > 1) = 12$), which results in the growth of thick islands, with a very wide distribution of film thickness (see Figure 3i). The simulation also predicts that, at the end of the growth, 13% of the surface remains covered by the silicene monolayer, which explains why the (1 × 1) spots of the substrate remains visible in Figure 1g.

On the contrary, no good fit can be obtained in the frame of a multilayer silicene growth. The best fits obtained in such framework are shown in Figure 3c for $T = 473$ K and in Figure 3e for $T = 505$ K. As it is clear from the poor agreement, this model fails to reproduce the behaviour observed for the Auger intensities above 1 ML. For both temperatures, the increase of the Si intensity is too small. For $T = 473$ K, the predicted decay of the Ag intensity is too slow whereas for $T = 505$ K, the complex behaviour of the signal cannot be reproduced. Both fits correspond to the formation of thick 3D islands above the monolayer as can be observed from the distributions shown in Figure 3h and Figure 3j.

It is also interesting to compare the simulation results with the LEED and STM observations. Figure 4a presents the comparison of the distribution of film thickness for 1 ML deposition at 200 K obtained by the Monte Carlo fit in comparison with the STM data obtained from the analysis of the STM image shown in Figure 2a. A very good agreement is found between the experimental and simulated distributions.

In Figure 4b is drawn the evolution of the surface area covered by the silicene layer as a function of Si coverage, for growth at

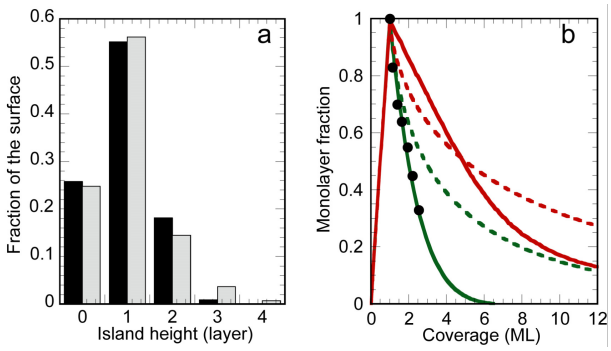

Figure 4: a) Histogram of the island heights for growth of 1 ML at 200 K. Comparison between the results of the growth simulation (grey) and the experimental values measured on the STM image shown in Figure 2a (black). b) Evolution of the surface fraction covered by the monolayer. Black dots: STM measurements during growth at 506 K. Green and red lines: results of growth simulations fitted on AES data at $T = 473$ K and $T = 505$ K respectively, in the framework of surfactant Ag (continuous lines) or not (dotted lines).

473 K and 505 K. For both temperatures, in a model of surfactant Ag (continuous lines), it first increases linearly up to 1 ML, and then decays with a decay length of 1.6 ML for $T = 473$ K and 7.8 ML for $T = 505$ K. A very good agreement is obtained between STM results for growth at 506 K, and growth simulations fitted on AES data at 473 K, in the framework of surfacting Ag atoms. On the contrary the simulations performed for AES data at 505 K indicate that a larger fraction of the surface remains covered by the monolayer. The simulations also predict the formation of thick islands after the completion of the monolayer, which are not observed by STM at such temperature, but are observed for growth at 540 K. For example, the height of the island shown in Figure 1g corresponds to around 35 Si layers. No correct agreement is found with the results of AES simulations performed in the framework of multilayer silicene growth (without surfactant Ag, dotted lines).

Thus, both STM and AES experiments indicate that as the temperature increases, a transition is observed between an imperfect layer-by-layer growth and a Stranski–Krastanov growth

mode (i_c = 1). This transition is observed by AES between 473 K and 505 K, and between 506 K and 540 K by STM. These differences may be due to the experimental uncertainties on the temperature measurements or to the different evaporation rates used during the experiments.

Conclusion

The quantitative analysis of the evolution of AES intensity during Si growth at different temperatures shows that the growth mechanism is different for low temperature deposition (T = 200 K) and in the regime described previously as "intermediate" (473–505 K). In particular, low temperature deposition results in a rough growth mode, with no mobility of Ag atoms. A very good agreement is obtained between AES and STM measurements for the distribution of island heights in a model with little interlayer diffusion. On the contrary, growth at intermediate temperatures results in a Ag surfactant mediated Si growth. A good agreement with AES, LEED, and STM measurements is obtained by considering that the Si islands film is terminated by the Ag/Si(111) ($\sqrt{3} \times \sqrt{3}$)R30° reconstruction. As temperature increases, thicker Si islands form and the film becomes more and more inhomogeneous, resulting in a larger fraction of the surface uncovered by the thick Si islands.

Experimental

Experiments were performed in two UHV set-ups with 10^{-10} mbar base pressure. The Ag(111) sample was cleaned by series of cycles of Ar ion sputtering at 0.6 keV followed by annealing at 850 K. Si was evaporated from a Si rod with a commercial Omicron EFM3 evaporator. For AES/LEED experiments, the evaporation rate was between 0.03 and 0.06 ML/min, whereas for STM experiments, it was around 0.004 ML/min. Auger peak-to-peak intensities were measured during growth with a Riber CMA Auger spectrometer working at 3 keV primary beam, 30° incidence, using a lock-in amplifier at 1 kHz with 0.4 V modulation amplitude. LEED patterns were obtained with an Omicron SPA-LEED apparatus, at ambient temperature after evaporation. STM images were obtained during growth with an Omicron VT-XA STM. Image corrections were performed using a home-made software described elsewhere [42]. Temperature measurements were performed with a thermocouple located on the sample heating stages, previously calibrated with another thermocouple soldered on the surface of a testing sample. As a result, if for a given sample in either set-up the precision on the reproducibility of the measure is of the order of 1K, the uncertainty on the absolute value of the temperature may be of the order of 10 to 20 K at 500 K. The previous analysis shows indeed that the measured temperature in the STM set-up is likely overestimated with respect to the one in the AES/LEED set-up.

Acknowledgements

This work was supported by French state funds managed by the ANR within the Investissements d'Avenir program under Reference ANR-11-IDEX-0004-02 and more specifically within the framework of the Cluster of Excellence MATISSE. We are grateful to Hervé Cruguel and Sébastien Royer for their technical support.

References

1. Vogt, P.; De Padova, P.; Quaresima, C.; Avila, J.; Frantzeskakis, E.; Asensio, M. C.; Resta, A.; Ealet, B.; Le Lay, G. *Phys. Rev. Lett.* **2012,** *108,* 155501. doi:10.1103/PhysRevLett.108.155501
2. Cahangirov, S.; Topsakal, M.; Aktürk, E.; Şahin, H.; Ciraci, S. *Phys. Rev. Lett.* **2009,** *102,* 236804. doi:10.1103/PhysRevLett.102.236804
3. Jamgotchian, H.; Colignon, Y.; Hamzaoui, N.; Ealet, B.; Hoarau, J. Y.; Aufray, B.; Bibérian, J. P. *J. Phys.: Condens. Matter* **2012,** *24,* 172001. doi:10.1088/0953-8984/24/17/172001
4. Lin, C.-L.; Arafune, R.; Kawahara, K.; Tsukahara, N.; Minamitani, E.; Kim, Y.; Takagi, N.; Kawai, M. *Appl. Phys. Express* **2012,** *5,* 045802. doi:10.1143/APEX.5.045802
5. Feng, B.; Ding, Z.; Meng, S.; Yao, Y.; He, X.; Cheng, P.; Chen, L.; Wu, K. *Nano Lett.* **2012,** *12,* 3507–3511. doi:10.1021/nl301047g
6. Bernard, R.; Borensztein, Y.; Cruguel, H.; Lazzeri, M.; Prévot, G. *Phys. Rev. B* **2015,** *92,* 045415. doi:10.1103/PhysRevB.92.045415
7. Lee, G.-W.; Chen, H.-D.; Lin, D.-S. *Appl. Surf. Sci.* **2015,** *354,* 187–195. doi:10.1016/j.apsusc.2015.01.155
8. Fukaya, Y.; Mochizuki, I.; Maekawa, M.; Wada, K.; Hyodo, T.; Matsuda, I.; Kawasuso, A. *Phys. Rev. B* **2013,** *88,* 205413. doi:10.1103/PhysRevB.88.205413
9. Kawahara, K.; Shirasawa, T.; Arafune, R.; Lin, C.-L.; Takahashi, T.; Kawai, M.; Takagi, N. *Surf. Sci.* **2014,** *623,* 25–28. doi:10.1016/j.susc.2013.12.013
10. Curcella, A.; Bernard, R.; Borensztein, Y.; Resta, A.; Lazzeri, M.; Prévot, G. *Phys. Rev. B* **2016,** *94,* 165438. doi:10.1103/PhysRevB.94.165438
11. Meng, L.; Wang, Y.; Zhang, L.; Du, S.; Wu, R.; Li, L.; Zhang, Y.; Li, G.; Zhou, H.; Hofer, W. A.; Gao, H.-J. *Nano Lett.* **2013,** *13,* 685–690. doi:10.1021/nl304347w
12. Fleurence, A.; Friedlein, R.; Ozaki, T.; Kawai, H.; Wang, Y.; Yamada-Takamura, Y. *Phys. Rev. Lett.* **2012,** *108,* 245501. doi:10.1103/PhysRevLett.108.245501
13. Chiappe, D.; Scalise, E.; Cinquanta, E.; Grazianetti, C.; van den Broek, B.; Fanciulli, M.; Houssa, M.; Molle, A. *Adv. Mater.* **2014,** *26,* 2096–2101. doi:10.1002/adma.201304783
14. Cahangirov, S.; Audiffred, M.; Tang, P.; Iacomino, A.; Duan, W.; Merino, G.; Rubio, A. *Phys. Rev. B* **2013,** *88,* 035432. doi:10.1103/PhysRevB.88.035432
15. Lin, C.-L.; Arafune, R.; Kawahara, K.; Kanno, M.; Tsukahara, N.; Minamitani, E.; Kim, Y.; Kawai, M.; Takagi, N. *Phys. Rev. Lett.* **2013,** *110,* 076801. doi:10.1103/PhysRevLett.110.076801
16. Gori, P.; Pulci, O.; Ronci, F.; Colonna, S.; Bechstedt, F. *J. Appl. Phys.* **2013,** *114,* 113710. doi:10.1063/1.4821339
17. Tsoutsou, D.; Xenogiannopoulou, E.; Golias, E.; Tsipas, P.; Dimoulas, A. *Appl. Phys. Lett.* **2013,** *103,* 231604. doi:10.1063/1.4841335
18. Chen, M. X.; Weinert, M. *Nano Lett.* **2014,** *14,* 5189–5193. doi:10.1021/nl502107v

19. Mahatha, S. K.; Moras, P.; Bellini, V.; Sheverdyaeva, P. M.; Struzzi, C.; Petaccia, L.; Carbone, C. *Phys. Rev. B* **2014,** *89,* 201416. doi:10.1103/PhysRevB.89.201416
20. Prévot, G.; Bernard, R.; Cruguel, H.; Borensztein, Y. *Appl. Phys. Lett.* **2014,** *105,* 213106. doi:10.1063/1.4902811
21. Sone, J.; Yamagami, T.; Aoki, Y.; Nakatsuji, K.; Hirayama, H. *New J. Phys.* **2014,** *16,* 095004. doi:10.1088/1367-2630/16/9/095004
22. Satta, M.; Colonna, S.; Flammini, R.; Cricenti, A.; Ronci, F. *Phys. Rev. Lett.* **2015,** *115,* 026102. doi:10.1103/PhysRevLett.115.026102
23. De Padova, P.; Vogt, P.; Resta, A.; Avila, J.; Razado-Colambo, I.; Quaresima, C.; Ottaviani, C.; Olivieri, B.; Bruhn, T.; Hirahara, T.; Shirai, T.; Hasegawa, S.; Asensio, M. C.; Le Lay, G. *Appl. Phys. Lett.* **2013,** *102,* 163106. doi:10.1063/1.4802782
24. De Padova, P.; Avila, J.; Resta, A.; Razado-Colambo, I.; Quaresima, C.; Ottaviani, C.; Olivieri, B.; Bruhn, T.; Vogt, P.; Asensio, M. C.; Le Lay, G. *J. Phys.: Condens. Matter* **2013,** *25,* 382202. doi:10.1088/0953-8984/25/38/382202
25. De Padova, P.; Ottaviani, C.; Quaresima, C.; Olivieri, B.; Imperatori, P.; Salomon, E.; Angot, T.; Quagliano, L.; Romano, C.; Vona, A.; Muniz-Miranda, M.; Generosi, A.; Paci, B.; Le Lay, G. *2D Mater.* **2014,** *1,* 021003. doi:10.1088/2053-1583/1/2/021003
26. Vogt, P.; Capiod, P.; Berthe, M.; Resta, A.; De Padova, P.; Bruhn, T.; Le Lay, G.; Grandidier, B. *Appl. Phys. Lett.* **2014,** *104,* 021602. doi:10.1063/1.4861857
27. De Padova, P.; Quaresima, C.; Ottaviani, C.; Sheverdyaeva, P. M.; Moras, P.; Carbone, C.; Topwal, D.; Olivieri, B.; Kara, A.; Oughaddou, H.; Aufray, B.; Le Lay, G. *Appl. Phys. Lett.* **2010,** *96,* 261905. doi:10.1063/1.3459143
28. Mannix, A. J.; Kiraly, B.; Fisher, B. L.; Hersam, M. C.; Guisinger, N. P. *ACS Nano* **2014,** *8,* 7538–7547. doi:10.1021/nn503000w
29. Shirai, T.; Shirasawa, T.; Hirahara, T.; Fukui, N.; Takahashi, T.; Hasegawa, S. *Phys. Rev. B* **2014,** *89,* 241403. doi:10.1103/PhysRevB.89.241403
30. Kawahara, K.; Shirasawa, T.; Lin, C.-L.; Nagao, R.; Tsukahara, N.; Takahashi, T.; Arafune, R.; Kawai, M.; Takagi, N. *Surf. Sci.* **2016,** *651,* 70–75. doi:10.1016/j.susc.2016.03.029
31. Mahatha, S. K.; Moras, P.; Sheverdyaeva, P. M.; Flammini, R.; Horn, K.; Carbone, C. *Phys. Rev. B* **2015,** *92,* 245127. doi:10.1103/PhysRevB.92.245127
32. Curcella, A.; Bernard, R.; Borensztein, Y.; Lazzeri, M.; Resta, A.; Garreau, Y.; Prévot, G. *2D Mater.* **2017,** *4,* 025067. doi:10.1088/2053-1583/aa65b8
33. Chen, J.; Du, Y.; Li, Z.; Li, W.; Feng, B.; Qiu, J.; Cheng, P.; Xue Dou, S.; Chen, L.; Wu, K. *Sci. Rep.* **2015,** *5,* 13590. doi:10.1038/srep13590
34. Borensztein, Y.; Curcella, A.; Royer, S.; Prévot, G. *Phys. Rev. B* **2015,** *92,* 155407. doi:10.1103/PhysRevB.92.155407
35. Lin, C.-L.; Hagino, T.; Ito, Y.; Kawahara, K.; Nagao, R.; Aoki, M.; Masuda, S.; Arafune, R.; Kawai, M.; Takagi, N. *J. Phys. Chem. C* **2016,** *120,* 6689–6693. doi:10.1021/acs.jpcc.6b00717
36. Chen, H.-D.; Chien, K.-H.; Lin, C.-Y.; Chiang, T.-C.; Lin, D.-S. *J. Phys. Chem. C* **2016,** *120,* 2698–2702. doi:10.1021/acs.jpcc.5b10208
37. De Padova, P.; Generosi, A.; Paci, B.; Ottaviani, C.; Quaresima, C.; Olivieri, B.; Salomon, E.; Angot, T.; Le Lay, G. *2D Mater.* **2016,** *3,* 031011. doi:10.1088/2053-1583/3/3/031011
38. Grazianetti, C.; Cinquanta, E.; Tao, L.; De Padova, P.; Quaresima, C.; Ottaviani, C.; Akinwande, D.; Molle, A. *ACS Nano* **2017,** *11,* 3376–3382. doi:10.1021/acsnano.7b00762
39. Jablonski, A.; Powell, C. J. *Surf. Sci. Rep.* **2002,** *47,* 33–91. doi:10.1016/S0167-5729(02)00031-6
40. Tanuma, S.; Powell, C. J.; Penn, D. R. *Surf. Interface Anal.* **1991,** *17,* 911–926. doi:10.1002/sia.740171304
41. Franchy, R. *Surf. Sci. Rep.* **2000,** *38,* 195–294. doi:10.1016/S0167-5729(99)00013-8
42. Wilson, A.; Bernard, R.; Vlad, A.; Borensztein, Y.; Coati, A.; Croset, B.; Garreau, Y.; Prévot, G. *Phys. Rev. B* **2014,** *90,* 075416. doi:10.1103/PhysRevB.90.075416

License and Terms